Multi-Mode Coaxial Transmon Qubits For Quantum Computing and Sensing

James Fox Wills
St Catherine's College
University of Oxford

A thesis submitted for the degree of
Doctor of Philosophy
Trinity 2022

For

Gammy and Gampy

Multi-Mode Coaxial Transmon Qubits For Quantum Computing and Sensing

James Fox Wills
St Catherine's College, University of Oxford

A thesis submitted for the degree of
Doctor of Philosophy

Trinity 2022

Abstract

Superconducting circuits are well established as a viable candidate for the realisation of quantum computers. Circuits based on the transmon qubit are now ubiquitous, owing to its simple design and reduced control wiring overhead. An issue with transmon qubit-based architectures is the always-on unwanted interactions that impose limits on gate speeds and introduce errors into their operation. In addition, understanding sources of noise and decoherence is essential to the low-error operation quantum computers.

This thesis describes the implementation of a multi-mode superconducting qubit in a coaxial circuit QED architecture. Constructed from three superconducting islands, connected via two Josephson junctions, the device possesses two transmon-like modes with orthogonal field symmetries. The unique polarisation of each mode allows for engineering dissipation and coupling in the system, extending functionality beyond the single-mode transmon. Experimental results on the unit-cell of the two-mode coaxial transmon are presented, demonstrating coherent control and simultaneous dispersive readout of the modes of the device. A predictive theory of charge sensitivity in a multi-mode superconducting qubit is presented, and experimental results in agreement of this theory are shown, observing sensitivity to four charge-parity configurations and two independent gate-charge offsets. The utility of a multi-mode qubit as a charge detector in spatially tracking local-charge drift of $\simeq 100\ \mu m$ length scales is also shown, demonstrating the use of these devices as tools in understanding charge-noise in superconducting circuits. Finally, a system of a pair of coupled two-mode coaxial transmons is introduced, demonstrating a highly mode-selective coupling architecture. A suppressed quantum crosstalk of 2 kHz between protected modes of the devices is measured, along with equal single qubit gate fidelities when operated both individually and simultaneously. A first characterisation of a microwave activated conditional phase interaction between computational modes driven via ancillary transitions (AT-MAP) is presented. Whilst not shown in this work, this state-dependent two-qubit interaction can be used to generate entanglement. Combined with the low crosstalk demonstrated, this shows the multi-mode qubit architecture is a promising candidate for the construction of larger scale quantum processors with fast gates and low crosstalk-related errors.

Acknowledgements

Firstly, I thank Dr. Peter Leek, for giving me the opportunity to work in this incredibly exciting and dynamic field.

Secondly, without Brian, none of this would have been possible. His wisdom, guidance, and relentless optimism has helped form me into the scientist I am today. From months of endless fridge cycles, to sketches of ideas on the back of napkins in the canteen, there was never a dull moment. I learnt so much, and look forward to working together in the future.

I owe much of this work to my immensely talented colleagues, both past and present. I particularly thank Giulio, Simone and Shuxiang. Not only did they indulge me in my aversion to the cleanroom, but working, learning and laughing together on this journey over the last four years has been thoroughly enjoyable. I also thank Joseph, Taka, Peter, Kitti and Martina for helping me at the beginning of my endeavour as a researcher, and Andy for being a consistent source of both knowledge and humour.

I have been fortunate enough to encounter many amazing people that have supported me during my time in Oxford, far too many to name. It has been a truly incredible experience that I will never forget. The college, JCR and boat club of St. Catherine's, Oxford, will always have a special place in my heart. I will cherish the memories made here dearly.

Finally, I thank my family: Mum, Dad, Hannah, Ed, and of course Archie. Their tireless love and encouragement has helped me immeasurably through these difficult years. I would not be here if it weren't for them, and for that I am truly grateful.

Contents

List of Figures

Chapter 1

Introduction

1.1 Motivation

Realising practical quantum computation requires the low-error operation of many fully controlled quantum bits with individual state readout and initialisation [1]. There are many physical systems being explored in the development of quantum computers, including: systems of trapped ions [2, 3], photonic structures [4], systems of neutral atoms [5], and silicon quantum dots [6]. Superconducting circuits are well established as a potential platform for quantum computation [7, 8]. One superconducting qubit variant, the transmon [9], has found enduring success due to its resilience to decoherence and simplicity in design. However the development of alternative qubit designs is an active area of research [10–13].

One particular issue transmon qubits suffer from is the always-on unwanted ZZ interactions that arise due to fixed dipole couplings between qubits. This quantum crosstalk causes non-negligible errors in both single-qubit and two-qubit computational operations [14], and scales quadratically with the coupling between qubits. As such, there is a trade-off to manage between two-qubit gates speeds and the contribution to errors from unwanted interactions. In addition, these static unwanted interactions cause dephasing and can limit the fidelity of parity measurements in some quantum error-correction schemes [15]. Mitigation of these contributions to errors is an active area of research, with candidates such as tunable couplers [16–19], level structure engineering [20, 21], auxiliary circuits modes [22], or active cancellation techniques with additional drive tones [23, 24]. Whilst effective, these methods add additional circuit components, tuning parameters such as flux that add sensitivities to noise [25], or contribute to active heat loads incompatible with current cryogenic hardware [26].

Here we investigate the multi-mode transmon qubit. The addition of a degree of freedom in the circuit results in an additional ancillary energy level and transition [27]. The use of these ancillary transitions has been explored widely within the field. Such uses include novel readout schemes for fast qubit state determination [28], as well as tunable coupling that limits contributions to decay due to the Purcell effect as a result of coupling to a lossy readout mechanism [29], and suppression of photon shot noise dephasing [30]. The energy level structures can also be utilised in multi-qubit operations, enabling generous resonance conditions and fast entangling operations [17], as well as native Toffoli class gates [31]. These new functionalities make multi-mode qubits potentially useful components in future quantum information processors.

Since the modes of these multi-mode systems are transmon-like, they are susceptible to the same decoherence mechanisms, and can exhibit more complex sensitivities to noise [32]. One such decoherence mechanism that affects superconducting circuits is low frequency, $1/f$-like charge noise [33]. This has been well characterised and studied in single-mode transmons, which are typically designed to operate in a charge-insensitive regime [34]. Alternatively, devices can be deliberately designed to be sensitive to charge noise, and operate as detectors of it, in order to better understand and characterise this source of decoherence [35–37].

The goal of this work is to explore how multi-mode transmon qubits can be engineered for usage in superconducting quantum information processors. We aim to exploit the multi-mode structure with a mode-selective coupling to generate protected states that can be used as computational modes, as well as coupled ancillary transitions that can allow for fast entanglement operations. This can alleviate the coupling strength constraints and unwanted interactions between computational modes that conventional transmon based architectures suffer from. In addition, we aim to explore charge-sensitivity in a multi-mode transmon qubit, ensuring that sensitivity to this decoherence mechanism can be suppressed. We aim to explore how this charge sensitivity allows the device to be used as a novel detector, and provide insights into the source of the decoherence mechanism. Understanding the origins of charge fluctuations can lead to reduction of errors in high-coherence quantum devices.

1.2 Thesis Synopsis

We begin in Chapter 2 by introducing the field of circuit quantum electrodynamics and superconducting quantum circuits. We present an overview of concepts that we explore throughout the work including charge noise, unwanted interactions, and multi-mode superconducting circuits.

Chapter 3 introduces the theoretical description of the device at the core of this work, the two-mode coaxial transmon. We explore the device Hamiltonian and the characteristic features it presents, as well as its sensitivity to charge noise and fabrication imperfections. We also introduce a system of coupled two-mode coaxial transmons, exploring the implementation of a mode-selective coupling, as well as introducing a novel two-qubit gate for entangling the protected modes of the system.

The first demonstration of the unit-cell of a two-mode coaxial transmon is shown in Chapter 4. We introduce the measurements used to characterise this and future devices, as well as demonstrating charge-insensitivity.

We explore charge sensitivity in a multi-mode superconducting qubit in Chapter 5. We observe sensitivity to four charge-parity configurations, and demonstrate a proof-of-principle experiment, utilising the multi-mode qubit as a detector of spatial charge fluctuations. This work has been published in [38].

In Chapter 6, we present measurements of a system of a pair of statically coupled two-mode coaxial transmon devices. We establish the highly mode-selective coupling architecture, as well as presenting measurements of a two-qubit state dependent interaction that is the prerequisite for an entangling gate.

Finally, in Chapter 7, we conclude by postulating the utility of these novel multimode devices to larger superconducting quantum processors. We summarise the main results of the thesis, and present possible directions for future work.

Chapter 2

Superconducting Quantum Circuits

In this chapter, we present an introduction to superconducting quantum circuits in the LC resonator and the transmon qubit. We introduce two sources of noise and decoherence in superconducting qubits—charge noise and quasiparticles—presenting an overview of current research into both areas.

An introduction to multi-qubit coupling is presented, along with two examples of multi-qubit interactions: the cross-resonance gate and microwave activated phase gate. We explore how static coupling introduces always-on unwanted ZZ interactions, and present an overview of current research into the mitigation and suppression of these error-inducing interactions.

Finally, we present an overview of research into multi-mode superconducting circuits, and an introduction to the coaxial circuit quantum electrodynamics architecture. In later chapters we present research that is built upon these two areas.

2.1 Superconducting Quantum Circuits

Weakly driven macroscopic electrical circuits with low dissipation exhibit quantum mechanical behaviour [39]. Constructing these circuits out of superconducting materials, such as aluminium or niobium-titanium alloys, enables the energy dissipation of the system to be close to zero, thus reaching the quantum mechanical regime.

Conventional cryogenic solutions such as dilution refrigeration can be utilised to cool circuits to temperatures of $\sim$ 20 mK, and typical circuits operate in the microwave frequency regime ($\approx 4 - 12$ GHz). At this temperature the thermal excitations of qubits are suppressed, such that excited state populations, p_e, are $\sim$ 0.1 %. Hence a quantum system can be assumed to be approximately in its ground state.

The physical length scale of superconducting quantum circuits ($d \approx 1$ mm) is smaller than the microwave frequency wavelength at which they resonate ($\lambda \approx 1$ cm). We use a lumped element treatment of electrical circuit components [40], however note that $d \approx 0.1\lambda$ is approaching the limit where this approximation is no longer valid. For any larger circuits, a distributed-element model is required.

The field of superconducting quantum circuits is not limited to the investigation of quantum information and quantum computing. Recent advancements have been made in quantum limited amplifiers [41], as well as single photon detectors for axion searches [42, 43], both utilising superconducting circuit engineering.

2.1.1 The LC Resonator

We first introduce the simple circuit of consisting of an inductor (L_R) in parallel with a capacitor (C_R), shown in Fig. 2.1 (a). The classical Hamiltonian of this circuit is given by [44],

$$H = \frac{Q^2}{2C_R} + \frac{\Phi^2}{2L_R}, \tag{2.1}$$

where Q is the charge on the capacitor, and Φ is the flux, defined as the time integral of the voltage. The quantum mechanical description of this circuit requires that we promote the charge and flux coordinates to operators. Following this assignment, the quantum-mechanical Hamiltonian of the circuit becomes,

$$\hat{H} = 4E_C\hat{n}^2 + \frac{1}{2}E_L\hat{\phi}^2, \tag{2.2}$$

where we have introduced the reduced flux operator $\hat{\phi} = (2\pi\Phi/\Phi_0)$, where $\Phi_0 = h/2e$ is the superconducting magnetic flux quantum, and number operator $\hat{n}$, correspond-

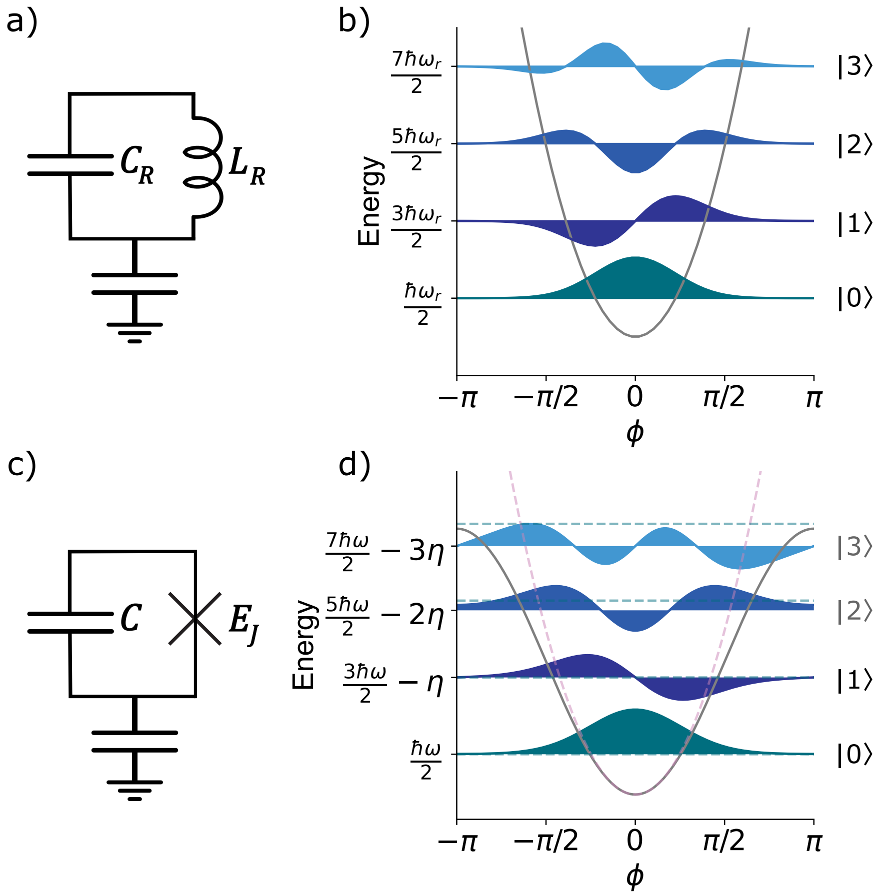

Figure 2.1: (a) Circuit diagram of an LC resonator. (b) Quadratic potential and wavefunctions of the first four energy levels of the quantum harmonic oscillator (QHO) as a function of superconducting phase ϕ. (c) Circuit diagram of a fixed frequency transmon qubit (d) Cosinusoidal potential and wavefunctions of the first four energy levels of the anharmonic oscillator as a function of superconducting phase ϕ. QHO potential and energy levels (dashed) plotted for comparison. Transmon wavefunctions calculated using [45].

ing to the excess number of Cooper pairs on the superconducting island. We also introduce $E_C = e^2/(2C_R)$ as the charging energy, and $E_L = (\Phi_0/2\pi)^2/L_R$ as the inductive energy.

This Hamiltonian is analogous to that of the quantum harmonic oscillator (QHO). The quadratic potential and wavefunctions are shown in Fig. 2.1 (b). Quantising the Hamiltonian a second time in the harmonic oscillator basis yields the Hamiltonian,

$$\hat{H} = \hbar\omega_r(\hat{a}_r^\dagger\hat{a}_r + \frac{1}{2}), \tag{2.3}$$

where $\hat{a}_r^{(\dagger)}$ is the annihilation (creation) operator, and $\omega_r = \sqrt{8E_L E_C}/\hbar = 1/\sqrt{LC}$ is the resonant frequency of the system. The energy levels of the QHO are equidistant, separated by energy $E_{m+1} - E_m = \hbar\omega_r$. As such, the transitions are not able to be selectively addressed.

2.1.2 The Transmon Qubit

One of the simplest and most successful designs for a superconducting circuit is the transmon qubit. This fixed frequency device can be designed in a regime such that sensitivities to decoherence mechanisms are effectively suppressed, without additional control requirements. As such, it is frequently a key component of scaling superconducting quantum circuit architectures [8].

In order to construct a transmon qubit, we first introduce a non-linear superconducting circuit component, formed of a superconductor, insulator, superconductor junction, known as Josephson junction [46]. The insulating barrier thickness (≈ 1 nm [47]) is significantly smaller than the superconducting coherence length (≈ 1600 nm [48]), such that a Cooper pair can tunnel between the superconducting layers without dissipation [46]. The Josephson junction behaves as a non-linear inductive element that has a potential energy ϵ_{pot} of the form,

$$\epsilon_{pot} = -E_J \cos(\varphi), \tag{2.4}$$

where $E_J = \Phi_0 I_c/(2\pi)$ is the Josephson energy, φ is the phase difference of Ginzburg-Landau order parameters across the junction [46], and I_c is the critical current of the superconductor. The Hamiltonian of the circuit formed by a Josephson junction in parallel with a capacitor, as shown in Fig. 2.1 (c), is given by [9, 49],

$$\hat{H} = 4E_C(\hat{n} - n_g)^2 - E_J \cos\hat{\varphi}, \tag{2.5}$$

where E_C is the charging energy, the operator $\hat{n}$ is the excess number of Cooper pairs on the island, with n_g being the effective offset charge of the device, measured in

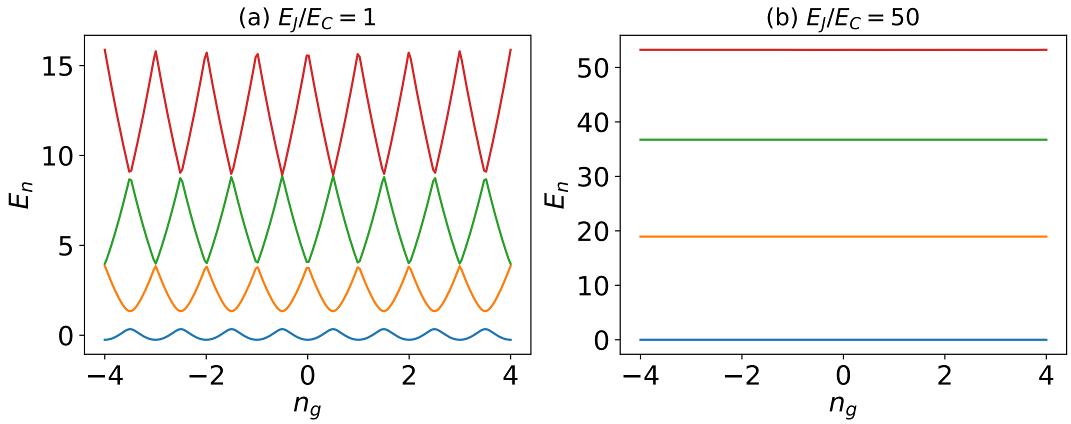

Figure 2.2: First four energy levels of the Hamiltonian of Eqn. 2.5, as a function of gate-charge offset n_g, in the charge qubit regime (a), and the transmon regime (b). Energy levels offset by $\bar{E}_0$.

units of $2e$. The eigenenergies of this Hamiltonian can be calculated by solving the Schrödinger equation $\hat{H}\psi = E\psi$. This can be solved exactly in the phase basis by using the Mathieu functions. The resulting wavefunctions are shown in Fig. 2.1 (d).

The Hamiltonian of Eqn. 2.5 shows a dependence on gate-charge offset n_g that causes a dispersion of the energy levels, shown in Fig. 2.2. We can understand the nature of this charge dispersion by employing a tight-binding model approximation. The periodic potential energy landscape with equal tunnel-barrier energy between adjacent lattice sites produces a dispersion relationship of the form [9],

$$E_m(n_g) \simeq E_m(n_g = 1/4) - \frac{\epsilon_m}{2}\cos 2\pi n_g, \tag{2.6}$$

where $E_m(n_g = 1/4)$ is the average energy of the mth energy level, and ϵ_m is the peak to peak value for the charge dispersion. In the limit of large Josephson energies, the magnitude of the dispersion is given by,

$$\epsilon_m \simeq (-1)^m E_C \frac{2^{4m+5}}{m!}\sqrt{\frac{2}{\pi}}\left(\frac{E_J}{2E_C}\right)^{\frac{m}{2}+\frac{3}{4}} e^{-\sqrt{8E_J/E_C}}. \tag{2.7}$$

Eqn. 2.7 shows an exponential suppression of charge dispersion with $\sqrt{E_J/E_C}$. We describe this circuit operating with a sufficiently high E_J/E_C such that transition frequencies are stable, with respect to gate-charge offset, as being in the *transmon* regime.

The nonlinearity the Josephson junctions adds ensures that the energy levels of the transmon are not equidistant. The well-resolved and nonuniformly spread spectral lines resemble those of an atom, hence the transmon qubit is sometimes described as an artificial atom. In contrast to the LC resonator, this nonlinearity allows us to selectively address transitions. The ground state ($|0\rangle$) and first excited state ($|1\rangle$) are used to form a *qubit*.

An effective Hamiltonian of the transmon qubit can be obtained by starting from Eqn. 2.5. We perform a second quantisation by expanding the cosine potential terms to fourth order, and assuming a weakly nonlinear oscillator-like behaviour. Keeping only counter-rotating terms produces,

$$\hat{H}/\hbar = \Big(\omega + \frac{\eta}{2}\left(\hat{a}^\dagger\hat{a} - 1\right)\Big)\,\hat{a}^\dagger\hat{a}, \tag{2.8}$$

where $\hbar\omega = E_1 - E_0 = \sqrt{8E_JE_C} - E_C$ is the frequency of the $|0\rangle \rightarrow |1\rangle$ transition, and $\eta = -E_C$ is the anharmonicity. Typical designed qubit parameters are such that $\omega/2\pi \approx 4 - 6$ GHz, and $\eta/2\pi \approx 100 - 200$ MHz, with $E_J/E_C \gtrsim 70$.

The Hamiltonian representing the subspace of the first two transmon levels $|0\rangle$ and $|1\rangle$ can be written as,

$$\hat{H}/\hbar = -\frac{\omega}{2}\hat{Z}, \tag{2.9}$$

where $\hat{Z} = |0\rangle\langle 0| - |1\rangle\langle 1|$.

2.2 Noise and Decoherence

2.2.1 Qubit Relaxation and Decoherence

We understand qubit relaxation and decoherence by first introducing the Bloch sphere representation of a two-level system. We can describe a qubit state as being any

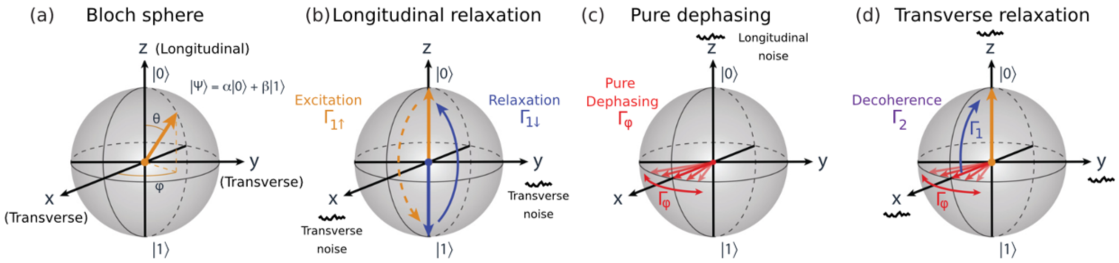

Figure 2.3: Energy relaxation and decoherence in the Bloch sphere description. (a) Bloch sphere representation of quantum state $|\psi\rangle$. (b) Illustration of longitudinal relaxation rate Γ_1, comprising of both relaxation (purple) and excitation (yellow) rates. (c) Illustration of pure dephasing Γ_ϕ as a loss of coherence in purely the $X-Y$ axis of the Bloch sphere. (d) Illustration of transverse relaxation (decoherence) Γ_2, as a combination of both pure dephasing (red) and longitudinal relaxation (purple). Figure from [51].

position on the surface of the unit sphere as in Fig. 2.3. The two basis states $|0\rangle$ and $|1\rangle$ are the north and south poles respectively. The states that lie as points on the equator represent all the equally weighted superposition states and cannot be interpreted classically [50]. In this picture, the quantum state $|\psi\rangle$ can be fully described in spherical polar coordinates by,

$$|\psi\rangle = \cos\left(\frac{\theta}{2}\right)|0\rangle + e^{i\phi}\sin\left(\frac{\theta}{2}\right)|1\rangle = \alpha|0\rangle + \beta|1\rangle . \tag{2.10}$$

Noise and the environment that the qubit is coupled to induce loss in the system [52]. We characterise this loss in two forms: the *longitudinal relaxation* rate Γ_1, and the *transverse relaxation* rate Γ_2 [51, 53].

The longitudinal relaxation rate Γ_1 is such called as it describes how well the system can maintain an eigenstate, along the Z-axis (quantisation axis) of the Bloch sphere. Γ_1 is given by,

$$\Gamma_1 = \frac{1}{T_1} = \Gamma_{1\downarrow} + \Gamma_{1\uparrow}, \tag{2.11}$$

where $\Gamma_{1\uparrow}$ corresponds to an excitation rate, and $\Gamma_{1\downarrow}$ corresponds to a relaxation rate, and T_1 is the characteristic decay time, which we refer to as the energy relaxation time. This longitudinal relaxation is caused by an exchange of energy with the environment of the qubit, causing either a loss of energy resulting in the relaxation rate $\Gamma_{1\downarrow}$, or an excitation mechanism causing the rate $\Gamma_{1\uparrow}$ [54, 55]. Since superconducting circuits are operated at $T = 20$ mK, the excitation rate $\Gamma_{1\uparrow}$ is low (as it is suppressed exponentially with $1/T$), and so the longitudinal relaxation rate is dominated by the energy relaxation rate.

The transverse relaxation rate describes how well the system can maintain coherence of a superposition state $|\psi\rangle = 1/\sqrt{2}(|0\rangle + |1\rangle)$ lying on the equator of the Bloch sphere. Γ_2 is given by,

$$\Gamma_2 = \frac{1}{T_2} = \frac{\Gamma_1}{2} + \Gamma_{\varphi}, \tag{2.12}$$

where Γ_ϕ is the pure dephasing rate, and Γ_1 is the longitudinal relaxation rate as before. The contribution due to Γ_1 is due to the superposition state being able to decay to the $|0\rangle$ state, with an average relaxation rate of $\Gamma_1/2$. The pure dephasing rate is a result of a loss of coherence along the $X - Y$ axis of the Bloch sphere. It is the result of a noise source that causes a shift in the qubit frequency, such as charge noise (discussed in Section 2.1.4) or photon shot noise [56]. The upper limit of transverse relaxation is given by $T_2 = 2T_1$.

In experimental chapters, we characterise the energy relaxation time T_1 and coherence time T_2 of measured devices to probe the noise sources and loss mechanisms. These characteristics are a common benchmark of performance in superconducting quantum devices.

2.2.2 Charge Noise

The Hamiltonian of Eqn. 2.5 shows a sensitivity to an effective offset charge n_g. This can be controlled via a capacitively controlled gate electrode, such that $n_g = C_gV_g/2e + Q_r/2e$, where C_g and V_g are the capacitance and gate voltage respectively, and Q_r is the environmentally induced offset charge [9]. The irregular fluctuations in this offset charge n_g are what we describe as charge noise (or equivalently electric field noise). Charge noise can arise from material factors such as defects within the substrate or material interfaces [37, 57–60], and fluctuating localised dipole-like two-level fluctuators (TLFs) [33, 60–63]. In addition, charge noise is theorised to arise from surface drifts [38], patch potentials and voltage fluctuations in control electronics.

We describe charge noise as being a low-frequency, $1/f^{\alpha}$-like noise source [64], such that the spectral density takes the form [35],

$$S_Q(f) = A^2/f^{\alpha}, \tag{2.13}$$

where A is the noise amplitude. The amplitude A and exponent α are dependent on the materials, geometry and environment of the device, however typical noise amplitudes range between $A^2 \simeq 10^{-4} - 10^{-3} e^2/\mathrm{Hz}$, with α observed to lie in the range $\simeq 1 - 2$ [32, 33, 35, 65–67].

Charge noise causes stochastic fluctuations in the qubit frequency. In the case where charge sensitivity is not suppressed, these frequency fluctuations cause pure dephasing, where the contribution to pure dephasing time (T_{φ}) due to charge noise is given by [68],

$$T_{\varphi} \approx \frac{2e\hbar}{|\epsilon_1|\pi A \sin 2\pi n_g}. \tag{2.14}$$

In addition to slow drifts in charge configuration due to the $1/f$ nature of charge noise, experiments on charge sensitive devices observe large discrete jumps in charge configuration. These jumps are accompanied by reduction in longitudinal relaxation time, and have been shown to be correlated over length scales of 600 μm [36]. It is understood that these large jumps are due to the absorption of ionising radiation, such as γ-rays and cosmic-ray muons, within the substrate causing a large charging event [35, 36, 69–72].

Where shielding from γ-rays can be achieved through the use of dense materials such as lead, mitigation of cosmic-ray muon impact events requires the use of deep underground facilities [71, 73]. Quantum error correction protocols require mitigation strategies to be developed in order to protect larger scale devices from correlated errors due to these effects [74–76] .

2.2.3 Quasiparticles

Excitations above the superconducting ground state are referred to as quasiparticles (QPs). They are superpositions of negatively charged electrons and positively charged holes, commonly formed when a Cooper pair is broken, presenting as unpaired electrons [77, 78].

In superconducting qubits, a QP tunnelling across a Josephson junction induces a change in the offset charge on the islands by an amount $1e$. This constitutes a change in the charge parity between the junction electrodes, which switches between "even" and "odd" parity configurations [79]. Typical transmon devices exhibit a QP tunnelling rate of 0.01 μs^{-1} [80–82]. In addition, these tunnelling events (that can be activated thermally or photon assisted [83]) can induce qubit transitions and cause either excitation, relaxation, or dephasing events, as shown in Fig. 2.4 [80, 84]. QP-induced excitation events are the dominant source of residual excited state populations in qubits ($p_e \simeq 10\%$) [80], and QP densities also constitute a significant form of loss in superconducting circuits (QP limited relaxation time $T_1^{QP} \simeq 200$ μs) [80, 85–88].

The ratio of thermally generated QP excitations to Cooper pairs, $x_{QP}^{th} = n_{QP}/n_{CP}$, is given by,

$$x_{QP}^{th} \approx \sqrt{2\pi k_B T/\Delta} e^{-\Delta/k_B T}, \tag{2.15}$$

where k_B is the Boltzmann constant, T is the temperature, and Δ is the superconducting band gap [88]. Experimentally measured QP densities of $10^{-6} - 10^{-8}$ per Cooper pair are significantly higher than what is predicted by this model [80, 81, 89]. In addition, measurements of decay and excitation events show that the distribution

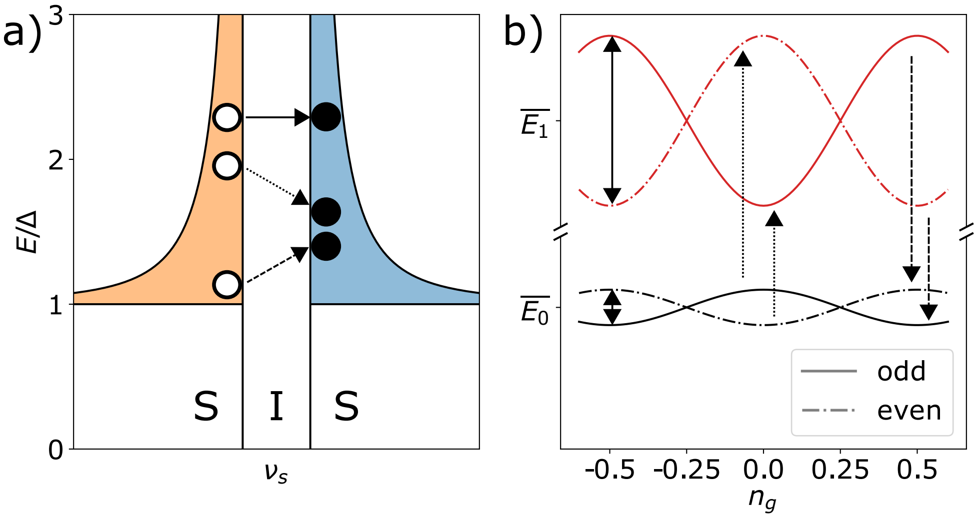

Figure 2.4: (a) Density of states (ν_s) in the leads of the Josephson junction. QP tunnelling events corresponding to relaxation, excitation and interband transition shown in dashed, dotted and solid lines respectively. (b) Lowest two energy levels of the transmon as a function of gate charge offset n_g, showing the two possible parity configurations (odd, even) for each level. QP tunnelling event induced transitions shown by arrows annotated as in (a). Figure adapted from [80].

of QPs is not consistent with what is expected of a thermal distribution. As such, the total density of QPs is a combination of thermal (equilibrium) QP density and an additional excess ("hot") nonequilibrium contribution x^0_{QP}, such that $x_{QP} = x^0_{QP} + x^{th}_{QP}$ [80, 86, 90, 91].

A simple model for QP dynamics is given by,

$$\frac{dx_{QP}}{dt} = g(t) - s x_{QP} - r x^2_{QP}, \tag{2.16}$$

where $g(t)$ describes the generation, s describes the trapping rate, and r describes the recombination rate of pairs of QPs forming cooper pairs [81]. Populations of QPs are in constant flux due to this generation and recombination.

Infra-red radiation with energy above the superconducting band gap ($\omega/2\pi > 2\Delta \approx 100$ GHz) is able to break Cooper pairs and contributes to this additional source of nonequilibrium QPs [92, 93]. The source of this IR radiation is most generally components, plates and shields within the dilution refrigerator at a higher temperature emitting blackbody radiation, and the path that it takes to impinge upon the qubit is theorised to be via the microwave input and output lines. Adequate filtering of these lines, along with the development of "light-tight" shielding is an active area of research and development [92–95]. In addition, the higher frequency modes of the qubit geometry can act as an antenna for radiation above this pair-breaking threshold frequency, thus careful consideration when designing qubits is required [96, 97].

Ionising radiation is an additional source of nonequilibrium QPs [70, 95]. Sources of this radiation include cosmic ray muons, gamma rays due to materials and internal sources such as packaging and connectors, or even the local environment or lab [98]. High energy radiation incident on the substrate can scatter to form electron-hole pairs, from which phonons can be created and transport energy through the bulk of the substrate. QPs are generated as a result of phononic downconversion processes at the substrate-superconductor boundary [69, 99]. This can cause spatially correlated errors as stated in the previous section [36]. Phonon traps can be introduced to reduce the generation of QPs due to phonon downconversion processes and can be formed of superconducting or normal metal backplanes [72, 100, 101], or more complex micromachined substrate features [102]. In addition, shielding can be introduced in order to protect devices from impinging ionising radiation [70, 71].

Where the flux of QP–generating radiation cannot be reduced due to shielding, the density of QPs can be reduced by increasing the trapping rate s. This can be achieved with the addition of QP traps, or active QP pumping [103, 104]. QP traps can be formed by the addition of a lower gap superconductor in the region of the Josephson junction, such that QPs relax to a lower energy state, and be trapped away from the Josephson junction [69, 105].

Investigations into the nature of decoherence due to QP tunnelling events and how the densities can be reduced are an active area of research. In this work, we introduce a shielding solution to reduce the incidence of pair-breaking photons from infra-red radiation, and show reductions in residual excited state populations (Appendix F). In addition, we introduce a device that has the potential to explore how QP tunnelling events affect energy dissipation in multiple modes (Chapter 5).

2.3 Engineering Qubit-Qubit Interactions

2.3.1 Coupling

It is required that quantum gates be able to be performed between qubits for quantum computation [1], which necessitates a form of inter-qubit coupling. This can be achieved with the use of additional tunable circuit components [16, 106], or by engineering a static capacitive or inductive coupling between qubits [51, 107]. In this work, we consider only static coupling between qubits characterised in two classes: *transverse* and *longitudinal* coupling [51].

The interaction Hamiltonian describing the transverse coupling is given by,

$$\hat{H}_{int}/\hbar = J(\hat{a}_i^\dagger \hat{a}_j + \hat{a}_i \hat{a}_j^\dagger), \tag{2.17}$$

where J is the strength of the interaction between modes i and j. It is such named as the Hamiltonian matrix elements describing the coupling are off-diagonal elements, and the coupling axis is orthogonal to the qubit quantisation axis. It is commonly engineered via a direct capacitive coupling between two transmon qubits [51, 107, 108]. We describe the interaction as a single photon exchange interaction, since two qubits on resonance will exchange a single excitation between them at a rate J. In the two level approximation, this interaction is also described as an $\hat{X}\hat{X}$ interaction, since the coupling term in the Hamiltonian is of the form $\hat{\sigma}_x \otimes \hat{\sigma}_x$, where $\hat{\sigma}_i$ is the Pauli operator.

The Hamiltonian describing longitudinal coupling is given by,

$$\hat{H}_{int}/\hbar = \chi_{ij} \hat{a}_i^\dagger \hat{a}_i \hat{a}_j^\dagger \hat{a}_j, \tag{2.18}$$

where χ_{ij} is the strength of the interaction between modes i and j. The coupling matrix elements describing the interaction are along the diagonal, as they are in the quantisation basis of the system. It can be a result of a purely inductive coupling, or more complex circuit engineering [20, 109]. In superconducting circuits, it is described as a state-dependent frequency shift, or cross-Kerr shift [110]. In the two level approximation, this interaction is also described as a $\hat{Z}\hat{Z}$ interaction, since the coupling term in the Hamiltonian is of the form $\hat{\sigma}_z \otimes \hat{\sigma}_z$, where $\hat{\sigma}_i$ is the Pauli operator.

In this work, we explore both transverse coupling in the context of capacitively coupling qubits, as well as strong cross-Kerr shifts as a result of circuit design.

2.3.2 Two-Qubit Gates

The set of implementations of two-qubit gates in superconducting circuits is extensive [51, 53, 111]. Here we focus on two examples of microwave-activated two-qubit gates between transversely coupled transmon qubits: the cross-resonance (CR) gate [112, 113] and the microwave-activated conditional phase (MAP) gate [114].

The CR gate is a driven interaction between two transversely coupled transmon qubits. In driving the control qubit at the frequency of the target mode, one induces rotations about the X-axis of the target qubit, conditional on the state of the control qubit. The speed at which the interaction occurs is dependent on the exchange interaction strength J, as well as the detuning between the qubits $\Delta_{0,1} = \omega_0 - \omega_1$. Whilst increasing the coupling strength J and reducing the detuning does increase the speed of the gate, the tradeoff is that this increases the strength of the additional unwanted ZZ interactions between qubit modes and sources of error, as discussed in Section 2.2.3.

The MAP gate is an off-resonantly driven interaction that arises from the coupling between transitions outside of the computational subspace. When the detuning between the two qubit modes, $\Delta_{0,1}$, is twice the anharmonicity, η_2, the $|12\rangle$ and $|03\rangle$ transitions (where $|ij\rangle$ denotes the state in which i (j) excitations are present in qubit 0 (1)) are approximately on resonance, as shown in Fig. 2.5. The coupling between

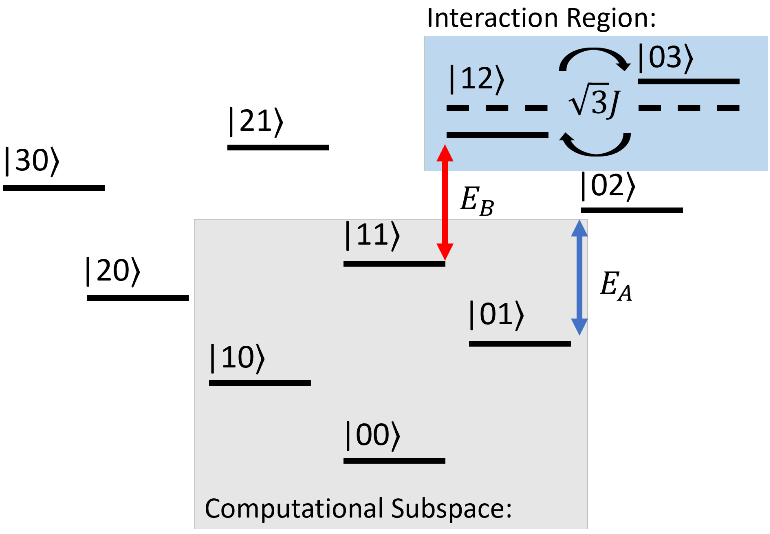

Figure 2.5: Truncated energy level diagram of two coupled transmon qubits. Computational subspace highlighted in grey. $|12\rangle$ and $|03\rangle$ transitions on resonance in interaction region (highlighted in blue). Transitions between $|01\rangle$ and $|02\rangle$, and $|11\rangle$ and $|12\rangle$ energy levels used in MAP interaction highlighted in blue and red respectively. Figure adapted from [114].

the two qubits leads to a splitting of these two energy levels, such that the energy difference between the $|01\rangle$ and $|02\rangle$ levels (labelled E_A), is different to the difference in energy between the $|11\rangle$ and $|12\rangle$ levels (labelled E_B). This interaction region can be driven off-resonantly leading to a Stark-shift induced phase accumulation on the target qubit, conditional on the state of the control qubit. The conditional-phase gate has a rate [114],

$$\begin{aligned}\zeta &\approx J_{11,20}J_{11,02}\left(\frac{1}{\Delta_{11,20}}+\frac{1}{\Delta_{11,02}}\right)+\frac{\Omega^2}{2\Delta_d}\frac{J^2_{12,03}}{J^2_{12,03}+\Delta_d(\omega_d-\Delta_{03,11})}\\ &=\zeta_0+\frac{\Omega^2}{2\Delta_d}\zeta_2,\end{aligned} \tag{2.19}$$

where $J_{ij,kl}$ is the matrix element describing the coupling between the $|ij\rangle$ and $|kl\rangle$ energy levels, $\Delta_{ij,kl}$ is the difference between the $|ij\rangle$ and $|kl\rangle$ energy levels, Ω and ω_d are the drive strength and frequency respectively, and $\Delta_d=\Delta_{12,11}-\omega_d$. ζ_0 and ζ_2 represent the always-on and microwave activated components of the interaction respectively.

This interaction exploits the increased coupling strength between higher transitions of transmon qubits, and the upper limit of gate speed is approximately $1/J$. Whilst the interaction is driven off-resonantly, higher power driving leads to leakage into higher levels, as well as dephasing of the computational subspace modes, causing errors in the gate operation.

Driving a two-qubit gate outside of the computational subspace reduces leakage errors into computational states [115], however, like the CR gate, the MAP gate requires very strict resonance conditions to be met in order to drive a fast gate. In Section 3.3.3, we introduce a novel conditional phase interaction based on the MAP interaction in multi-mode superconducting circuits. The gate relies on energy levels outside the computational subspace, and the architecture entirely suppresses the always-on interactions that cause errors in CR gates. In addition, by utilising multiple possible ancillary transitions to drive the interaction, there is a much wider range of resonance conditions that can be met, reducing sensitivity to fabrication tolerances.

2.3.3 Always-On Unwanted ZZ Interactions

In the anharmonic oscillator approximation, the Hamiltonian of two fixed-frequency transmon qubits ($i = 0, 1$), of frequency $\omega_i/2\pi$ and anharmonicity $\eta_i/2\pi$, statically coupled with an exchange interaction of strength J, is given by,

$$\hat{H}/\hbar = \sum_{i=(0,1)} \left(\omega_i + \frac{\eta_i}{2}\left(\hat{a}_i^\dagger \hat{a}_i - 1\right)\right) \hat{a}_i^\dagger \hat{a}_i + J(\hat{a}_0^\dagger \hat{a}_1 + \hat{a}_0 \hat{a}_1^\dagger). \tag{2.20}$$

The entanglement rate of sets of two-qubit gates (including the CR and MAP gates) is determined by the exchange interaction strength J [114, 116–118], thus it is desirable to maximise the coupling to ensure fast and high fidelity gates in systems with finite coherence. When diagonalised in the dispersive limit ($J \ll \Delta_{0,1}$), this static coupling results in a state-dependent qubit frequency shift, known as the ZZ

shift [117, 119]. This is the frequency by which one qubit transition frequency shifts, when the other qubit to which it is coupled is in the excited state. Derived from second-order perturbation theory, this shift $\chi_{0,1}$ is given by [24],

$$\chi_{0,1} = (E_{11} + E_{00} - E_{01} - E_{10})/\hbar = \frac{2J^2(\eta_0 + \eta_1)}{(\eta_1 - \Delta_{0,1})(\eta_0 + \Delta_{0,1})}, \tag{2.21}$$

where $\Delta_{0,1} = \omega_0 - \omega_1$, is the detuning between qubit frequencies, and E_{ij} is the energy of the level corresponding to i (j) excitations in qubit 0 (1).

We describe this ZZ shift as an always-on unwanted interaction (or quantum crosstalk) since it introduces errors in both single-qubit and two-qubit operations [14, 15, 113, 120–123]. If we wish to use superconducting circuits for quantum computing applications, these errors need to be reduced. We outline some of the methods to mitigate these unwanted interactions in four main categories.

The first is introducing tunability into the coupling between the two qubit modes. This can be in the form of a flux tunable transmon [106, 124–127], or more sophisticated circuits [16, 19, 128–132]. By designing the interactions, one introduces regimes in which very high on/off coupling ratios can be achieved, such that the static qubit-qubit interaction is cancelled out. Whilst the addition of flux tunable components does introduce additional DC control requirements, as well as flux sensitivities that can impact gate operation[25], high fidelity two-qubit gates have been achieved in fixed-frequency transmons in these architectures [131, 133].

The second method is to introduce additional static circuit components to mediate the qubit-qubit coupling. This can be in the form of a coupling bus resonator [116], or more sophisticated multi-path coupling (MPC) designs that enable anti-nodes at frequencies in which the unwanted interaction is suppressed [134]. Work on MPC based architectures has demonstrated a cross-resonance based CNOT gate in 180 ns, with an error of 2.3×10^{-3} [134], a factor of 2 improvement over the previous best record error of 5×10^{-3} [120]. The MPC architecture retains circuit simplicity and adds no extra control requirements, however, the bandwidth of the region in which ZZ interactions is suppressed can be narrow, thus making the performance of the device highly sensitive to fabrication errors.

Thirdly, the ZZ interaction can be actively suppressed by manipulating higher energy levels of the system with off-resonant drive tones [23, 24]. This method can be used to both enhance and suppress the ZZ interaction between statically coupled transmon qubits, and has been used to demonstrate both high fidelity CZ gates and CNOT gates (gate time of 90 ns with an error of $0.19 \pm 0.02\%$ [24]). The off-resonant nature of the drive scheme allows greater flexibility and reduces frequency crowding constraints on qubits, however, the additional continuous drive tones provide an additional active heat load on cryogenic systems when scales increase, and can have a detrimental impact on qubit coherence when driven at high powers.

Finally, by inspection of Eqn. 2.21, it is clear that the static interaction can be eliminated if the anharmonicities η_0 and η_1 are equal and opposite. This can be achieved in novel qubit designs [21, 135–137].

The suppression of always-on unwanted interactions to achieve high fidelity single-qubit and two-qubit operations is an active area of research. In Chapter 3 and Chapter 6, we introduce a method of suppressing the ZZ interaction in fixed frequency qubits with static coupling that maintains circuit simplicity and avoids additional control or tuning requirements.

2.4 Multi-Mode Superconducting Circuits

The use of Josephson junction based superconducting circuits as qubits for investigations into atomic physics, artificial atoms, and quantum information is widespread [7, 138]. The transmon qubit previously introduced has a single degree of freedom and presents a single ladder based energy level structure, as shown in Fig. 2.6 (a). The anharmonic nature of the structure lends itself to using the lowest two energy levels

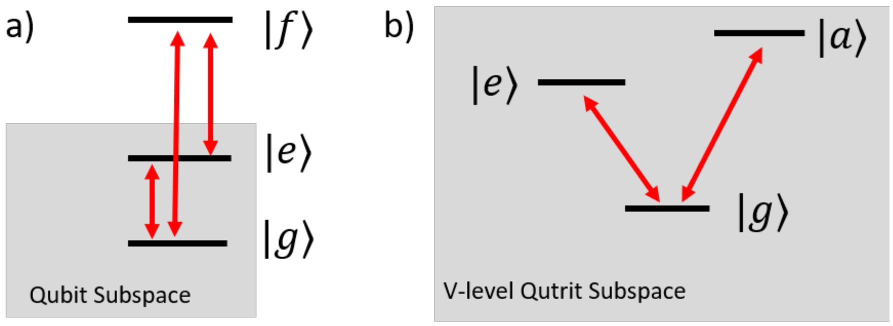

Figure 2.6: (a) Ladder type energy level structure of the transmon. Highlighted area shows the subspace that is used as a qubit. Red lines indicate allowed transitions. (b) V-shaped energy level structure of the two-mode system. Red arrows indicate allowed transitions.

as a qubit. The flexibility of superconducting circuits allows us to develop more complex alternative designs [10–13] and engineer the energy level structure of quantum systems. One such structure that has previous applications in nitrogen-vacancy centres in diamond [139] and trapped ion based quantum computers [2] is the V-shaped energy-level structure.

We understand a V-level energy structure as a qubit formed by a ground state $|g\rangle$ and excited state $|e\rangle$, with an additional ancillary energy level $|a\rangle$, as shown in Fig. 2.6 (b). The ancillary level is coupled to the ground level $|g\rangle$, forming the ancillary transition, whilst the transition between the $|e\rangle$ and $|a\rangle$ states is suppressed [27]. We describe this system as a multi-mode device, since the transitions are independently addressable modes with distinct properties. We refer to the $|g\rangle \rightarrow |e\rangle$ transition as a qubit mode, and the $|g\rangle \rightarrow |a\rangle$ as the ancillary mode.

The multi-mode energy level structure described was first introduced in the field of superconducting circuits in the work of Gambetta et. al. [29] with a device known as the tunable coupling qubit (TCQ). This device consists of three superconducting islands, connected via two Josephson junctions, as shown in Fig. 2.7. The addition of a second degree of freedom introduces a second transmon-like mode in the device, and a V-shaped energy level structure [17, 18, 140–142]. The premise of this device is that

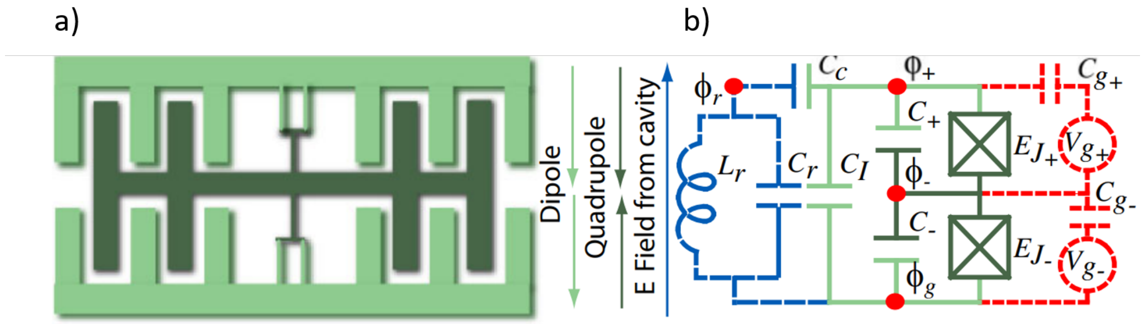

Figure 2.7: (a) Schematic of the three island tunable coupling qubit device. Arrows show electric dipole and quadrupole moments of the device. (b) Equivalent circuit of the tunable coupling qubit device (green) with capacitances (C), Josephson energies (E_J), coupled to an LC resonator (blue) for readout purposes. Figure and caption adapted from [29].

the transverse coupling between each mode and the readout resonator can be tuned, such that there is a bright state $|B\rangle$ dispersively coupled to a readout resonator, and a dark state $|D\rangle$ that has no coupling to the readout mechanism [143, 144].

This selective coupling of modes to the readout mechanism can be utilised in several ways in the measurement of a qubit. Firstly, one can create a decoherence free subspace (DFS) with respect to Purcell decay via the lossy readout channel. This coupling suppressed regime has additional benefits in that it can be used to suppress dephasing due to thermal photons populating the readout resonator [20, 30]. Secondly, one can couple the ancillary transition very strongly to the readout mechanism [145]. Due to the strong coupling between modes of the V-shaped structure, this allows for extremely fast quantum non-demolition readout of the qubit mode, with the state-of-the-art experiments observing single-shot readout fidelities of 97.4% using 50 ns readout pulses [28].

An additional utilisation of the multi-mode structure is in two-qubit gates and entanglement operations. By moving the coupling between qubits outside of the computational subspace, one can allow for far-detuned computational transitions with minimised single-qubit-gate crosstalk [146], while retaining gate speeds comparable to fixed coupled transmons [147, 148]. The versatility of the energy level structure can also allow for native multi-modal gates with higher connectivity within the multidimensional Hilbert space [31, 149].

2.5 Coaxial cQED Architecture

Conventional 2D planar superconducting circuit architectures require the routing of control and readout lines across the surface of the substrate. Signals propagate along coplanar waveguide structures to address circuit elements. In an architecture where qubits are arranged in a grid-like array of $N \times N$, the number of qubits increases as N^2, whereas the available space for routing signals to the device depends on the perimeter, and only increases as $4N$. As the density of wiring increases, this can lead to issues with connectivity and addressability, as well as control line crosstalk as wiring becomes more tightly packed. Large arrays of qubits are required to implement error-correction protocols [150, 151], and investigating the issues of addressability and connectivity is an active area of research [152–154].

In this work, we construct superconducting quantum devices in a coaxial circuit quantum electrodynamics architecture [155]. Developed at the University of Oxford, this architecture consists of a qubit formed of a concentric inner and outer superconducting island connected via a Josephson junction forming a coaxial transmon (coaxmon), as shown in Fig. 2.8. Dispersive readout is achieved via a lumped element resonator, fabricated on the opposing side of the substrate [156]. Signals are delivered via capacitively-coupled coaxial control lines, out of the plane of the substrate. The coaxial geometry allows for selective mode-matching between elements, with no galvanic connections to the substrate, or added fabrication complexity.

It is simple to consider extending the architecture to large arrays of qubits via a simple tiling, alleviating the constraints of control wiring in the plane of the substrate. Since it's development in 2017, two-qubit gates [157–159], as well as high coherence

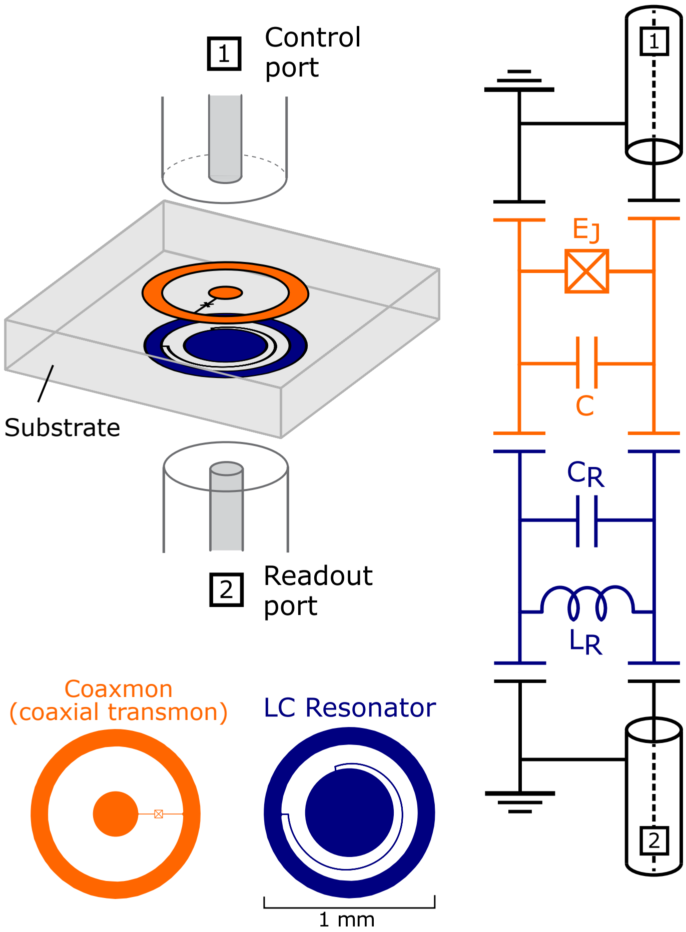

Figure 2.8: Schematic and equivalent circuit diagram of the coaxial circuit QED architecture. The coaxial transmon (coaxmon) components are shown in orange, and the LC resonator components, used for dispersive readout, are in blue.

and low crosstalk in a 2×2 array [160], have been demonstrated in this architecture. In addition, more complex engineering, such as fast flux control [157], have been demonstrated in coaxial cQED.

In this work, we implement a multi-mode qubit within the coaxial cQED architecture. The architecture allows us to build natural symmetries into the system, generating both symmetry protected modes and strongly coupled modes. Engineering these symmetry protections allows for low crosstalk, as well as protection from decay through the coaxial control lines.

Chapter 3

Theory of the Two-Mode Coaxial Transmon

Here we introduce the device at the core of this work, the two-mode coaxial transmon. We first present the theoretical background of the multi-mode device and explore the predicted behaviour and sensitivities to fabrication asymmetries and charge noise. We show how the design can be engineered for potential use in readout and sensing applications. Finally, we then explore how multiple two-mode coaxial transmon devices can be coupled together, and how we can generate entanglement between modes of the system.

3.1 Two-Mode Coaxial Transmon

3.1.1 Circuit Quantisation and Device Hamiltonian

A transmon qubit is a simple superconducting circuit consisting of a capacitance in parallel with a Josephson junction, and is insensitive to charge fluctuations across the capacitor in the regime of large Josephson-to-charging energy ratio, E_J/E_C [9]. Here we work with a circuit with two transmon-like modes, built from three superconducting islands and two Josephson junctions, depicted in Fig. 3.1 (a).

We begin analysing the behaviour of the circuit by performing circuit quantisation methods. The Hamiltonian of the circuit can be derived from [39],

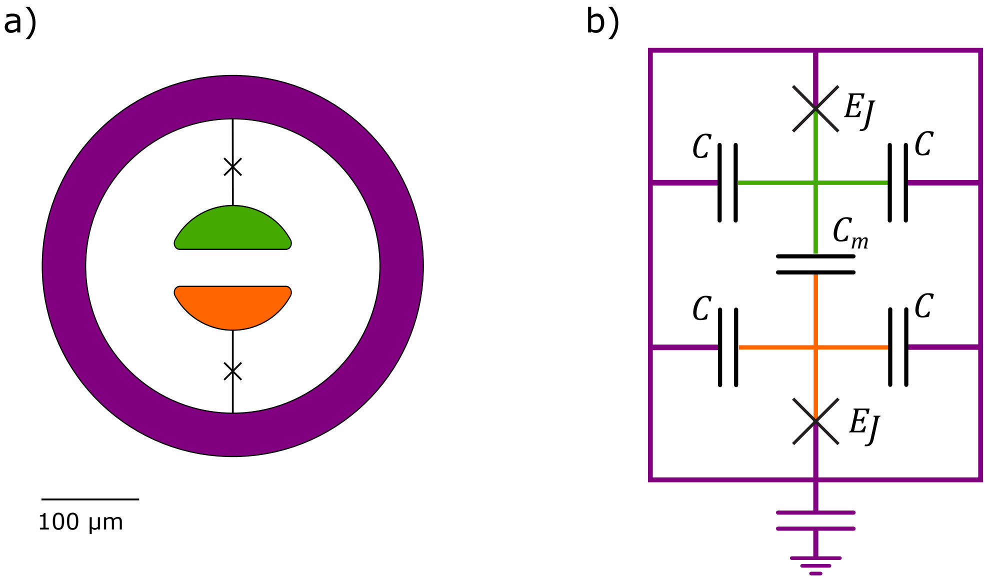

Figure 3.1: (a) A simplified schematic of the device shows a coaxial pad geometry with a split inner conductor resulting in three superconducting islands. The two inner islands (green and orange) are labelled 1 and 2 (the exact assignment is symmetrically invariant), and outer island (purple) is labelled island 3. Two near-identical Josephson junctions with phase φ_1, φ_2 are used resulting in two non-degenerate modes (Δ, Σ). (b) An equivalent circuit of the two-mode coaxial transmon. The two inner superconducting islands are connected by a coupling capacitance (C_m), and connected to the outer superconducting island by Josephson junction (E_J) and capacitance $(2C)$.

$$H = \frac{1}{2}\vec{q}^{\,t}[\boldsymbol{C^{-1}}]\vec{q} + \epsilon_{pot}, \tag{3.1}$$

where the independent variables q_i correspond to degrees of freedom and ϵ_{pot} is the potential energy. $\boldsymbol{C}$ is derived from the constructed capacitance matrix $\boldsymbol{C'}$ of the circuit, where,

$$\boldsymbol{C'} = \begin{pmatrix} 2C + C_m & -C_m & -2C \\ -C_m & 2C + C_m & -2C \\ -2C & -2C & -4C \end{pmatrix}, \tag{3.2}$$

where, C corresponds to the capacitance between the inner island and the outer island, and C_m corresponds to the capacitance between the two inner islands, as shown in the circuit diagram in Fig. 3.1 (b). We transform from $\boldsymbol{C'}^{-1} \to \boldsymbol{C}^{-1}$ by eliminating the row and column corresponding to a reference ground of the circuit. We make the choice of the outer island being the reference ground, and eliminating the third row and column of the matrix $\boldsymbol{C'}$ to transform to $\boldsymbol{C}$, such that

$$\boldsymbol{C^{-1}} = \frac{1}{2(C^{*2} - C_m^2)} \begin{pmatrix} C^* & C_m \\ C_m & C^* \end{pmatrix}, \tag{3.3}$$

where $C^* = C(\frac{C+2C_m}{C+C_m})$ the total shunting capacitance of each island.

The potential energy ϵ_{pot} of the circuit is due to the Josephson junctions, giving non-linear function of the Josephson phases $\hat{\varphi}_i$, written as,

$$\epsilon_{pot} = -E_J \cos\hat{\varphi}_1 - E_J \cos\hat{\varphi}_2, \tag{3.4}$$

where E_J is the Josephson energy of the junctions. For simplicity, we assume here that the junctions are identical, and explore the effect of asymmetry in Section 3.1.4.

We choose the degrees of freedom q_i to correspond to the charge operator of the two inner superconducting islands, and label as ($\hat{Q}_1$, $\hat{Q}_2$). We rescale this to the dimensionless Cooper-pair number operator $\hat{n}_i = \hat{Q}_i/2e$. From this we are able to derive the Hamiltonian of the two-mode coaxial transmon as,

$$\begin{aligned}\hat{H} =& 4E_C(\hat{n}_1 - n_{g1})^2 + 4E_C(\hat{n}_2 - n_{g2})^2 + 4E_p(\hat{n}_1 - n_{g1})(\hat{n}_2 - n_{g2}) \\ & - E_J \cos\hat{\varphi}_1 - E_J \cos\hat{\varphi}_2,\end{aligned} \tag{3.5}$$

where the charging energy $E_C = e^2C^*/2(C^{*2} - C_m^2)$, and $E_p = e^2C_m/(C^{*2} - C_m^2)$ is the coupling energy between the two modes [32]. n_{gi} correspond to gate charge offsets of the two independent inner islands 1 and 2.

The Hamiltonian of this system is identical to that of two resonantly-coupled transmons, the eigenmodes of which are sum and difference modes with $\hat{\varphi}_\Sigma = \hat{\varphi}_1 + \hat{\varphi}_2$ and $\hat{\varphi}_\Delta = \hat{\varphi}_1 - \hat{\varphi}_2$ respectively. In the sum and difference mode basis, the Hamiltonian of the circuit becomes:

$$\hat{H} = 8E_{C_\Sigma}(\hat{n}_\Sigma - n_{g\Sigma})^2 + 8E_{C_\Delta}(\hat{n}_\Delta - n_{g\Delta})^2 - 2E_J \cos\frac{\hat{\varphi}_\Sigma}{2} \cos\frac{\hat{\varphi}_\Delta}{2}, \tag{3.6}$$

where $E_{C_\Sigma} = E_C + E_p/2 = e^2/2(C^* - C_m)$ and $E_{C_\Delta} = E_C - E_p/2 = e^2/2(C^* + C_m)$ are the charging energies of the sum and difference modes respectively. $\hat{n}_{\Sigma(\Delta)}$ corresponds

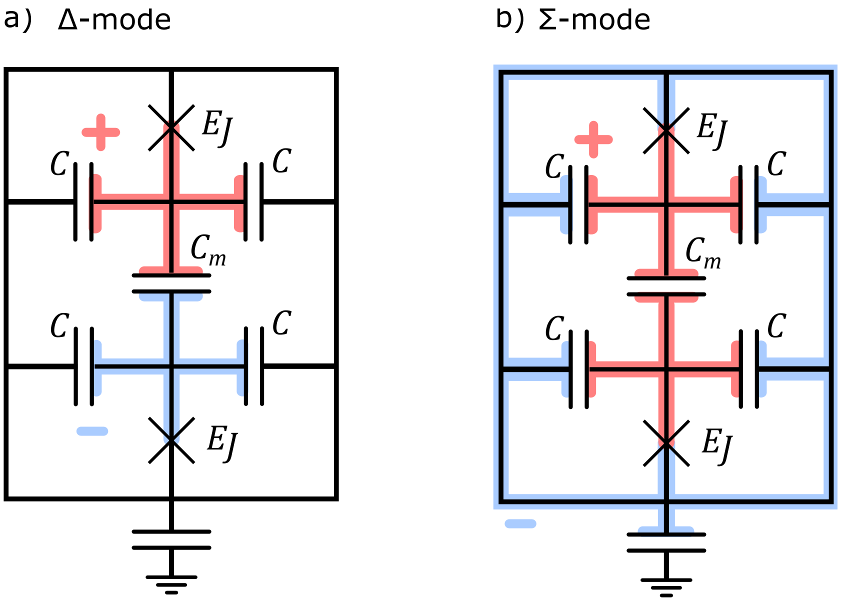

Figure 3.2: Illustration of electric field oscillations (positive (red) and negative (blue)) of the modes of the two-mode coaxial transmon. (a) Δ-mode, corresponding to out-of-phase oscillations of the two inner superconducting islands. (b) Σ-mode, corresponding to in-phase oscillations of the two inner superconducting islands. Outer island also participates, oscillating out-of-phase with the two inner islands.

to the number operator of the sum (difference) modes. This Hamiltonian shows a dependence on gate-charge offsets $n_{g\Sigma}$ and $n_{g\Delta}$, corresponding to the sum and difference of gate-charge offsets of the two inner islands, n_{g1} and n_{g2}. We explore the effects of offset-charge sensitivity in Section 3.1.6.

In this representation, it is clearer that the first two excited states of this system correspond to an excitation in either the in-phase (Σ-mode), or out-of-phase oscillations (Δ-mode) of the two inner superconducting islands, shown in Fig. 3.2. The antisymmetric mode is lower in frequency, has an electric dipole moment, and couples well to electric fields polarised in the plane of the device. The symmetric mode is higher in frequency, has an electric quadrupole moment, and couples well to radial fields and coaxial control ports. This difference in polarisation symmetry can be used for Purcell protection [29].

3.1.2 Effective Hamiltonian

We can obtain an approximate effective Hamiltonian of the two-mode coaxial transmon by starting from the Hamiltonian of Eqn. 3.6 and expanding the cosine potential terms to fourth order. This yields,

$$\begin{aligned}\hat{H} &= 8E_{C_\Sigma}\hat{n}_\Sigma^2 + 8E_{C_\Delta}\hat{n}_\Delta^2 \\ &\quad - 2E_J\left(1 - \frac{1}{2}\left(\frac{\hat{\varphi}_\Sigma}{2}\right)^2 + \frac{1}{4!}\left(\frac{\hat{\varphi}_\Sigma}{2}\right)^4 - \ldots\right)\left(1 - \frac{1}{2}\left(\frac{\hat{\varphi}_\Delta}{2}\right)^2 + \frac{1}{4!}\left(\frac{\hat{\varphi}_\Delta}{2}\right)^4 - \ldots\right) \\ &= 8E_{C_\Sigma}\hat{n}_\Sigma^2 + 8E_{C_\Delta}\hat{n}_\Delta^2 \\ &\quad - 2E_J\left(1 - \frac{1}{2}\left(\frac{\hat{\varphi}_\Sigma}{2}\right)^2 - \frac{1}{2}\left(\frac{\hat{\varphi}_\Delta}{2}\right)^2 + \frac{1}{4!}\left(\frac{\hat{\varphi}_\Sigma}{2}\right)^4 + \frac{1}{4!}\left(\frac{\hat{\varphi}_\Delta}{2}\right)^4 + \frac{1}{4}\left(\frac{\hat{\varphi}_\Sigma}{2}\right)^2\left(\frac{\hat{\varphi}_\Delta}{2}\right)^2\right),\end{aligned} \tag{3.7}$$

Here we make a canonical transformation from the number and phase operators, $\hat{n}_i$ and $\hat{\varphi}_i$ (where $i = \Sigma, \Delta$), to the creation and annihilation operators $\hat{a}_i^\dagger$, $\hat{a}_i$ of the harmonic oscillator basis, such that,

$$\begin{aligned}\hat{\varphi}_{\Sigma(\Delta)} =& \sqrt{\xi_{\Sigma(\Delta)}}(\hat{a}_{\Sigma(\Delta)}^\dagger + \hat{a}_{\Sigma(\Delta)}) \\ \hat{n}_{\Sigma(\Delta)} =& \frac{i}{2\sqrt{\xi_{\Sigma(\Delta)}}}(\hat{a}_{\Sigma(\Delta)}^\dagger - \hat{a}_{\Sigma(\Delta)}),\end{aligned} \tag{3.8}$$

where $\hat{a}_{\Sigma(\Delta)}^{(\dagger)}$ is the annihilation (creation) operator of the Σ-mode (Δ-mode), and ξ_i is the characteristic impedance of the mode i, a dimensionless normalisation factor. This transformation preserves the commutation relations for the conjugate flux $\hat{\Phi}_i$ and charge $\hat{Q}_i$ since,

$$\left[\hat{\Phi}_i, \hat{Q}_i\right] = \left[\frac{\Phi_0}{2\pi}\hat{\varphi}_i, 2e\hat{n}_i\right] = \frac{i\hbar}{2}\left[\hat{a}_i^\dagger + \hat{a}_i, \hat{a}_i^\dagger - \hat{a}_i\right] = i\hbar. \tag{3.9}$$

We can first obtain the plasma frequencies of each mode by inserting the relations in Eqn. 3.8 into Eqn. 3.7, and collecting the second order terms. This yields the second order approximate Hamiltonian of mode i, $\hat{H}_i^{(0)}$, given by,

$$\hat{H}_i^{(0)} = 8E_{C_i}\hat{n}_i^2 + E_J\frac{\hat{\varphi}_i^2}{4} = \frac{-8E_{C_i}}{4\xi}(\hat{a}_i^\dagger - \hat{a}_i)^2 + \frac{E_J\xi}{4}(\hat{a}_i^\dagger + \hat{a}_i)^2. \tag{3.10}$$

Assuming a weakly non-linear harmonic oscillatorlike behaviour, and ignoring counter rotating terms, collecting terms yields the Hamiltonian of each mode i as,

$$\hat{H}_i^{(0)} = \hbar\omega_i^{(0)}\left(\hat{a}_i^\dagger\hat{a}_i + \frac{1}{2}\right), \tag{3.11}$$

where we have defined

$$\xi_i = \sqrt{\frac{8E_{C_i}}{E_J}}, \tag{3.12}$$

giving the plasma frequency of each mode as,

$$\omega_i^{(0)} = \frac{\sqrt{8E_JE_{C_i}}}{\hbar}. \tag{3.13}$$

In order to obtain the anharmonicities (deviations from the harmonic oscillator energy levels) of the modes, we consider the fourth order terms in the previous expansion. By taking the relations in Eqn. 3.8 and inserting them into Eqn. 3.7, now taking into account fourth order terms, we obtain the fourth order approximate Hamiltonian, $\hat{H}^{(1)}$, given by,

$$\begin{aligned}\hat{H}^{(1)} =& \hbar\omega_\Sigma\hat{a}_\Sigma^\dagger\hat{a}_\Sigma + \hbar\omega_\Delta\hat{a}_\Delta^\dagger\hat{a}_\Delta - \frac{E_{C_\Sigma}}{24}(\hat{a}_\Sigma^\dagger + \hat{a}_\Sigma)^4 - \frac{E_{C_\Delta}}{24}(\hat{a}_\Delta^\dagger + \hat{a}_\Delta)^4 \\ &- \frac{\sqrt{E_{C_\Sigma}E_{C_\Delta}}}{4}(\hat{a}_\Sigma^\dagger + \hat{a}_\Sigma)^2(\hat{a}_\Delta^\dagger + \hat{a}_\Delta)^2.\end{aligned} \tag{3.14}$$

The eigenenergies of this Hamiltonian can be found using the expectation value $\langle k|\,\hat{H}^{(1)}\,|k\rangle$, where $|k\rangle$ are Fock state eigenvectors. The energy of mode i in state $|k\rangle$ (whilst the opposite mode is in the ground state) is given by,

$$E_k^{(i)} = \hbar\omega_i\left(k + \frac{1}{2}\right) - \frac{E_{C_i}}{24}(6k^2 + 6k + 3). \tag{3.15}$$

The anharmonicity, η_i, of each mode is the deviation in energy of higher energy levels from the harmonic oscillator energy, given by,

$$\begin{aligned}\eta_i =& \frac{(E_2^{(i)} - E_1^{(i)}) - (E_1^{(i)} - E_0^{(i)})}{\hbar} \\ =& \frac{(\hbar\omega_i^{(0)} - E_{C_i}) - (\hbar\omega_i^{(0)} - E_{C_i}/2)}{\hbar} \\ =& \frac{-E_{C_i}}{2\hbar}.\end{aligned} \tag{3.16}$$

We obtain the fourth order correction to the mode frequency ω_i as,

$$\omega_i = \omega_i^{(0)} - \frac{E_{C_i}}{2\hbar} = \frac{\sqrt{8E_J E_{C_i}}}{\hbar} - \frac{E_{C_i}}{2\hbar}. \tag{3.17}$$

The coupling between the Σ-mode and Δ-mode is non-linear as a result of the junctions in the circuit. The $\hat{a}_\Sigma^\dagger \hat{a}_\Sigma \hat{a}_\Delta^\dagger \hat{a}_\Delta$ term in the Hamiltonian is a purely longitudinal (ZZ) coupling, the coefficient of which is the state-dependent frequency shift, also know as the cross-Kerr shift $\chi_{\Sigma\Delta}$, given by,

$$\chi_{\Sigma\Delta} = \sqrt{E_{C_\Sigma} E_{C_\Delta}} = 2\sqrt{\eta_\Sigma \eta_\Delta}. \tag{3.18}$$

Finally, we arrive at the effective Hamiltonian of the two-mode coaxial, $\hat{H}_Q$ transmon, given by,

$$\begin{aligned}\hat{H}_Q/\hbar =& \omega_\Sigma * \hat{a}_\Sigma^\dagger \hat{a}_\Sigma + \omega_\Delta * \hat{a}_\Delta^\dagger \hat{a}_\Delta - \eta_\Sigma/2 * \hat{a}_\Sigma^{\dagger\,2} \hat{a}_\Sigma{}^2 - \eta_\Delta/2 * \hat{a}_\Delta^{\dagger\,2} \hat{a}_\Delta{}^2 \\ &- \chi_{\Sigma\Delta} * \hat{a}_\Sigma^\dagger \hat{a}_\Sigma \hat{a}_\Delta^\dagger \hat{a}_\Delta.\end{aligned} \tag{3.19}$$

This effective Hamiltonian describes two anharmonic oscillator modes with a purely non-linear coupling between them.

3.1.3 V-Shaped Qutrit Energy Level Structure

Both modes are very strongly coupled to each other through the junctions of the device. Notably, the non-linear coupling ($\chi_{\Sigma\Delta}$) is larger than their respective anharmonicities (η_Σ, η_Δ). This produces addressable transitions that make up an effective V-shaped qutrit energy diagram [27], as shown in Fig. 3.3 (a). The states are labelled as $|nm\rangle$, where $n(m)$ corresponds to the number of excitations in the Σ-mode

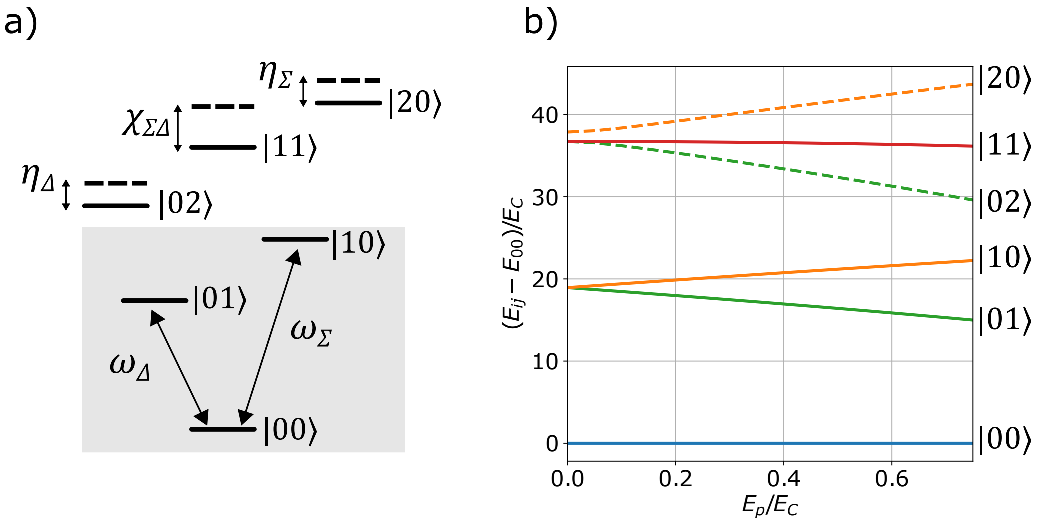

Figure 3.3: (a) Truncated energy level diagram of the two-mode coaxial transmon illustrating anharmonicities ($\eta_{\Sigma,\Delta}$), and state-dependent shift ($\chi_{\Sigma\Delta}$). States labelled as $|nm\rangle$ where $n(m)$ corresponds to the number of excitations in the Σ-mode (Δ-mode). The V-shaped qutrit subspace is highlighted in grey. (b) Eigenenergies of the first 6 energy levels of the two-mode coaxial transmon, as a function of relative coupling energy E_p/E_C, for $E_J = 50E_C$. Result obtained from numerical diagonalisation of the Hamiltonian of Eqn. 3.5. Figure adapted from [29].

(Δ-mode). The wavefunctions of the lowest six energy eigenstates are shown in Fig. 3.4.

We have the potential to use the qutrit system for all-microwave two-qubit gates [146, 147], using one transition as a computational bit and the other to generate entanglement with other qutrits. This allows for far-detuned computational transitions for minimised single-qubit-gate crosstalk, while retaining gate speeds comparable to fixed coupled transmons. These features make the two-mode transmon a potentially useful component for an extensible quantum computing architecture.

3.1.4 Effect of Asymmetry

In our derivation of the Hamiltonian of the circuit, we assumed that the two Josephson junctions were of identical Josephson energy E_J. Whilst this is a parameter regime that we target, the reality of the nanofabrication process is that there are local deviations in the junction energies across a chip scale device. Here we investigate the

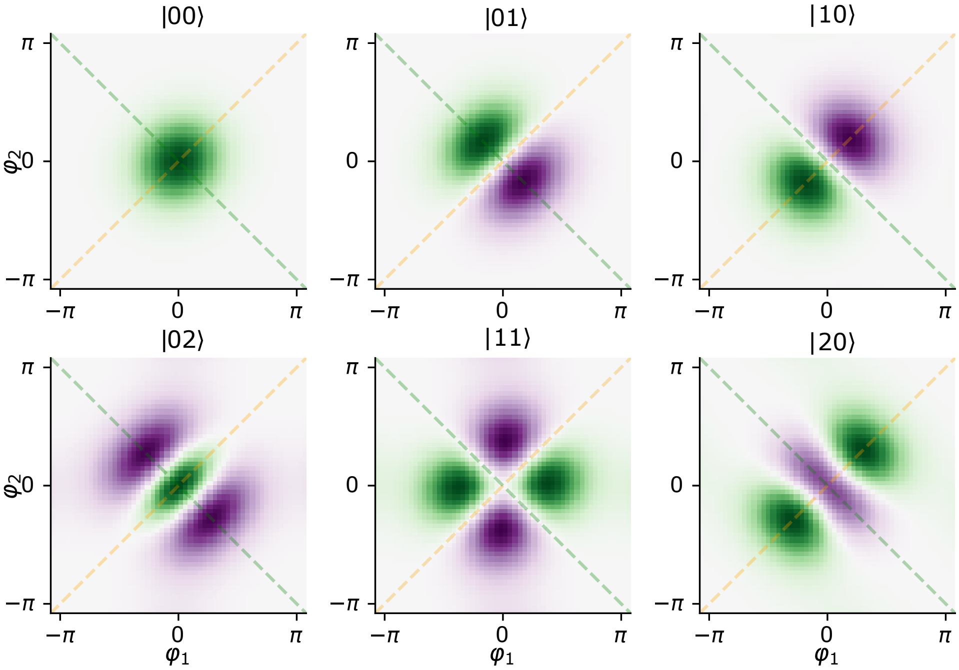

Figure 3.4: Wavefunctions of the six lowest energy eigenstates of the two-mode coaxial transmon in the phase basis. Diagonal dashed lines indicate the summation ($(\varphi_1+\varphi_2)$, orange) and difference ($(\varphi_1-\varphi_2)$, green) phases. States labelled as $|nm\rangle$ where $n(m)$ corresponds to the number of excitations in the Σ-mode (Δ-mode). Wavefunctions generated using [45].

effect of the junction energy asymmetry in the single two-mode coaxial transmon. [1]

We start with the original Hamiltonian of the two-mode coaxial transmon, as given in Eqn. 3.5. In this asymmetric case, we have two non-identical Josephson junctions, of energy E_{J1} and E_{J2}. In the charge and phase basis of $\hat{n}_{1,2}$ and $\hat{\varphi}_{1,2}$, the circuit has the Hamiltonian given by,

$$\begin{aligned}\hat{H} =& 4E_C(\hat{n}_1-n_{g1})^2+4E_C(\hat{n}_2-n_{g2})^2+4E_p(\hat{n}_1-n_{g1})(\hat{n}_2-n_{g2})\\ &-E_{J1}\cos\hat{\varphi}_1-E_{J2}\cos\hat{\varphi}_2,\end{aligned} \tag{3.20}$$

where the parameters E_C, E_p and $n_{g1,2}$ are defined as before. From here, we change

---

[1] We also assumed that the capacitances of the inner islands to the outer island C is identical for both islands. This capacitance is given by the geometry of the islands, which is fabricated via photolithographic methods. In general, the local deviation of this process is small, and the features are very large, thus we neglect this asymmetry. The junction asymmetry is the dominating effect in this system.

to the sum and difference basis of $\hat{\varphi}_\Sigma = \hat{\varphi}_1 + \hat{\varphi}_2$, and $\hat{\varphi}_\Delta = \hat{\varphi}_1 - \hat{\varphi}_2$. With the charging energies defined as previously, we obtain the Hamiltonian given by,

$$\begin{aligned}\hat{H} =& 8E_{C_\Sigma}(\hat{n}_\Sigma - n_{g\Sigma})^2 + 8E_{C_\Delta}(\hat{n}_\Delta - n_{g\Delta})^2 \\ & - (E_{J1} + E_{J2}) \cos\frac{\hat{\varphi}_\Sigma}{2} \cos\frac{\hat{\varphi}_\Delta}{2} + (E_{J1} - E_{J2}) \sin\frac{\hat{\varphi}_\Sigma}{2} \sin\frac{\hat{\varphi}_\Delta}{2}.\end{aligned} \tag{3.21}$$

The key difference between the Hamiltonian of Eqn. 3.6 and Eqn. 3.21 is the second term in the potential energy component given by $(E_{J1} - E_{J2}) \sin\frac{\hat{\varphi}_\Sigma}{2} \sin\frac{\hat{\varphi}_\Delta}{2}$. It is clear that this term vanishes to zero in the symmetric case that $E_{J1} = E_{J2}$, however, in the asymmetric case this term introduces an additional coupling between the Σ-mode and Δ-mode. In a similar way to previously, we can calculate this coupling by expanding the potential terms about zero to fourth-order and performing a canonical transformation to the harmonic oscillator basis. Expanding the potential terms in the Hamiltonian of Eqn. 3.21 yields,

$$\begin{aligned}&\hat{H} = 8E_{C_\Sigma}\hat{n}_\Sigma^2 + 8E_{C_\Delta}\hat{n}_\Delta^2 \\ &- (E_{J1} + E_{J2}) \left(1 - \frac{1}{2}\left(\frac{\hat{\varphi}_\Sigma}{2}\right)^2 + \frac{1}{4!}\left(\frac{\hat{\varphi}_\Sigma}{2}\right)^4 - \dots\right)\left(1 - \frac{1}{2}\left(\frac{\hat{\varphi}_\Delta}{2}\right)^2 + \frac{1}{4!}\left(\frac{\hat{\varphi}_\Delta}{2}\right)^4 - \dots\right) \\ &+ (E_{J1} - E_{J2}) \left(\left(\frac{\hat{\varphi}_\Sigma}{2}\right) - \frac{1}{3!}\left(\frac{\hat{\varphi}_\Sigma}{2}\right)^3 + \dots\right)\left(\left(\frac{\hat{\varphi}_\Delta}{2}\right) - \frac{1}{3!}\left(\frac{\hat{\varphi}_\Delta}{2}\right)^3 + \dots\right).\end{aligned} \tag{3.22}$$

Inserting the operators of Eqn. 3.8 into Eqn 3.22 yields a $(\hat{a}_\Sigma^\dagger + \hat{a}_\Sigma)(\hat{a}_\Delta^\dagger + \hat{a}_\Delta)$ term (due to the $\hat{\varphi}_\Sigma \times \hat{\varphi}_\Delta$ resulting from the expansion of the sinusoidal potential), corresponding to a transverse coupling between the two modes. The coefficient of this term in the Hamiltonian yields the coupling strength, g_{xx}. We isolate the transverse coupling component of the Hamiltonian due to the asymmetry as $H_{asym.}$, given by,

$$\begin{aligned}\hat{H}_{asym.} &= (E_{J1} - E_{J2}) \left(\frac{\hat{\varphi}_\Sigma}{2}\right)\left(\frac{\hat{\varphi}_\Delta}{2}\right) \\ &= \frac{(E_{J1} - E_{J2})}{4} \sqrt{\xi'_\Sigma \xi'_\Delta}(\hat{a}_\Sigma^\dagger + \hat{a}_\Sigma)(\hat{a}_\Delta^\dagger + \hat{a}_\Delta) \\ &= \frac{(E_{J1} - E_{J2})}{\sqrt{E_{J1} + E_{J2}}} \sqrt[4]{E_{C_\Sigma} E_{C_\Delta}}(\hat{a}_\Sigma^\dagger + \hat{a}_\Sigma)(\hat{a}_\Delta^\dagger + \hat{a}_\Delta) \\ &= g_{xx}(\hat{a}_\Sigma^\dagger + \hat{a}_\Sigma)(\hat{a}_\Delta^\dagger + \hat{a}_\Delta),\end{aligned} \tag{3.23}$$

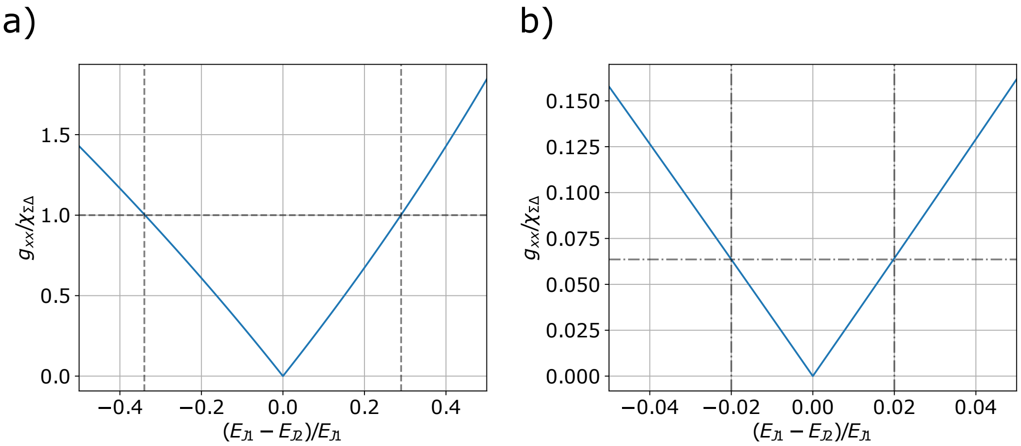

Figure 3.5: Transverse to longitudinal coupling ratio ($g_{xx}/\chi_{\Sigma\Delta}$) as a function of junction asymmetry. Plotted from Eqn. 3.23 (a) Vertical dashed lines show point at which $g_{xx} = \chi_{\Sigma\Delta}$ at a junction asymmetry of ≈ 30 %. (b) Vertical dashed lines show junction asymmetry of 2%, corresponding to usual fabrication process variations. Relative transverse coupling is less than 7% of $\chi_{\Sigma\Delta}$, indicated by horizontal line.

where[2] $\xi_i' = \sqrt{\frac{16E_{C_i}}{(E_{J1}+E_{J2})}}$.

In Fig. 3.5, we plot the strength of the transverse coupling due to junction asymmetry. Whilst the device appears very sensitive to junction asymmetries, we note that in the nanofabrication process, we are able obtain a spread in junction energies on a single chip of 2% [161]. Further post processing techniques can also be applied to reduce this spread and resulting asymmetries further in future works [162].

This additional potential term and subsequent transverse coupling manifests itself in two areas that we investigate. The first is charge sensitivity, where the asymmetry leads to a difference in the magnitude of the maximum charge dispersion measured. The second is in a system of two coupled two-mode coaxial transmons, where the asymmetry leads to unwanted coupling between protected modes. We outline both these effects in Section 3.1.6 and Section 3.3.2 respectively.

---

[2] This is the same definition as before with $E_J \to (E_{J1} + E_{J2})/2$, is the average junction energy.

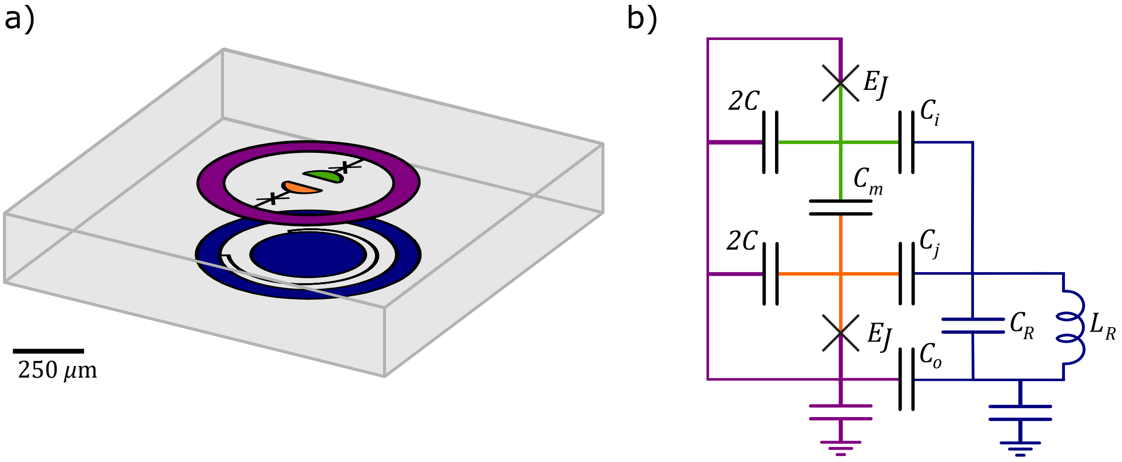

Figure 3.6: (a) A simplified schematic of the device shows a coaxial pad geometry with a split inner conductor resulting in three superconducting islands. A lumped element LC resonator (blue) on the opposing side of substrate allows for dispersive readout of modes. (b) Simplified equivalent circuit of the two-mode coaxial transmon coupled to a linear resonator (of inductance L_R, and capacitance C_R) via inner island to inner island capacitances (C_i, C_j) and outer to outer island capacitance (C_o). Islands coloured as in (a).

3.1.5 Qubit-Resonator Unit-Cell

Here we describe the unit-cell of our architecture, comprising of a two-mode coaxial transmon, coupled to a linear resonator, shown in Fig. 3.6 (a). The qubit and resonator are situated on opposite sides of a substrate, and the coupling between them is due to the capacitances between the five superconducting islands. We show a simplified circuit diagram of the system in Fig. 3.6 (b), neglecting cross-capacitances between the inner islands of the qubit and outer island of the resonator, and vice versa.

We write the Hamiltonian of the two-mode coaxial transmon transversely coupled to a linear resonator as,

$$\hat{H}/\hbar = \hat{H}_Q/\hbar + \omega_r(\hat{a}_r^\dagger\hat{a}_r + 1/2) + g_{\Sigma r}(\hat{a}_\Sigma^\dagger + \hat{a}_\Sigma)(\hat{a}_r^\dagger + \hat{a}_r), \tag{3.24}$$

where $\hat{a}_r^{(\dagger)}$ is the annihilation (creation) operator for the resonator mode, ω_r is the resonator mode frequency, and $g_{\Sigma r}$ is the coupling between the resonator mode and

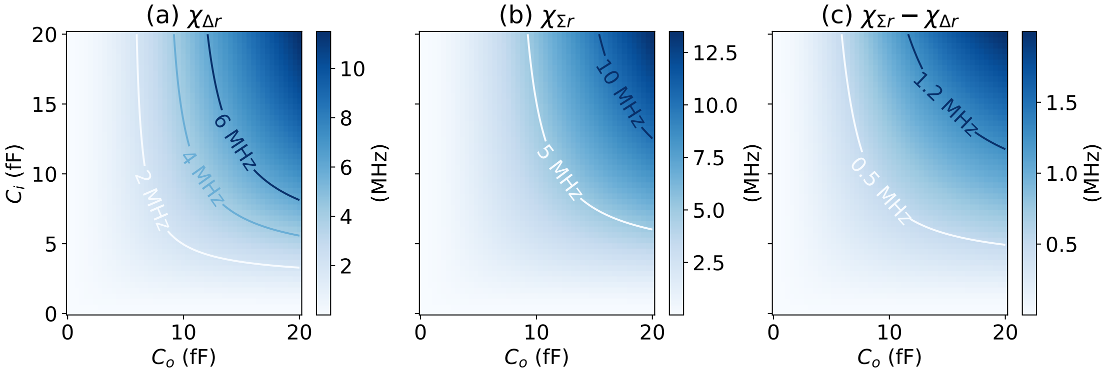

Figure 3.7: State dependent shift χ_{ir} between the linear resonator and Δ-mode (a), and resonator and Σ-mode (b), as a function of the inner to inner island capacitance ($C_i = C_j$), and outer to outer island capacitance (C_o). (c) Difference between $\chi_{\Sigma r}$ and $\chi_{\Delta r}$. Results obtained from quantum circuit analysis (QuCat) simulation of circuit in Fig. 3.6 (b). [164]

the Σ-mode. Due to the symmetry of the Δ-mode, there is no direct transverse coupling to the resonator mode.

The coupling between the resonator and Σ-mode results in a state-dependent frequency shift $\chi_{\Sigma r}$. In the dispersive limit [163], where $g \ll (\omega_r - \omega_\Sigma)$, this shift is given by,

$$2\chi_{\Sigma r} \approx \frac{2g_{\Sigma r}^2 \eta_\Sigma}{(\omega_r - \omega_\Sigma)((\omega_r - \omega_\Sigma) + \eta_\Sigma)} \approx 2\eta_\Sigma \left(\frac{g_{\Sigma r}}{(\omega_r - \omega_\Sigma)} \right)^2, \tag{3.25}$$

given the additional approximation that $\eta_\Sigma \ll (\omega_r - \omega_\Sigma)$.

Whilst the Δ-mode has no direct coupling to the readout resonator, it does inherit a state-dependent frequency shift, $\chi_{\Delta r}$ due to its coupling to the Σ-mode. This frequency shift is given by [28],

$$2\chi_{\Delta r} \approx \frac{2g_{\Sigma r}^2 \chi_{\Sigma\Delta}}{(\omega_r - \omega_\Sigma)((\omega_r - \omega_\Sigma) + \chi_{\Sigma\Delta})} \approx 2\chi_{\Sigma\Delta} \left(\frac{g_{\Sigma r}}{(\omega_r - \omega_\Sigma)} \right)^2, \tag{3.26}$$

in the limit that $\chi_{\Sigma\Delta} \ll (\omega_r - \omega_\Sigma)$. Notably, the frequency shift $\chi_{\Delta r}$ does not depend on the detuning between the Δ-mode and the readout resonator, alleviating any constraints on the qubit frequency in terms of Purcell limit or readout speed.

We explore how this allows us to perform dispersive readout of the multi-mode state in Chapter 4. In Fig. 3.7, we show how the state-dependent frequency shift between each mode and the readout resonator changes as a function of the capacitances shown in the circuit in Fig. 3.6 (b), by using a quantum circuit analyser tool [164] simulation of the circuit. We make the assumption that the capacitances of the inner islands to the readout resonator island ($C_{i,j}$) are equal, and choose values of C, C_m, L_R and C_R to achieve mode frequencies and anharmonicities that match device regimes in experimental chapters. This shows that by modifying the design to reduce the capacitive coupling between the five superconducting islands, one can reduce the coupling between the qubit modes and readout resonator. This demonstrates the engineerability of our architecture, but also that we are not in the regime of other TCQ devices where this coupling can be tuned to zero. In addition, since $\chi_{\Delta r} \neq \chi_{\Sigma r}$, we can implement a joint readout of both modes using a single readout resonator [165].

3.1.6 Charge Sensitivity [3]

The Hamiltonian of Eqn. 3.6 shows a dependence on gate-charge offsets $n_{g\Sigma}$ and $n_{g\Delta}$, corresponding to the sum and difference of gate-charge offsets of the two inner islands, n_{g1} and n_{g2}. Plots of the energy levels E_{00}, E_{01}, E_{10} and E_{11} are shown in Fig. 3.8, for several values of E_J/E_C. As in the case of the transmon qubit [9], we observe the dispersion in energy levels due to the offset charge decreases rapidly with the ratio of E_J/E_C.

We can understand the nature and behaviour of charge dispersion in Eqn. 3.5 in a transmon regime ($E_C, E_p \ll E_J$) by using a 2D tight-binding approximation (see Appendix A).[4] In Fig. 3.9 (a), the potential energy landscape shows that for each energy minimum, there are four neighbouring lattice sites dependent on n_{g1} and n_{g2}, with an equal tunnel-barrier energy between them. This will produce a dispersion relationship of the form $E(n_{g1}, n_{g2}) \sim (\cos n_{g1} + \cos n_{g2})$.

---

[3] Parts of this work have been published in [38]

[4] We note this method can be extended to n degrees of freedom for more complex multi-mode devices.

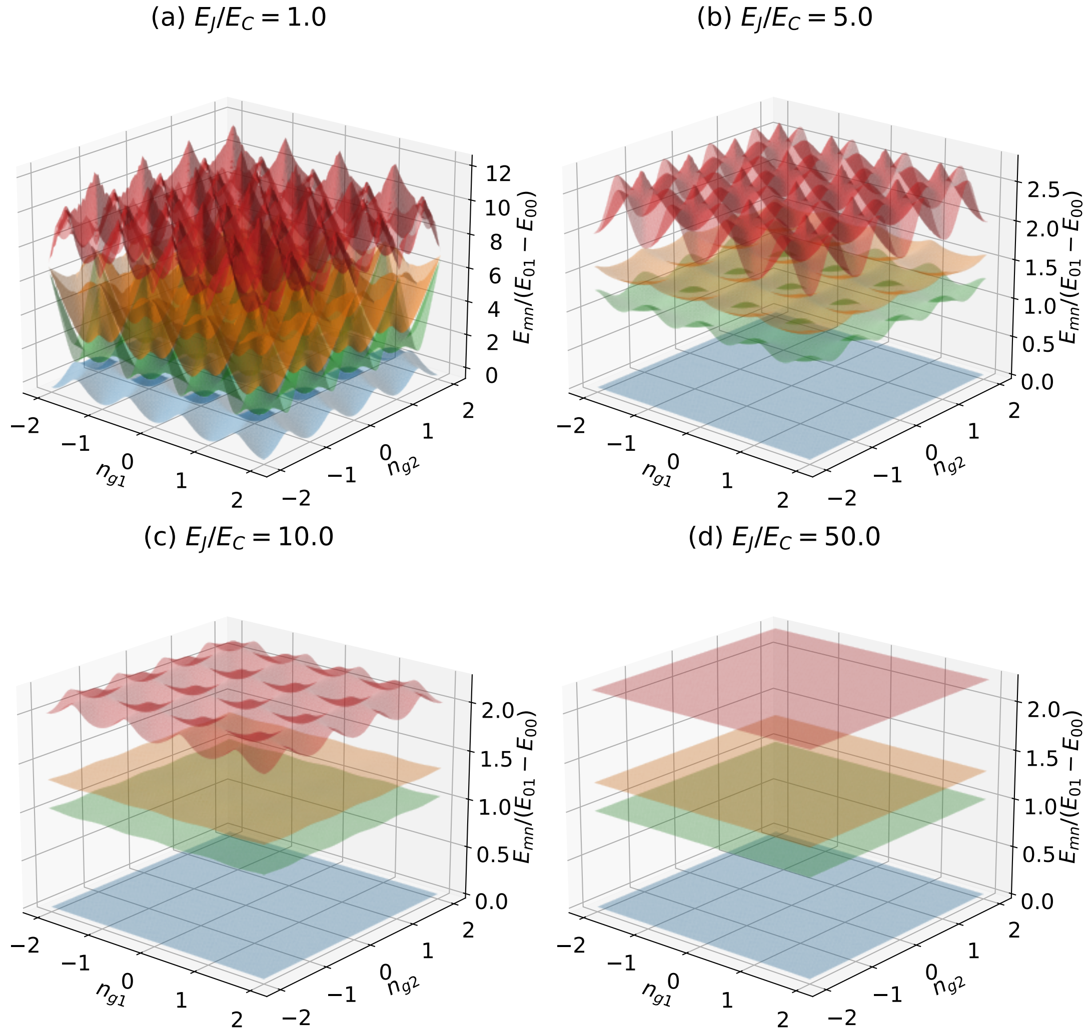

Figure 3.8: Eigenenergies E_{mn} of the $|00\rangle$ (blue), $|01\rangle$ (green), $|10\rangle$ (orange) and $|11\rangle$ levels of the charge sensitive two-mode coaxial transmon Hamiltonian of Eqn. 3.5, as a function of gate charge offsets (n_{g1}, n_{g2}) for different Josephson energy to charging energy ratios E_J/E_C (with constant $E_p = 0.4E_C$). Eigenenergies in units of lowest mode transition energy ($E_{01} - E_{00}$) evaluated at degeneracy point $n_{g1} = n_{g2} = 0.5$. Zero point chosen as bottom of $m = n = 0$ level.

This can be represented in terms of the sum and difference offset charges, $n_{g\Sigma}$ and $n_{g\Delta}$, as:

$$E_{mn}(n_{g\Sigma}, n_{g\Delta}) \approx \overline{E_{mn}} + \frac{\epsilon_{mn}}{4} \cos \pi n_{g\Sigma} \cos \pi n_{g\Delta}, \tag{3.27}$$

where ϵ_{mn} is the maximum measured charge dispersion for the E_{mn} level, where $m(n)$ is the number of excitations in the Σ-mode (Δ-mode).

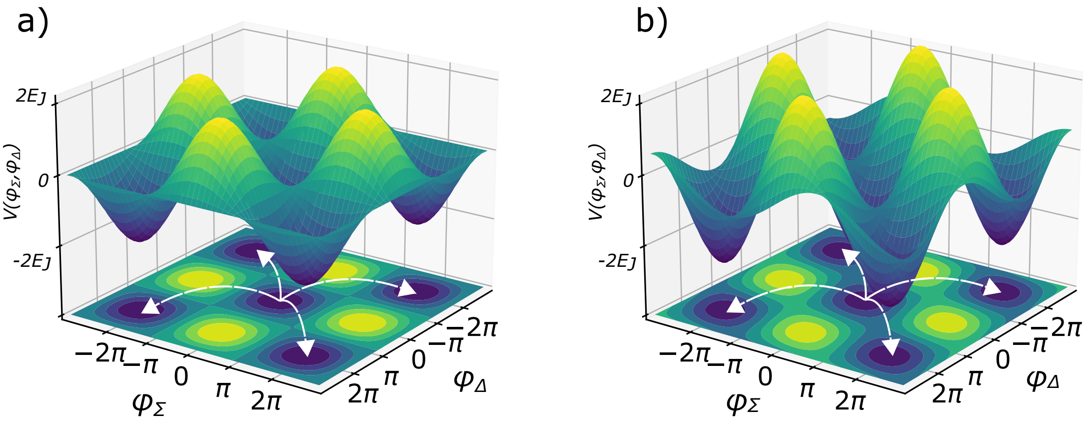

Figure 3.9: (a) The $V(\varphi_\Sigma, \varphi_\Delta) = -2E_J \cos\frac{\varphi_\Sigma}{2}\cos\frac{\varphi_\Delta}{2}$ periodic potential energy landscape of the device, where local minima are 2π periodic along the diagonals. White dashed arrows indicate the four possible tunnelling routes to nearest neighbouring lattice sites. The probability of tunnelling to a neighbouring well in each of the four directions is equal in the symmetric case. ($E_{J1} = E_{J2}$) (b) The $V(\varphi_\Sigma, \varphi_\Delta) = -(E_{J1} + E_{J2})\cos\frac{\hat{\varphi}_\Sigma}{2}\cos\frac{\hat{\varphi}_\Delta}{2} + (E_{J1} - E_{J2})\sin\frac{\hat{\varphi}_\Sigma}{2}\sin\frac{\hat{\varphi}_\Delta}{2}$ potential energy landscape of the device in the asymmetric case ($E_{J2} = 0.6E_{J1}$). The potential barrier between adjacent nearest neighbouring lattice sites is not equal.

One source of decoherence is sudden changes in offset charge due to tunnelling of quasiparticles across Josephson junctions from one superconducting island to another [80]. This corresponds to jumps in either $n_{g1} \to n_{g1} + 0.5$, $n_{g2} \to n_{g2} + 0.5$, otherwise denoted as jumps in charge parity Odd (O) to Even (E) or Even to Odd. This results in four different parity configurations, two for each mode in the system. Fig. 3.10 (a) shows the energy-level dispersion with dependence on four parity configurations (OO, EO, OE, EE), with a maximum dispersion of ϵ_{mn}.

In Fig. 3.10 (b) we show numerical calculation of charge dispersion ϵ_{mn} as a function of E_J and E_C for $E_p = 0.4E_C$, obtained by calculating the eigenvalues of the Hamiltonian in Eqn. 3.5 in the charge basis. We use a semi-analytical wavefunction approach [166] to derive an analytical form of this dependence:

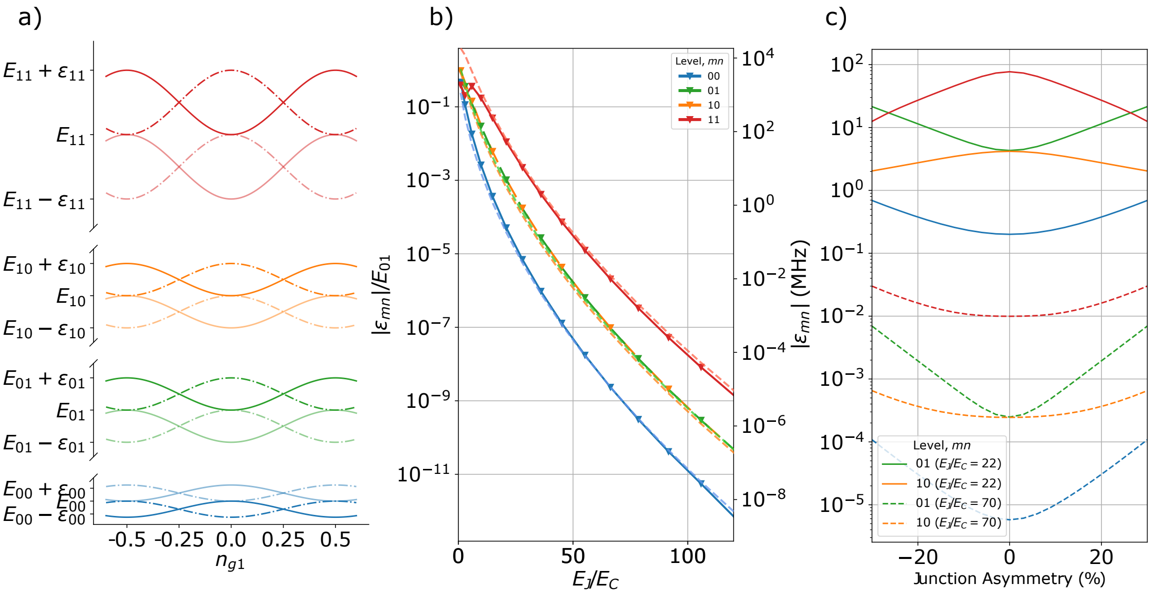

Figure 3.10: (a) Dispersion of eigenenergies of the four lowest energy levels of the qubit Hamiltonian as a function of gate charge offset n_{g1}, with constant gate charge offset n_{g2}, showing the four possible parity configurations (OO, EO, OE, EE). (b) Comparison of numerical (solid) and tight binding model (dashed) calculations of charge dispersion for the lowest four energy levels of the qubit Hamiltonian, as a function of the ratio E_J/E_C. The right vertical scale gives the charge dispersion in MHz for a lowest transition frequency of 5 GHz. (c) Magnitude of charge dispersion of the lowest four energy levels as a function of the junction asymmetry, for charge sensitive device ($E_J/E_C = 22$, solid lines, measured in Chapter 5), and charge suppressed device ($E_J/E_C = 70$, dashed lines, measured in Chapter 4).

$$\begin{aligned}\epsilon_{mn} \approx\ & A_0 E_J \frac{2^{2(m+n)}}{m!n!} \\ & \times \left(\frac{E_J}{E_C(1+E_p/2)}\right)^{m/2} \left(\frac{E_J}{E_C(1-E_p/2)}\right)^{n/2} \\ & \times \exp\left\{-\left(\sqrt{\frac{2E_J}{E_C(1+E_p/2)}}+\sqrt{\frac{2E_J}{E_C(1-E_p/2)}}\right)\right\}.\end{aligned} \tag{3.28}$$

This charge dispersion follows an exponential suppression, and in the limit $E_p \to 0$, the exponent term tends towards the value for the standard transmon. The factor A_0 is obtained empirically by fitting to the numerical calculation of charge dispersion, shown in Fig. 3.10 (b).

As previously calculated, any asymmetry in the Josephson junction energies can have a significant effect on the behaviour of the device. Here, we note the junction asymmetry modifies the potential term, as shown in Fig. 3.9 (b). This changes our previous assumption that the tunnel-barrier energies between adjacent lattices are equal. Since the dominant term in the calculation of the magnitude of charge dispersion is the overlap of these adjacent wavefunctions modulated by the potential, this will result in a non-equal maximum charge dispersion of each mode. We show this calculated numerically in Fig. 3.10 (c).

Each mode is sensitive to both charge offsets, i.e. if there are fluctuations in $n_{g\Sigma}$, this can be observed in dispersion of the Δ-mode. Importantly, this means that a single mode can detect fluctuations in both offset charges simultaneously.

We note that whilst the multi-mode qubit structures posses more complex charge sensitivities, we present a method to suppress this sensitivity. In the same way the transmon qubit is designed to have high E_J/E_C ratio, we can also increase the ratio of Josephson energy to charging energies to suppress the sensitivity to low-frequency charge noise.

In experimental chapters, we explore devices with a range of parameter regimes and magnitudes of charge sensitivity. In Chapter 5, we present results of experiments on a highly charge-sensitive two-mode coaxial transmon, and utilise the complex multi-mode device as a spatial detector of surface charge.

3.2 Inverted Two-mode Coaxial Transmon

The versatility of superconducting circuits allows us to easily modify designs in order to achieve more desirable parameter regimes. Here we present a modified design of a three-island, two-junction, coaxial superconducting qubit device, which we name the inverted two-mode coaxial transmon.

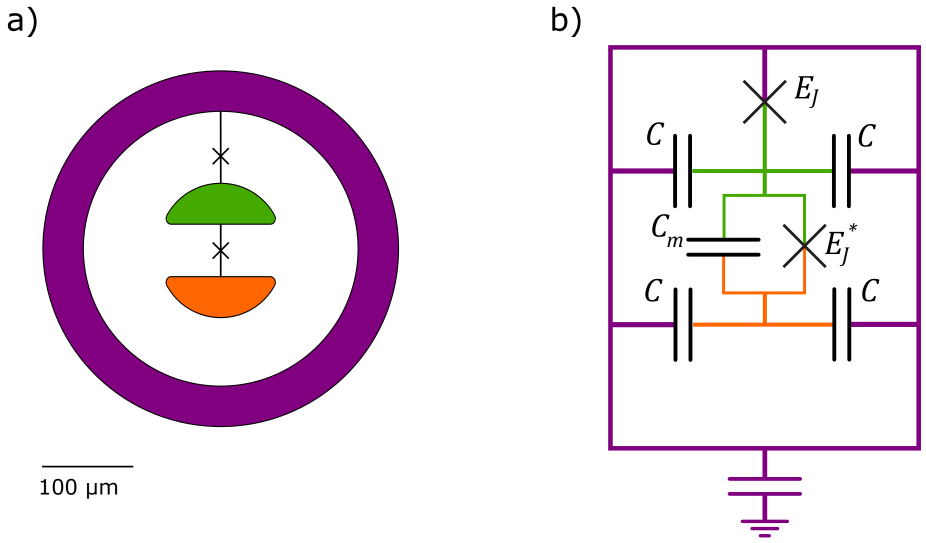

Figure 3.11: (a) Simplified schematic of the inverted two-mode coaxial transmon. Inner superconducting islands connected by Josephson Junction (E_J^*). Outer superconducting island connected via Josephson junction (E_J) to upper inner superconducting island (green). (b) Equivalent circuit diagram of the inverted two-mode coaxial transmon. Inner islands connected via capacitance (C_m) and Josephson junction (E_J^*) between them. Inner islands connected to outer island via capacitance ($2C$), and upper inner island (green) connected to outer island via Josephson junction (E_J)

3.2.1 Device Design

The circuit of this design is shown in Fig. 3.11, where the notable modification is the moving of one of the junctions to be between the two inner islands. Whilst this does break the symmetry of the device, and the symmetry protection aspects that the previous device presented possesses, the effect is that the frequencies of the Σ-mode and Δ-mode are reversed ($\omega_\Delta > \omega_\Sigma$). The device still has two modes, however, the higher frequency mode has an electric dipole moment, and the lower frequency mode has an electric quadrupole moment, inverted to the previous device presented.

3.2.2 Potential Use Cases

This inversion in the polarisation of the electric fields of the two modes of the device lends itself to novel use cases. One such architecture we can consider is coupling the higher frequency mode to a uniform electric field (due to the dipole-like nature of the mode), in a 3D electromagnetic environment.

The simplest example of this is to consider embedding a substrate with the inverted two-mode coaxial transmon fabricated on inside a 3D cavity. In this case, the cavity would couple to the higher frequency dipole-like mode, allowing for dispersive readout, whilst the lower frequency quadrupole like-mode would be protected[5]. This architecture can also be exploited to generate a global coupling scheme between many inverted two-mode coaxial transmon devices, with a selective local control.

The second example of the inverted two-mode coaxial transmon embedded in a 3D electromagnetic environment architecture we consider is that of a waveguide. The useful characteristic of a waveguide is that it acts as a microwave transmission line, with a cutoff frequency given by,

$$f_c = \frac{1}{2a\sqrt{\mu\epsilon}} = \frac{c}{2a}, \tag{3.29}$$

where a is the width of the waveguide, μ (ϵ) is the relative permeability (permittivity) of the transmission medium, and c is the speed of light through the medium. Below this frequency, no waves can propagate through the waveguide [167].

This high pass filtering mechanism allows us to engineer a system such that the higher frequency dipole-like modes can couple to, and be addressed by, the waveguide (with frequencies above f_c), whereas the lower frequency quadrupole-like modes can be placed below the waveguide cutoff frequency. This adds an additional layer of protection, since the lower frequency modes cannot couple to the waveguide mode, and are below the cutoff frequency.

This has multiple possible applications, notably in the areas of multiplexing readout, well as single microwave photon detection [168–170].

---

[5] Protected with respect to decoherence as a result of being coupled to a cavity [30]. Breaking the symmetry does introduce a transverse coupling between the Σ-mode and Δ-mode, such that the protected mode would be susceptible to Purcell losses, albeit mediated via the higher frequency mode which would act as a Purcell filter.

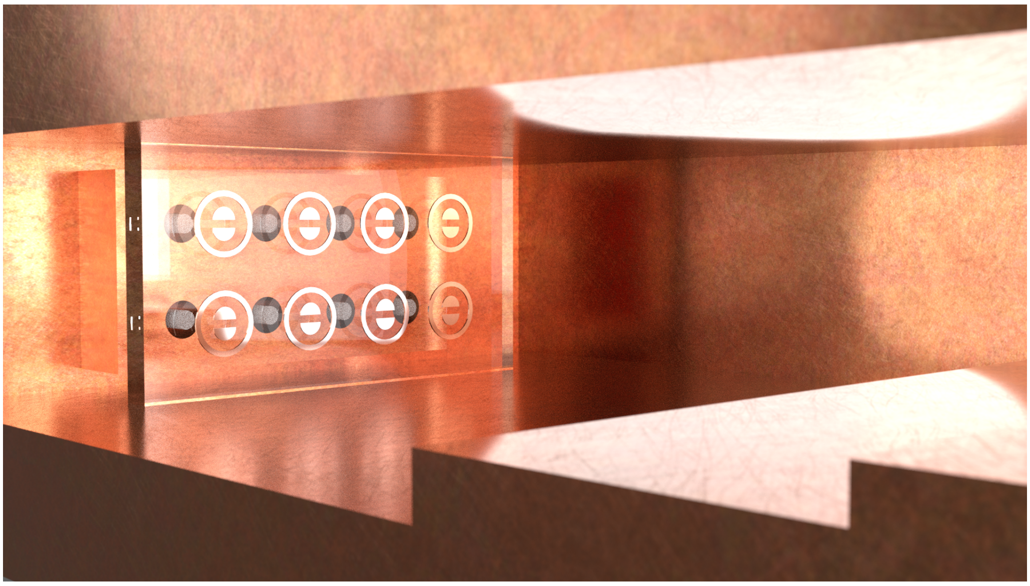

Figure 3.12: 3D render of an inverted two-mode coaxial transmon device embedded in a 3D waveguide architecture. Higher frequency dipole-like modes couple to the waveguide mode, allowing addressability of multiple devices from a single control port. Coaxial control lines protrude into the waveguide from behind the substrate to address the protected, lower frequency, quadrupole-like modes.

Whilst we introduce this modified device and conjecture of the potential use cases, we do not present any experimental demonstration or results. Incorporating multimode qubits in 3D waveguides is the subject of ongoing investigations, for usage in multiplexed readout, and photon detection applications. We show a visualisation of this experiment in Fig. 3.12.

3.3 Coupled Two-mode Coaxial Transmon Architectures

In this section, we introduce a system consisting of two statically-coupled two-mode coaxial transmons, depicted in Fig. 3.13. We investigate the coupling of the four modes of the system, and show that we are able to engineer a highly mode-selective coupling, using the spatial symmetries of the modes. This allows us to demonstrate the use of two protected modes of the system as computational modes, with no measurable quantum crosstalk (unwanted ZZ interactions) between them. In addition,

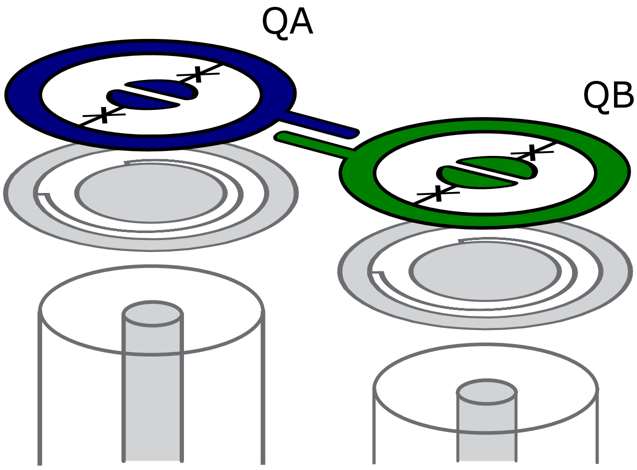

Figure 3.13: Simplified schematic of a pair of two-mode coaxial transmon devices QA (blue) and QB (green). Outer islands coupled together via an overlapping arm capacitor. LC resonators on opposing side of substrate allow for selective readout of each two-mode coaxial transmon device, as in Section 3.1.5, along with coaxial control lines, as described in Chapter 2, for addressing the device and readout resonator.

we present a theory of how a microwave activated conditional phase gate can be operated, utilising the coupled ancillary modes of the system (AT-MAP).

This system of two coupled two-mode coaxial transmons (labelled as QA and QB) has four modes: QA-Σ-mode, QA-Δ-mode, QB-Σ'-mode and QB-Δ'-mode. We label the four mode state of the device as $|ijkl\rangle$, where $i(j)$ correspond to the number of excitations in the QA-Σ-mode (QA-Δ-mode), and $k(l)$ corresponds to the number of excitations in the QB-Σ'-mode (QB-Δ'-mode). This is more clearly pictured when we write the wavefunction of the system as $|\psi\rangle = |\Sigma\Delta\Sigma'\Delta'\rangle$

3.3.1 Device Hamiltonian and Mode-Selective Coupling

The system we explore in this work comprises of a pair of two-mode coaxial transmons, coupled together via an overlapping arm capacitor, as depicted in Fig. 3.13 (a). In the coupled anharmonic oscillator approximation, this system has the Hamiltonian:

$$\hat{H}_{Total}/\hbar = \hat{H}_{QA} + \hat{H}_{QB} + \hat{H}_{int}, \tag{3.30}$$

a) Σ-mode - Σ'-mode

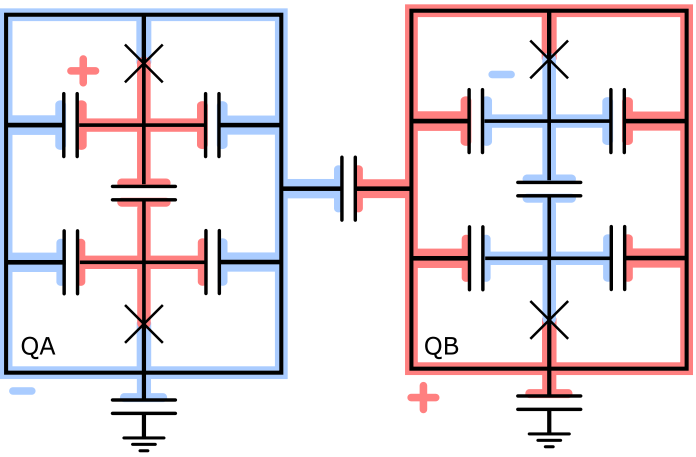

b) Δ-mode - Δ'-mode

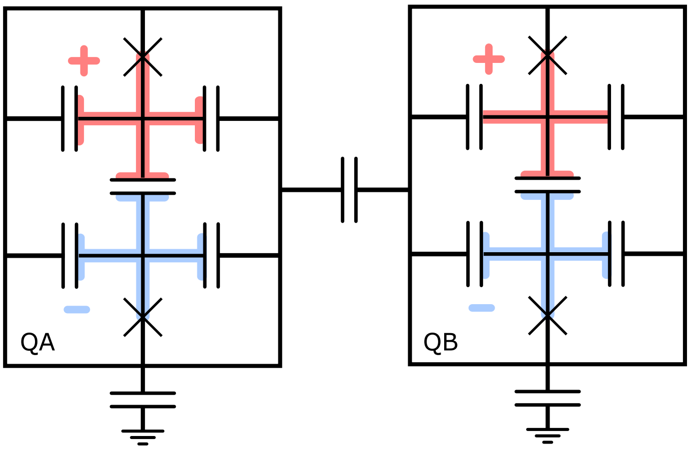

Figure 3.14: Mode selective coupling in two-mode coaxial transmons. (a) Illustration of electric field oscillations and superconducting island participation in both QA Σ-mode and QB Σ′-mode. Modes hybridise due to coupling capacitance between outer islands of devices. (b) Illustration of electric field oscillations and superconducting island participation in both QA Δ-mode and QB Δ′-mode.

where $\hat{H}_{QA}$ and $\hat{H}_{QB}$ are the two-mode device Hamiltonians of Eqn. 3.6, and $\hat{H}_{int}$ is the interaction Hamiltonian, given by:

$$\hat{H}_{int}/\hbar = J(\hat{a}^\dagger_{\Sigma}\hat{a}_{\Sigma'} + \hat{a}_{\Sigma}\hat{a}^\dagger_{\Sigma'}). \tag{3.31}$$

Here, J is the exchange interaction strength between the symmetric modes of each device, labelled as $\Sigma^{(\prime)}$ for QA (QB). Since the capacitor couples on the outer islands of the devices, only modes in which the outer islands participate in will couple across the devices, as shown in Fig. 3.14 (a). This is true for the symmetric Σ-modes of each device, hence there is an exchange interaction between them, identical to that of statically coupled fixed frequency transmon devices. However, as the outer island does not participate in the antisymmetric Δ-modes, that correspond to out-of-phase oscillations on the two inner islands of the device, as shown in Fig. 3.14 (b), there is no direct coupling between these modes across the device. In addition, the introduction of the transverse coupling between symmetric modes does not introduce a perturbative cross-Kerr shift between antisymmetric modes [146]. As such we are able to create a mode-selective coupling in this system, where only the symmetric Σ-modes of each device are coupled, and the antisymmetric Δ-modes are protected from each other.

This structure lends itself to using the Δ-modes of the system as protected computational modes, whilst using the coupled Σ-modes as communication modes. By removing the direct coupling between computational modes, we eliminate the always-on unwanted interaction that introduces errors into computations within fixed-frequency, statically coupled, transmon systems.

3.3.2 Effect of Junction Asymmetry

As introduced previously in Section 3.1.4, asymmetry in the junction energies of the two-mode coaxial transmon introduces an additional transverse coupling between the Σ-mode and Δ-mode. The introduced mode-selective coupling is engineered to suppress any coupling between computational modes, however, this asymmetry induced transverse coupling between each pair of Σ and Δ-modes does introduce a coupling between the protected Δ-modes across the two devices, mediated by the ancillary transitions.

To demonstrate this, we first construct the Hamiltonian of coupled two-mode coaxial transmon system in the anharmonic oscillator approximation, with an ad-

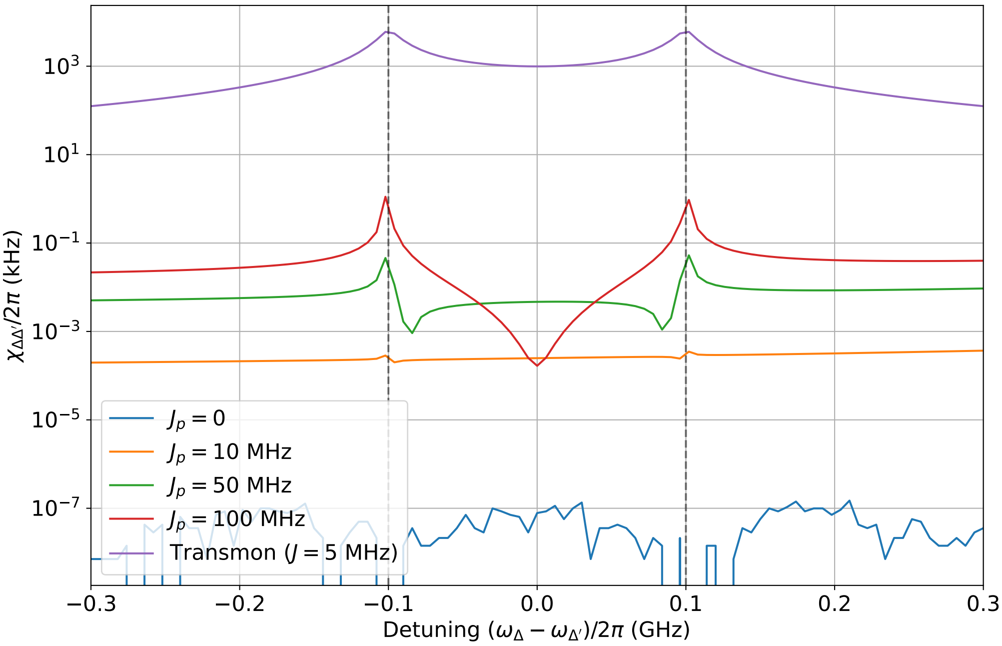

Figure 3.15: State-dependent frequency shift $\chi_{\Delta\Delta'}$ between the protected, computational, Δ-modes, of QA and QB, as a function of Δ-mode detuning, for increasing parasitic exchange coupling J_p. State-dependent frequency shift of two coupled single mode transmon (purple) with $J = 5$ MHz (and equivalent ω and η) shown for comparison. Vertical dashed lines indicate anharmonicities ($\eta_i/2\pi = 0.1$ GHz). Results obtained from numerical diagonalisation of Hamiltonian in Eqn. 3.32.

ditional junction-asymmetry-induced parasitic coupling between the Σ-modes and respective Δ-modes (of strength J_p, calculated from Eqn. 3.23) such that the system Hamiltonian is given by,

$$\hat{H}_{asym.}/\hbar = \hat{H}_{Total}/\hbar + J_p(\hat{a}_\Sigma^\dagger \hat{a}_\Delta + \hat{a}_\Sigma \hat{a}_\Delta^\dagger) + J_p(\hat{a}_{\Sigma'}^\dagger \hat{a}_{\Delta'} + \hat{a}_{\Sigma'} \hat{a}_{\Delta'}^\dagger). \tag{3.32}$$

We numerically calculate the eigenenergies of this Hamiltonian using a QuTip [171] simulation, using a range of values J_p, and the system parameters: $\omega_\Delta/2\pi = 5$ GHz, $\omega_\Sigma/2\pi = 7$ GHz, $\omega_{\Sigma'}/2\pi = 7.1$ GHz, $\eta_i/2\pi = 0.1$ GHz, $\chi_{\Sigma\Delta}/2\pi = \chi_{\Sigma'\Delta'}/2\pi = 0.2$ GHz, $J/2\pi = 10$ MHz. We obtain the state-dependent frequency shift between the computational modes, $\chi_{\Delta\Delta'}$, as a function of the detuning between these modes, shown in Fig. 3.15. Note this frequency shift is a perturbative cross-Kerr shift as a result of the parasitic transverse coupling, not a direct longitudinal coupling between the two Δ-modes. We choose values of J_p approximately corresponding to a 0% ($J_p/2\pi = 0$ MHz), 1% ($J_p/2\pi = 10$ MHz), 5% ($J_p/2\pi = 50$ MHz) and 10% ($J_p/2\pi = 100$ MHz) asymmetry in internal device Josephson junction energies, and assume J_p to be equivalent across both coupled devices for simplicity. The obtained $\chi_{\Delta\Delta'}$, shown in Fig. 3.15, shows that even with a large asymmetry in internal junction energies, the resulting frequency shift is orders of magnitude smaller than the equivalent to the always-on unwanted ZZ interaction in coupled transmon circuits. The typical spread in nanofabricated junction energies of 2% on a chip (corresponding to a 2% asymmetry in the junctions of a single device), result in $\chi_{\Delta\Delta'} \sim 10$ Hz. This is immeasurable with current experimental sensitivities.

3.3.3 AT-MAP Interaction

In order for the coupled two-mode coaxial transmon system to be used for quantum computation, it is necessary to be able to perform two-qubit gate operations between computational modes. Whilst the Δ-modes of the device have suppressed quantum crosstalk between them, making them favourable for computational states, there is no direct coupling and so conventional two-qubit gates (as described in Section 2.2.2) are not possible. Here we describe how we can use the ancillary modes of the device to generate an entanglement between these computational modes.

3.3.3.1 Perturbation Theory and Gate Operation

In 3.16 (a), we show a simplified truncated energy level diagram of the coupled system. Due to the capacitive coupling between the outer islands of the devices, there is an exchange interaction of strength J between the ancillary Σ-modes of the system, shown in the highlighted dark blue region of Fig. 3.16 (a). When these transitions are on resonance, they will experience a splitting due to the interaction and avoided

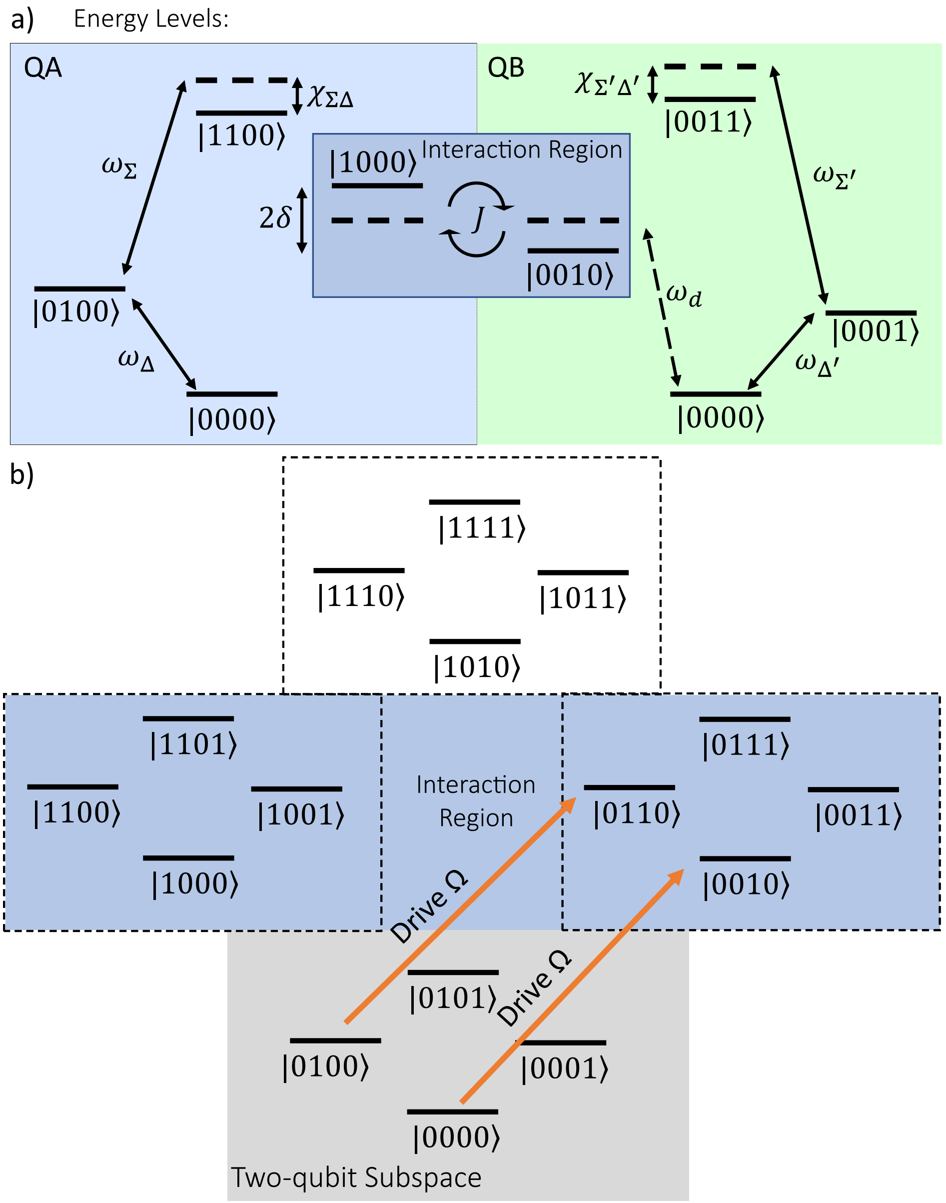

Figure 3.16: Energy levels of the truncated coupled two-mode coaxial transmon system. (a) Energy levels in the separate two-mode coaxial transmon picture. Each device has a V-shaped energy level structure, with the ancillary transitions (Σ-modes) on resonance, causing a conditional splitting 2δ. Dotted arrow shows where AT-MAP interaction is driven, when QA Δ-mode is operated as the control, and QB Δ'-mode is the target. (b) Energy level diagram in the tensor product of computational modes and ancillary modes picture. Highlighted interaction region shows where ancillary transitions are excited. Grey region shown computation subspace of the two Δ-modes. Difference in transition energies between $|0000\rangle \rightarrow |0010\rangle$ and $|0100\rangle \rightarrow |0110\rangle$, (of magnitude δ) leads to driven AT-MAP interaction, shown by orange arrows.

crossing of the energy levels. Even if the transitions are not exactly on resonance, they will still undergo a splitting of 2δ, where,

$$\delta = \frac{1}{2}\left(\sqrt{4J_{\Sigma\Sigma'}^2 + \Delta_{\Sigma\Sigma'}^2} - \Delta_{\Sigma\Sigma'}\right), \tag{3.33}$$

where $\Delta_{\Sigma\Sigma'} = \omega_\Sigma - \omega_{\Sigma'}$ is the detuning between the Σ-modes, $J_{\Sigma\Sigma'}$ is the interaction strength between the ancillary transitions.

We describe this as a conditional splitting due to the large internal mode cross-Kerr shift $\chi_{\Sigma\Delta}$. This ensures a difference between the energies of the $|0000\rangle \rightarrow |0010\rangle$ and $|0100\rangle \rightarrow |0110\rangle$ transitions, where the QA Δ-mode is used as the control mode, given by δ as shown in Fig. 3.16 (b).

In order to use this mechanism for a two-qubit gate operation, we utilise the ac-Stark effect. Introducing an external drive of amplitude Ω, detuned from a transition by Δ_d, we can shift the energy level by an amount Ω^2/Δ_d, provided this quantity is small. Due to the strong longitudinal coupling between the Σ-mode and Δ-mode of each device, we can drive the ancillary transitions off-resonantly and accumulate a phase ϕ on the $|0000\rangle$ state relative to the $|0001\rangle$ state. When driving the target qubit ancillary transition off-resonantly in the interaction region, as shown in Fig. 3.16 (a), the conditional splitting of the coupled ancillary modes previously described leads to a phase accumulation dependent on the state of the Δ-mode of the control device. As such, we are able to obtain a conditional phase rotation in the Δ-mode of the target device (QB), dependent on the state of the Δ-mode of the control device (QA). This is how we drive an all-microwave conditional phase gate via the ancillary transitions (AT-MAP), and are able to generate an entanglement operation between two modes with no direct coupling between them.

The interaction can be analytically described through perturbation theory. We first constructing the diagonalised matrix of the Hamiltonian of Eqn. 3.30 up to the

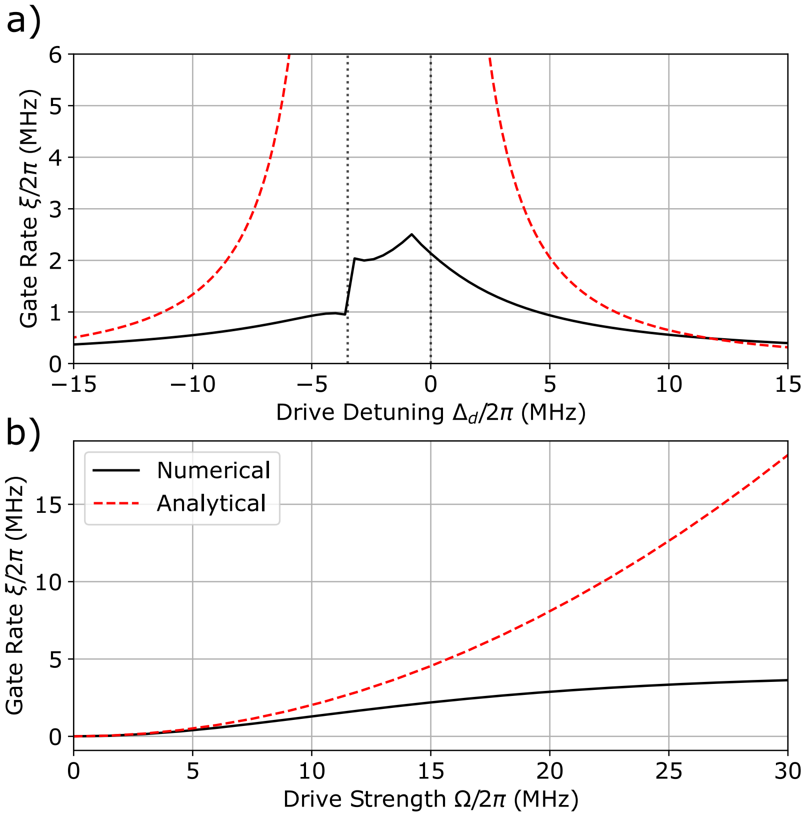

Figure 3.17: Perturbative analysis of the AT-MAP interaction. (a) Gate rate ξ as a function of detuning between drive and target mode ancillary transition ($\Delta_d = \omega_d - \omega_\Sigma$), for a drive strength of $\Omega/2\pi = 5$ MHz. Vertical dashed lines indicate asymptotes at $\Delta_d = 0$ and $\Delta_d/2\pi = \delta/2\pi = 3.8$ MHz. (b) Gate rate ξ as a function of drive strength, at a detuning of $\Delta_d/2\pi = 15$ MHz. Numerical result (black, solid) calculated from an $N = 6$ level simulation of the coupled two-mode coaxial transmon Hamiltonian. Analytical result (red, dashed) plotted from Eqn. 3.35.

two-photon excitation manifold and model the AT-MAP interaction as a drive term on the target mode ancillary transition, given by,

$$\hat{H}_d = \Omega(\hat{a}^\dagger_{\Sigma'} + \hat{a}_{\Sigma'}). \tag{3.34}$$

We move to the rotating frame of the drive term of frequency ω_d, and diagonalising the matrix using a second order Schreiffer-Wolff transformation [172], we obtain a gate rate of:

$$\xi = (E_{0101} - E_{0001} - E_{0100} + E_{0000})/\hbar \approx \frac{\Omega^2 \delta}{\Delta_d(\Delta_d - \delta)}, \tag{3.35}$$

where Ω is the drive strength, δ is the splitting of the ancillary transitions, and $\Delta_d = \omega_d - \omega_\Sigma$ is the drive detuning. This is defined as the microwave induced ZZ interaction between the protected Δ-modes of the system. We plot the analytical result, along with the result of a $N = 6$ level numerical simulation of the system with parameters listed in Section 3.3.2 (with $J_p = 0$), in Fig. 3.17. Our analytical expression identifies the asymptotic behaviour of the interaction when $\Delta_d = 0$, and $\Delta_d = \delta$, indicating when the ancillary transition is driven on resonance. However, we observe the perturbative result breaks down for strong drive strengths, and small detunings. In experiments, we use larger drive strengths in an attempt to maximise gate speeds.

We see that there is poor agreement between our analytical results and numerical calculation for small detunings or large drive strengths. This is due to our analytical calculation treating the perturbations of the transverse coupling between ancillary modes and the additional drive term separately, and is also seen in [114]. A more thorough treatment considering both perturbations simultaneously, as in [173], could produce more accurate results, but is beyond the scope of this work.

To demonstrate how this conditional phase interaction can be used as a two-qubit gate between protected computational modes, we perform a simulation of the time dynamics of the coupled two-mode coaxial transmon system under a constant off-resonant drive to an ancillary transition. Constructing the Hamiltonian of Eqn. 3.30, with parameters $\omega_\Delta/2\pi = 4$ GHz, $\omega_\Sigma/2\pi = 7$ GHz, $\omega_{\Delta'}/2\pi = 4.5$, $\omega_{\Sigma'}/2\pi = 7.1$ GHz, $\eta_i/2\pi = 0.1$ GHz, $\chi_{\Sigma\Delta}/2\pi = \chi_{\Sigma'\Delta'}/2\pi = 0.25$ GHz, $J/2\pi = 15$ MHz, we introduce a time varying drive term of the form

$$\hat{H}_{drive}/\hbar = \Omega \cos(\omega_d t)(\hat{a}^\dagger_{\Sigma'} + \hat{a}_{\Sigma'}), \tag{3.36}$$

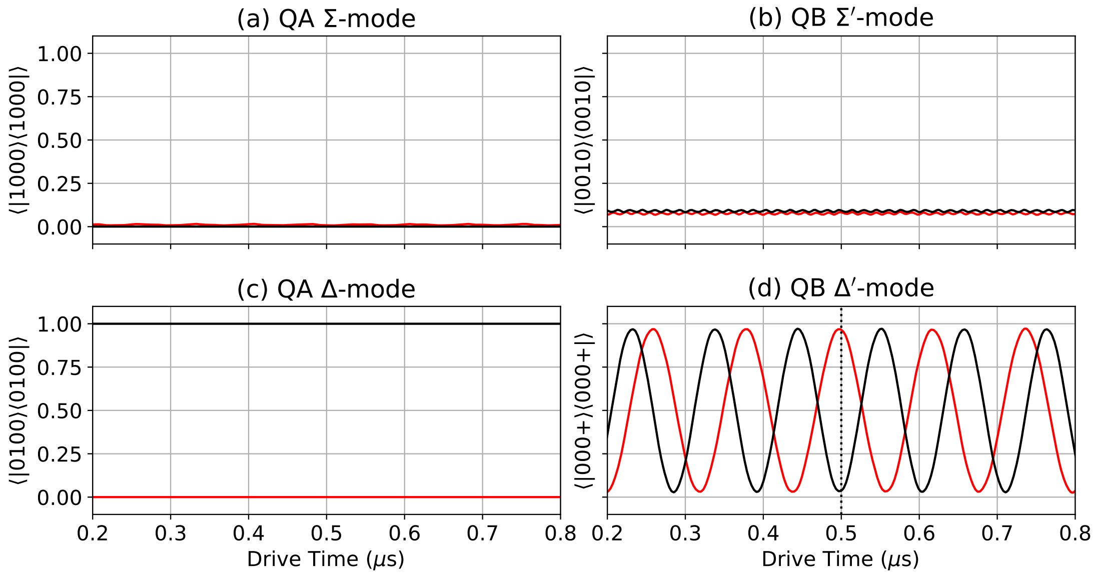

Figure 3.18: Driven simulation of the AT-MAP gate procedure, described in main text. Excited state population of the QA Σ-mode (a), QB Σ′-mode (b) and QA Δ-mode (c), with the control mode (QA Δ-mode) initialised in the ground (red) or excited state (black). (d) Expectation of the $|+\rangle\langle+|$ operator of the target mode (QB Δ′-mode) as a function of AT-MAP interaction drive time with the control mode initialised in the ground (red) or excited (black) state. Target mode initialised in the $|+\rangle = 1/\sqrt{2}(|0\rangle + |1\rangle)$ state. Oscillations indicate rotation around the Z axis of the Bloch sphere. Vertical dashed line at 500 ns shows when oscillations are maximally out of phase, such that a conditional π phase shift occurs.

where $\Omega/2\pi = 50$ MHz is the drive amplitude, and $\omega_d/2\pi = \omega_{\Sigma'}/2\pi - 50$ MHz is the drive frequency. Using a master equation solver [171], we are able to observe the time evolution of the system under set initial conditions. The two initial condition cases we observe are when the control mode (QA-Δ-mode) is in the ground or excited state.

In Fig. 3.18 (a) (b) and (c), we show the expectation of the labelled modes being in the excited state when the interaction is driven. As expected, the control qubit ancillary transition (QA Σ-mode, Fig. 3.18 (a)) shows no excited state population, and the control qubit computational mode is in the ground or excited state dependent on the initialisation. The target qubit ancillary transition (QB Σ′-mode, Fig. 3.18 (b)) shows a small amount of excited state population, since it is being driven off-resonantly (detuned by 50 MHz). We note that the excited state population is very similar for the two control states, due to the drive detuning (50 MHz) being much larger than the target qubit ancillary transition frequency shift ($(E_{0110} - E_{0010} - E_{0100} + E_{0000})/\hbar = \chi_{\Sigma'\Delta}/2\pi \sim 5$ MHz). In Fig. 3.18 (d) we show the expectation of the $|+\rangle\langle+|$ operator of the target qubit computational mode (QB Δ'-mode). The oscillations visible show the Bloch vector rotating about the Z axis at a rate dependent on the state of the control mode. When these oscillations are maximally out-of-phase, the target mode accumulates a phase $\phi = \pi$ relative to the phase accumulated when the control mode is in the ground state. This is how we implement a conditional phase gate, also described as a $[ZZ]_\pi$, or CZ gate.

3.3.3.2 Resonance Conditions

As this gate is driven outside the computational subspace of the Δ-modes, we can utilise other transitions of the multi-mode device that are coupled in order to perform this interaction. In this system, the $|1000\rangle$-$|0010\rangle$, $|1100\rangle$-$|0011\rangle$, $|1100\rangle$-$|0010\rangle$ and $|1000\rangle$-$|0011\rangle$ energy levels will all have an exchange coupling of strength $J_{|ijkl\rangle|mnop\rangle}$, where $J_{|ijkl\rangle|mnop\rangle}$ is the matrix element corresponding to the interaction between the $|ijkl\rangle$ and $|mnop\rangle$ transitions, due to their spatial symmetry. This will lead to a conditional splitting δ as before that can be used in the same way as previously described in order to perform the AT-MAP interaction. This allows us much greater flexibility in frequency allocation when designing these devices for multi-qubit gate operations, as there are four possible resonance conditions that can be met in order to maximise gate speed:

$$\begin{aligned} \omega_\Sigma &= \omega_{\Sigma'} \\ \omega_\Sigma &= \omega_{\Sigma'} - \chi_{\Sigma'\Delta'} \\ \omega_\Sigma - \chi_{\Sigma\Delta} &= \omega_{\Sigma'} \\ \omega_\Sigma - \chi_{\Sigma\Delta} &= \omega_{\Sigma'} - \chi_{\Sigma'\Delta'} \end{aligned} \tag{3.37}$$

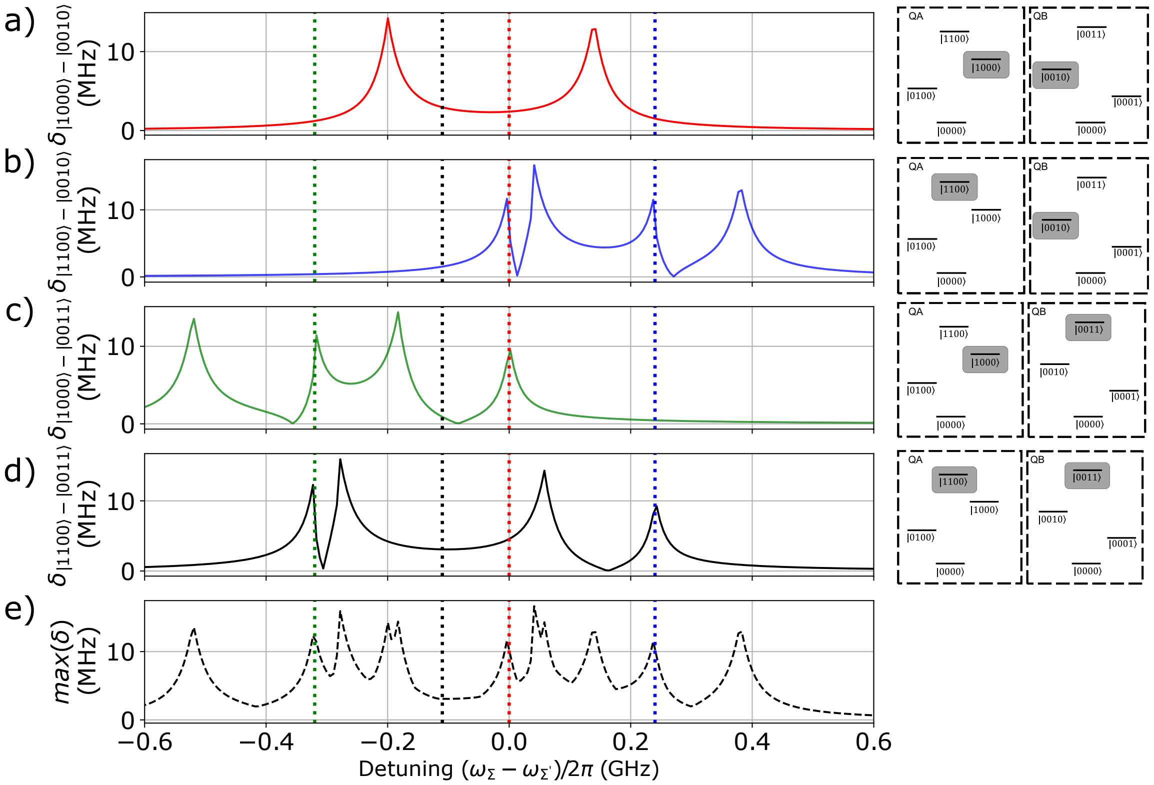

Figure 3.19: Conditional energy level splitting δ of the four possible pairs of ancillary transitions around which the AT-MAP interaction can be driven, as a function of detuning between Σ-modes. Vertical dashed lines show locations of the four resonance conditions in Eqn. 3.37. Energy level diagrams (right) of coupled two-mode coaxial transmon system, as in Fig. 3.16, with the pair of transitions on resonance in each case highlighted in grey. Result from numerical diagonalisation of Hamiltonian in Eqn. 3.30, with parameters from device measured in Chapter 6 (parameters shown in Table 6.1)

In Fig. 3.19, we plot the state dependent shift between all four of these possible resonant transitions, as a function of the detuning between the Σ-modes of the devices, and highlight the frequencies at which each resonance condition is met. In each case, even if the resonance condition is not exactly met, there is still a conditional shift of at least 2 MHz across all possible pairs of ancillary transitions, shown in Fig. 3.19 (e). By having the freedom to operate the gate using different transitions, there is much more flexibility when it comes to hitting frequency targets in fabrication. In contrast to cross resonance, where optimal gate speeds are obtained when the qubits are in the straddling regime and separated by ≈ 100 MHz, there is a frequency range of $2\chi_{\Sigma\Delta} \approx 500$ MHz where fast gate operation is possible. The additional peaks in the spectrum are due to the anharmonicities of each ancillary transition ($\eta_{\Sigma,\Sigma'}$).

An additional benefit of this multi-mode structure and AT-MAP gate scheme is that there is no limit imposed on the interaction strength J between the ancillary transitions. Unlike CR based architectures where this coupling is small in order to reduce unwanted always-on interactions, due to the symmetry of the modes, the Δ-modes will always be protected, and so the engineered coupling can be significantly larger by comparison.

There are potential issues and sources of error when operating the AT-MAP gate in the mode-selective architecture. The most significant is leakage into the ancillary modes of the system. Whilst we aim to reduce this by driving off-resonantly, there may be some non-negligible population in these Σ-modes if the gate is driven at high drive amplitudes. Due to the large $\chi_{\Sigma\Delta}$ state dependent shift between the Σ-mode and Δ-mode of each device, any unwanted population in the ancillary modes will cause significant errors when addressing the computational mode. Secondly, there are additional frequency collision conditions to consider in this off-resonant AT-MAP gate implementation. Whilst the computational modes will be protected, care needs to be taken when designing the ancillary mode frequencies to ensure gates can be driven selectively in larger arrays of devices. We note that since this gate is driven far (≈ 1 GHz) from Δ-mode transitions, unwanted off-resonant driving of the computational modes resulting in Stark-shift induced phase errors is minimal.

Whilst we operate the system using the Σ-modes as ancillaries to drive this particular gate, it is also possible to use this structure for 4-qubit interactions and perform Toffoli class gates. A simple extension of our AT-MAP interaction is to use the target ancillary mode as an additional control mode, thus implementing a CCCPhase gate.

3.4 Conclusion

In conclusion, we have presented a theoretical introduction to the two-mode coaxial transmon device. The addition of a second transmon-like mode within the unit-cell of the coaxial circuit QED architecture presents multiple opportunities in the development of superconducting-circuits-based quantum computers, for both readout mechanisms and two-qubit gates. We have outlined how the sensitivities of device to charge-noise can be suppressed, and how a mode-selective coupling can be engineered. Finally, we showed how one can drive a conditional interaction between protected modes in a system of coupled two-mode coaxial transmons, introducing a microwave activated conditional phase interaction driven via ancillary transitions (AT-MAP).

The theoretical work in this chapter presents the premise for experimental work conducted in this thesis, demonstrating the unit-cell operation and characterisation measurements (Chapter 4), investigating charge sensitivity and use-case as a detector of spatial charge fluctuations (Chapter 5), and generating entanglement between protected modes in a coupled two-mode coaxial transmon system (Chapter 6).

Chapter 4

Demonstration of the Two-Mode Coaxial Transmon

In this chapter, we present results of experiments performed on a single unit cell two-mode coaxial transmon. We show how the Hamiltonian can be characterised through two-tone spectroscopy methods, as well as the operation and optimisation of simultaneous dispersive readout of the two modes. We characterise energy relaxation and coherence with time-resolved measurements, and demonstrate how a fast inter-modal gate can be implemented utilising the large cross-Kerr shift of the device.

4.1 Device Design

We design the device using the simulation methods outlined in Appendix B in order to obtain the parameters shown in Table 4.1 (shown on page 77). These parameters are targeted in order to reduce the effects of charge noise in the system, as well as have a sufficiently high cross-Kerr shift between modes, useful for performing fast gates. The parameters are also targeted to allow two-qubit gate operations between multiple two-mode coaxial transmons, presented in Chapter 6. Whilst we aim for mode transition frequencies in the range of 4 - 6 GHz, fabrication processes mean that these cannot always accurately be matched. As such, we focus on device parameters defined by large scale features such as pad geometry (E_C, E_p), that are photo-lithographically patterned and have much higher tolerances.

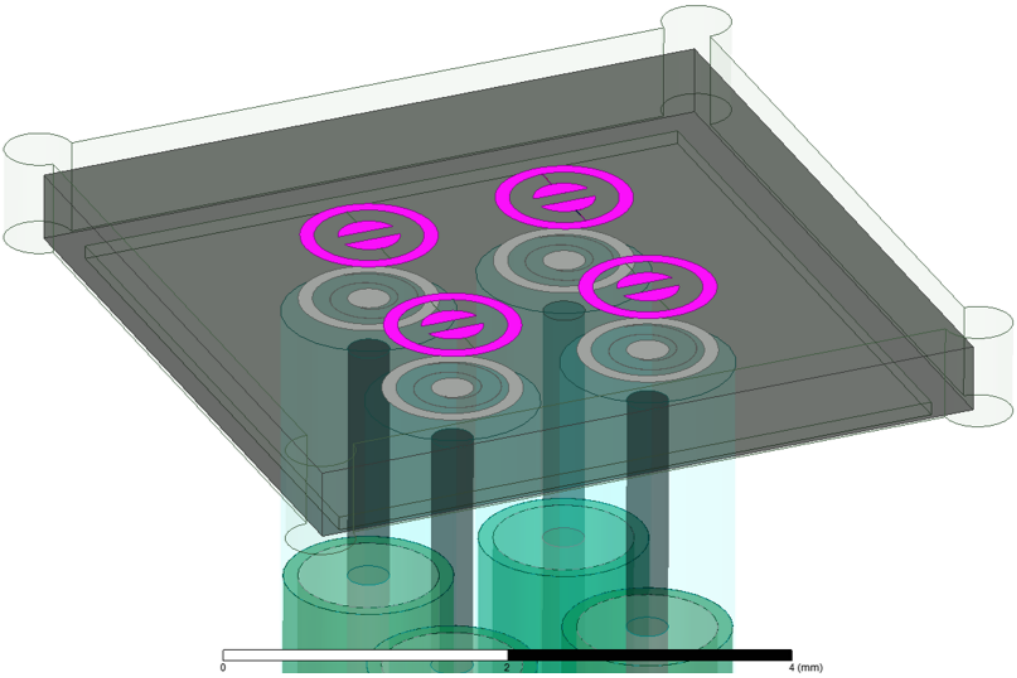

Figure 4.1: 3D model of device used in Ansys HFSS simulation aided design. The chip consists of 4 two-mode coaxial transmon devices (purple), on the opposing side of a silicon substrate (black) to coaxial spiral resonators (white), used for dispersive readout. The model shows the four coaxial control and readout lines suspended above the readout resonators. A single-sided control wiring configuration is used to address both readout resonators and modes of the device via the same control port.

The devices are fabricated using a double sided, wafer scale nanofabrication process on a 0.5 mm silicon wafer. Following an HF surface treatment, aluminium is deposited onto both sides of the substrate, and photolithography and etching methods are used to pattern large scale features of the devices, such as qubit islands and resonators. Electron beam lithography and double-angle evaporation of aluminium is used to pattern the small scale Josephson junction features. Details of the process are outlined in Appendix C (p162-170) of [161]. The resulting wafer is diced into 5 × 5 mm chips. The device measured is shown in Fig. 4.2 (a).

For these experiments, we mount the device in an aluminium sample holder, placed within a light-tight μ-metal magnetic shield, anchored to the 20 mK stage of a dilution refrigerator, operating in the standard cQED experimental setup presented

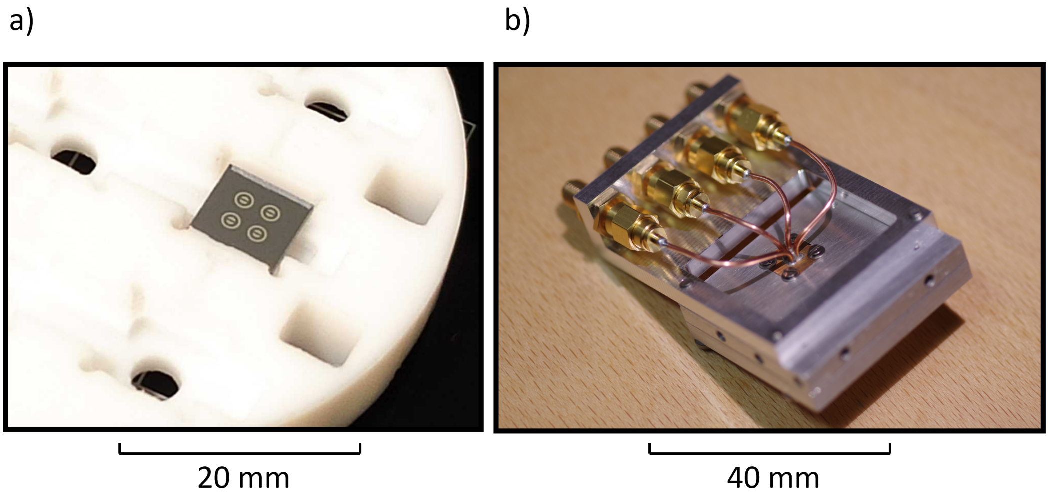

Figure 4.2: (a) 5mm x 5mm x 0.5mm silicon substrate with nanofabricated two-mode coaxial transmon device measured in these experiments. Substrate is sitting in a custom machined PTFE holder, designed to protect the reverse side with readout resonators photo-lithographically patterned. (b) Sample holder in which the two-mode coaxial transmon chip is mounted. Four wires shown are the coaxial control and readout pins for addressing both the resonators and qubit devices.

in Appendix C. The device is secured in place in the sample holder using small quantities of indium, placed in the corners of the chip pocket of the sample holder, shown in Fig. 4.1. The sample holder, shown in Fig. 4.2 (b), has a single sided wiring configuration, such that both the qubit and resonator are addressed through the same coaxial control port. Experimentally, this is achieved by combining the signals externally to the cryogenic system. Whilst this does reduce the overall wiring requirement and passive heat load of the control wiring, it can introduce difficulties when driving qubits through the resonator, since out-of-band signals will be filtered. Additional care is also taken to ensure output amplifiers are not saturated by qubit control signals, with the use of bandpass filters.

4.2 Readout Characterisation

The Hamiltonian describing the system of a two-mode coaxial transmon coupled to a linear resonator is given by,

$$\hat{H}/\hbar = \hat{H}_Q/\hbar + \omega_r(\hat{a}_r^\dagger \hat{a}_r + 1/2) + g_{\Sigma r}(\hat{a}_r^\dagger + \hat{a}_r)(\hat{a}_\Sigma^\dagger + \hat{a}_\Sigma) \tag{4.1}$$

where $\hat{H}_Q$ is the Hamiltonian of the two-mode coaxial transmon in Eqn. 3.6, $\hat{a}_r^{(\dagger)}$ is the annihilation (creation) operator for the resonator mode, ω_r is the resonator mode frequency, and $g_{\Sigma(\Delta)r}$ is the coupling between the resonator mode and the Σ-mode (Δ-mode). This weak coupling between each transmon mode and the resonator mode leads to a modal-state-dependent resonator frequency shift of $\chi_{\Sigma(\Delta)r}$. In the dispersive limit, $g \ll (\omega_r - \omega_\Sigma)$, the interaction Hamiltonian ($\hat{H}_{int}$) is of the form,

$$\hat{H}_{int}/\hbar = \sum_{i=\Sigma,\Delta} \chi_{ir} \hat{a}_r^\dagger \hat{a}_r \hat{a}_i^\dagger \hat{a}_i \tag{4.2}$$

where the frequency shift $\chi_{\Sigma(\Delta)r}$ is defined as previously in Chapter 3.

This state-dependent frequency shift, $\chi_{\Sigma(\Delta)r}$, is the mechanism that allows us to readout the state the device. By probing the resonator frequency, we can determine whether each mode is in the ground or excited state.

When characterising the readout resonator, we perform a weak continuous measurement. In the steady state regime, this populates the resonator in a coherent state of average photon number $\langle n \rangle$. When performing qubit control operations and pulse sequences, we use a pulsed measurement scheme, such that there are no photons in the resonator, and thus no stark-shifts of the qubit, during qubit control sequences. Qubit measurement is then achieved by sending a ≈ 5 μs soft square pulse to the resonator and analysing the response as outlined in Appendix D.

4.2.1 Resonator Spectroscopy

We use a two-port Vector Network Analyser (VNA) connected to the input and output line of the experiment setup to identify readout resonator frequencies initially. To calibrate the room temperature attenuation required, we identify the power required to reach the bifurcation regime [174], and add an extra 10 dB of attenuation to the readout signal generation such that the dynamic range of the readout signal generation setup is insufficient to reach the power required to reach this transient regime. Experimentally, this leads to approximately 50 dB of attenuation at room temperature, to ensure that we are always operating in the low photon number regime of the system.

When in the low power regime, we fit the measured signal by treating the modes as a single port resonator connected to a feed line, the complex $S_{11}(f)$ is given by,

$$S_{11} = \frac{(Q_e - Q_0)/Q_e + j2Q_0\delta f}{(Q_e + Q_0)/Q_e + j2Q_0\delta f} \tag{4.3}$$

where f_0 is the resonant frequency of the mode, $\delta f = (f - f_0)/f$, Q_e is the external quality factor, and Q_0 is the internal quality factor [175].

Due to the finite length of the transmission line, there is an additional phase change as the signal propagates through the line, given by $e^{j(x.\delta x+\theta)}$, where $\delta x = (f - f_0)/f_0$, and v and θ are free parameters. There is also some damping caused by the microwave cables, which can be approximated with linear dependence, given by $a + b.\delta x$. An additional offset for power reflected back without crossing the device is modelled as $I_c + iQ_c$. These additional components are fitted to the data far from resonance and then added to the original model for $S_{11}(f)$, giving the equation we fit the measured resonator signal to as,

$$S_{11,meas}(f) = (a + b.\delta x)S_{11}(f)e^{j(v.\delta x+\theta)} + (I_C + iQ_c) \tag{4.4}$$

The measured and fitted resonator spectroscopy for this device measured is shown in Fig 4.3, with a frequency of $\omega_r/2\pi = 9.317$ GHz and linewidth of $\kappa_r/2\pi = 1.9$ MHz.

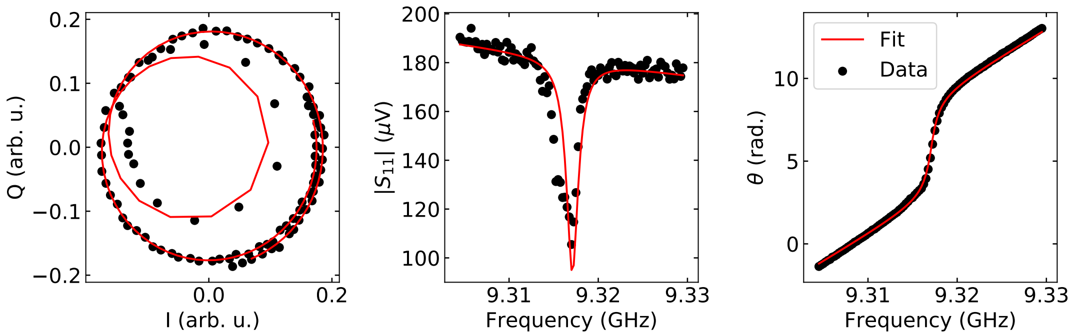

Figure 4.3: Resonator spectroscopy response (black) fitted to Eqn 4.4 (red), showing the real and imaginary components (left), magnitude (center) and phase response (right). From the fit we extract the resonator frequency $\omega_r/2\pi = 9.317$ GHz and linewidth of $\kappa_r/2\pi = 1.9$ MHz, with $Q_0 = 20600$ and $Q_e = 6600$.

4.2.2 Joint Dispersive Readout of a Multi-Mode Device

Since the Σ-mode and Δ-mode of the two-mode coaxial transmon have different detunings and couplings to the readout resonator, they induce a different state-dependent shift in the resonator frequency $\chi_{\Sigma(\Delta)r}$. This allows us to perform a joint dispersive readout of the two-mode state of the device [165]. We observe this when performing a resonator spectroscopy measurement, conditional on the state of the multi-mode device, as shown in Fig. 4.4.

By observing the real and imaginary components of the readout signal S with sufficient measurement averaging, we can identify the centres of each state distribution on the IQ plane at each readout frequency. In the ideal case, we wish to identify a frequency for which the angle between the $|10\rangle$, $|00\rangle$ and $|01\rangle$ distributions is 90°. This is such that when measuring a readout signal, we can rotate the IQ plane to observe only a single axis and measure the state of each mode independently of the other. Being able to independently determine the state of each mode of the multi-mode device allows us to firstly ensure independent control and tuning, as well as effectively measure leakage and unwanted state populations when performing multi-qubit operations. It is a form of localised readout multiplexing and demonstrates the additional capability of the multi-mode unit cell compared to the standard coaxial

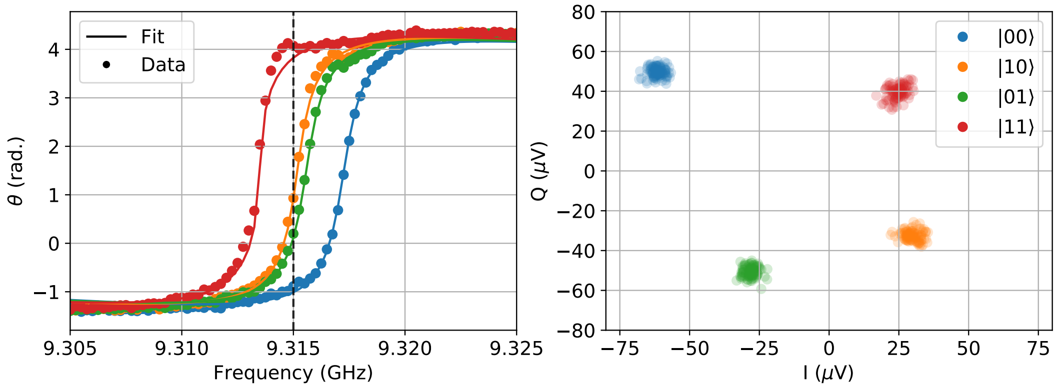

Figure 4.4: Joint readout of the two-mode coaxial transmon. (left) Phase responses of the readout resonator fitted to Eqn. 4.4, conditioned on the $|00\rangle$ (blue), $|10\rangle$ (orange), $|01\rangle$ (green) and $|11\rangle$ (red) states being prepared, from which we can extract each $\chi_{\Sigma(\Delta)r}$. Dotted vertical line indicated frequency (9.315 GHz) we use for readout to maximally distinguish the $|10\rangle$ and $|01\rangle$ states. (right) IQ plane showing signal distributions resulting from 100 measurements preparing the two-mode system in the same four states as previous. Each measurement is averaged 1000 times to improve signal to noise.

transmon device.

An example of the joint dispersive readout of the multi-mode device is shown in Fig. 4.4. During readout, the state of the two-mode system collapses to the $|00\rangle$, $|01\rangle$, $|10\rangle$ or $|11\rangle$ state. When performing averaged measurements the state is approximated by the interpolated distance between the $|00\rangle$ cluster centre and $|10\rangle$ or $|01\rangle$ clusters.

4.3 Hamiltonian Characterisation through Spectroscopy

4.3.1 Qubit Spectroscopy

In order to determine the transition frequencies of the modes of the two-mode coaxial transmon, we perform a continuous wave (CW) spectroscopy measurement. This consists of probing the resonator at it's previously determined frequency ω_r, whilst simultaneously applying a weak continuous drive tone of frequency ω_d to the control port, sweeping the frequency range where we expect to observe the mode frequencies ($\sim 4-6$ GHz). Any transition coupled to the resonator that is driven on resonance will cause the resonator frequency to shift, and will thus induce a change in the readout signal that is measured.

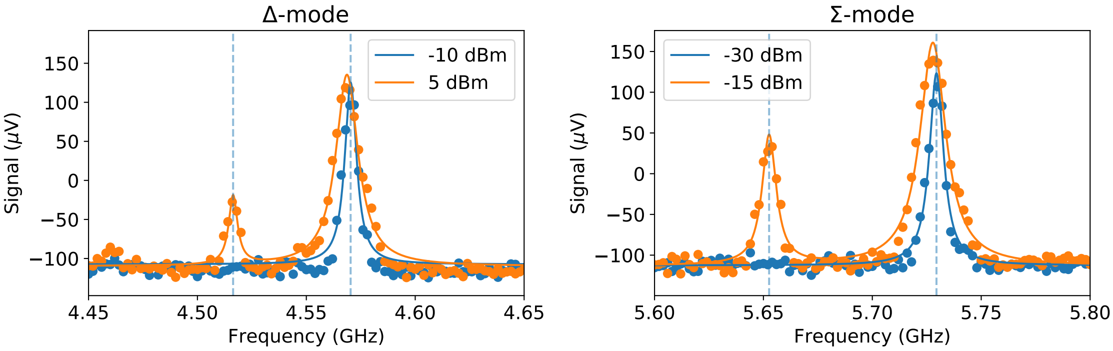

Figure 4.5: Qubit Spectroscopy of the Δ-mode (left) and Σ-mode (right). Driving at low powers (blue) results in a single peak corresponding to the frequency of the $|0\rangle \rightarrow |1\rangle$ transition. At higher powers (orange), this first lineshape is broadened and a second smaller peak emerges, corresponding to the $(|0\rangle \rightarrow |2\rangle)/2$ transitions. Data is fitted to Lorentzian lineshapes, with vertical dashed lines indicating fitted frequencies of transitions.

From the first two spectral peaks that emerge we identify the $|00\rangle \rightarrow |10\rangle$ and $|00\rangle \rightarrow |01\rangle$ transitions, at the frequencies $\omega_\Sigma = 5.74$ GHz and $\omega_\Delta = 4.58$ GHz. These are single photon transitions and so require the least power in order to drive. Note that ~ 20 dB higher power is required to drive the Δ-mode than the Σ-mode. This is likely due to the mode match (mismatch) between the Σ-mode (Δ-mode) and the coaxial drive field, as well as the difference in detuning from the readout resonator which acts as a filter of the control signal.

The next transitions that appear at increasing drive power negatively detuned from the single photon transitions in spectroscopy measurement are the two photon $\frac{|00\rangle \rightarrow |20\rangle}{2}$ and $\frac{|00\rangle \rightarrow |02\rangle}{2}$ transitions, as shown in Fig. 4.5. From these frequencies we extract the anharmonicity from $\omega_i = (\omega_{\Sigma(\Delta)} - \eta_{\Sigma(\Delta)})/2$, where ω_i is the two photon transition frequency, and we find $\eta_\Sigma = 154$ MHz and $\eta_\Delta = 108$ MHz.

Next we would like to measure the signature of the large cross-Kerr shift ($\chi_{\Sigma\Delta}$) between the two modes. In principle we should be able to observe this transition

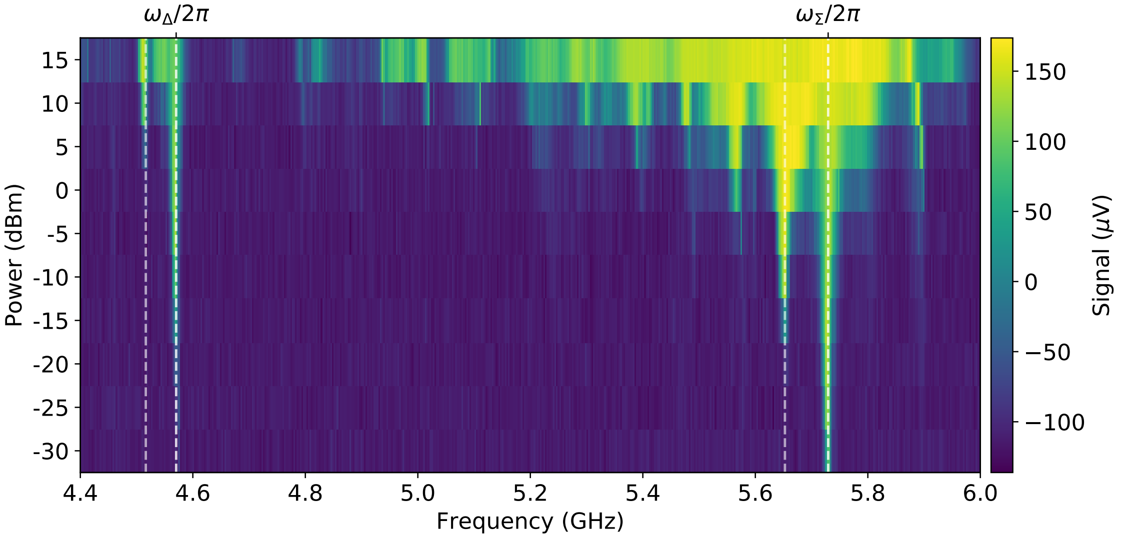

Figure 4.6: Wide qubit spectroscopy measurement at increasing drive power. Vertical dashed lines indicate previously identified transitions from Fig. 4.5.

in spectroscopy around $\omega_{(|00\rangle \to |11\rangle)/2}/2\pi \approx 5$ GHz, based on our design parameters. In Fig. 4.6 we show a spectroscopy measurement of the device in the 4.4 - 6 GHz range. A set of spectral lines can be seen to appear at high power in the range 4.8 GHz $< \omega_d/2\pi <$ 5.4 GHz. One of these spectral lines may be the 2-photon $\frac{|00\rangle \to |11\rangle}{2}$ transition, but it is difficult to distinguish from other multi-photon transitions of the device. In order to unambiguously distinguish these transitions, we turn to two-tone spectroscopy.

4.3.2 Two-tone Spectroscopy

In order to obtain more information from spectroscopic measurements, we employ a method of two-tone spectroscopy[1]. We use two continuous tones to drive the qubit and sweep both frequencies at a fixed power, creating a two-dimensional spectroscopic result. This allows us to probe a multitude of resonance conditions, which will be different for each transition photon number, yielding a unique spectroscopic signature

---

[1] We note that strictly this is a three-tone measurement consisting of two qubit drive tones and a readout tone (although a pulsed readout method is used here). It should not be misinterpreted as being the same as other experimental methods describing a two-tone spectroscopy, consisting of a single qubit tone and readout tone.

for each.

Experimentally, we use two nominally identical signal generators to output the continuous tones, and combine the signals at room temperature. We use a power high enough to observe the transitions of interest over the full 4 - 6 GHz initially. This does result in significantly larger broadening of the easier to drive transitions of the Σ-mode, and so these are probed additionally at lower power in a smaller frequency range. However, the aim of this spectroscopic method is to identify the blue sideband transition $((|00\rangle \rightarrow |11\rangle)/2)$ between the Σ-mode and Δ-mode, in order to measure the cross-Kerr shift $\chi_{\Sigma\Delta}$.

The spectroscopic signature is dependent on the photon number of each transition. The simplest example is a single photon transition, that can be driven equally well by each drive tone. This manifests as a "+" type feature, as shown in Fig. 4.7 (a). When each drive tone is at the transition frequency, the resonance condition that $f_{A/B} = f_t$ is met.

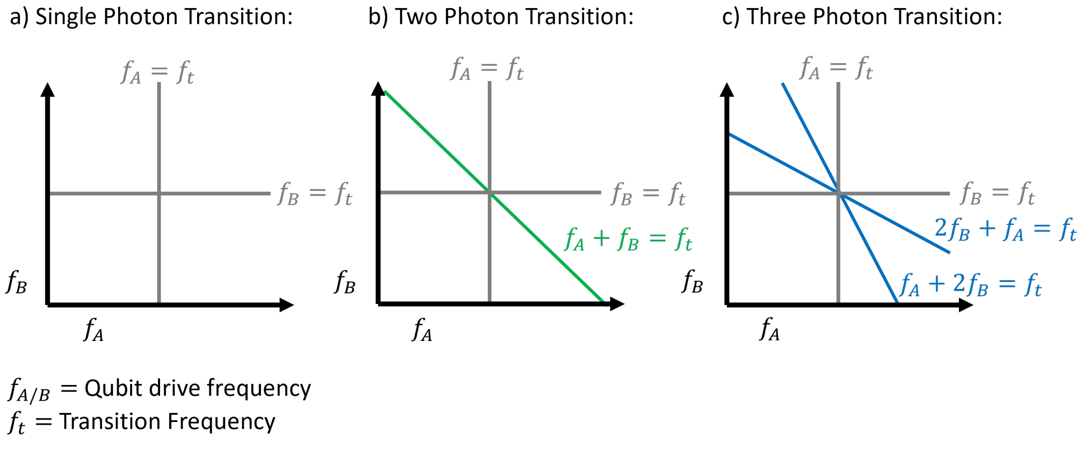

Figure 4.7: Spectroscopic signature of a single-photon (a), two-photon (b) and three-photon (c) transition, as outlined in the main text. Axes correspond to the frequencies of the two generators (A and B) providing the drive tones.

The second example is a two-photon transition. Like the single-photon transition, the resonance condition can also be met by a single drive tone if the power is high enough, resulting in a "+" feature. Additionally, there is the resonance condition from the combination of the drive tones, such that $f_A + f_B = f_t$. This condition is met at every point along the line, $f_A = f_t - f_B$, resulting in a diagonal line of gradient -1 in the spectroscopic signature, as shown in Fig. 4.7 (b). This feature is how we identify two-photon transitions in our spectroscopy measurements.

The third most prominent feature is a three-photon transition. The single drive resonance condition is unlikely to be met, since it requires a higher power than the previous two examples, so the characteristic "+" shape is unlikely to be visible. The three photon resonance condition is met when two photons from one drive tone mix with an additional photon from the other drive tone, such that $2\hbar\omega_{A/B} + \hbar\omega_{B/A} = E_t$. This condition can be met in two different ways; two photons from drive A mixing with a single photon from drive B, or two photons from drive B mixing with two photons from drive A. This results in two lines where the resonance condition is met, $2f_A + f_B = f_t$ and $f_A + 2f_B = f_t$, as shown in Fig 4.7. (c). This signature is how we identify three photon transitions in the spectroscopic result.

There are additional spectral signatures that can often be visible in two-tone spectroscopy methods when using high drive powers able to excite much higher photon number transitions. An additional more complex higher power feature is the driving of a single photon transition with a red sideband. That is where three drive photons interact with the transition, such that $2f_A - f_B = f_t$, resulting in two diagonal lines of positive gradient passing through the transition frequency. We only observe this when driving the Σ-mode at high powers.

In Fig. 4.8 we show the result of the wide two-tone spectroscopy measurement. With the knowledge of the spectroscopic signatures of each photon number transition, we are more easily able to identify features of the device. As with previous spectroscopy measurements, the higher frequency Σ-mode transitions are easier to drive than the lower frequency Δ-mode transitions, and so appear more prominently at the same power. The two prominent cross shaped features at 4.57 GHz and 5.73

GHz are the $|0\rangle \rightarrow |1\rangle$ transitions of the Δ-mode and Σ-modes previously identified. One additional feature highlighted by this spectroscopy measurement, is the faint diagonal line between the two transitions, passing through 5.03 GHz. This corresponds to the two-photon Bell-Rabi transition, or $(|00\rangle \rightarrow |11\rangle)/2$ transition. From this we extract the cross-Kerr shift $(\omega_\Sigma + \omega_\Delta - 2\omega_{(|00\rangle\rightarrow|11\rangle)/2})/2\pi = \chi_{\Sigma\Delta}/2\pi = 269$ MHz. In Fig. 4.8 (b) we show the two-tone spectroscopy plot with the identified transitions overlaid for additional clarity. These transitions are also highlighted on the energy level diagram of the two-mode coaxial transmon, shown in Fig. 4.8 (c).

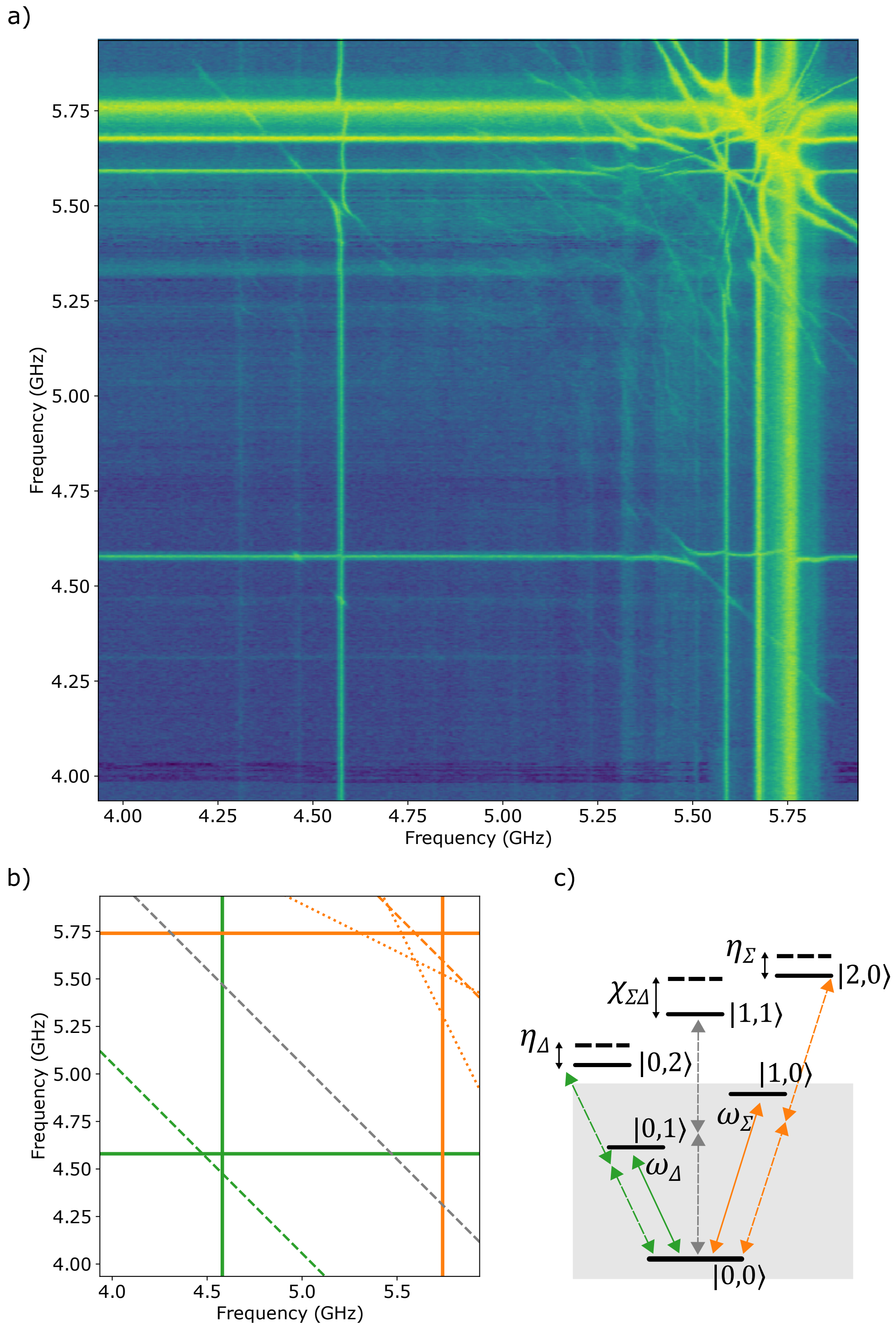

Figure 4.8: (a) Two-tone spectroscopy measurement result of the two-mode coaxial transmon. (b) Spectroscopy measurement with transitions of the Σ-mode (orange) and Δ-mode (green) highlighted. Grey diagonal dashed line shows the two-photon $|00\rangle \rightarrow |11\rangle$ transition. (c) Energy level diagram of the two-mode coaxial transmon with identified transitions labelled.

4.3.3 Hamiltonian Parameters

From the spectroscopic measurement of the transitions frequencies we obtain the first estimate of the mode frequencies, anharmonicities and cross-Kerr shifts ω_Σ, ω_Δ, η_Σ, η_Δ, $\chi_{\Sigma\Delta}$, $\chi_{\Sigma r}$ and $\chi_{\Delta r}$. More accurate measurements of the transition frequencies can be obtained through time-resolved measurements, outlined in section 4.4.3.

In order to obtain the Josephson energy, charging energies and coupling energies (E_J, E_C and E_p) of the two-mode coaxial transmon Hamiltonian, given by Eqn. 3.6 and restated here as,

$$\begin{aligned}\hat{H} =& 4E_C(\hat{n}_1 - n_{g1})^2 + 4E_C(\hat{n}_2 - n_{g2})^2 + 4E_p(\hat{n}_1 - n_{g1})(\hat{n}_2 - n_{g2}) \\ & - E_J \cos\hat{\varphi}_1 - E_J \cos\hat{\varphi}_2,\end{aligned} \tag{4.5}$$

we construct the Hamiltonian in the charge basis and numerically diagonalise using QuTip [171]. We can write analytical equations relating the frequencies obtained to the Hamiltonian parameters as outlined in Chapter 3, however, since they are derived from a finite truncation of the cosine terms in Eqn. 4.5, they are only approximate. As such, the numerical diagonalisation procedure is a more accurate method of obtaining these parameters.

Using this procedure, we obtain the values shown in Table 4.1. This table also shows the simulated parameters using the methods outlined in Appendix B, and show a good agreement with what is measured. From the values of E_J, E_C and E_p, we can determine that we do not expect there to be any resolvable charge dispersion in the $|0\rangle \rightarrow |1\rangle$ transitions from our predictive model described in Section 3.1.6 ($\epsilon \sim 100$ Hz). These methodologies and results show that we are able to effectively design and simulate these two-mode coaxial devices, and show that measured parameters are in agreement with those designed.

Table 4.1: Device Parameters

	Sim.	Measured
LC Resonator		
Frequency f_r (GHz)	-	9.32
Linewidth $\kappa_r/2\pi$ (MHz)	-	1.9
Dispersive Shift $2\chi_{\Delta r}/2\pi$ (MHz)	-	1.7
Dispersive Shift $2\chi_{\Sigma r}/2\pi$ (MHz)	-	2.1
Δ - Mode		
Transition Frequency $\omega_\Delta/2\pi$ (GHz)	-	4.58
Anharmonicity $\eta_\Delta/2\pi$ (MHz)	120	108
Σ - Mode		
Transition Frequency $\omega_\Sigma/2\pi$ (GHz)	-	5.74
Anharmonicity $\eta_\Sigma/2\pi$ (MHz)	140	154
Cross Kerr Shift $\chi_{\Sigma\Delta}/2\pi$ (MHz)	230	269
E_J (GHz)	-	16
E_C (GHz)	-	0.23
E_p (GHz)	-	0.1

4.4 Demonstration of Coherence

4.4.1 Pulsed Control

We now proceed to use time-resolved measurement techniques to characterise the coherence of our two-mode coaxial transmon.

Driving one of the qubit mode transitions on resonance induces Rabi oscillations at a rate proportional to the drive amplitude [176]. As shown in Fig. 4.9, the Rabi rate increases with the generator drive power. The differences in Rabi rate of the Σ-mode and Δ-mode for equivalent drive power are due to the differences in the geometry of the field polarisation of each mode and coupling to the drive line, as well as the detuning between the mode and the resonator through which they are being driven [177].

We define pulses by R_θ, where R is the axis of rotation on the Bloch sphere (X, Y

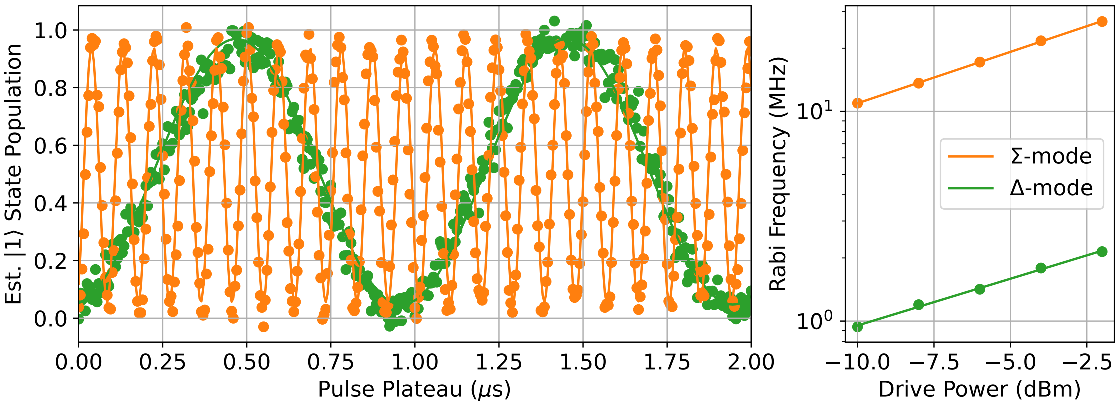

Figure 4.9: Rabi oscillations of the Δ-mode (green) and Σ-mode (orange) $|0\rangle \rightarrow |1\rangle$ transitions. Data from measuring each mode separately is fitted to a cosine oscillation, and excited state populations are estimated from the IQ plane voltages. (right) Extracted oscillation frequencies (Rabi frequency) as a function of generator drive power.

and Z) and θ is the angle of rotation. For instance a rotation of π around the X axis, resulting in a qubit mode initialised in the ground state becoming excited, is written as X_π. The frequency of the pulse determines which mode is excited. We follow the same procedures as previous works to calibrate pulse frequencies and amplitudes [158, 161]. Since the time domain measurements to obtain energy relaxation and coherence parameters are insensitive to small state preparation and measurement errors, we do a single calibration of frequency and amplitude, and do not apply higher order corrections such as DRAG [178] or use pulse train calibration methods [179]. We use a truncated Gaussian pulse of form,

$$\Omega(t) = A_0 \exp\left(-\frac{t^2}{(t_0/2)^2}\right), \tag{4.6}$$

where A_0 is the amplitude, and $2/\pi t_0$ is the Gaussian envelope width. Qubit control pulses are generated using single sideband modulation methods, outlined in Appendix E.

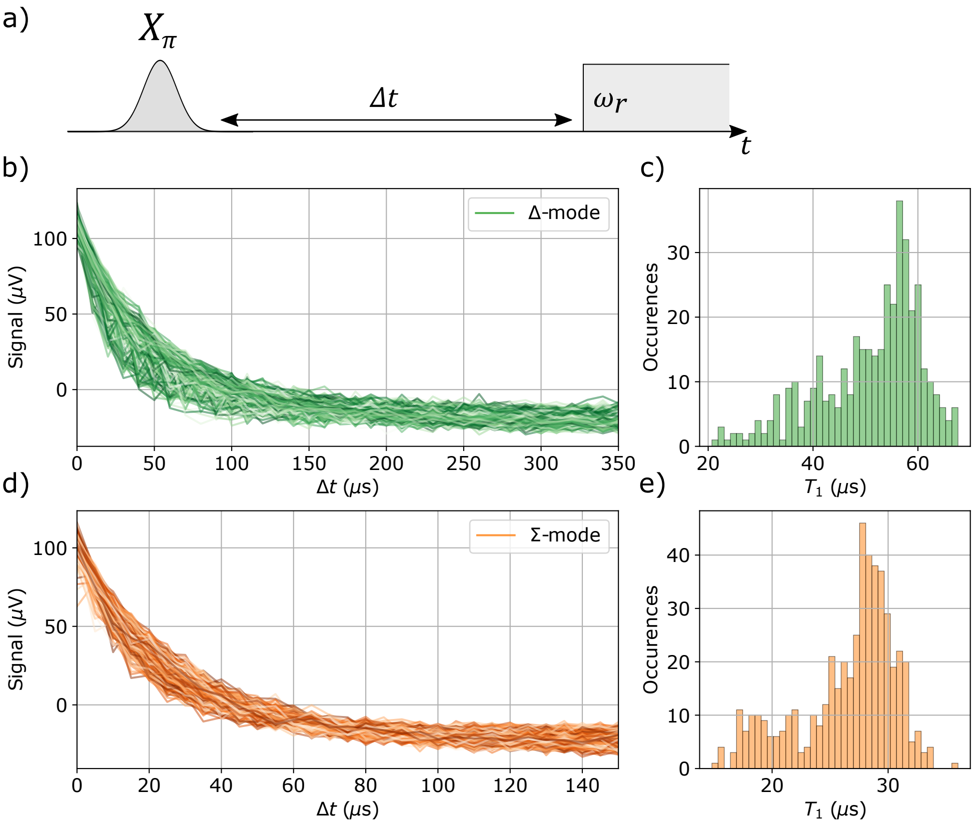

Figure 4.10: Energy Relaxation (a) Pulse scheme of the energy relaxation T_1 measurement. (b) (d) Repeated measurement signals as a function of delay (Δt). Traces follow an exponential decay, fitted to $S(\Delta t) = a + be^{-\Delta t/T_1}$, in order to extract the energy relaxation time T_1. (c) (e) Histograms of the fitted T_1 extracted from the measurements. Statistics are from 409 repeated measurements of the Δ-mode (501 measurements of the Σ-mode).

4.4.2 Energy Relaxation

To measure the energy relaxation of a particular mode, we use an X_π pulse to initialise the mode in the excited state, and then wait some delay period Δt before measuring, as shown in the pulse sequence in Fig. 4.10 (a). Sweeping the delay period results in a measured signal of an exponential decay of the form $S(\Delta t) = a + be^{-\Delta t/T_1}$, where the decay constant $T_1 = 1/\Gamma_1$ is the energy relaxation time, and a and b are offsets due to the state preparation fidelity and final state (residual excited state population).

We repeat this measurement 100s of times over the course of a few hours, or overnight, in order to build statistics of the energy relaxation rate. In a small time

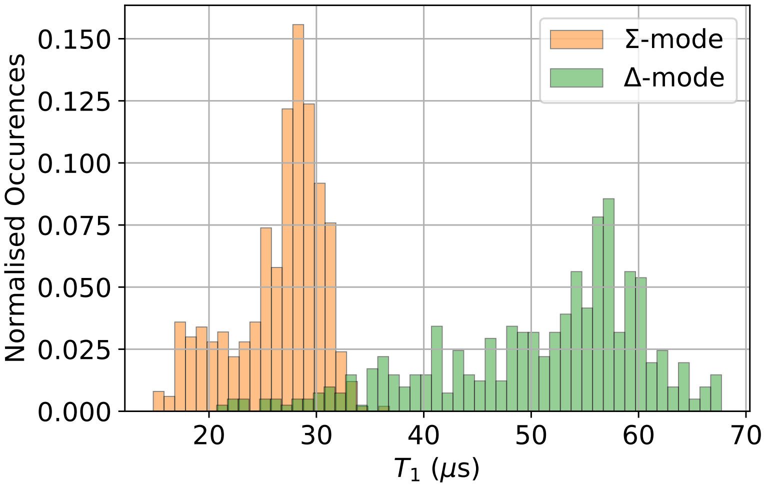

Figure 4.11: Overlaid normalised histograms of extracted T_1 parameters for each mode.

window where the system is stable, the distribution of T_1 can be approximated to be a Gaussian distribution, however, over long periods of time, various re-combinations of local defects and loss mechanisms cause the relaxation rate to change [180, 181]. As such, these long measurements of T_1 follow multi-modal Gaussian distributions due to the multiple loss mechanism configurations throughout the measurement period. We report the mean fitted value of the measurements as the measured T_1 for simplicity.

In Fig. 4.10 (b), we show the resulting traces and distributions of fitted T_1 from the energy relaxation measurements. We measure the energy relaxation of each mode separately, and find the Σ-mode has a $T_1^{\Sigma} = 27\ \mu\text{s}$ ($4\ \mu$s), and the Δ-mode has a $T_1^{\Delta} = 51\ \mu\text{s}$ ($10\ \mu$s).

The fact that $T_1^{\Delta} \gg T_1^{\Sigma}$ is likely to originate from the intentional difference in geometry between the two modes, and hence their coupling to the coaxial output ports. Another possible contribution is the difference in detuning and coupling to the readout resonator [29], and corresponding losses as a result of the Purcell effect. Further work is required to determine these contributions in detail.

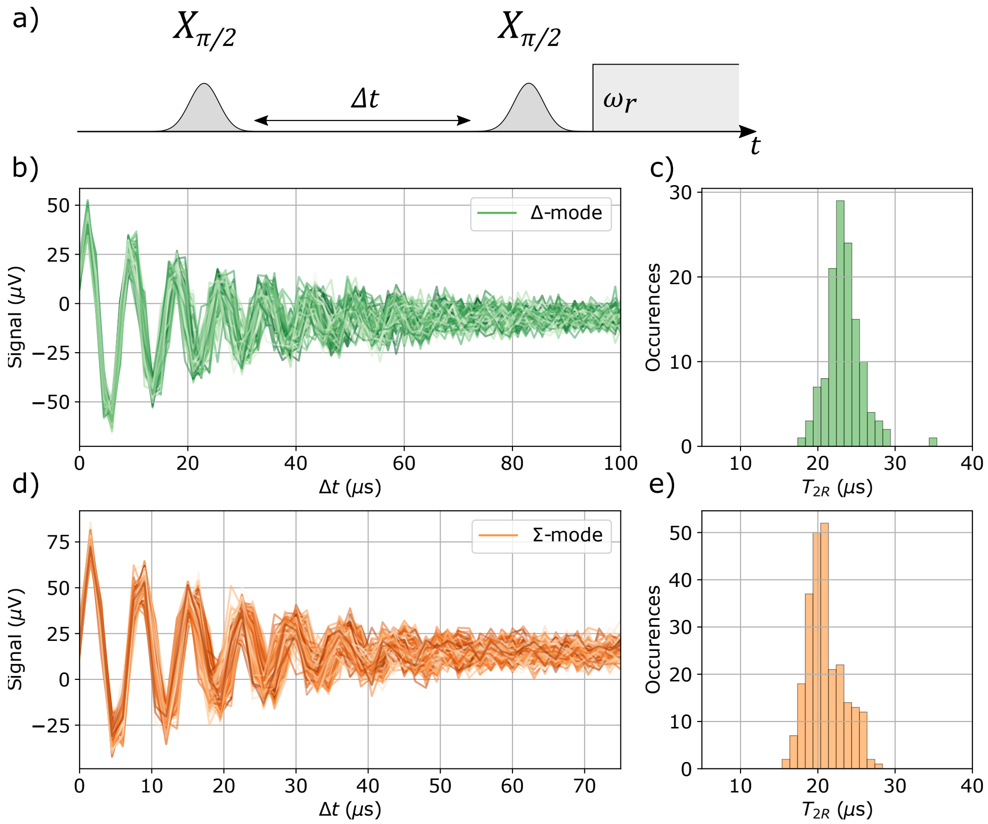

Figure 4.12: Ramsey Oscillations (a) Pulse scheme of the Ramsey oscillation T_2^* measurement. (b) (d) Repeated measurement signals as a function of pulse spacing (Δt). Traces follow a decaying oscillation, fitted to $S(\Delta t) = a + b\cos(2\pi\Delta f\Delta t + \phi)e^{(-\Delta t/T_2^*)}$, in order to extract the Ramsey coherence time T_2^*. (c) (e) Histograms of the fitted T_2^* extracted from the measurements. Statistics are from 131 repeated measurements of the Δ-mode (251 measurements of the Σ-mode).

4.4.3 Ramsey Oscillations

The transverse relaxation rate, $1/T_2^* = 1/2T_1 + 1/T_\phi$, describes the rate at which the coherence of a superposition state, i.e. one lying on the equator of the Bloch sphere, is lost. It is affected by both energy relaxation events and pure dephasing (Γ_ϕ).

To measure T_2^*, we first place the mode in a superposition with an $X_{\pi/2}$ pulse. We then allow the system to freely evolve for a time Δt, before returning the state to the Z basis with a second $X_{\pi/2}$ pulse. When the control pulses are slightly detuned from the transition frequency, the state precesses about the Z axis at a rate Δf during the free evolution, where Δf is the detuning between the drive frequency and transition frequency. We use this method to more accurately determine the mode transition frequencies.

We fit the resulting signal trace to a decaying oscillation of the form $S(\Delta t) = a + b\cos(2\pi\Delta f\Delta t + \phi)e^{(-\Delta t/T_2^*)}$, where a, b and ϕ are amplitude and offset parameters. As with energy relaxation measurements, we repeat the Ramsey oscillation measurement $n \approx 100$ times to build statistics of the mechanism. This also allows us to track any qubit frequency drifts over a long period of time. In the case of a charge sensitive device, the signal has multiple frequency components due to the multiple parity configurations and charge dispersion. As shown in Section 4.5, this device is insensitive to charge noise and so Ramsey oscillations have only a single frequency component.

In Fig. 4.12 we show the fitted traces and distributions of fitted T_2^* for the Σ-mode and Δ-mode. We measure a $T_2^{*\Sigma} = 21$ μs (2 μs) and $T_2^{*\Delta} = 24$ μs (7 μs) for Σ-mode and Δ-mode respectively. We calculate a pure dephasing rate of $1/\Gamma_\phi^\Sigma = 35$ μs and $1/\Gamma_\phi^\Delta = 32$ μs. In combination with the similar Spin-Echo coherence time, this suggest that the modes are suffering dephasing due quasistatic noise processes, such as a poorly thermalised readout resonator and control lines, as the optimum filter location had not been identified at the time of this experiment.

4.4.4 Spin-Echo

In Fig. 4.13, we show the pulse sequence for a Spin-echo sequence. Whilst similar to the Ramsey interferometry pulse sequence, the additional X_π pulse between the two $X_{\pi/2}$ pulses has the effect of refocusing the inhomogeneous contributions to dephasing. As such, the measurement is less sensitive to low-frequency ($< \Delta t$) noise. Conversely to the Ramsey experiments, we choose the frequency of the pulses to be on resonance, since the frequency detuning would be refocused away.

Through an ensemble measurement, we expect the signal to decay to a mixed

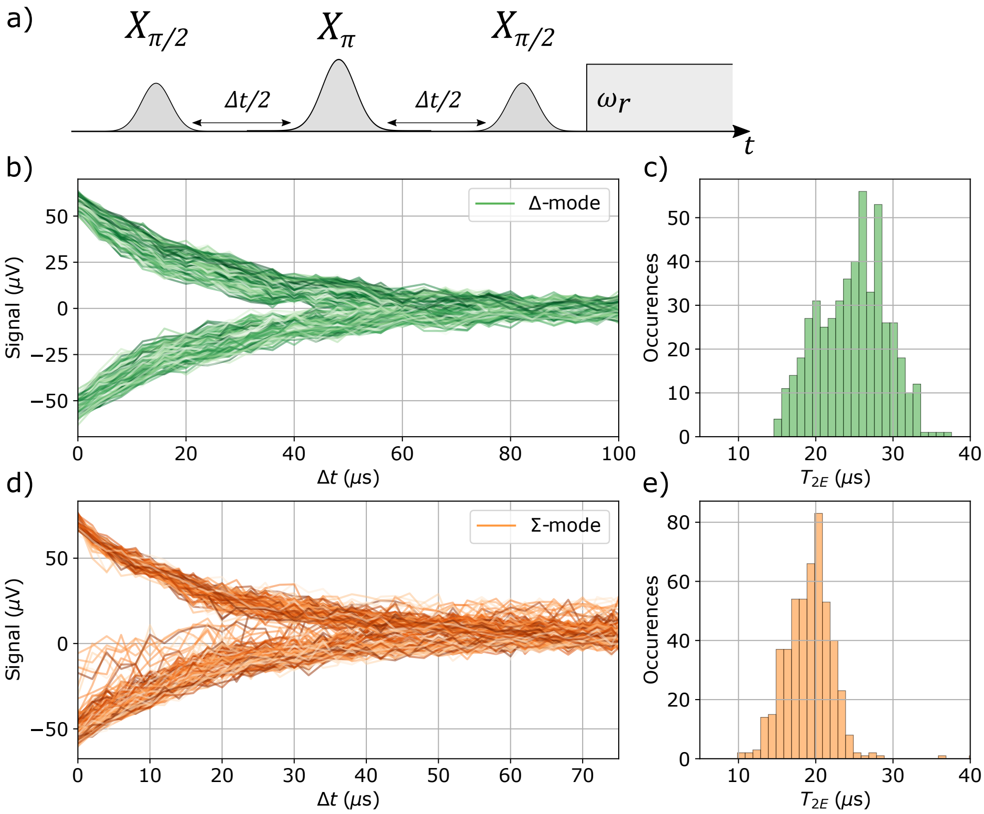

Figure 4.13: Spin-echo sequence (a) Pulse scheme of the spin-echo T_{2E} measurement. (b) (d) Repeated measurement signals as a function of pulse spacing (Δt). Traces follow an exponential decay, fitted to $S(\Delta t) = a + be^{-\Delta t/T_{2E}}$, in order to extract the coherence time T_{2E}. (c) (e) Histograms of the fitted T_{2E} extracted from the measurements. Statistics are from 502 repeated measurements of the Δ-mode (502 measurements of the Σ-mode).

state. To ensure this assumption is correct, and the measurement is performing as expected, we repeat the measurement changing the sign of the final control pulse. As such, we obtain two sets of decay curves, one pertaining to the final state of the qubit being $|0\rangle$, and the other $|1\rangle$. Since both curves decay to the same point, we know the measurement is behaving as expected. We repeat the measurement many times to build statistics and fit the resulting signals to an exponential decay, $S(\Delta t) = a + be^{-\Delta t/T_{2E}}$.

In Fig. 4.13 we show the resulting traces and distributions of fitted values of T_{2E}. We find $T_{2E}^{\Sigma} = 19$ μs (4 μs) and $T_{2E}^{\Delta} = 25$ μs (4 μs) for Σ-mode and $\Delta-$mode respectively.

In contrast to the differing energy relaxation rates of the modes, the T_{2E} values are very similar. In addition, they are far from the limit $T_2 = 2T_1$. This indicates the modes suffer from dephasing due to high frequency noise, such as excess residual photons in the resonator and improperly filtered control lines. Additional work is needed to improve this filtering and thermalisation to ensure lower dephasing rates in devices. From other works [80], it is clear that devices are sensitive to the exact placement of filters within shielding configurations. Additionally, design and materials choices in sample holders and devices could aid thermalisation of chips.

4.5 Charge Insensitivity

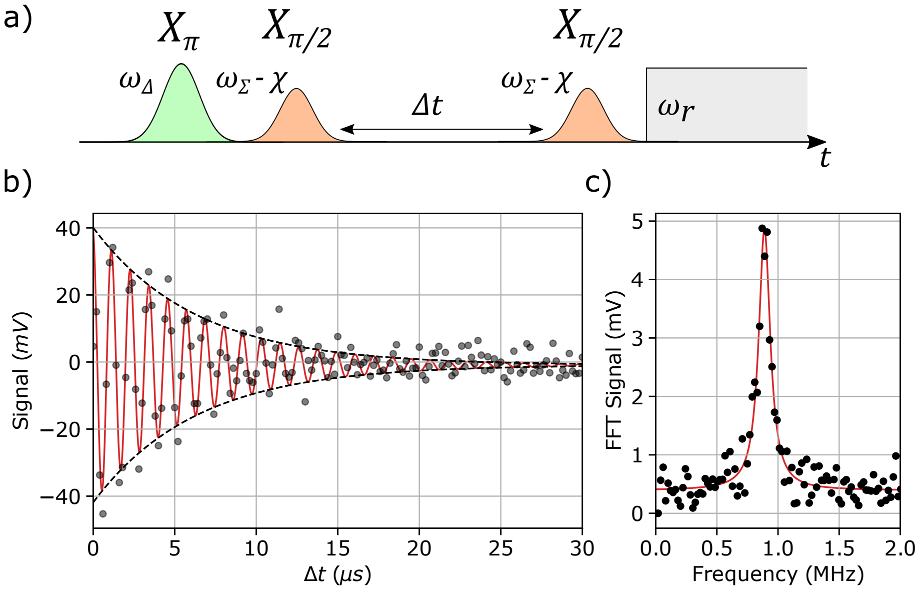

Figure 4.14: Ramsey interferometry on the $|01\rangle - |11\rangle$ transition of the charge insensitive two-mode transmon. (a) Pulse sequence for the Ramsey interferometry measurement. (b)(c) Ramsey oscillation and Fourier transform of the measurement, with data points in black, and fits in solid lines. The data in (b) is fitted to a decaying oscillation, and the dashed lines show an exponential decay envelope with the same decay constant. The data in (c) is fitted to a single Lorentzian peak.

In order to demonstrate a suppression of offset charge sensitivity in this device, we perform Ramsey interferometry measurements on the $|01\rangle - |11\rangle$ transition. From our predictive model, we expect a maximum charge dispersion of $\epsilon_{11}/h \approx 10$ kHz.

To measure this dispersion, we first prepare the system in the $|01\rangle$ state using a X_π pulse, at a frequency ω_Δ. We then place the system in a superposition using a $X_{\pi/2}$ pulse, at a frequency $\omega_\Sigma - \chi$. The system is then left to idle for time Δt, before a second $X_{\pi/2}$ pulse is applied, as shown in the pulse scheme, shown in Fig. 4.14 (a). As with the previous Ramsey interferometry measurements, the experiment is sampled many times, and so we expect to average over all possible parity configuration.

In Fig. 4.14, we show the measured Ramsey oscillation, and fast Fourier transform (FFT), for this transition. In contrast to the measurements performed on the charge sensitive device, shown in a later chapter, the oscillation is comprised of a single frequency component. This is demonstrated in the FFT of the decaying oscillation, shown in Fig. 4.14 (c), where we are unable to distinguish a further frequency component, to a resolution of 10 kHz. This demonstrates this device design iteration has a suppressed sensitivity to charge noise.

4.6 Fast Inter-Modal Gates

The rich energy level structure of multi-mode devices lend themselves naturally to many intrinsic forms of two-qubit gate. For example, due to the large cross-Kerr shift ($\chi_{\Sigma\Delta}$) a CNOT gate between the Σ-mode and Δ-mode (where the Σ-mode is the control and the Δ-mode is the target) can be implemented by driving the $|10\rangle \rightarrow |11\rangle$ transition for half a Rabi period. Additionally, a Bell state can be prepared by driving the Bell-Rabi transition ($|00\rangle \rightarrow |11\rangle$) with a strong drive pulse producing a two-photon transition, for a quarter of a Rabi period.

4.6.1 Microwave Activated Inter-modal Phase Gate

In this experiment, we implement an all-microwave phase accumulation by driving the ancillary transition of the two-mode system. We use the Δ-mode as our target

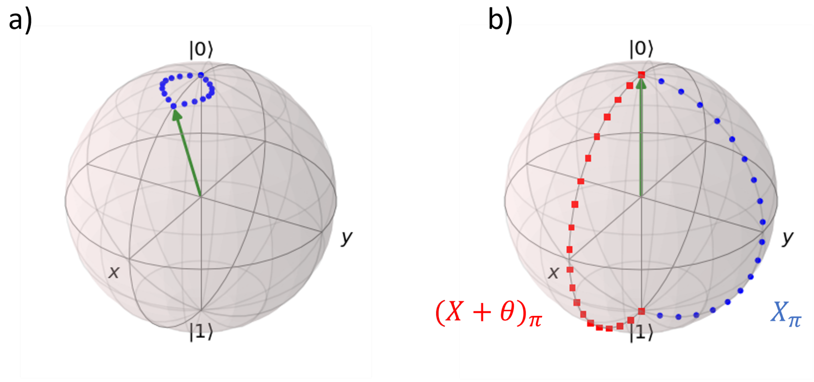

Figure 4.15: Microwave Activated Phase Accumulation. (a) Illustration of Bloch vector trajectory when driving off-resonantly. Phase accumulates at rate Ω^2/Δ, and if sufficiently detuned, the mode remains in the ground state. (b) Bloch vector trajectory for an on-resonant 2π excursion. The first pulse (blue) places the mode in the excited state, and the second (red) returns the mode to the ground state along a different axis, such that the mode accumulates an additional phase component.

mode, and the Σ-mode as the ancillary transition. Due to the strong cross-Kerr shift ($\chi_{\Sigma\Delta}$), we can drive these phase interactions at a very fast rate, making them ideal for reduced error operations.

As outlined previously, one of the motivations for the additional mode in the system is to allow for a protected mode for computation, and an ancillary mode for communication. This is such that in larger processor, the coupling strength between communication modes can become significantly larger than in standard configurations, allowing for fast two-qubit operations, whilst retaining the protection of the computational mode. The interaction we demonstrate here is the basis for the microwave activated conditional phase gate via ancillary transitions (AT-MAP), used to generate entanglement between protected computational modes of two coupled two-mode coaxial transmons, described in Chapter 3.

There are two ways in which we can accumulate a phase in the Δ-mode by driving the ancillary Σ-mode transitions. The first method of phase accumulation is via an off-resonant drive. Driving detuned from the ancillary mode transitions induces an ac-Stark shift, and yields a phase accumulation of Ω^2/Δ, where Ω is the drive strength and Δ is the detuning between drive and ancillary mode transition, to first order approximation. If the drive is sufficiently weak and detuned, then the excitation of the ancillary mode transition will be minimal. This method is illustrated in Fig. 4.15 (a).

The second method is to drive on resonance for a full Rabi period. A full 2π rotation around the Bloch sphere returns the ancillary mode to the ground state but with an $e^{i\phi} = -1$ phase accumulated relative to the excited state. By applying an X_π pulse, and then a second R_π pulse, where the phase of the second pulse is varied, we can return the ancillary mode to the ground state whilst accumulating an arbitrary phase. The speed of this interaction is twice the single qubit gate speed, which for the Σ-mode is in the 10s of ns, however, it does require careful calibration of the pulse amplitudes to ensure that the ancillary mode returns to the ground state after the interaction. Single-qubit-gate errors are the dominant source of infidelity in this on-resonant interaction. This method is illustrated in Fig. 4.15 (b)

Whilst a phase gate in itself is not a novel concept, and hardware efficient virtual Z-gates present significantly fewer errors [182], the key concept here is that we are implementing a phase accumulation driving $\approx$ 1 GHz detuned from the mode we will be using as a computational mode in future experiments. This is sufficiently far outside the computational subspace of the system, and so will result in fewer errors.

4.6.2 Interaction Spectroscopy

In order to measure the phase accumulated in the Δ-mode due to the Z-gate operation, we perform a modified echo sequence, shown in Fig. 4.16. The first $X_{\pi/2}$ pulse on the Δ-mode puts the system in the $\frac{1}{\sqrt{2}}(|00\rangle + |01\rangle)$ state. Following this, the Z pulse is applied, driving $\sim$ 200 MHz detuned from the Σ-mode transition (ω_Σ). Due to the ac-Stark shift, this induces a phase accumulation in the $|00\rangle$ state., causing the system to evolve to the state $\frac{1}{\sqrt{2}}(e^{i\phi}|00\rangle + |01\rangle)$. The echo pulse refocuses and mitigates any additional low frequency noise that may interfere with pulse calibration. The overall sequence maps the phase accumulated due to the pulse to the $\langle Z \rangle$ measurement basis, such that when measuring the Δ-mode, $P(|0\rangle) = \frac{1}{2}(1 - \cos(\phi))$, and $P(|1\rangle) = \frac{1}{2}(1 + \cos(\phi))$. For example, if the Z-gate were to induce a full Z_π rotation, the measurement would show the Δ-mode of the system in the $|0\rangle$ state. In the case where the Σ-mode has some excited state population due to the interaction, such as driving on resonance for less than a full Rabi period or the off-resonant drive causes some excitation, the final state is more complicated. In a system of multiple two-mode coaxial transmons being used for computational purposes, any excitation in the Σ-mode would cause significant errors in the operation of gates on the corresponding Δ-mode. As such, when performing multi-modal gates, we aim to minimise the excited state population of the Σ-mode, and use it purely as an ancillary or communication mode.

We start by characterising this interaction through spectroscopy. We fix the pulse length at 300 ns and sweep the amplitude and frequency from 5.2 – 5.9 GHz.

In Fig. 4.16 (b) we show the signal corresponding to the Δ-mode population, thus a measure of the phase accumulation. In (c) we show the population of the Σ-mode. In this region we observe a non-negligible accumulation of Σ-mode excited state population, around the Σ-mode transition at 5.7 GHz, as well as additional non-negligible excited state populations of this mode at frequencies detuned by $\eta_\Sigma/2$, $\chi_{\Sigma\Delta}$ and $\chi_{\Sigma\Delta} - \eta_\Sigma/2$. Due to the characterstic large $\chi_{\Sigma\Delta}$ of the system, there is an extremely large range of frequencies in which this interaction can be driven. This is significant for when designing two-qubit gates in systems of multiple two-mode coaxial transmons, as outlined in Chapter 3.

In addition to the magnitude of the phase accumulated, we can also measure the sign. We achieve this by modifying the echo pulse scheme such that the final pulse is a $Y_{\pi/2}$, again at the Δ-mode frequency ω_Δ. In Fig. 4.17, we show the same

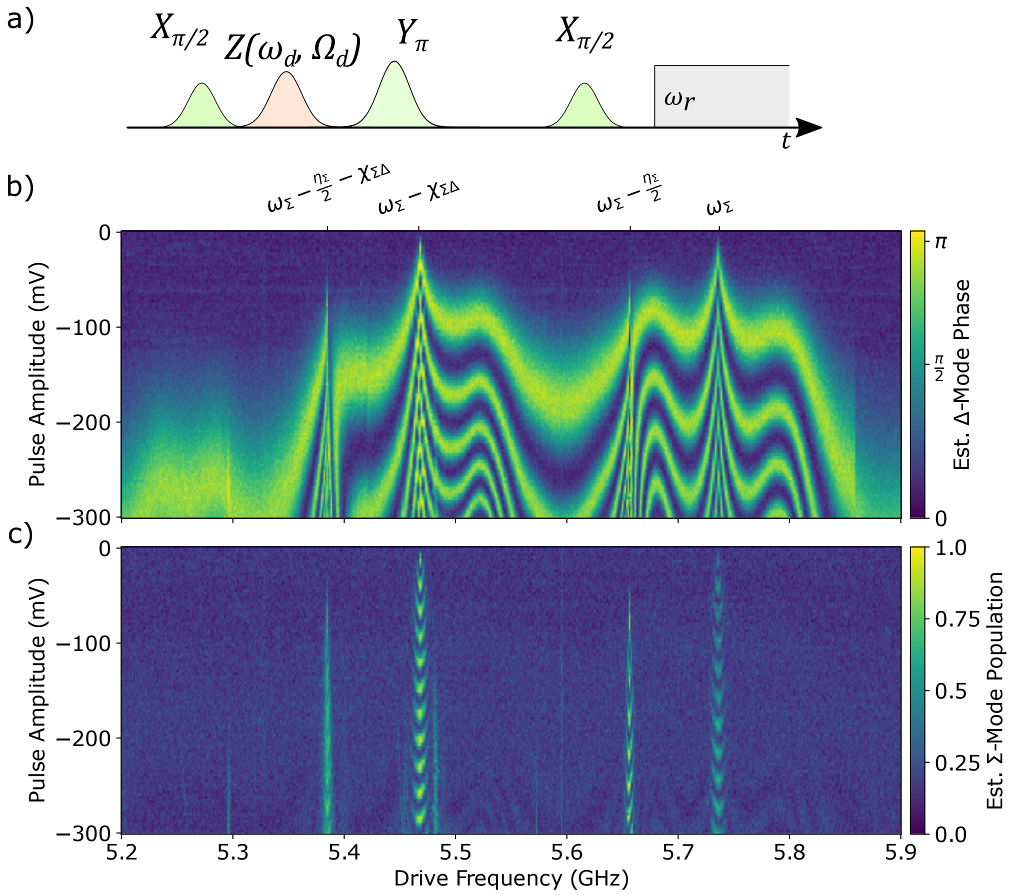

Figure 4.16: Microwave activated phase interaction spectroscopy. (a) Pulse scheme for the phase accumulation detection. (b) Δ-mode signal, identifying the phase accumulated in the interaction. Sharp features occur when on resonance with transitions of the Σ-mode, labelled above the axes. (c) Corresponding population of the Σ-mode transition simultaneously measured.

interaction spectroscopy measurement with this modified pulse scheme. As expected, the Σ-mode structure remains the same, however we observe a change in the sign of the phase accumulated. Above ω_Σ, and below $\omega_\Sigma - \chi_{\Sigma\Delta}$, we observe one sign of the phase accumulated, however, between the two transitions the sign is opposite. This enables the interaction to be tuned for both positive and negative phase accumulation gates.

In order to clearly illustrate the on-resonance and off-resonance driving regimes, we can look at the results of the phase interferometry measurement at two specific drive frequencies, $\omega_d = \omega_\Sigma$ and $\omega_d = \omega_\Sigma - \chi_{\Sigma\Delta} + 2\pi \times 50$ MHz. In Fig. 4.18, we show

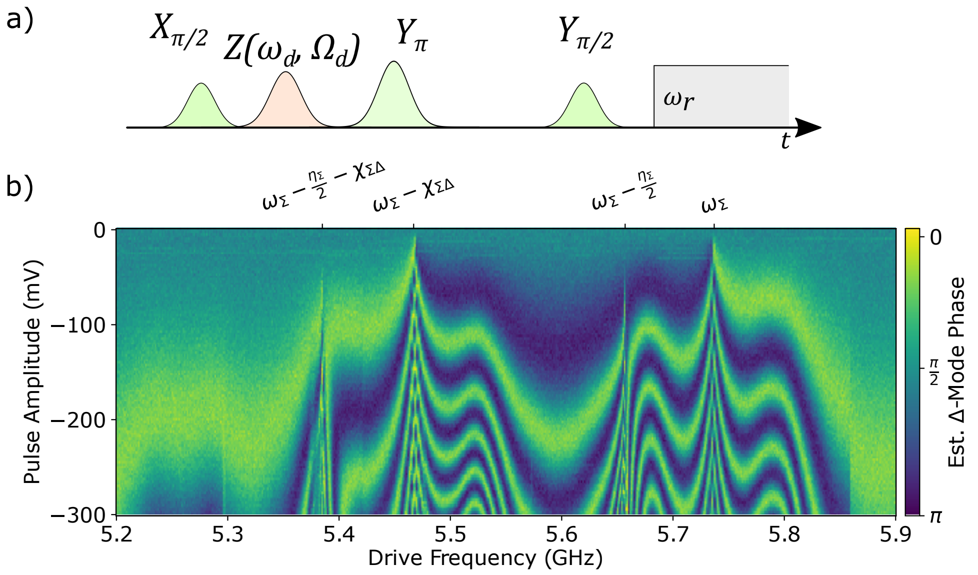

Figure 4.17: Microwave activated phase interaction spectroscopy sign. (a) Pulse scheme for the detection of the sign of the accumulated phase. As previous, however with the final pulse as a $Y_{\pi/2}$ rotation. (b) Measured Δ-mode signal. The shape is the same as Fig. 4.16, however the oscillation change colour in between the ω_Σ and $\omega_\Sigma - \chi_{\Sigma\Delta}$ features, indicating the phase accumulated changes sign.

the Δ-mode and Σ-mode populations resulting from driving the ancillary transition on resonance at 5.73 GHz. As expected, this is driving Rabi oscillations on the Σ-mode, as shown by Fig. 4.18 (b). Since it requires a full 2π to rotation to induce a π phase accumulated in the Δ-mode, we observe oscillations at half the frequency in the Δ-mode. In contrast to this, in Fig. 4.19, we show the Δ-mode and Σ-mode populations resulting from driving at 5.52 GHz, 50 MHz detuned from the $|01\rangle \rightarrow |11\rangle$ transition, at $\omega_\Sigma - \chi_{\Sigma\Delta}$. We observe the expected $\cos(Ax^2)$ shaped oscillation feature in the Δ-mode, whilst observing no excitation of the ancillary Σ-mode. This regime allows us to maintain high speed driving of the interaction, whilst retaining a minimal leakage into the ancillary transition, ideal for reducing errors in further single qubit rotations of the Δ-mode.

In Fig. 4.20, we show demonstrate how the speed of the off-resonant interaction increases with drive amplitude. We fix the frequency at 5.521 GHz, 50 MHz detuned

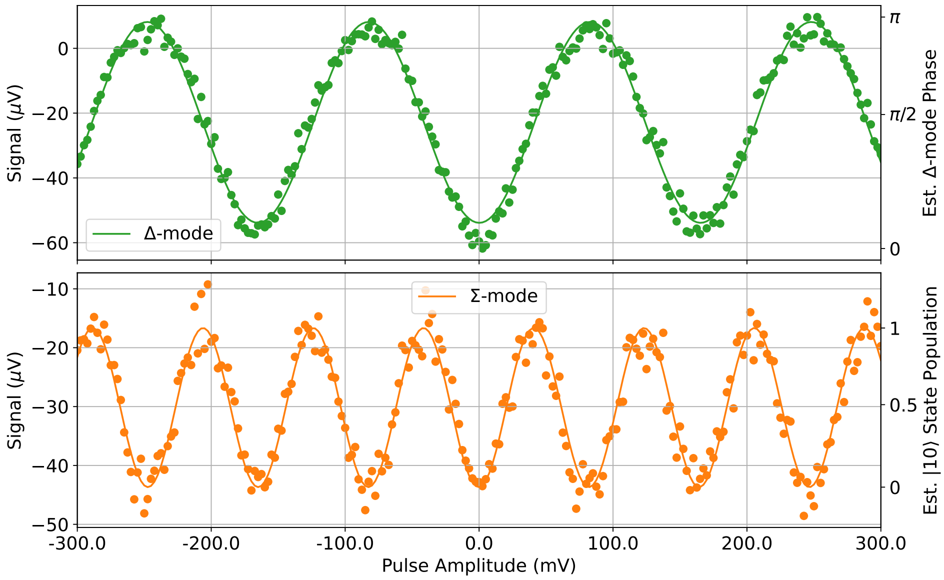

Figure 4.18: Simultaneous measurement of both modes when driving this phase interaction on resonance with the Σ-mode. The drive frequency and pulse length (100 ns) are fixed, and the amplitude of the pulse is swept. In the Σ-mode, we simply see amplitude Rabi oscillations, and fit the data to a cosine oscillation. We also see a cosinusoidal oscillation in the Δ-mode signal, at half the frequency of the Σ-mode oscillation. A pulse amplitude of 80 mV results in a full 2π rotation of the Σ-mode, and $\phi = \pi$ phase accumulated in the Δ-mode.

from the $|01\rangle \rightarrow |11\rangle$ transition ($\omega_\Sigma - \chi_{\Sigma\Delta}$). In this regime, we have already shown that the ancillary transition has minimal leakage. We sweep the drive amplitude and interaction pulse length, observing the oscillations increasing in frequency as the drive amplitude increases. In Fig. 4.20, we observe the smallest pulse length for which there is a full oscillation, corresponding to a phase accumulation of $\phi = \pi$, is 30 ns. However, the speed of this interaction could be increased with a higher drive power since there is no detectable leakage into the Σ-mode.

4.7 Conclusion

In conclusion, we have presented the first experimental methods and results of measuring a two-mode transmon in a coaxial cQED architecture. We have outlined the spectroscopic methods and procedures used to obtain the Hamiltonian parameters

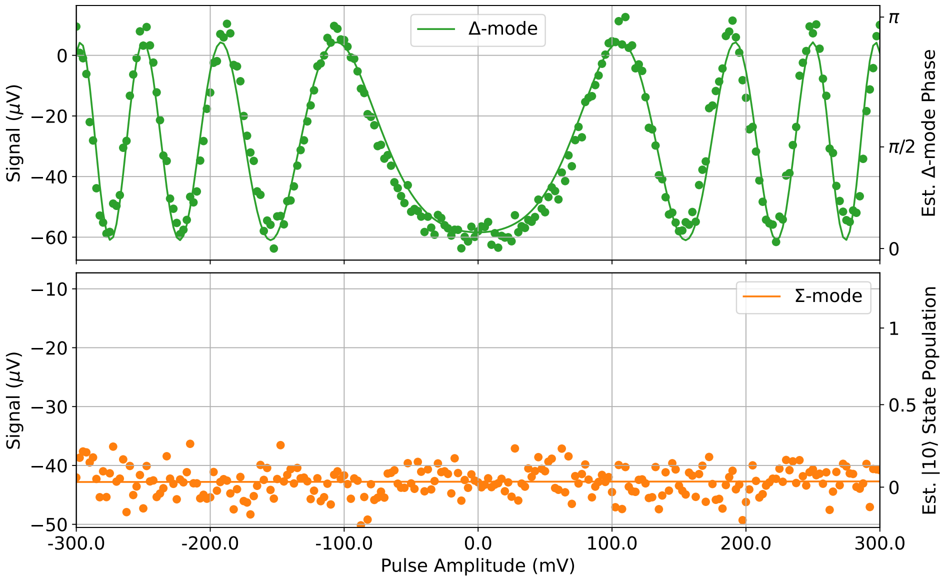

Figure 4.19: Simultaneous measurement of both modes when driving this phase interaction off resonantly, 50 MHz above the $\omega_\Sigma - \chi_{\Sigma\Delta}$ features. The Δ-mode mode signal follows a $\cos(\Omega x)^2$ shape, and data is fitted to this function. The flat signal of the Σ-mode signal shows there is no leakage into this mode in this off-resonant regime, optimum for reducing errors in subsequent single qubit gates.

of these devices, and shown that they are in agreement with simulated parameters. We show that these devices can be coherently controlled in time domain measurements. We have also shown how one can implement a microwave activated phase accumulation (or Z rotation) in the Δ-mode by driving the ancillary Σ-mode transition, detuned by $\sim$ 1 GHz from the computational subspace. This interaction can be driven in the on-resonant regime, or off-resonantly, where leakage into the ancillary mode is minimised. Due to the strong cross-Kerr shift between the modes, this interaction has a very wide frequency range in which it can be driven, and can be driven at speeds equivalent to single qubit gate operations (30 ns). This microwave activated phase interaction will be used in Chapter 6 as the basis of the microwave activated conditional phase gate, driven via ancillary transitions (AT-MAP, described in Chapter 3).

The methods outlined here form the basis of how we characterise devices in further experiments. The time domain measurements are very typical of standard su-

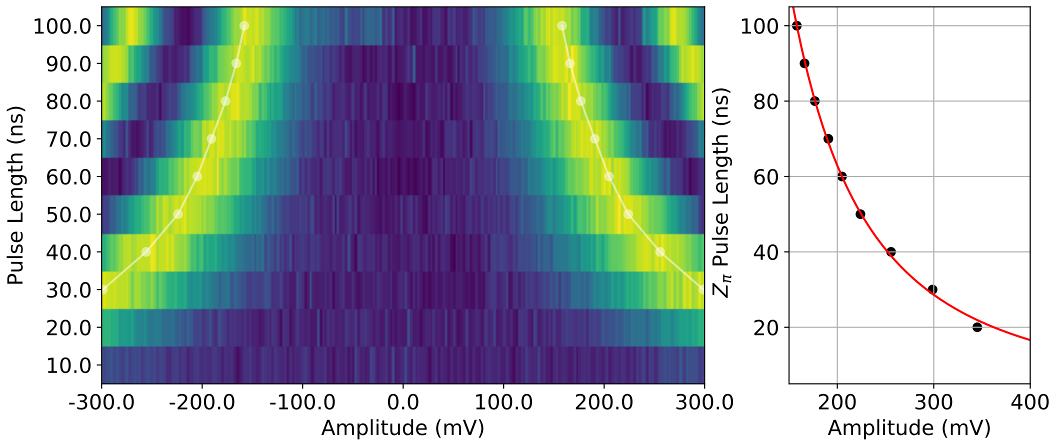

Figure 4.20: Demonstration of a Z_π gate speed. The drive frequency is fixed at 5.521 GHz, in the off-resonant regime. The pulse length and amplitude are swept. The signal follows the same $\cos(Ax)^2$ shape as in Fig. 4.19. From fitting to this shape, we extract the amplitude for which a $\phi = \pi$ phase is accumulated, and a Z_π gate is implemented, as shown by the white dotted line. We also show this Z_π gate length as a function of amplitude, fitting to a $1/\Omega^2$ line (red). This shows the interaction can be sped up with increasing drive amplitude to 20 ns or lower. The signal generator delivering this phase interaction tone is set to output a power of 3 dBm, and so there is still range to deliver more power to increase the interaction speed further.

perconducting circuit experiments, however identifying the $|00\rangle \rightarrow |11\rangle$ transition and characterising the cross-Kerr shift of the device requires two-tone spectroscopy methods.

The interaction between the two-mode coaxial transmon and readout resonator is not optimised in this experiment, and further design work can be done to adjust couplings to reduce losses due to the Purcell effect [29]. In addition, the Δ-mode is very weakly coupled to the drive line, due to the geometry and polarisation of the electric field component. Whilst not explored in this work, a stronger coupling between the coaxial control line and the dipole like asymmetric mode would result in much faster single qubit gates, and higher fidelity operations. Additional optimisation of the filtering of coaxial lines is also needed in order to reduce the dephasing rate due to high frequency noise sources, such as resonator photon number fluctuations.

Chapter 5

Charge Sensitivity in the Two-Mode Coaxial Transmon

In this chapter, we characterise charge sensitivity in a two-mode coaxial transmon[1]. We demonstrate how these devices show unique sensitivities to charge-parity configurations and charge-offset biases. Using Ramsey interferometry, we observe sensitivity to four charge-parity configurations and track two independent charge-offset drifts over hour timescales. We show how the predictive theory for charge sensitivity in such multi-mode qubits previously derived agrees with our results. Finally, we demonstrate the utility of a multi-mode qubit as a charge detector by spatially tracking local-charge drift.

Understanding decoherence mechanisms, such as charge noise, is vital to the application of superconducting qubits in a low-error quantum processor. In turn, a charge-sensitive multi-mode transmon could prove a useful tool for identifying the origins of such charge fluctuations in high-coherence quantum devices.

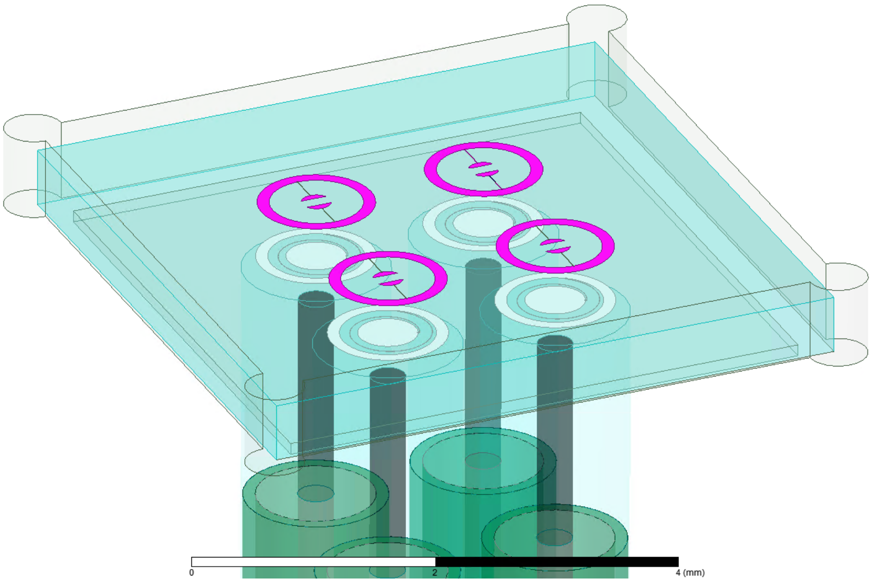

Figure 5.1: 3D model of the charge-sensitive two-mode coaxial transmon chip mounted in the sample holder. Four devices (purple) with readout resonators (white) are fabricated on opposing sides of a sapphire substrate (light blue). Four coaxial control lines are held below the readout resonators, used for both readout and control signals. Circular voids in corner of sample holder shows where indium is placed to ensure the chip is securely mounted in the sample holder.

5.1 Device Design

A 3D model of the charge-sensitive two-mode coaxial transmon device[2] is shown in Fig. 5.1. In the same way as the previous chapter, both the readout resonator and device are addressed by the same coaxial control port, fixed in place above the resonator. The electromagnetic properties of the device is simulated using an eigenmode solver in Ansys HFSS to obtain mode frequencies and electric and magnetic field distributions. This information is used in EPR calculations in order to obtain anharmonicities and cross-Kerr shifts, shown in Table 5.1.

There are notable differences in the design of this two-mode coaxial transmon device compared to others measured in this work. Whilst the geometry of the outer

---

[1] Work from this Chapter has been published in [38].

[2] We note that this device is fabricated using aluminium on a sapphire substrate, and measured in a dilution refrigerator fitted with a 100 mK shield, rather than the light-tight shield. Details of this fabrication recipe are in Appendix A of [157] (p157-159).

island is the same, the inner islands of the devices are significantly smaller (radius of 125 μm, gap of 120 μm) than the previously presented device (radius of 220 μm, gap of 125 μm). If we consider the Hamiltonian of the device and the charging energy $E_C = e^2C^*/2(C^{*2} - C_m^2)$, with $C^* = C(\frac{C+2C_m}{C+C_m})$, and coupling energy between the two modes $E_p = e^2C_m/(C^{*2} - C_m^2)$, reducing the capacitance C between the outer and inner islands has a significant effect on the charging energy E_C. This is shown in the simulated anharmonicities $\eta_{\Sigma(\Delta)}/2\pi$ being much larger than previously presented devices.

The result of this is that this particular design is much more sensitive to charge noise, and has a much higher charge dispersion. From the simulated E_C and range of targeted E_J parameters, the charge dispersion, ϵ_{mn}, is expected to be in the range of $1 - 10$ MHz. Since this is large compared to typical transmon dephasing rates, we expect it to be clearly measurable via spectroscopy and Ramsey interferometry. As such, this design presents an ideal platform for use in measuring and understanding charge noise dynamics in a multi-mode system, as well as testing the predictive theory of charge dispersion, presented in Chapter 3.

5.2 Hamiltonian Characterisation Through Spectroscopy

5.2.1 Two-Tone Spectroscopy

In Fig. 5.3, we show the full two-tone spectroscopy measurement result for the charge-sensitive two-mode coaxial transmon. From the spectroscopic signatures, we identify the single-photon transitions of the Σ-mode and Δ-modes and extract the mode frequencies $\omega_\Sigma/2\pi = 6.71$ GHz and $\omega_\Delta/2\pi = 5.51$ GHz. These transitions are labelled in Fig. 5.3 (b).

We observe the Σ-mode transitions are broadened more than the Δ-mode transitions, since these modes are easier to drive as they are both coupled to the control

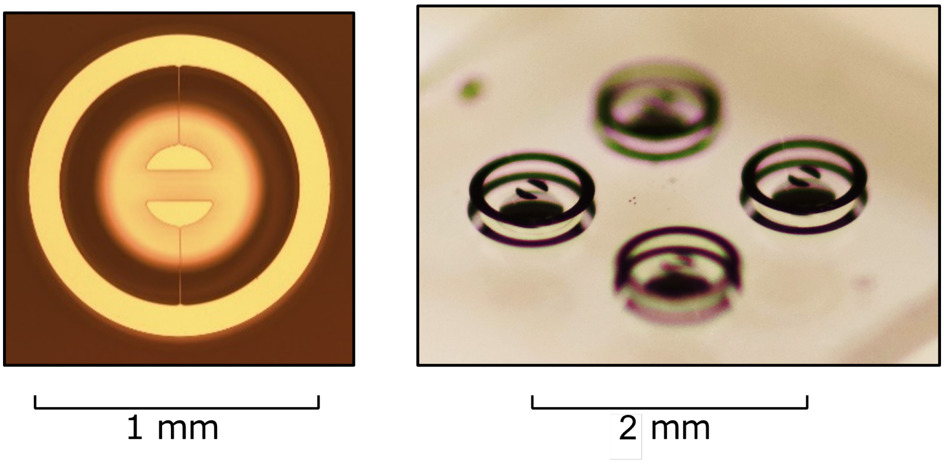

Figure 5.2: (left) Optical microscope image of the fabricated charge sensitive two-mode coaxial transmon device. Since a sapphire substrate is used in this device, it is possible to observe both the qubit device and resonator patterned on the opposite side of the substrate. (right) Photograph of the charge-sensitive two-mode coaxial transmon device, again showing both the qubit devices and resonators patterned on opposite sides of the substrate. Whilst a 4-device chip is fabricated, we only measure and present results for one of the devices on the substrate.

line more strongly, and have a smaller detuning to the readout resonator through which they are being driven. Additionally, at the Σ-mode transition frequency, we observe a clear three-photon red sideband transition signature, indicated by the two diagonal lines of positive gradient coinciding at the Σ-mode transition. This is a three-photon destructive interference mixing process with the resonance condition $2\hbar\omega_{A/B} - \hbar\omega_{B/A} = \hbar\omega_{\Sigma}$, where $\omega_{A(B)}/2\pi$ is the drive frequency of generator $A(B)$.

From the spectroscopic signatures of the two-photon transitions detuned from the main mode frequencies, we identify the $(|0\rangle \rightarrow |2\rangle)/2$ transitions for the Δ-mode and Σ-mode, identified by the green and orange diagonal dashed lines in Fig. 5.3 (b). From these, we extract the anharmonicities of the modes to be $\eta_{\Delta}/2\pi = -0.38$ GHz and $\eta_{\Sigma}/2\pi = -0.34$ GHz, consistent with our simulations. Additionally there is the three-photon $(|00\rangle \rightarrow |30\rangle)/3$ visible at 6.37 GHz, indicated by the two orange diagonal dotted lines.

We identify the $|00\rangle - |11\rangle$ transition at $(\omega_{\Delta} + \omega_{\Sigma} - \chi_{\Sigma\Delta})/4\pi = 5.86$ GHz, showing

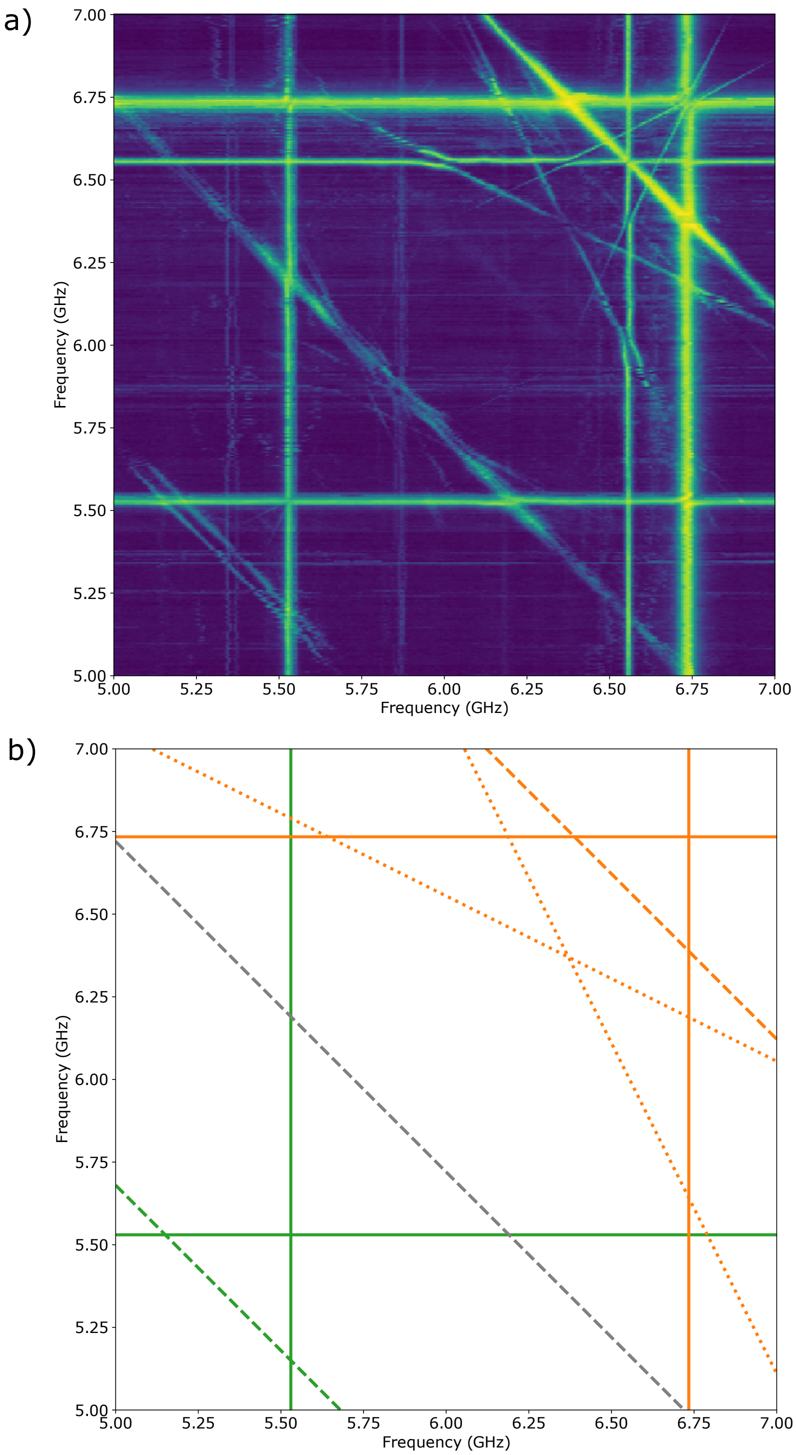

Figure 5.3: (a) Two-tone spectroscopy measurement result of the two-mode coaxial transmon. (b) Spectroscopy measurement with transitions of the Σ-mode (orange) and Δ-mode (green) highlighted. Grey diagonal dashed line shows the two-photon $|00\rangle \rightarrow |11\rangle$ transition.

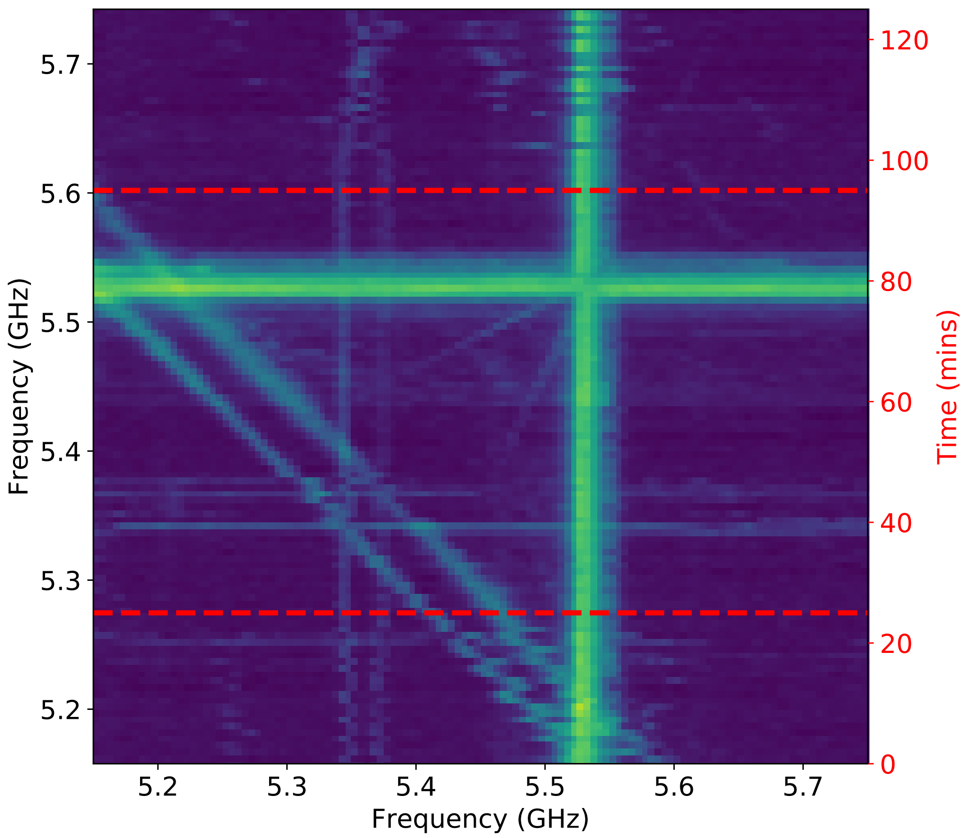

Figure 5.4: Detailed section of the two-tone spectroscopy measurement showing the Δ-mode $(|0\rangle \rightarrow |2\rangle)/2$ transition. The X frequency axis is the fast swept parameter, and the Y frequency axis is the slow swept parameter. We label the time taken for the overall measurement on the right Y-axis label (red).

an inter-modal state-dependent shift of $\chi_{\Sigma\Delta}/2\pi = 0.50$ GHz. Whilst the deviation between the simulated result and measured result is within the same limit as previously measured devices of approximately 20%, further investigation into refinement of simulation and mesh detail is required to improve this accuracy.

In Fig. 5.4, we show a zoom of the Δ-mode $|0\rangle \rightarrow |1\rangle$ and $(|0\rangle \rightarrow |2\rangle)/2$ transitions. We observe an additional feature at the higher photon number transition due to the high charge dispersion of the system. The X frequency axis is the fast axis as it is swept first, whilst the Y frequency axis is the slow axis. As such, the slow drifts in charge configuration are more visible in the two vertical spectroscopic lines. Observing the region from $t = 0$ mins to $t = 25$ mins, indicated by the red dashed line in Fig. 5.4, the configuration changes with each sweep, indicated by the moving transition frequency lines around 5.35 GHz. From $t = 25$ mins to $t = 95$ mins, the system remains in a more stable configuration, before again returning to a more transient regime. This dispersion and charge sensitivity can also be observed in the additional features around the Δ-mode $|0\rangle \rightarrow |1\rangle$ transition. Due the wide range of this measurement and reduced local resolution, we do not resolve the four frequency peaks, corresponding to the four parity configurations of the two-mode coaxial transmon, as detailed in Chapter 3.

5.2.2 Hamiltonian Parameters

We restate the previously defined Hamiltonian of the charge sensitive two-mode coaxial transmon here as,

$$\begin{aligned}\hat{H} =& 4E_C(\hat{n}_1 - n_{g1})^2 + 4E_C(\hat{n}_2 - n_{g2})^2 + 4E_p(\hat{n}_1 - n_{g1})(\hat{n}_2 - n_{g2}) \\ & - E_J \cos\hat{\varphi}_1 - E_J \cos\hat{\varphi}_2.\end{aligned} \tag{5.1}$$

From the parameters obtained in spectroscopy measurements, we use numerical methods to estimate values of $E_J/h = 11$ GHz, $E_C/h = 0.5$ GHz, and $E_p/h = 0.2$ GHz, as defined in Chapter 3. The table of parameters of device measured is shown in Table 5.1. Notably, in comparison to previous devices measured, the anharmonicity is large in this device. Whilst this is more optimum for the operation of fast single qubit gates with lower leakage into higher states, it comes at the cost of higher sensitivity to charge noise.

Table 5.1: Device Parameters

	Sim.	Measured
LC Resonator		
Frequency f_r [GHz]	-	9.72
Linewidth $\kappa_r/2\pi$ [MHz]	-	2.8
Dispersive Shift $2\chi_{\Delta r}/2\pi$ [MHz]	-	3.9
Dispersive Shift $2\chi_{\Sigma r}/2\pi$ [MHz]	-	4.9
Δ - Mode		
Transition Frequency $\omega_\Delta/2\pi$ [GHz]	-	5.51
Anharmonicity $\eta_\Delta/2\pi$ [MHz]	330	380
Σ - Mode		
Transition Frequency $\omega_\Sigma/2\pi$ [GHz]	-	6.71
Anharmonicity $\eta_\Sigma/2\pi$ [MHz]	310	340
Cross Kerr Shift $\chi_{\Sigma\Delta}/2\pi$ [MHz]	650	500
E_J [GHz]	-	11
E_C [GHz]	-	0.5
E_p [GHz]	-	0.2

Given these parameters, we estimate a charge dispersion of the lowest two modes to be 4 MHz and 4.1 MHz, calculated numerically. This predicted charge dispersion and E_J/E_C regime is shown in Fig. 5.5 for the charge-sensitive (A) and charge-insensitive (B, from Chapter 4) devices measured.

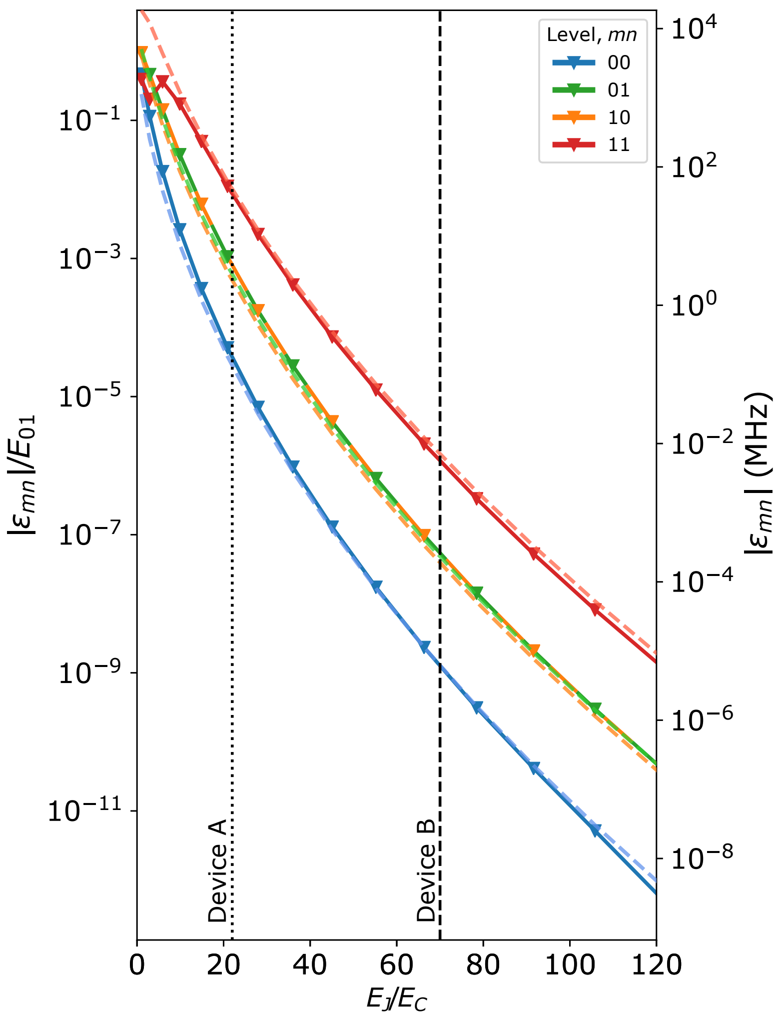

Figure 5.5: Comparison of numerical (solid) and tight binding model (dashed) calculations of charge dispersion for the lowest four energy levels of the qubit Hamiltonian, as a function of the ratio E_J/E_C. The right vertical scale gives the charge dispersion in MHz for a lowest transition frequency of 5 GHz. Vertical dotted (dashed) line shows the regime of the charge sensitive Device A, $E_J/E_C = 22$ (charge suppressed Device B, $E_J/E_C = 70$). Figure from [38]

5.3 Coherence Characterisation

We now move to time-domain measurements using pulsed control of modes. X_π and $X_{\pi/2}$ pulses are calibrated using amplitude Rabi oscillations as previously outlined in Chapter 4. We again observe that the Δ-mode requires more power to drive since it is detuned further from the readout resonator through which it is being driven, as well having a different field polarisation to the coaxial control port.

We present measurements and statistics of energy relaxation and spin-echo sequences. Due to the charge dispersion, the Ramsey oscillations have unique characteristics and so are presented separately in Section 5.4. Detailed statistics of T_2^* for each mode are not taken for this device.

5.3.1 Energy Relaxation

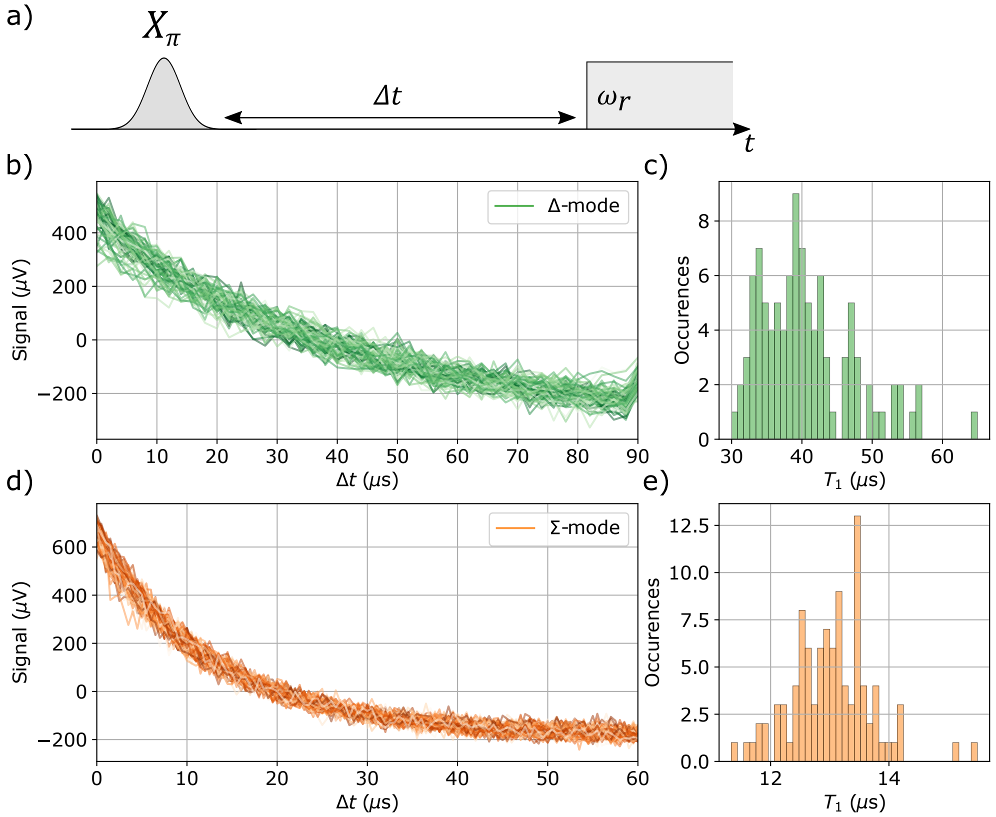

Figure 5.6: Energy Relaxation (a) Pulse scheme of the energy relaxation T_1 measurement. (b) (d) Repeated measurement signals as a function of delay (Δt). Traces follow an exponential decay, fitted to $S(\Delta t) = a + be^{-\Delta t/T_1}$, in order to extract the energy relaxation time T_1. (c) (e) Histograms of the fitted T_1 extracted from the measurements. Statistics are from 101 repeated measurements.

We measure the energy relaxation rate ($\Gamma_1 = 1/T_1$) of each mode by exciting them with a calibrated X_π pulse, and waiting a delay time Δt before measuring, as depicted in the pulse sequence shown in Fig. 5.6 (a). As previously, we expect the subsequent measurement signal as a function of delay time to follow an exponential decay. We plot the measured signals in Fig. 5.6 (b) and (d). We repeat each averaged measurement 101 times in order to build statistics. Each trace is fitted to an equation of the form $S(\Delta t) = a + be^{-\Delta t/T_1}$, where a and b are offsets. The histograms of the fitted values of T_1 of the Δ-mode (green) and Σ-mode (orange) are shown in Fig. 5.6 (c) and (e) respectively.

From these repeated measurement we extract average fitted energy relaxation times of $T_1^\Sigma = 13.5$ μs and $T_1^\Delta = 40.7$ μs for the Σ-mode and Δ-mode respectively. We again attribute the difference in these values for each mode to the difference in field polarisations, detuning and coupling to the readout resonator, and control port coupling. In contrast to previous measurements of T_1 presented in Chapter 4, the distributions of fitted relaxation times follow more closely a single modal Gaussian distribution. This can partly be attributed to the measurement being conducted over a short period (3 hours), and so fewer loss channel recombination events that affect relaxation rates occur [180].

5.3.2 Spin-Echo

We perform a spin-echo sequence in order to obtain the coherence time T_{2E}, as depicted in Fig. 5.7 (a). Whilst we expect the charge sensitivity to induce significant noise and decoherence, the additional echo pulse in the sequence refocuses these low-frequency noise contributions to dephasing. In this measurement, each point is averaged to provide an ensemble measurement, and the sequence is repeated 101 times to build statistics. The resultant trace of signal as a function of delay Δt is $S(\Delta t) = a + be^{-\Delta t/T_{2E}}$. We plot these traces in Fig. 5.7 (b) and (d) for the Δ-mode (green) and Σ-mode (orange).

The resulting distributions of fitted T_{2E} values are shown in Fig. 5.7 (c) and (e). From the repeated measurements, we extract average fitted values of $T_{2E}^\Sigma = 13.1$ μs

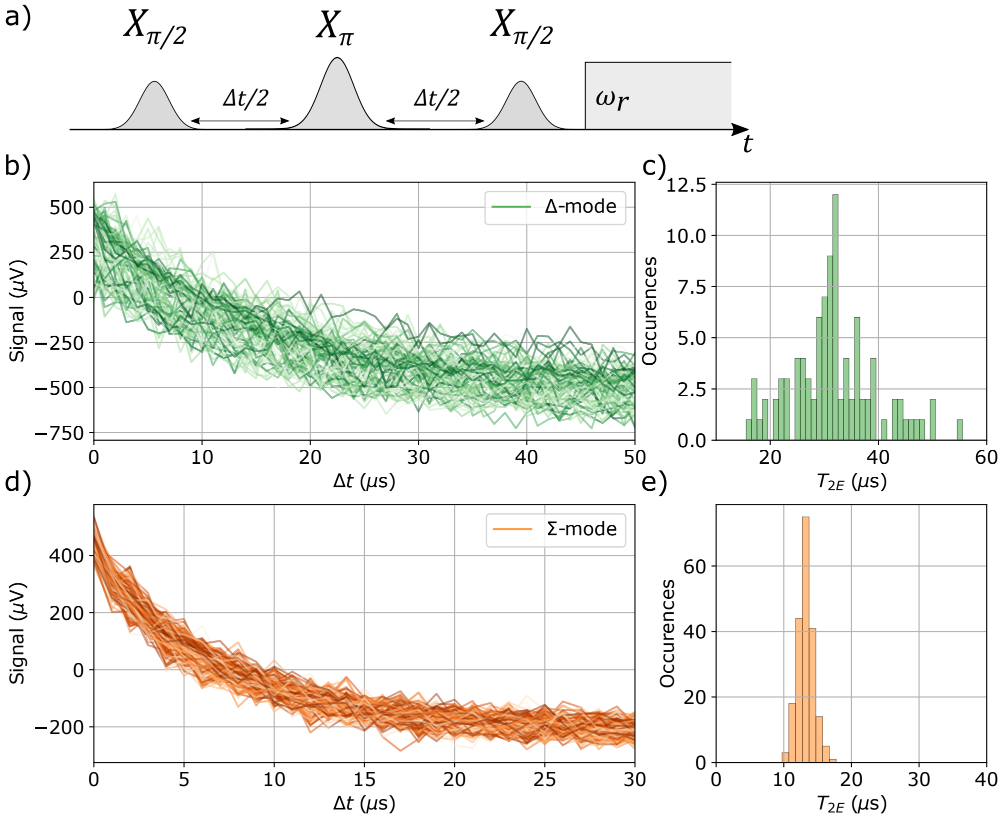

Figure 5.7: Spin-echo sequence (a) Pulse scheme of the spin-echo T_{2E} measurement. (b) (d) Repeated measurement signals as a function of pulse spacing (Δt). Traces follow an exponential decay, fitted to $S(\Delta t) = a + be^{-\Delta t/T_{2E}}$, in order to extract the coherence time T_{2E}. (c) (e) Histograms of the fitted T_{2E} extracted from the measurements. Statistics are from 101 repeated measurements.

and $T_{2E}^{\Delta} = 33.8$ μs for the Σ-mode and Δ-mode respectively. We note again that the distributions follow more closely a single mode Gaussian distribution, and that the coherence times are far from the limit $T_{2E} = 2T_1$, suggesting that the modes are susceptible to additional dephasing from high frequency noise sources such as poorly thermalised readout resonators and control lines.

5.4 Charge Configuration Detection

5.4.1 Ramsey Interferometry

We use Ramsey interferometry in order to measure energy dispersion. A mode is prepared in a superposition state using an $X_{\pi/2}$ pulse, allowed to idle for time Δt,

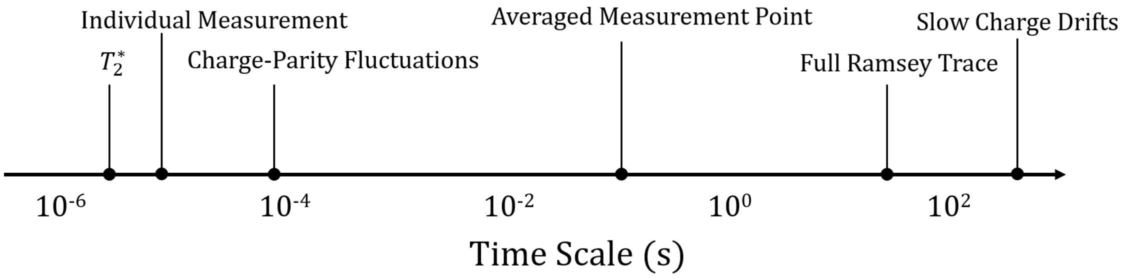

Figure 5.8: Time scales of the measurement and physical processes involved in the Ramsey interferometry measurement.

before a second $X_{\pi/2}$ pulse is applied, as shown in the pulse sequence in Fig. 5.9 (a). We detune the frequency of the control pulses from the average mode frequency by approximately 3.5 MHz to prevent aliasing for large frequency excursions. At each Δt, we sample 2500 times, taking approximately 100 ms to acquire. Typical transmon devices exhibit a quasiparticle tunnelling rate of 0.01 μs^{-1} [80], therefore we expect to average over all possible parity configurations during the measurement. As a result, we expect to observe four frequency components in a Ramsey oscillation, corresponding to the four parity configurations. We show an illustration of the relevant time scales of the measurement and physical processes involved in the Ramsey interferometry, shown in Fig. 5.8.

In Fig. 5.9 we show example Ramsey oscillations measured for both the Δ - mode and Σ - mode. Fig. 5.9 (c) and (e) show the fast Fourier transform (FFT) of the Ramsey oscillations, in which we observe four distinct frequency components. We fit the FFT data to four identical Lorenztian peaks, which are symmetric about the average frequency, $\overline{E_{0\Sigma(\Delta)}}$. The separation of the two inner peaks closest to the symmetry point, is labelled as Δf_1, and the separation of the two outermost peaks is labelled as Δf_2, as shown in Fig. 5.9. Using our tight-binding model, we find that:

$$\begin{aligned}\Delta f_1 &= \frac{\epsilon_{mn}}{h}\sin \pi n_{g\Sigma} \sin \pi n_{g\Delta},\\ \Delta f_2 &= \frac{\epsilon_{mn}}{h}\cos \pi n_{g\Sigma} \cos \pi n_{g\Delta}.\end{aligned} \tag{5.2}$$

This allows us to determine the charge configuration from the energy dispersion. Repeating this measurement, we are able to track frequency fluctuations due to correlated and anti-correlated charge-noise dynamics over extended periods of time.

Note that there are several technical shortcomings of our demonstration experiment, which can be remedied in the future. Firstly, there is no gate charge control in this current architecture, which prevents us from resolving jumps or drifts larger than 0.5e for n_{g1} and n_{g2}. This limits our ability to determine a charge noise spectral density at this time [35], but can be alleviated with the incorporation of local control of static electric fields via gate electrodes. Secondly, the time taken to acquire each Ramsey oscillation trace limits the ability to observe changes in charge configuration faster than two minutes. This can be remedied using higher fidelity readout with a parametric amplifier, or a more efficient sampling of Ramsey delay times.

There are practical shortcomings to this method of Ramsey interferometry, in addition to those stated previously. Firstly, in order to observe four frequency peaks in the Fourier transform of the Ramsey oscillation, the drive frequency must be detuned at least half the maximum charge dispersion (ϵ_{mn}). In the mode with the largest charge dispersion, this creates difficulty in driving the transitions with the largest detuning. This is visible in the time series Fourier transform data of the Δ-mode measurement in Fig. 5.10, where the higher frequency peaks show significantly less contrast to the background signal. When fitting, we utilise the fact that the four frequencies are symmetric about an average transitions frequency, as shown in Fig. 5.9 (c) and (e). From the time series measurements we extract this symmetry point first, before proceeding to a brute force grid search of Δf_1 and Δf_2 (with the condition that $\Delta f_2 > \Delta f_1$ by definition) for each trace in order to fit the spectrum. This allows us to restrict the number of free variables when fitting and account for lower signal to noise in the measurements with larger charge dispersion.

The second practical shortcoming is that if the drive detuning is not at least half

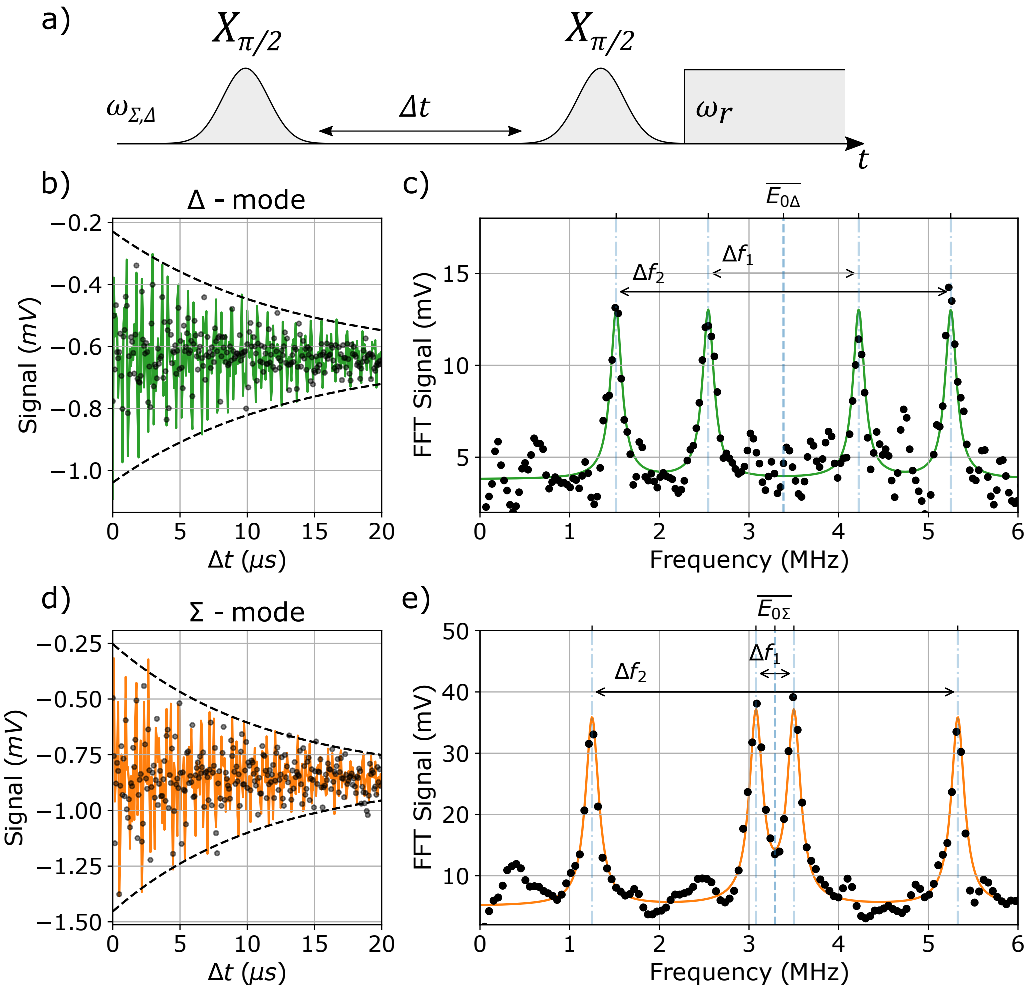

Figure 5.9: Ramsey interferometry based measurement of charge bias configuration. Experimental measurement of charge dispersion and four parity configurations in the coaxial multi-mode qubit, with data points in black and fits in solid lines. (a) Pulse sequence for the Ramsey interferometry measurement. (b) (c) Ramsey oscillation performed on the Δ-mode. The solid line in (b) shows a decaying oscillation with frequency components, and decay constant, obtained from fitting the Fourier transform of the oscillation, shown in (c). The dashed line shows an exponential decay envelope with this same fitted decay constant. The Fourier transform of the measured Δ-mode Ramsey oscillations shows four frequency peaks, corresponding to the four possible parity configurations. The data is fitted to four Lorentzian peaks, symmetric about the average frequency. We define the separation of the inner peaks to be Δf_1, and the separation of the outer peaks to be Δf_2. From this separation of frequency peaks we can extract the charge bias configuration. (d) (e) Ramsey oscillation and Fourier transform of measured oscillation performed on the Σ-mode. Figure from [38].

the maximum dispersion, there can be some aliasing of frequency peaks in the Fourier transform data, since the system is being driven between the four transition frequencies. For later measurements in charge configuration tracking we use the Σ-mode, since it has a lower charge dispersion and aliasing is not an issue. Future refinements of this Ramsey interferometry method could drive at the average transition frequency ($\overline{E_{0i}}$), to avoid the aliasing issue. This would reduce the detuning between the drive frequency and the transition frequencies, resulting in a lower oscillation frequency of the Ramsey trace (which would subsequently only have two frequency components). Further improvements would involve optimising the sampling rate for faster signal acquisition.

5.4.2 Interleaved Ramsey Interferometry

Since both the Σ-mode and Δ-mode are sensitive to the sum and difference offset-charge configurations ($n_{g\Sigma}$, $n_{g\Delta}$), only one mode needs to be measured in order to obtain the charge configuration. However, we expect each mode to have a different maximum charge dispersion (ϵ_{mn}) and so the configuration of the four parity configuration transition frequencies will appear different when measuring each mode. Here, we perform an interleaved measurement of the Σ-mode and Δ-mode, in order to investigate the differing frequency configurations for the same offset-charge configuration.

The interleaved measurement consists of performing a full Ramsey oscillation measurement, as in the pulse sequence in Fig. 5.9 (a), first on the Δ-mode, and then immediately afterwards on the Σ-mode. This process is repeated over the course of four hours to obtain a time series measurement. As in Fig. 5.9 (b) and (d), the resulting traces are decaying oscillations with four frequency components. We take the Fourier transform of each of these oscillations and plot the resulting time series measurement of the frequency configurations in Fig. 5.10.

We fit the each resulting FFT data to a sum of four Lorentzian line shapes, with an inner peak separation (Δf_1) and outer peak separation (Δf_2) as defined previously. The time series measurement of these extracted peak configuration parameters are

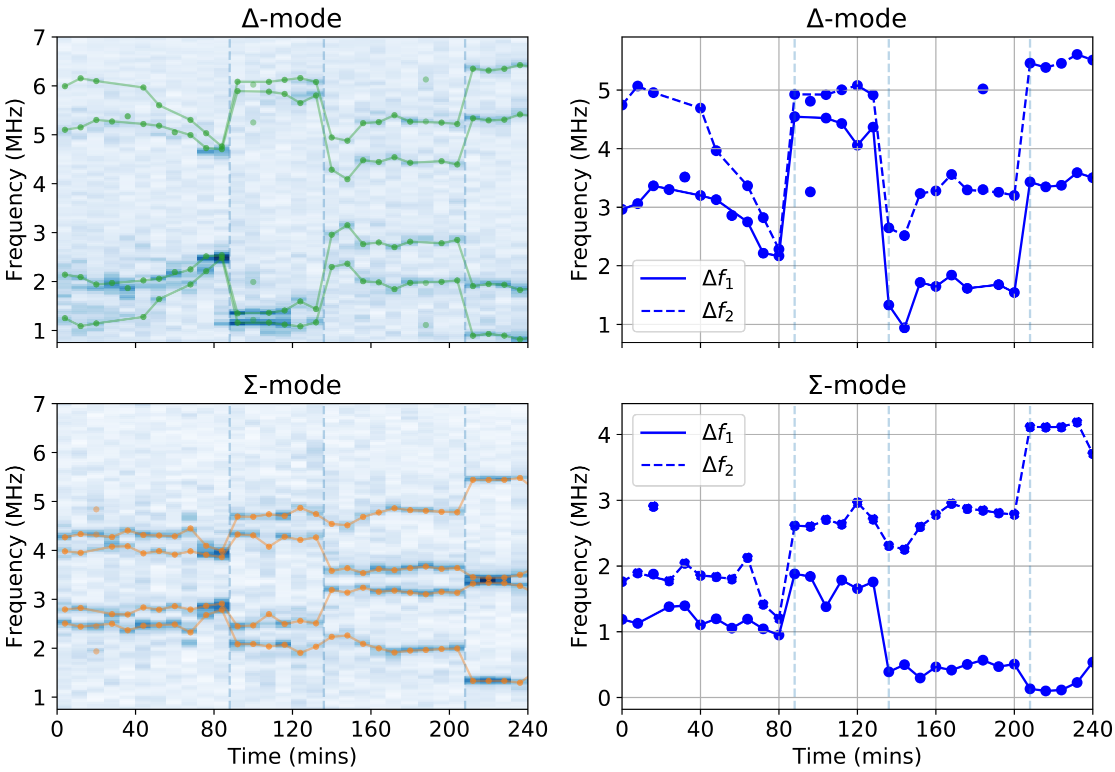

Figure 5.10: Interleaved time series Ramsey intereferometry of the Δ-mode and Σ-mode. (Left) Fourier transform of repeated Ramsey measurements, as shown in Fig. 5.9, performed interleaved on the Δ-mode and Σ-mode over a period of four hours. Each vertical cut is fit to a sum of four Lorentzian peaks, centred about an average frequency. The position of each of the four fitted peaks is shown by the overlaid dots. The connecting line illustrates the dynamics of the peak movement, filtering out data with poor signal to noise and fits. (Right) Tracking of fitted inner peak separation (Δf_1) and outer peak separation (Δf_2) extracted from the time series measurement (left). Line demonstrates filtered peak dynamics. Dashed vertical lines on each plot show the occurrence of large discrete jumps in offset-charge configuration, observable simultaneously across each mode of the device.

shown in Fig. 5.10.

In these time series measurements of frequency configuration, we observe the two key characteristics of charge noise within our system. The first is a slow drift in configuration, such as that seen from $T = 0$ minutes to $T = 80$ minutes in Fig. 5.10. The second characteristic is discrete jumps in charge configuration, as indicated by the sudden change in frequency configuration. These events are indicated by the vertical dashed lines in Fig. 5.10. The precise attribution of the cause of these two unique characteristics requires further investigation, however, we speculate the slow drifts are due to a localised reconfiguration of a charge distribution within the region of the device (such as a charge moving on the surface of the substrate). The sudden jumps are more commonly attributed to ionising radiation events [36].

Since both modes are sensitive to both offset-charge configurations $(n_{g\Sigma}, n_{g\Delta})$, as expected, the sudden jumps in frequency configuration are observable in both modes at the same time. Some asymmetry in the fabrication of the device will cause a difference in the magnitude of the maximum charge dispersion (ϵ_{mn}) measured, and so the exact frequency configuration of each mode will present differently. However, we expect the configuration in the number of peaks visible in each mode to be the same between each measurement. Each Ramsey oscillation trace takes approximately two minutes to acquire, which is not sufficient time for the low frequency charge noise drifts to substantially change.

As we observe in the time series measurements in Fig. 5.10, both modes show nominally the same frequency configuration. From $T = 80$ minutes, to $T = 140$ minutes, both show a stable configuration of four peaks, and following the sudden jump, both modes show a slow drift predominantly of the outer peaks before becoming stable again. From $T = 210$ minutes to the end of the measurement, there is a difference in the configuration between the two modes. The Δ-mode shows four peaks with a large inner and outer peak separation, whereas the Σ-mode has a much smaller inner peak separation. We attribute this to the fact the outer island is not a perfect ground, as in our models. As such, it presents an extra degree of freedom in the charge configuration. In turn, this could create a phase difference between the modes, thus causing the difference in observed charge configuration. Further investigation is required to determine the effect this additional degree of freedom has on the device.

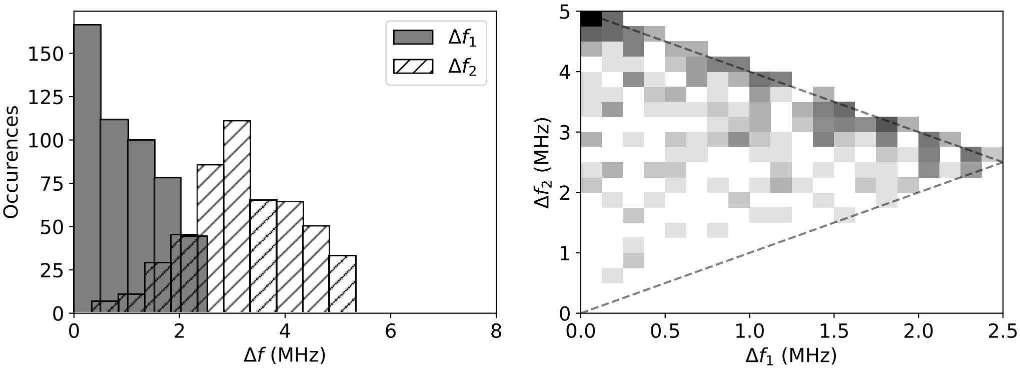

Figure 5.11: Monte-Carlo simulation of frequency configurations from 300 randomly generated pairs of offset-charge configurations. (Left) Histogram of Δf_1 (solid) and Δf_2 (hatched). (Right) 2D histogram of extracted pairs of Δf_1 and Δf_2. Diagonal lines enclose region in which measurable parameters lie, given a set maximum charge dispersion of 5 MHz.

5.4.3 Charge Dispersion

Since we have no method of local control of static electric fields in this architecture, we are unable to directly control the offset-charge configuration of the device. As such, it is not possible to directly measure the maximum charge dispersion (ϵ_{mn}) by tuning the charge configuration to this point. Instead, we perform many repeated measurements of the frequency configurations of each mode to build up a statistical distribution.

To understand what the distribution of frequency separations Δf_1 and Δf_2 looks like, we perform a Monte-Carlo simulation. We take 300 randomly generated pairs of gate charge offsets $n_{g\Sigma}$ and $n_{g\Delta}$, and generate the four transition frequencies corresponding to the four parity configurations, as per Eqn. 3.27, given a set maximum charge dispersion of 5 MHz. From this we extract the inner and outer peak separations and plot 1D and 2D histograms of these parameters, shown in Fig. 5.11.

We measure each mode independently over the course of the experiment run and obtain 10 hours of time series Ramsey measurements. From the fittable data, we extract the corresponding inner and outer peak separations and plot histograms, shown in Fig. 5.12. This consist of 868 individual Ramsey measurements for the Δ-mode, and 343 measurements for the Σ-mode. We note that in the measurements of the Δ-mode, as previously stated when discussing practical shortcomings, the drive detuning is less than half the maximum charge dispersion, and so outer peak separations above 7 MHz are not measurable. Despite this, since we know the maximum inner peak separation is half the maximum charge dispersion, from Eqn. 5.2, we can still obtain an approximate value of the maximum charge dispersion of the mode. In the Σ-mode measurements, we observe a distribution that is much more characteristic of what we expect, given the previous Monte-Carlo simulation in Fig. 5.11.

Through repeated Ramsey interferometry of the device, monitored over the course of 10 hours, we find a maximum dispersion of $\epsilon_{10}/h = 5$ MHz ($\epsilon_{01}/h = 10$ MHz) for the Σ-mode (Δ-mode). This is consistent with the order of magnitude of our predicted values of 4 MHz (4.1 MHz). The larger difference between ϵ_{10} and ϵ_{01} is due to asymmetries in the Josephson energies of the junctions, caused by fabrication imperfections, as shown in Fig. 3.10 (c).

5.5 Spatially Resolved Charge Detection

Offset-charge sensitive devices are used in investigations into the source of charge noise in superconducting qubit systems. An individual single-island charge-sensitive transmon device can be used as a detector of localised charge noise sources [35]. If we consider a mobile charge on the surface substrate, an offset-charge will be induced on the superconducting island, depending on how far away the charge is from the island. This presents a first order spatially resolved detection of a surface charge. However, with a single island device, only a singular dimension of locality can be ascertained, the distance between the charge and the island of the device.

In the charge-sensitive two-mode coaxial transmon device, the circuit has an additional superconducting island. This acts as a second detection antenna, allowing

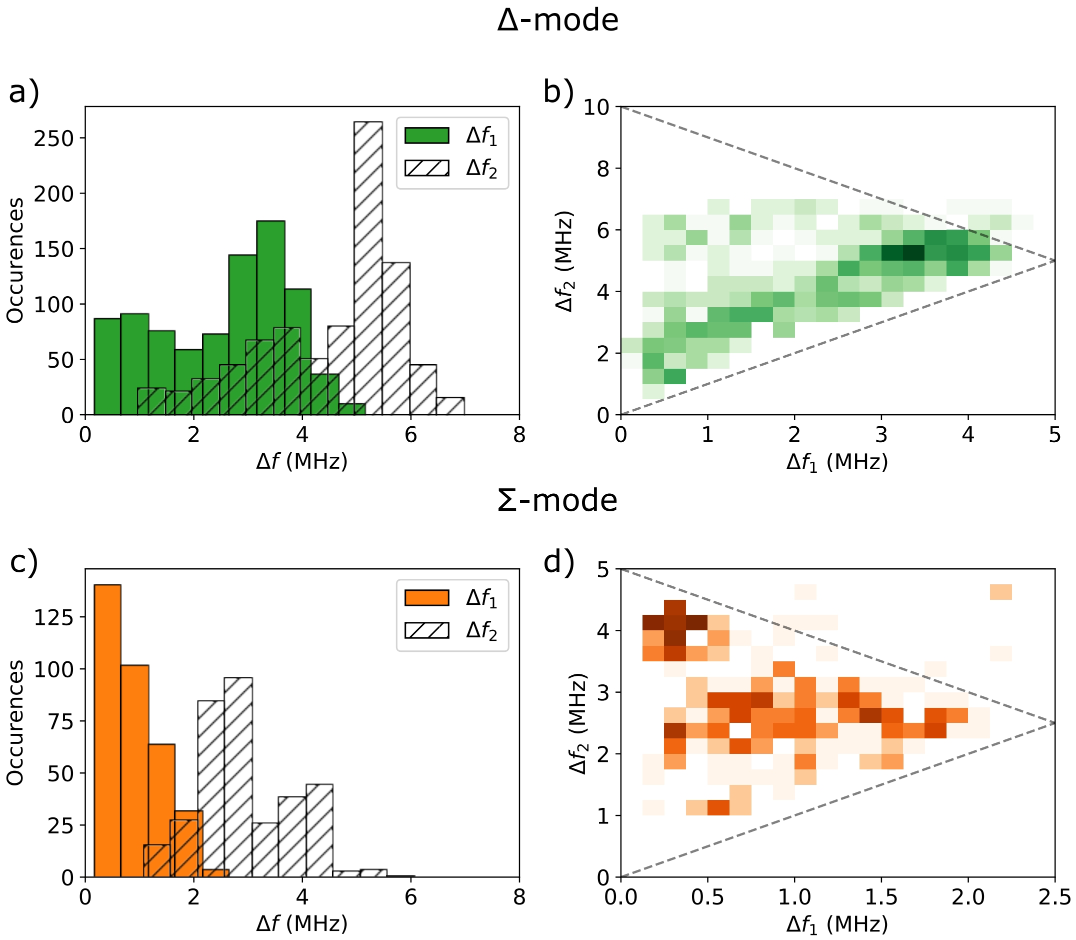

Figure 5.12: Statistical distributions of measured charge dispersion. (a) (c) Histograms of measured inner peak separation (Δf_1, solid) and outer peak separation (Δf_2, hatched). (b) (d) 2D histograms of the simultaneously measured inner and outer peak separations. Diagonal lines show region in which all possible measurements occur, given by the area between the line $y = x$, and $y = -x + \epsilon_{mn}$. From this we approximately extract the maximum charge dispersion.

an additional dimension of localisation in spatially resolving a surface charge.

In this section, we present a methodology of spatially resolving a surface charge using the previously presented Ramsey interferometry measurement.

5.5.1 Spatial Charge Sensitivity

Here we aim to simulate the charge bias induced by a point charge (1e) on the surface of the substrate. We note that unlike many architectures, the coaxial cQED architecture used here does not posses an on-chip ground plane. The qubit devices

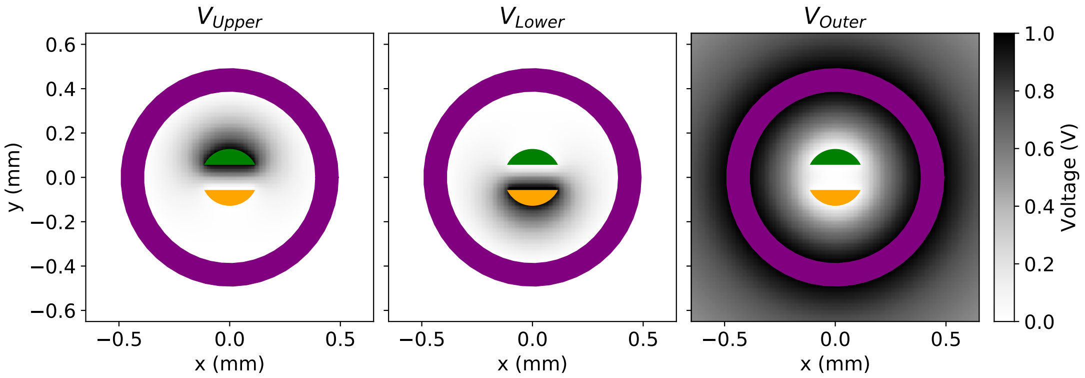

Figure 5.13: Simulated surface potential due to a 1V excitation on the upper (left), lower (middle) or outer (right) island of the device.

are floating on the surface of the substrate. The ground of the system is taken to be the aluminium sample holder in which the chip is placed. Since there is no direct galvanic connection between the sample holder and the on-chip circuitry, the capacitance of each island to the ground of the sample holder needs to be considered in these capacitance calculations.

Here we use an ANSYS Maxwell electrostatic simulation to obtain a capacitance matrix for the system, using the 3D model of the device and sample holder shown in Fig. 5.1. From this we obtain a capacitance to ground of $C = 200$ fF for the outer island to ground, and $A = 10$ fF for each of the inner islands to ground.

Following this, we simulate the potential on the surface of the substrate due to an excitation of 1 V on each of the islands. These simulation results are shown in Fig. 5.13. Using these results, we calculate the charge bias induced in the summation ($n_{g\Sigma}$) and difference ($n_{g\Delta}$) charge configurations as,

$$\begin{aligned} n_{g\Sigma} &= (\alpha V_{Upper} + \alpha V_{Lower} - \beta V_{Outer})/2, \\ n_{g\Delta} &= (V_{Upper} - V_{Lower})/2 \end{aligned}, \tag{5.3}$$

where $\alpha = C/(2A + C)$, $\beta = 4A/(2A + C)$, calculated using a four-island circuit model (including the ground). The factor of 1/2 is to rescale into units of (2e).

Using this calculation, in Fig. 5.14 we show the charge bias induced in each

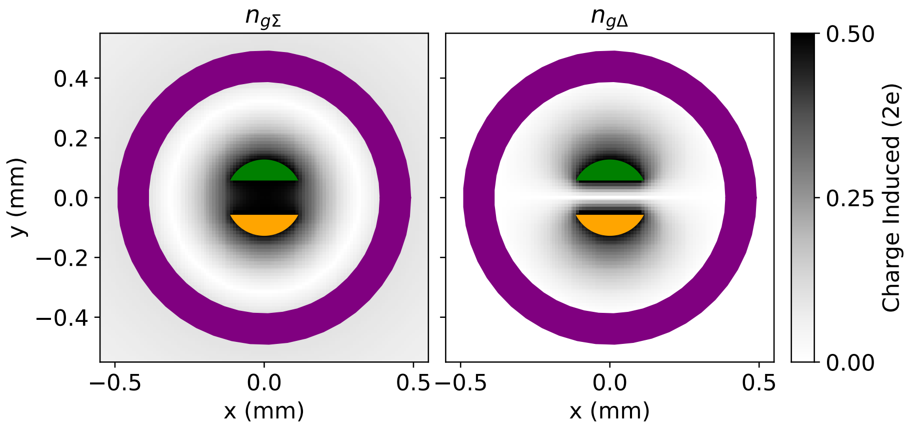

Figure 5.14: Simulation of charge bias induced by a point charge (1e) in the summation ($n_{g\Sigma}$, left), and difference ($n_{g\Delta}$, right) charge configurations on the two inner islands.

configuration due to the point charge on the surface of the substrate. We note that this is an assumption, and the same effect would be true of a wider surface charge distribution with a centre-of-charge at this point. In addition, we do not consider effects in the bulk of the substrate. We use this map of charge bias induced in time-series spatial tracking of charge configuration.

By taking the gradient of the scalar field of charge bias induced, we can identify the spatial sensitivity of the device, shown in Fig. 5.15. Observing the magnitude of this gradient in the upper two plots, the areas of high contrast show where a small movement of the surface charge will induce a large change in charge bias configuration. Since our Ramsey interferometry is relatively slow and takes approximately two minutes to acquire a single trace, depending on the velocity of the surface charge, the charge configuration can change during the course of the measurement and cause a poor signal acquisition. This can either manifest as very high instability of the frequency configuration over time, or the Fourier transform data not showing four clear peaks. We use this localised spatial sensitivity to make an argument for a potential source of charge noise in superconducting quantum devices.

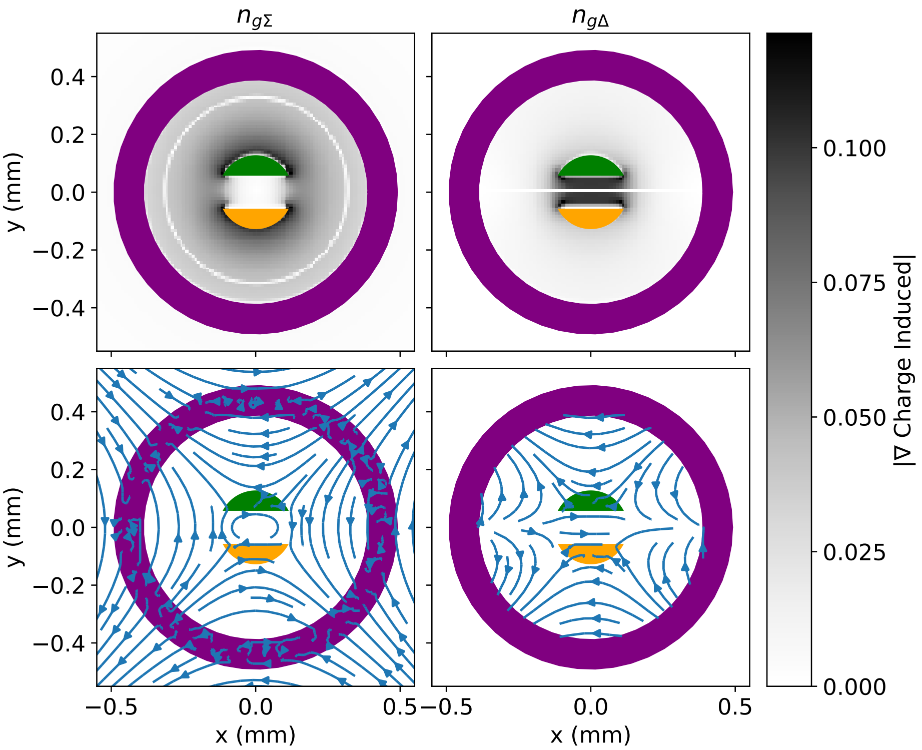

Figure 5.15: Spatial sensitivity of charge bias induced. (Upper) Magnitude of gradient of the charge bias induced plotted in Fig. 5.14. High contrast areas around the two inner islands show where a small movement of a surface charge can induce a largest change in offset charge configuration. (Lower) Streamline plot of the vector field $\vec{\nabla}$(charge induced) in the $n_{g\Sigma}$ and $n_{g\Delta}$ configurations.

5.5.2 Biangulation of Surface Charge Location

We now use the device to demonstrate a proof-of-concept detector of localised charge fluctuations. By repeating the Ramsey interferometry we can track the frequency dispersion Δf_1 and Δf_2, and using our tight-binding model, we are able to infer a time-series measurement of charge configuration of $n_{g\Sigma}$ and $n_{g\Delta}$. We find the expected spatial charge sensitivity of these sum and difference modes using an electrostatic simulation, shown in Fig. 5.14 (d) and (e). As the induced gate-charge offsets $n_{g\Sigma}$ and $n_{g\Delta}$ exhibit different spatial sensitivities, we can deduce the position of a potential surface-charge distribution centre on the device[3], using a biangulation method.

---

[3] We note that whilst localisation of a singular charge ($1e$) is discussed and used in modelling, experimentally the tracking is of an average of a distribution of many charges on the surface of the

For a given value of $n_{g\Sigma}$, we use the simulation data shown in Fig. 5.14 (left) to identify an area where a charge ($1e$) would induce a gate-charge offset of that value. We repeat this for a corresponding value of $n_{g\Delta}$ with the simulation data shown in Fig. 5.14 (right). The overlap of these two individually obtained areas allows us to identify the location of the centre of a charge distribution ($1e$) on the surface of the substrate. However, the precise quadrant in which the surface charge is located cannot be determined due to the symmetry of the system. As a result, the measured offset charge could be in any one of four equivalent locations on the surface of the substrate. Future devices could use three or more islands, and incorporate a symmetry breaking geometry, in order to more accurately triangulate surface charge position.

5.5.3 Time Series Measurements of Charge Configuration

We perform a demonstrative tracking experiment using repeated Ramsey interferometry measurement over a 150 minute period, as shown in Fig. 5.16, and Fig. 5.17. We observe both slow frequency drifts corresponding to fluctuating charge configuration, as well as a singular large frequency jump, indicative of non-equilibrium charge dynamics [69]. We convert the measured frequency dispersion to give a spatial estimation of charge location at time T = 0, T = 50, and T = 100 minutes, indicated by the dashed vertical lines on Fig. 5.16 (b).

From $T = 0$ to $T = 50$ minutes, we observe a slow drift in surface charge moving outwards away from the inner islands of the device. The uncertainty in position from $T = 50$ onwards is high, as the device is not sensitive to spatial fluctuations far from the two inner islands, shown by the lower gradient in the simulation of induced charge in Fig. 5.15. In this period we also observe a much clearer signal in the raw FFT data of Fig. 5.16 (a), consistent with the charge configuration remaining stable throughout the individual Ramsey oscillation measurement.

---

substrate, and cannot be concretely be attributed to the dynamics of a single charge.

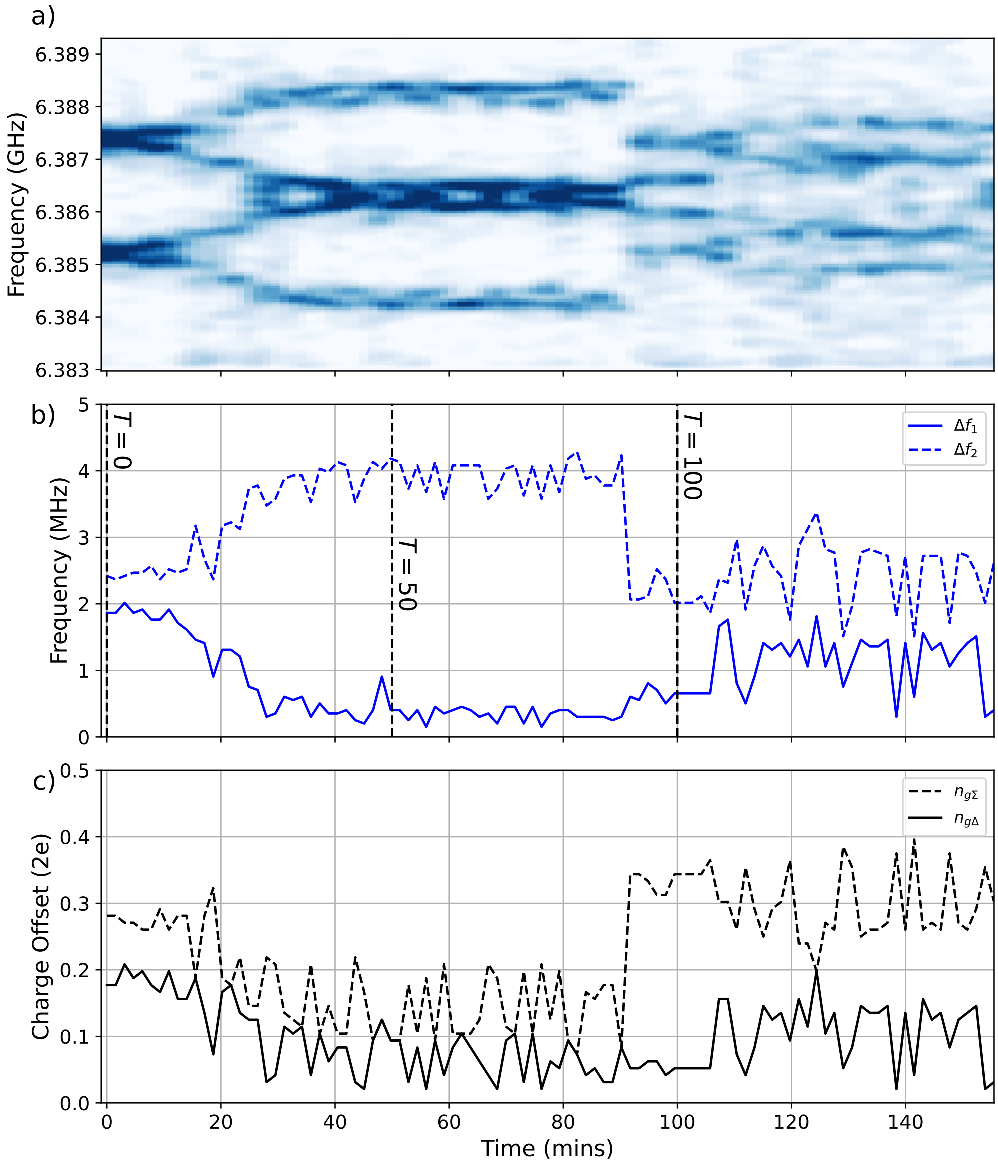

Figure 5.16: Time series measurement of charge dispersion. (a) Fourier transform of repeated Ramsey oscillation experiments performed on the Σ-mode, over a period of 2.5 hours as shown in Fig. 5.9. (b) Tracking of inner frequency peak separation (solid line), Δf_1, and outer frequency peak separation (dashed line), Δf_2, from time series measurement shown in (a). Black vertical dashed lines highlight $T = 0$ mins, $T = 50$ mins and $T = 100$ mins. (c) Gate charge offsets $n_{g\Sigma}$ (dashed), $n_{g\Delta}$ (solid), extracted from peak separations using Eqn. 5.2. Figure from [38].

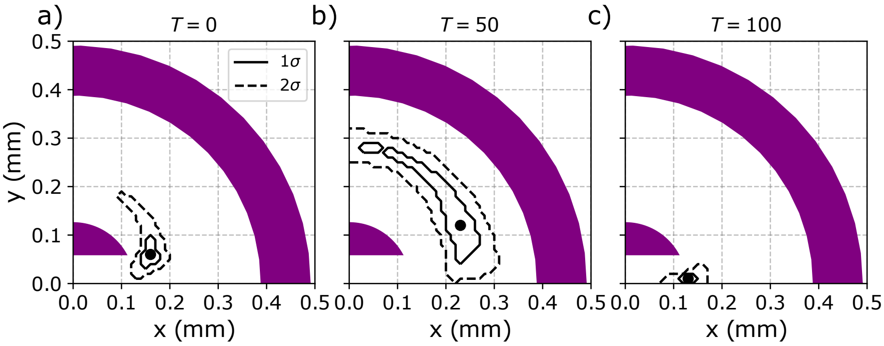

Figure 5.17: Spatial charge tracking. (a), (b), (c) Mapping of charge configuration to physical location of charge distribution centre on substrate at highlighted times shown in Fig. 5.16 (b). Uncertainty in position due to error in fitting of Fourier transform data, shown for 1σ (solid line) and 2σ (dashed line), with the most likely position indicated by the black dot. One quarter of the device is shown due to the four-fold symmetry of the system. Figure from [38].

From $T = 100$ onwards, we observe a shift in the surface charge distribution towards the two inner islands of the device. In this region, we have a much higher spatial resolution, shown by the larger gradient in simulation of induced charge from Fig. 5.15. As such, any small movement in surface charge distribution will cause a larger shift in charge configuration of the device. We observe this as a noisier measurement of frequencies shown in Fig. 5.16 (b). This is also shown in the raw FFT data where the peaks are less clear in this region, consistent with the charge configuration changing during the course of the measurement. With an improved measurement rate, this detector could be used for observing spatial charge fluctuations with a resolution of less than 100 μm.

5.6 Conclusion and Outlook

In this Chapter, we have investigated charge sensitivity in a two-mode transmon. Our results show observations of multiple charge parity configurations, and show agreement with a predictive theory for charge sensitivity using a tight binding approximation. In addition, we show this sensitivity can be suppressed for high coherence quantum computing applications.

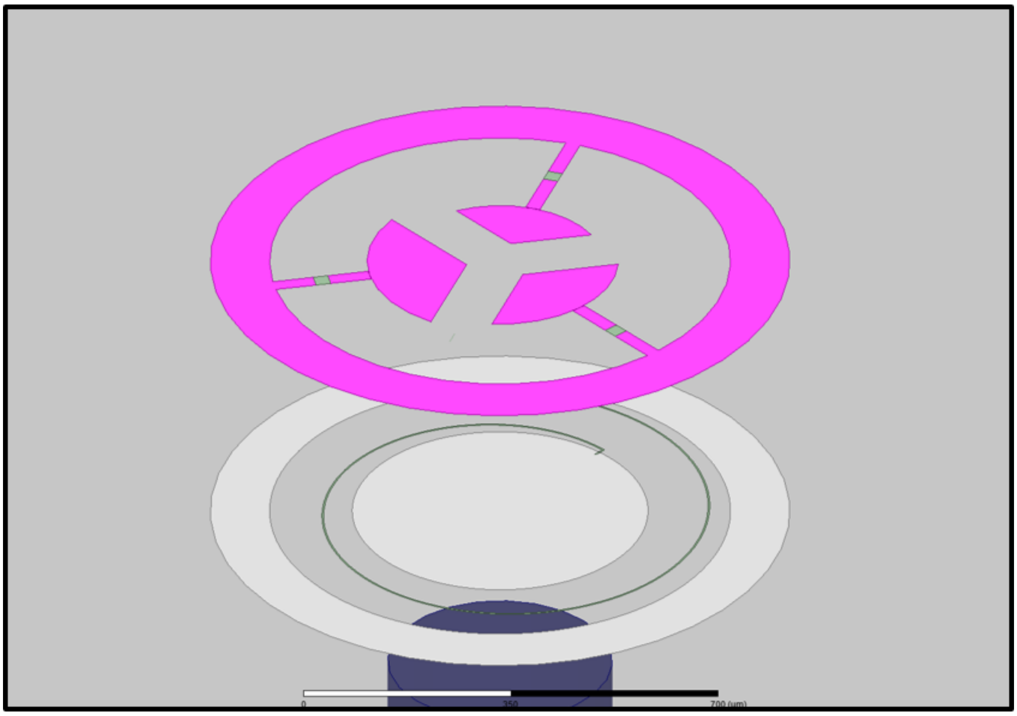

Figure 5.18: Illustration of an asymmetric 3-island multi-mode coaxial transmon (purple) and readout resonator (white) unit cell, designed for the triangulation of surface charge.

We use a two-mode device in the charge-sensitive regime to demonstrate proof-of-principle spatially-resolved charge detection. Combining a similar device with high fidelity state readout in future would enable detection of parity jumps between three-superconducting islands, and determine how quasi-particle tunnelling events affect energy dissipation in multiple modes. If local control of static electric field were incorporated in a future device via gate electrodes, it would become possible to unambiguously translate frequency fluctuations to precise charge configurations, for precise detection of local differential charge-noise vs. global charge-noise. We hence propose such multi-mode charge-sensitive qubits as potentially powerful tools for ongoing investigations into sources of decoherence in superconducting quantum devices.

By performing a time-series measurement of charge configuration, we observe the two main characteristics of measurements of charge sensitive transmon devices. We observe a sudden jump in charge configuration, previously investigated and attributed to ionising radiation [36]. Whilst our model attributes the observed slow drifts in the charge configurations to movement of a charge on the surface of the substrate, it is more likely to be the result of a movement of a distribution of charges on the surface of the substrate. This movement of charge distribution is in contrast to previous postulates of a uniform flux of charge incident upon the device [35]. We argue that the varying stability in measured frequency configuration and identified areas of high spatial sensitivity from our simulation further suggest this. When the surface charge is identified to be closer to the centre of the device, the frequency configuration is observably less stable over time, whereas when the charge is located closer to the outer island, the configuration is more stable.

This conclusion prompts further investigation into this source of decoherence with an optimised multi-mode device. A limitation of the symmetry of the device is that we are unable to localise a charge beyond a single quarter of the device. In addition, the Ramsey interferometry measurement methodology is very slow due to the averaging required to obtain good signal to noise ratio. We suggest a further investigation into tracking of surface charge could utilise a three-island multi-mode device with asymmetric islands, as shown in Fig. 5.18. This would allow for a more direct triangulation of the suspected surface charge distribution movement, and further suggest methods of mitigation in future superconducting circuit devices. There is a trade-off with the added circuit complexity and asymmetry. The device has three modes, with eight parity configurations for each transition, making Ramsey interferometry measurements challenging.

Chapter 6

Extension to Multi-Qubit Circuits

In previous chapters, we introduced the concept of the two-mode coaxial transmon, and the behaviour and operation of the unit-cell. We demonstrated how charge-noise affects these systems and how to mitigate against these sources of decoherence. Whilst it is important to understand these systems at a small scale, ultimately our aim is to create large arrays of qubits and be able to demonstrate multi-qubit interactions across an array of devices, utilising the tileability of the coaxial cQED architecture. This paves the way to using these two-mode coaxial transmons as useful computational devices, and reducing errors in superconducting quantum devices by exploiting the characteristics of the multi-mode system.

In this chapter, we present experimental results on statically-coupled two-mode coaxial transmon qubits in which we utilise spatial symmetries to introduce highly mode-selective coupling. We demonstrate an all-microwave activated conditional phase interaction with the potential to generate a fast entanglement operation between computational modes. Through simultaneous readout of both computational and ancillary modes, we show minimal leakage outside of the computational basis due to the entanglement operation.

6.1 Device Design

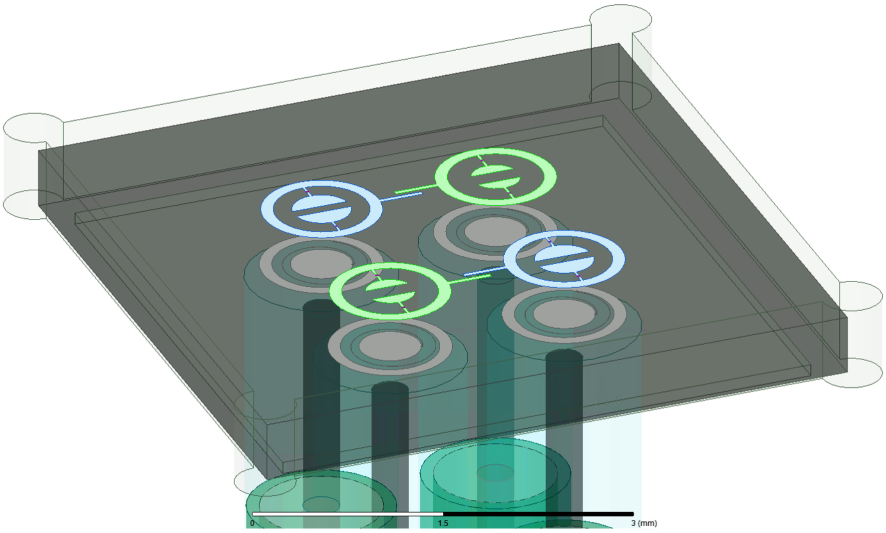

Figure 6.1: 3D model of the coupled two-mode coaxial transmon device. QA (blue) has dimensions: inner island radius = 240 μm, inner island gap = 90 μm. QB (green) has dimensions: inner island radius = 200 μm, inner island gap = 150 μm. Both devices have the same outer island geometry, with inner radius of 389.5 μm, and outer radius of 489.5 μm. Overlapping arm capacitors (separation = 40 μm, overlap = 100 μm), provide coupling between outer islands.

To introduce a coupling between the two two-mode coaxial transmon devices, we use two overlapping arms to introduce a capacitance between the outer islands of the devices. In a similar fashion to other coupled coaxial transmon devices [159], this introduces an exchange interaction of strength J, dependent on the size of the capacitance. As outlined in Chapter 3, this is how we implement a selective coupling between the two higher frequency, quadrupole-like, modes of the system. Since the outer island does not participate in the lower frequency, dipole-like, modes of the system, we do not expect them to have any direct coupling due to this additional capacitance introduced.

The device and sample holder are simulated using ANSYS HFSS, using the 3D model shown in Fig. 6.1. Eigenmode simulations are performed to identify the four transition frequencies, with subsequent EPR calculations using the simulated fields

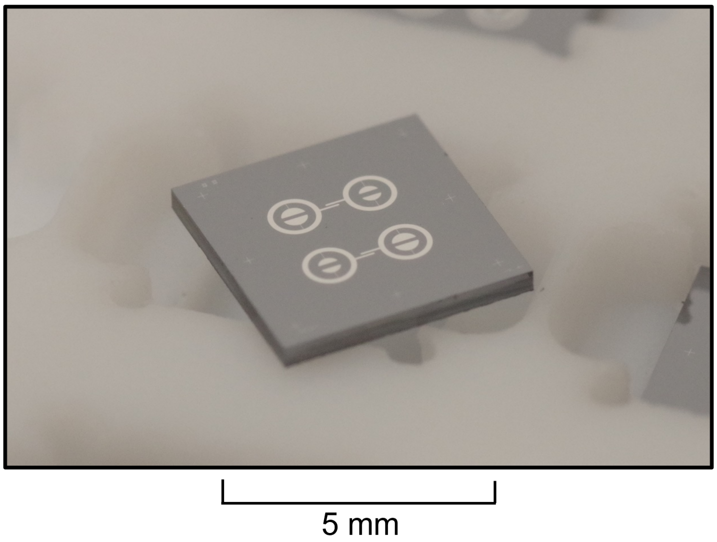

Figure 6.2: Photograph of the measured two-mode coaxial transmon device. Fabricated chips have two pairs of qubits, with nominally identical parameters.

to obtain self and cross-Kerr shifts, using the methodology outlined in Appendix B. We design this system with the intention of implementing the ancillary transition driven microwave activated phase gate (AT-MAP) previously introduced, targeting the resonance condition $\omega_\Sigma = \omega_{\Sigma'}$ (ancillary transitions on resonance). Target junction inductances of $L_J = 9$ nH (11 nH) ($E_J = 18$ GHz (14.5 GHz)) are identified and used in the simulations to obtain the transition frequencies of QA (QB). The parameters obtained from these simulations are shown in Table 6.1 (on page 136).

Once designed, we fabricate the device using the same process as the device in Chapter 4. We use photolithography to pattern large scale features (qubit islands, coupling arms, and readout resonators) on both sides of a 0.5 mm thick silicon wafer. Electron beam lithography is then used to pattern the smaller Josephson junction features. Following this process, the wafer is diced into 5×5 mm chips (shown in Fig. 6.2), where a suitable candidate for measurement is selected using room temperature resistance measurements. Once identified, the chip is mounted inside an aluminium sample holder within a μ-metal magnetic and light-tight shield, anchored to the 20 mK stage of a dilution refrigerator, operating with a standard cQED experimental

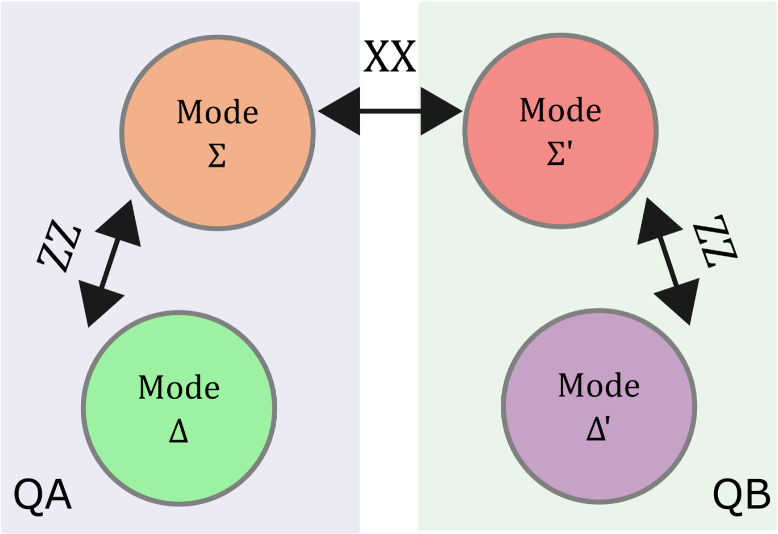

Figure 6.3: Labelling and colour scheme of the coupled two-mode coaxial transmon system. Arrows show the engineered type of coupling between each mode. We highlight the Δ-mode and Σ-mode of QA in green and orange (as in previous chapters), and highlight the $\Delta^{'}$-mode and $\Sigma^{'}$-mode of QB in purple and red respectively.

setup, outlined in Appendix C.

For consistency and clarity with notation, we label one two-mode coaxial transmon QA, with corresponding it's Δ-mode and Σ-mode (as previously defined). The second two-mode coaxial transmon we label QB, and it's corresponding modes $\Delta^{'}$-mode and $\Sigma^{'}$-mode. This labelling structure and corresponding colour identification is outlined in Fig. 6.3. Recall that in this architecture, we identify the Σ-modes as our ancillary (or communication) transitions, and the Δ-modes as the protected computational modes.

6.2 Readout Characterisation

We perform continuous wave (CW) spectroscopy measurements in the low power regime to obtain the parameters of each readout resonator. We fit the real and imaginary part of each signal using Eqn. 4.4, plotting the corresponding data and fits in Fig. 6.4. We find the resonant frequency of $\omega_r/2\pi = 8.204$ GHz ($\omega_r/2\pi = 8.676$ GHz), with a linewidth of $\kappa_r/2\pi = 500$ kHz ($\kappa_r/2\pi = 470$ kHz) for QA (QB). Notably,

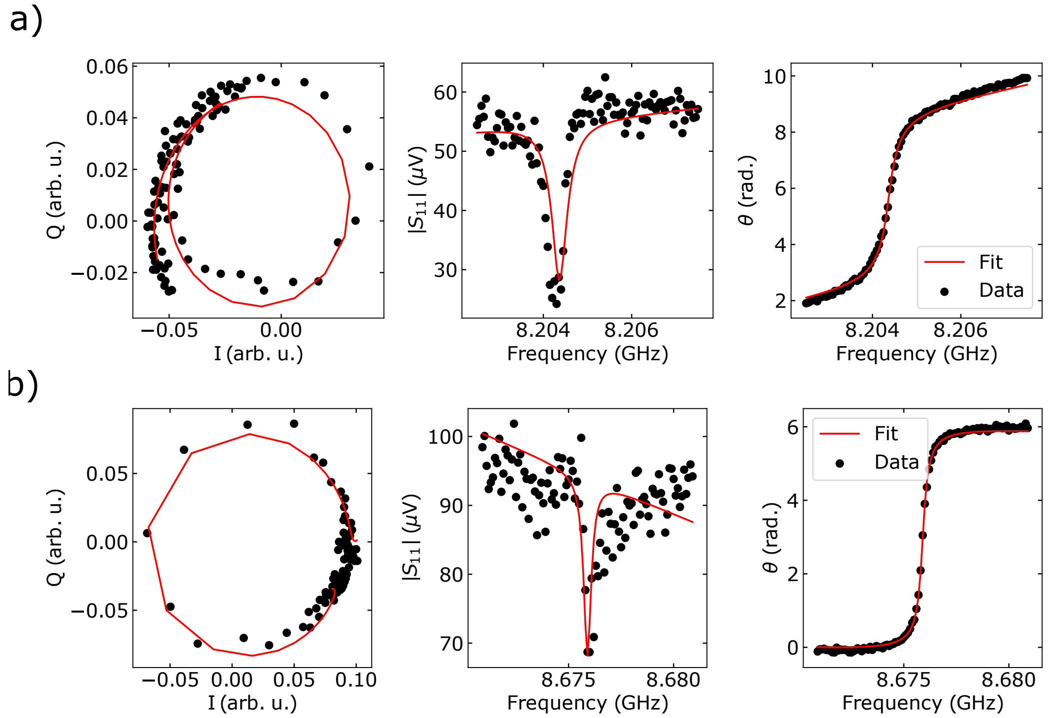

Figure 6.4: Measured resonator complex (left), magnitude (centre) and phase (right) responses for QA (a) and QB (b). Data (black) is fitted to Eqn. 4.4 (red). From this fitting we extract internal quality factors $Q_0 = 67000$ ($Q_0 = 134000$), with external quality factors $Q_e = 22000$ ($Q_e = 21000$) for QA (QB), reported to the nearest thousand.

the linewidths are much smaller than the previous devices measured.

In Fig. 6.5, we show the readout resonators phase responses when the modes of the two-mode coaxial transmons are prepared in the excited state. From this, we extract the state dependent shift of the modes and corresponding resonators χ_{ir}, shown in Table 6.1. Due to the ratios of $\chi_{\Sigma r}/\chi_{\Delta r}$ and χ_{ir}/κ_r, we are able to identify a frequency for which we can optimally simultaneously readout both modes of each device. This is shown in the IQ plane plot of Fig. 6.5, where the angle between the $|10\rangle$, $|00\rangle$ and $|01\rangle$ state signal distributions is 90°. When performing experiments, we can calibrate to identify the signal rotation required such that the measurement of one mode is in the real axis, and the measurement of the other mode is in the imaginary axis. This is beneficial when we characterise entanglement operations and

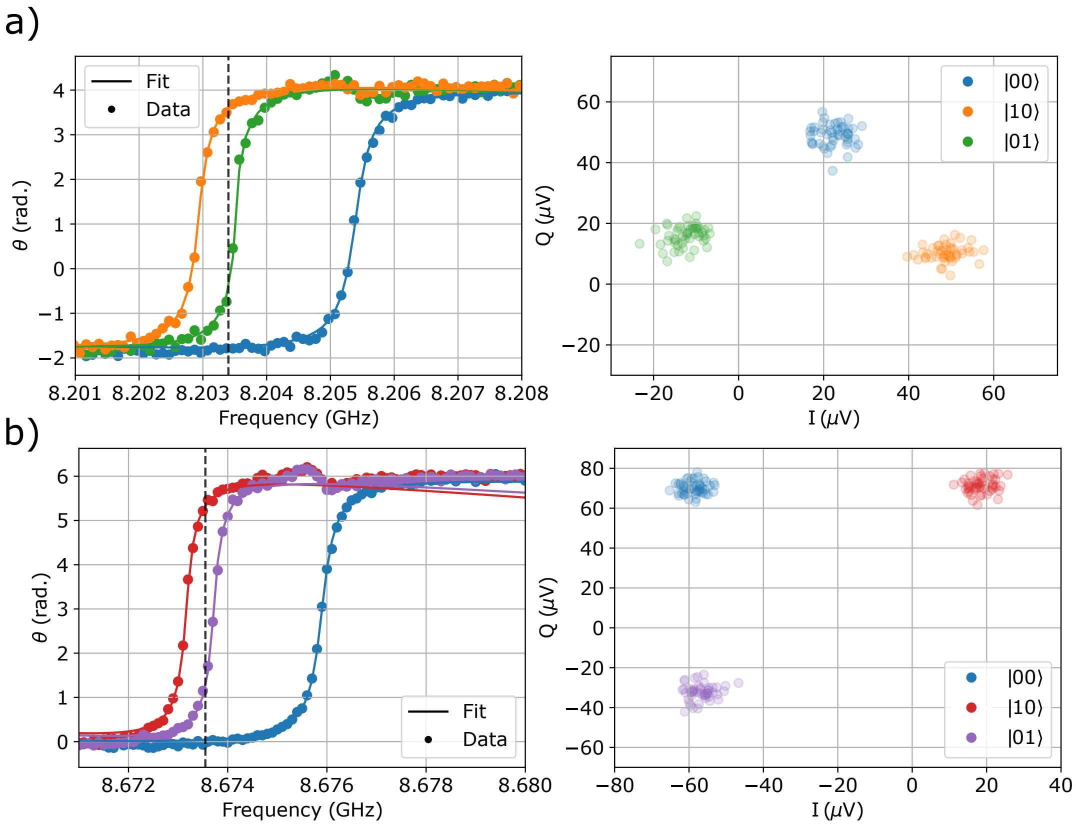

Figure 6.5: (Left) Phase response of the readout resonator as a function of the two-mode coaxial transmons (QA upper, QB lower) being prepared in the $|00\rangle$, $|10\rangle$ and $|01\rangle$ state. Vertical dashed lines show chosen readout frequency for simultaneous readout. Data (dot) is fitted (line) to Eqn. 4.4. (Right) IQ plane distributions of readout signals measured when the two-mode coaxial transmon is prepared in the $|00\rangle$, $|10\rangle$ and $|01\rangle$ state, and the readout resonator is probed at the frequencies indicated in (left).

wish to show minimal leakage outside the computational subspace.

6.3 Hamiltonian Parameters

Using qubit spectroscopy methods previously introduced, we are able to identify the transition frequencies for each of the modes of the system. For Qubit A (Qubit B), we find the transition frequencies to be $\omega_\Delta/2\pi = 3.89$ GHz and $\omega_\Sigma/2\pi = 5.13$ GHz ($\omega_{\Delta'}/2\pi = 4.21$ GHz and $\omega_{\Sigma'}/2\pi = 5.24$ GHz), with anharmonicities of $\eta_\Delta/2\pi = -90$ MHz and $\eta_\Sigma/2\pi = -140$ MHz ($\eta_{\Delta'}/2\pi = -150$ MHz and $\eta_{\Sigma'}/2\pi = -200$ MHz). By identifying the $|00\rangle - |11\rangle$ transition for each device, we are obtain the cross-Kerr shifts $\chi_{\Sigma\Delta}/2\pi = 240$ MHz and $\chi_{\Sigma'\Delta'}/2\pi = 320$ MHz for Qubit A and Qubit B respectively. With these parameters we approximately achieve the resonance condition for the AT-MAP interaction $\omega_{\Sigma} - \chi_{\Sigma\Delta} \approx \omega_{\Sigma'} - \chi_{\Sigma'\Delta'}$.

Using a numerical simulation [171], we construct and estimate for the Hamiltonian parameters E_J, E_C and E_p, which are summarised in Table 6.1. As shown in the table, the extracted values of E_J are approximately 20% and 25% lower than what was designed and simulated. As a result, the E_J/E_C ratios, also listed in Table 6.1, are sufficiently low that the modes are weakly and measurably charge-sensitive ($\epsilon_{01/10} \sim 100$ kHz). We observe this in Ramsey oscillations, shown in Section 6.4.2.

6.4 Coherence Characterisation

6.4.1 Energy Relaxation

In order to measure the energy relaxation rate ($\Gamma_1 = 1/T_1$) of each mode, we use a calibrated X_π pulse to prepare the mode in the excited state, then wait a delay period Δt, before reading out the state. The pulse sequence is illustrated in Fig. 6.6 (a). We perform this measurement on each mode individually.

We repeat this measurement ~ 100 times in order to build statistics, and plot the measured traces for each mode in Fig. 6.6. As expected the traces follow an exponential decay, which we fit to an equation of the form $S(\Delta t) = a + be^{-\Delta t/T_1}$, in order to extract the energy relaxation time T_1.

The histograms of extracted T_1 values for each respective mode are plotted in Fig. 6.6. As with previous experiments, the two Δ-modes have a lower energy relaxation rate due to the symmetry of the electric fields and weaker coupling to the loss mechanisms of the readout resonator and coaxial control port. The quadrupole-like Σ-modes both have similar values and distributions of energy relaxation rates, shown in Fig. 6.7.

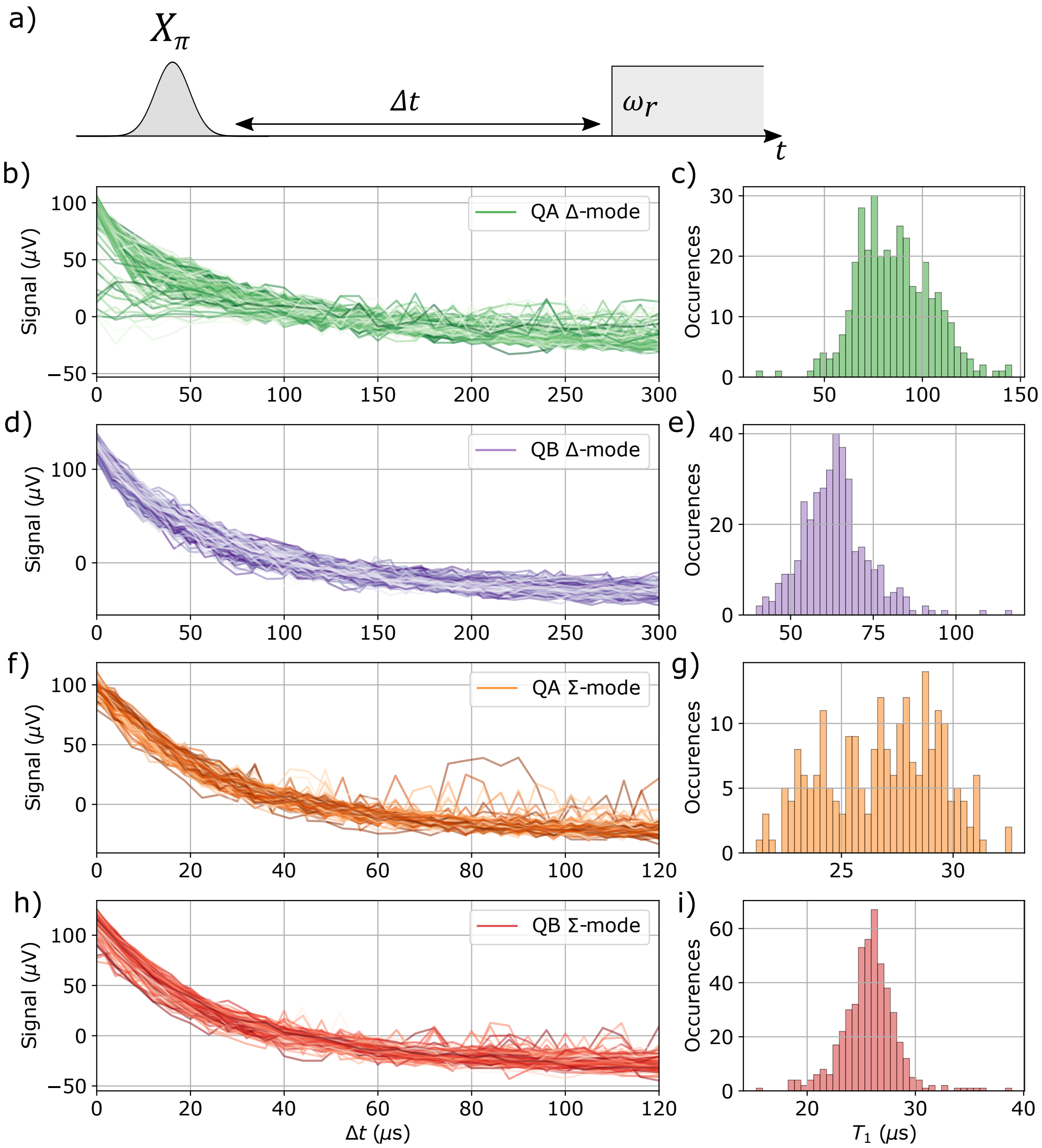

Figure 6.6: (a) Pulse scheme of the energy relaxation rate measurement. (Left) Resulting traces from multiple measurements of the energy relaxation rate of each mode labelled. (Right) Histogram of extracted T_1 calculated by fitting each trace (left) to an exponential decay of the form $S(\Delta t) = a + be^{-\Delta t/T_1}$, where a and b are constant amplitude and offsets.

As previously discussed, the distribution of measured T_1 varies with time in these longer measurements, as two-level-systems and loss channels reconfigure [180]. We report the arithmetic mean of the extracted T_1 values, and standard deviation σ, summarised in Table 6.1. Whilst we report these values, we note that the presented

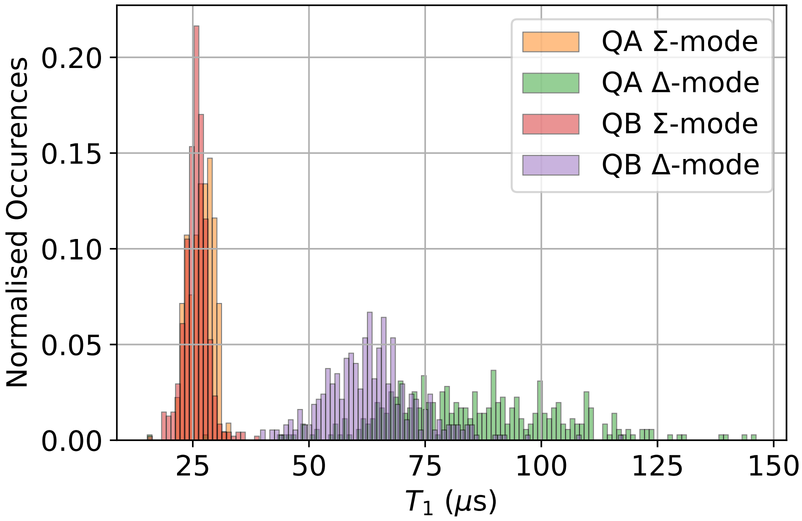

Figure 6.7: Combined normalised histograms of extracted T_1 values from each mode of the coupled two-mode coaxial transmon device.

distributions provide more detailed insights into the dynamics of the energy relaxation properties of the modes.

6.4.2 Ramsey Oscillations

We measure the transverse relaxation rate $1/T_2^* = 1/2T_1 + 1/T_\phi$ using a Ramsey oscillation measurement. Using a calibrated $X_{\pi/2}$ pulse amplitude and detuned drive frequency, we prepare the mode in a superposition state, and allow it to evolve for a time Δt. We then return the state to the measurement basis with a second detuned $X_{\pi/2}$ pulse, before measuring. This is shown in the pulse sequence in Fig. 6.8 (a). When Δt is varied, we expect the resulting signal to follow a decaying oscillation, with the frequency of the oscillation corresponding to the detuning between the control pulse and transition frequency.

Whilst the devices were designed to be insensitive to charge noise, we resolve a charge dispersion of roughly 50 kHz for the modes of Qubit A, and 200 kHz for the modes of Qubit B. This is due to the Josephson energies, E_J, of the fabricated devices being lower than what was designed. In later measurements, we use the Δ-mode of

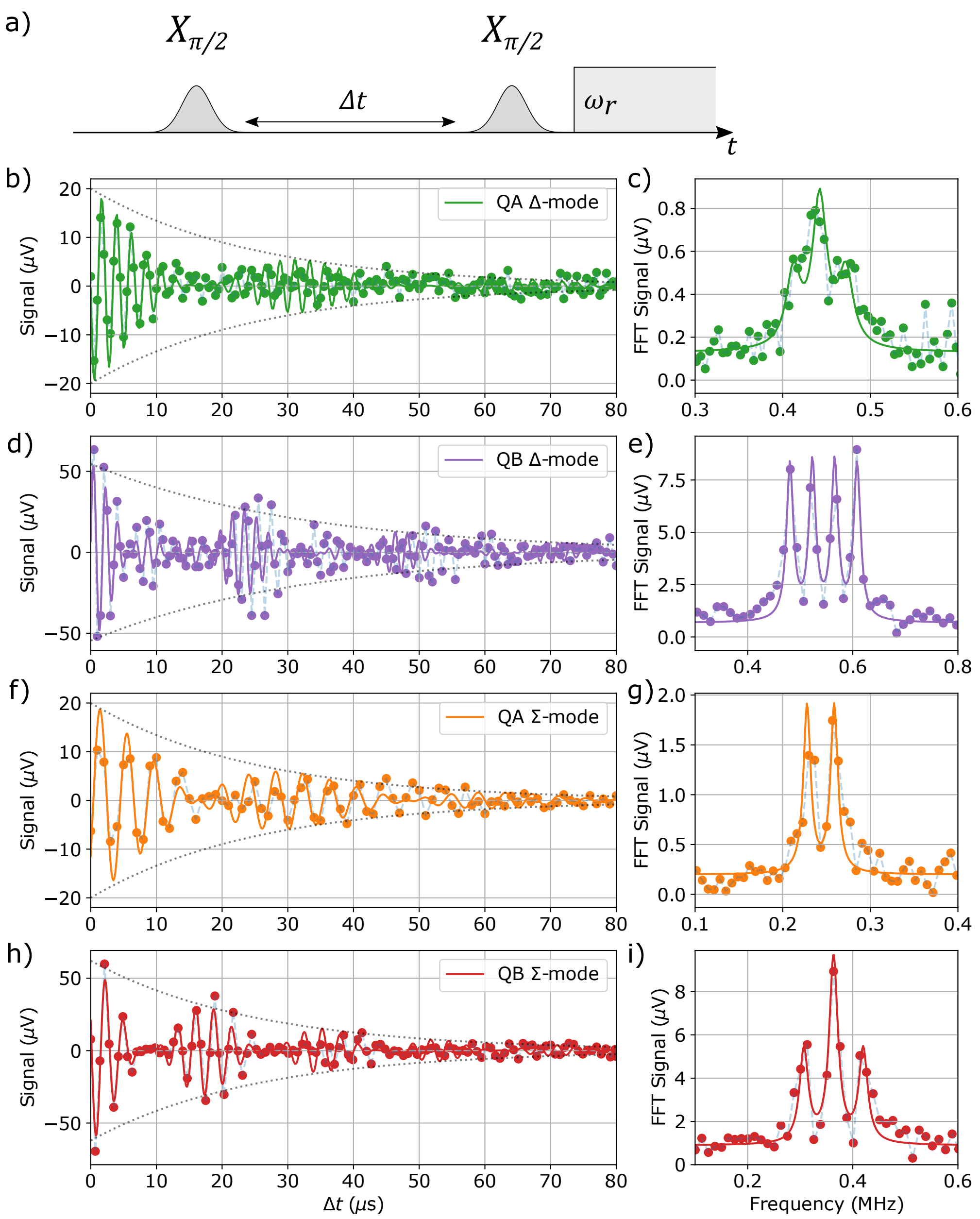

Figure 6.8: (a) Pulse sequence for the transverse relaxation rate measurement. (Left) Example measured Ramsey oscillation traces. Data (dots) is fitted (line) to the product of an exponential decay sum of four cosinusoidal oscillations. The decay constant and frequency components are extracted from the fitting of the Fourier transform data. (Right) Fast Fourier transform of the Ramsey oscillation (left). Data (dots) is fitted (lines) to the sum of four equal Lorentzian lineshapes, symmetric about the mean detuning. This method is presented in further detail in Chapter 5.

QA as a target mode, since it has the lower charge dispersion of the two computational modes. We do not perform thorough measurements of charge dispersion and charge-offset configuration tracking in this experiment, as we did in the previous chapter, hence quoted values of charge dispersion are approximate.

In Fig. 6.8, we show examples of the Ramsey oscillation measurements, and corresponding fast Fourier transforms (FFT), as in Chapter 5. We note that the dispersion measured here is an order of magnitude smaller than the designed charge-sensitive device previously presented (MHz), due to the engineering of the capacitance of the device. From the measured decaying oscillation, we first fit the FFT data to a sum of four Lorentzian lineshapes (of equal linewidth), symmetric about the mean detuning between the drive frequency and transition frequencies. We use the extracted frequencies and linewidth as the frequency components and decay constant to fit to the Ramsey oscillation data. The indicated dotted line illustrates the decay envelope corresponding the the extracted linewidth, showing a decay constant of $T_2^* = 25\ \mu$s for each mode ($T_2^* = 32\ \mu$s for QB Δ-mode). Since these modes are weakly charge-sensitive, we do not report repeated fitting or statistics of Ramsey dephasing rates.

6.4.3 Spin-Echo

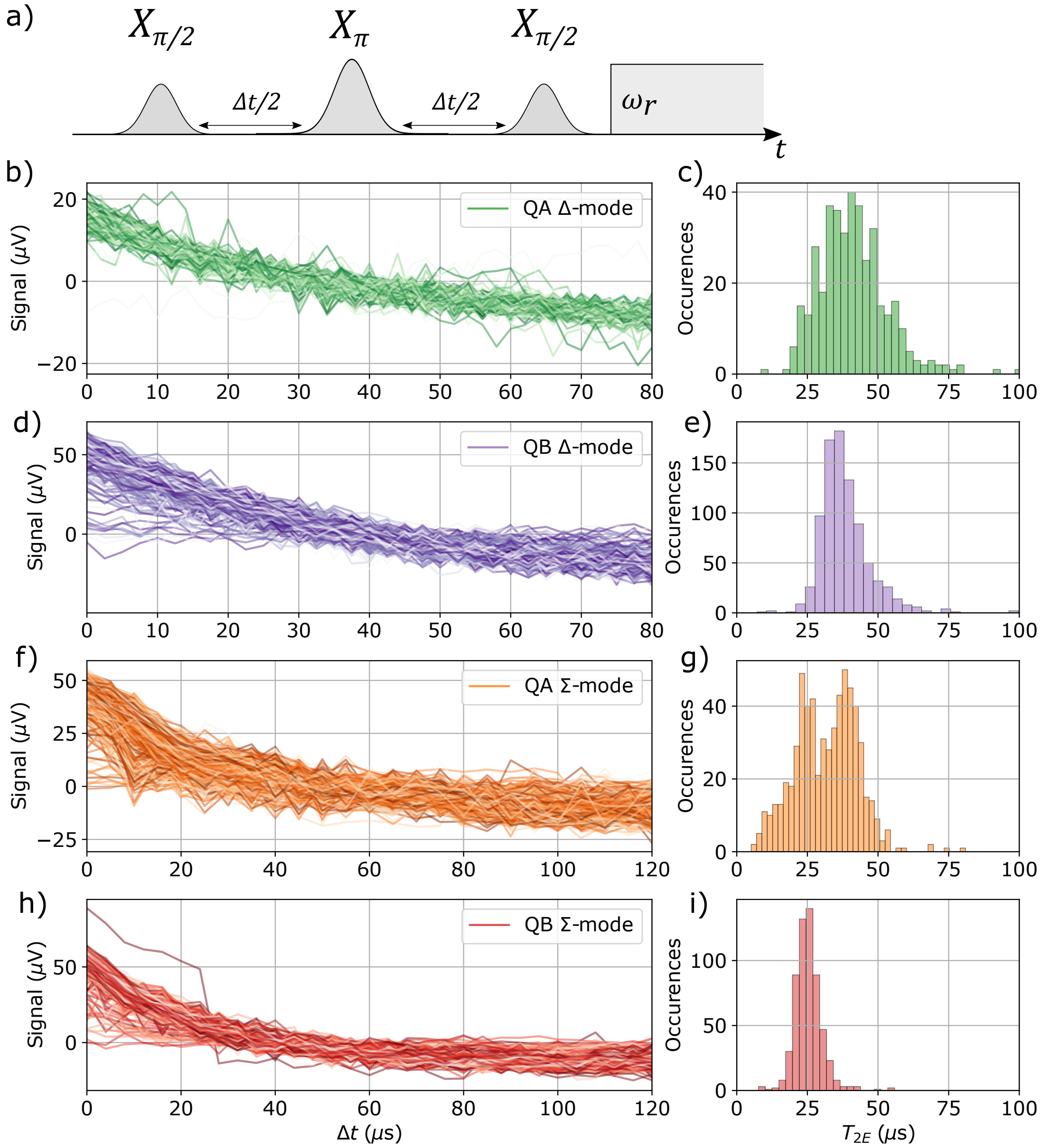

Figure 6.9: (a) Pulse sequence of the Spin-Echo coherence measurement. (Left) Measured traces from repeated Spin-Echo experiments. Data is fitted to an exponential decay, from which the coherence time T_{2E} is extracted. (Right) Histograms of extracted T_{2E} values. Modes labelled as per the colour scheme in Fig. 6.3.

The Ramsey oscillation method of measuring transverse relaxation rate is susceptible to quasistatic noise (over the scale of Δt). As previously, we introduces an "echo" pulse at the midpoint of the free evolution to refocus inhomogenous contributions to dephasing. The pulse sequence is shown in Fig. 6.9 (a). The resulting signal measured as a function of Δt follows an exponential decay.

In Fig. 6.9, we show the measured spin-echo traces for each of the four modes. These traces are fitted to an exponential decay of the form $S(\Delta t) = a + b e^{-\Delta t/T_{2E}}$, from which the coherence time T_{2E} is extracted. In Fig. 6.9 we also show the histograms of the extracted T_{2E} values. We report the arithmetic means and standard deviations, shown in Table 6.1.

We once again note that the extracted coherence times T_{2E} are below the fundamental limit of $2T_1$, however the Δ-mode coherence times are larger than the estimated Ramsey decay $T_2^* \approx 25\ \mu\text{s}$. Firstly, this suggests that the modes are susceptible to high frequency noise sources, such as photon shot noise from the readout resonator. Secondly, this suggests that, in this device, charge noise is a notable source of decoherence. Further design and optimisation work is required to tune the coupling of the qubit modes to the resonator to improve coherence [30], and reduce the sensitivity to charge noise [38] (the latter can be achieved by increasing the Josephson energy E_J as was designed).

6.5 Device Parameters

We summarise the results of the characterisation measurements performed on individual modes in Table 6.1.

We note there is a large disparity between the target frequencies and measured frequencies. This is due to Josephson energies obtained through fabrication of devices in this particular wafer being lower than what was designed. Whilst this can sometimes occur due to the sensitivity of the fabrication process, we note that the effects we wish to investigate are insensitive to global variations in fabricated frequencies. What is important is the local variation in Josephson energies, since asymmetry introduces unwanted coupling, and resonance conditions may be missed. In our process, the chip

Table 6.1: Device Parameters

Device:	QA Sim.	QB Sim.	Qubit A	Qubit B
LC Resonator				
Frequency f_r (GHz)	-	-	8.20	8.68
Linewidth $\kappa_r/2\pi$ (kHz)	-	-	500	470
Dispersive Shift $2\chi_{\Delta r}/2\pi$ (MHz)	-	-	1.9	2.1
Dispersive Shift $2\chi_{\Sigma r}/2\pi$ (MHz)	-	-	2.5	2.7
Δ - Mode				
Transition Frequency $\omega_\Delta/2\pi$ (GHz)	4.48	4.95	3.89	4.21
Anharmonicity $\eta_\Delta/2\pi$ (MHz)	86	150	90	150
T_1 (μs)	-	-	86 (19)	63 (10)
T_2 Echo (μs)	-	-	41 (13)	39 (10)
Σ - Mode				
Transition Frequency $\omega_\Sigma/2\pi$ (GHz)	5.96	6.01	5.13	5.24
Anharmonicity $\eta_\Sigma/2\pi$ (MHz)	170	170	140	200
T_1 (μs)	-	-	27 (3)	26 (3)
T_2 Echo (μs)	-	-	32 (11)	25 (6)
Cross Kerr Shift $\chi_{\Sigma\Delta}/2\pi$ (MHz)	230	320	240	320
E_J (GHz)	18	14.5	14.5	11
E_C (GHz)	0.21	0.29	0.21	0.29
E_p (GHz)	0.12	0.11	0.11	0.13
E_J/E_C	86	50	69	38
E_p/E_C	0.57	0.38	0.52	0.45

level spread of Josephson energies is 2 % [161], corresponding to a frequency spread of approximately ±50 MHz.

6.6 Mode-Selective Coupling

With the basic parameters of each mode characterised, we move on to measuring the coupling between the four modes.

6.6.1 Conditional Ramsey Oscillations

In order to measure the state-dependent frequency shift between modes (χ_{ij}), we employ a method of conditional Ramsey interferometry. As with previous Ramsey experiments, we can use these measurements to precisely identify transition frequencies, since the frequency of the oscillations is given by the detuning between the drive frequency and transition frequency.

The pulse sequence we employ in these measurements is shown in Fig. 6.10 and 6.11 (a). In each measurement of frequency shift we perform the experiment twice. The first with the control mode prepared in the ground state (indicated by the identity gate I in the pulse scheme), before measuring the Ramsey oscillation on the target mode. In the second measurement, we prepare the control mode in the excited state using an on-resonant calibrated X_π pulse, before running the same Ramsey oscillation measurement on the target mode. In each case, the $X_{\pi/2}$ control pulses on the target mode are at the same frequency, detuned from the calibrated transition frequency by approximately 500 kHz.

The difference between the two frequencies of the Ramsey oscillations yields the state-dependent frequency shift χ_{ij} between the target and control modes. For two transmon modes that are transversely coupled (as in the case of the two ancillary Σ-modes), recall from Eqn. 2.21 that the frequency shift is related to the exchange interaction strength J via,

$$\chi_{ij} = \frac{2J^2(\eta_i + \eta_j)}{(\Delta_{ij} + \eta_i)(\Delta_{ij} - \eta_j)}, \tag{6.1}$$

where Δ_{ij} is the detuning between the modes i and j, and η is the respective anharmonicity. From the measurement of $\chi_{\Sigma\Sigma'}$, we are able to extract the exchange interaction strength J. Note that this equation is only true of modes with a purely transverse coupling between them, and the resulting χ_{ij} is a perturbative cross-Kerr shift.

As discussed previously, the modes of this particular system are weakly charge sensitive. This can lead to complications when conducting Ramsey based measurements, as illustrated in Fig. 6.8. In these measurements, we perform the Ramsey oscillation sequence on the modes of QA (using them as the target modes), since it has the lower charge dispersion of the two devices. We ensure that the sequence length is sufficient to resolve the corresponding frequency components of the Fourier transform, and is fast enough to reduce frequency drifts due to changes in the charge configuration. We also note that the charge dispersion is small compared to the drive detuning.

6.6.1.1 $\Sigma - \Sigma'$ Mode Coupling

We first use the conditional Ramsey oscillation measurement to obtain the coupling between the two higher frequency Σ-modes of the system. Recalling from Chapter 3, and Fig. 6.3, we expect these modes to have a significant measurable state-dependent shift between them, as is designed.

In Fig. 6.10 (b), we show the resulting two traces for the conditional Ramsey experiment performed with the QA Σ-mode as the target, and QB Σ'-mode as the control. We note the red trace (control mode prepared in the excited state) has a lower contrast, since the control pulses are significantly further detuned and hence have a lower fidelity. In Fig. 6.10 (c) we show the fast Fourier transform of the decaying oscillations shown in Fig. 6.10 (b). We fit these to a Lorentzian lineshape to determine the frequency of the oscillations, and hence the detuning between the drive frequency and transition frequency. The difference between the two extracted frequencies yields the state dependent shift.

From this measurement, we identify a state-dependent shift of $\chi_{\Sigma\Sigma'} = 2.679$ MHz (± 6 kHz). Using Eqn. 6.1, we extract an exchange interaction strength of $J = 9.3$ MHz.

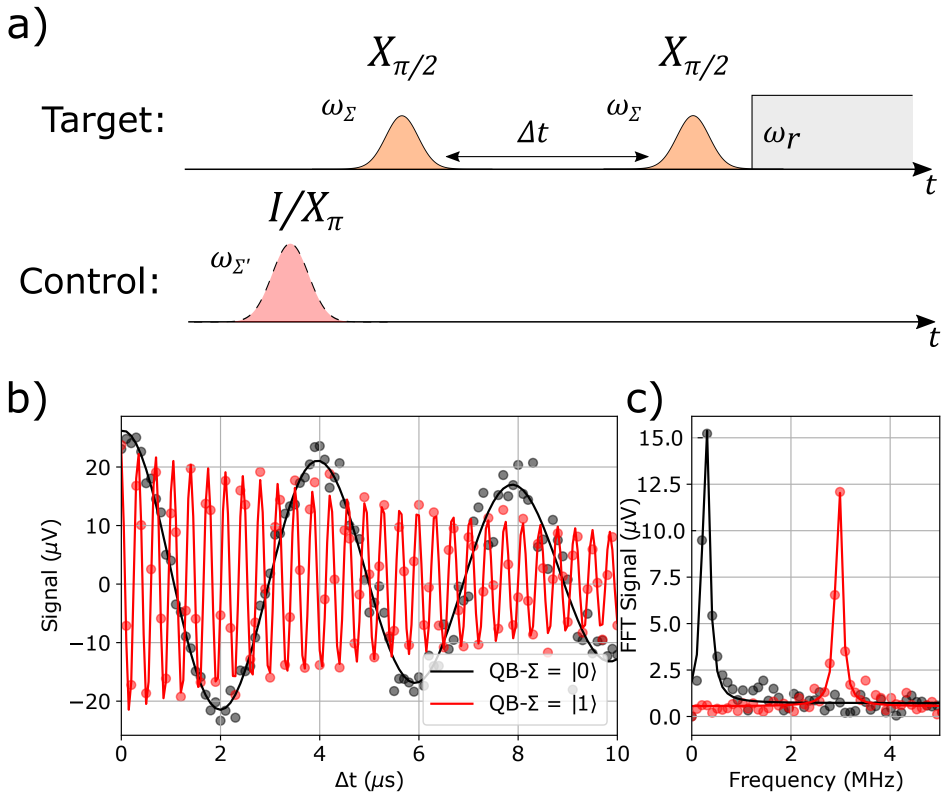

Figure 6.10: (a) Pulse sequence of the conditional Ramsey experiment. (b) Resulting traces of the two Ramsey oscillation measurements, corresponding the control mode in the ground state (black) and excited state (red). Data (dots) is fitted (line) to a decaying oscillation, with the frequency component extracted from the Fourier transform data. (c) Fast Fourier transform of the decaying oscillation traces in (b). Data (dots) is fit (line) to a Lorentzian lineshape in order to extract the frequency of oscillations. Drive detuning, $(\omega_d - \omega_\Sigma)/2\pi = -284$ kHz.

6.6.1.2 $\Delta - \Delta'$ Mode Coupling

We next use the conditional Ramsey oscillation measurement to obtain the coupling between the two computational Δ-modes of the system.

In Fig. 6.11 (b) we show the measured traces resulting from the two conditional Ramsey experiments. By inspection, these show no difference in the frequency of oscillation between the two, and appear qualitatively the same. In Fig. 6.11 (c) we show the two FFTs of the decaying oscillations, again showing two Lorentzian lineshapes of qualitatively the same frequency.

From fitting the two Lorentzian lineshapes in Fig. 6.11 (b), we identify the de-

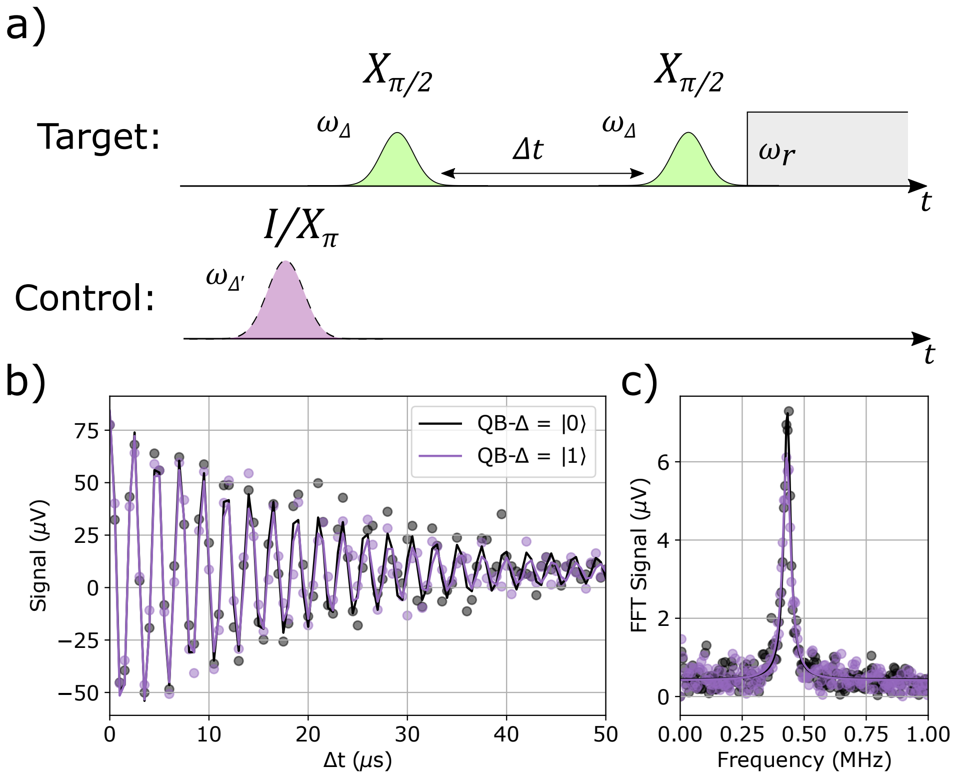

Figure 6.11: (a) Pulse sequence for the conditional Ramsey experiment. The control mode is prepared in the ground or excited state by either an identity gate (I) or X_π gate respectively. (b) Measured traces of conditional Ramsey oscillations on the target (QA Δ-mode) corresponding to the control mode (QB Δ'-mode) being prepared in the ground (black) or excited state (purple). Data (dots) is fitted (solid line) to a decaying oscillation. (c) Fast Fourier transform of the corresponding decaying oscillation traces in (b). Data (dots) is fitted (solid line) to a single peaked Lorentzian, from which the frequency is extracted. Drive detuning, $(\omega_d - \omega_\Delta)/2\pi = -431$ kHz.

tuning between the control pulse and the $|0000\rangle \rightarrow |0100\rangle$ transition to be $\omega_d/2\pi - \omega_{|0000\rangle\rightarrow|0100\rangle}/2\pi = 431.6$ kHz (± 0.4 kHz), and detuning between the control pulse and the $|0001\rangle \rightarrow |0101\rangle$ transition to be $\omega_d/2\pi - \omega_{|0001\rangle\rightarrow|0101\rangle}/2\pi = 429.6$ kHz (± 0.5 kHz). This yields a state-dependent shift $\chi_{\Delta\Delta'}/2\pi = (E_{0101} + E_{0000} - E_{0100} - E_{0001})/h = 2.0$ kHz (± 0.6) kHz.

This presents one of the main results in demonstrating the mode-selective coupling structure in our system. In a system of four modes, we are able to show that we can selectively couple two modes, and have a greatly suppressed coupling between protected modes.

Recalling the result obtained in Fig. 3.15, if this frequency shift were purely a result of junction energy asymmetry, it would suggest an error significantly larger than the previously reported 2% junction energy spread. We postulate this coupling is likely due to the geometric coupling of two coincidentally oriented electric dipoles. As such, this can be eliminated by orientating the adjacent two-mode coaxial transmons perpendicularly.

6.6.1.3 Cross-Mode Coupling

For completeness, we also note that the cross modes (QA-Δ - QB-Σ', QA-Σ - QB-Δ') will also have some state-dependent frequency shift between them. This is important to understand in our architecture, since these frequency shifts are indicative of how fast we are able to perform the AT-MAP interaction between the computational modes.

In Fig. 6.12 we show the corresponding conditional Ramsey oscillation traces for the cross-coupling measurements. The pulse scheme is the same as in the previous experiments. The measurements are repeated at two different detunings in order to ascertain the exact frequency shift and allow for any aliasing in the FFT data. In the case of these traces, the drive frequency is between the two transition frequencies, and so the state-dependent frequency shift is determined by the sum of the fitted frequencies.

By fitting a Lorentzian lineshape to the fast Fourier transform data in Fig. 6.12 (b) and (d), we obtain shifts of $\chi_{\Sigma\Delta'}/2\pi = 1.292$ MHz ($\pm$6 kHz), and $\chi_{\Delta\Sigma'}/2\pi = 0.699$ MHz ($\pm$8 kHz).

We note that this state-dependent shift is not a result of a direct coupling, since there is no direct coupling in the circuit design or bare device Hamiltonian. It is instead a coupling mediated by the Σ-mode, in the same fashion as the coupling between the Δ-mode and readout resonator. The values measured here are consistent with values obtained in EPR simulation methods.

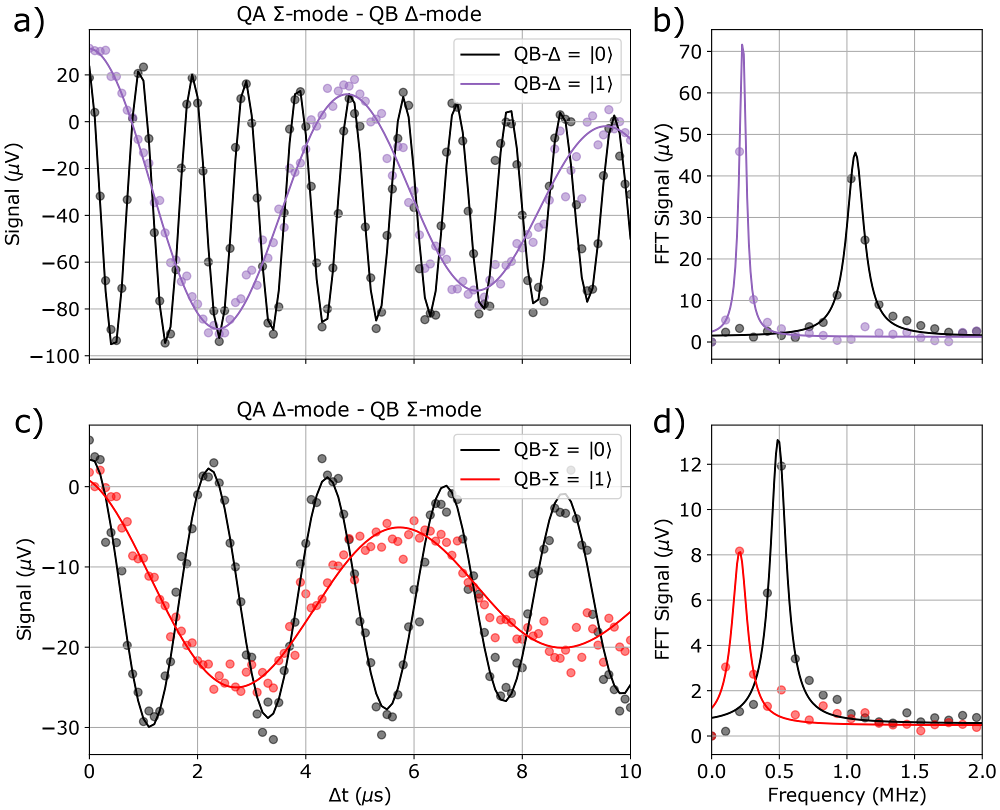

Figure 6.12: (a)(c) Measured traces of conditional Ramsey oscillations on the target ((a) QA Σ-mode, (c) QA Δ-mode) corresponding to the control mode ((a) QB $\Delta^{'}$-mode (c) QB $\Sigma^{'}$-mode) being prepared in the ground (black) or excited state (purple/red). Data (dots) is fitted (solid line) to a decaying oscillation. (b)(d) Fast Fourier transform of the corresponding decaying oscillation traces in (a)(c). Data (dots) is fitted (solid line) to a single peaked Lorentzian, from which the frequency is extracted. Drive detuning, $(\omega_d - \omega_{\Sigma(\Delta)})/2\pi = -1.062$ MHz (-492 kHz).

6.6.2 Randomised Benchmarking

In addition to measuring the state-dependent frequency shifts of each mode, we use individual and simultaneous randomised benchmarking to quantify the selective addressability and crosstalk between the computational modes [183–185].

At each step m in the randomised benchmarking sequence, we construct $k = 50$ random sequence seeds, sampling rotations from the single qubit rotation Clifford group. To improve signal to noise, each sequence measured is repeated 1000 times and an average signal taken. Given we start in the ground state, and with the inversion gate at the end, the entire sequence amounts to an identity gate (I). If the gate error is modelled as a depolarising channel with parameter α, the probability the sequence yields the initial state (ground state) is given by,

$$P = \alpha^m + \frac{1-\alpha^m}{2^n} = \frac{2^n-1}{2^n}\alpha^m + \frac{1}{2^n} = A_0\alpha^m + B_0 \tag{6.2}$$

where m is the number of Cliffords, n is the number of qubits, and A_0 and B_0 are amplitude and offset parameters respectively. Thus the sequence exponentially decays with sequence length and parameter α.

The randomised benchmarking procedure extends naturally to many qubits, however we only use the single qubit result, where $n = 1$. From the depolarising parameter α, we calculate the error per Clifford (EPC) as,

$$EPC = \frac{1}{2}(1-\alpha) \tag{6.3}$$

In order to obtain the error due to a particular gate, one can implement an interleaved randomised benchmarking procedure. This is beyond the scope of what we are interested in, hence we only take the average error per single qubit rotation. Since each Clifford rotation is compiled using a combination of physical gates, we can extract the average error per gate (EPG) as,

$$EPG = \frac{1}{2}(1-\alpha^{1/N_g}) \tag{6.4}$$

where N_g is the average number of physical gates per Clifford rotation ($N_g = 2.2$)[1].

For completeness, we also present the error per gate in the ideal case, where fidelity is only limited by coherence. This coherence limited error per gate (EPG$_{c.l.}$) is given by,

$$EPG_{c.l.} = (3 - e^{-\tau_g/T_1} - 2e^{-\tau_g/T_{2E}})/6 \tag{6.5}$$

where τ_g is the physical gate time.

---

[1] The gateset in this experiment is composed of only $X_{\pi/2}$ and $Y_{\pi/2}$ gates, hence the larger average number of physical gates than if X_π and Y_π gates were also used.

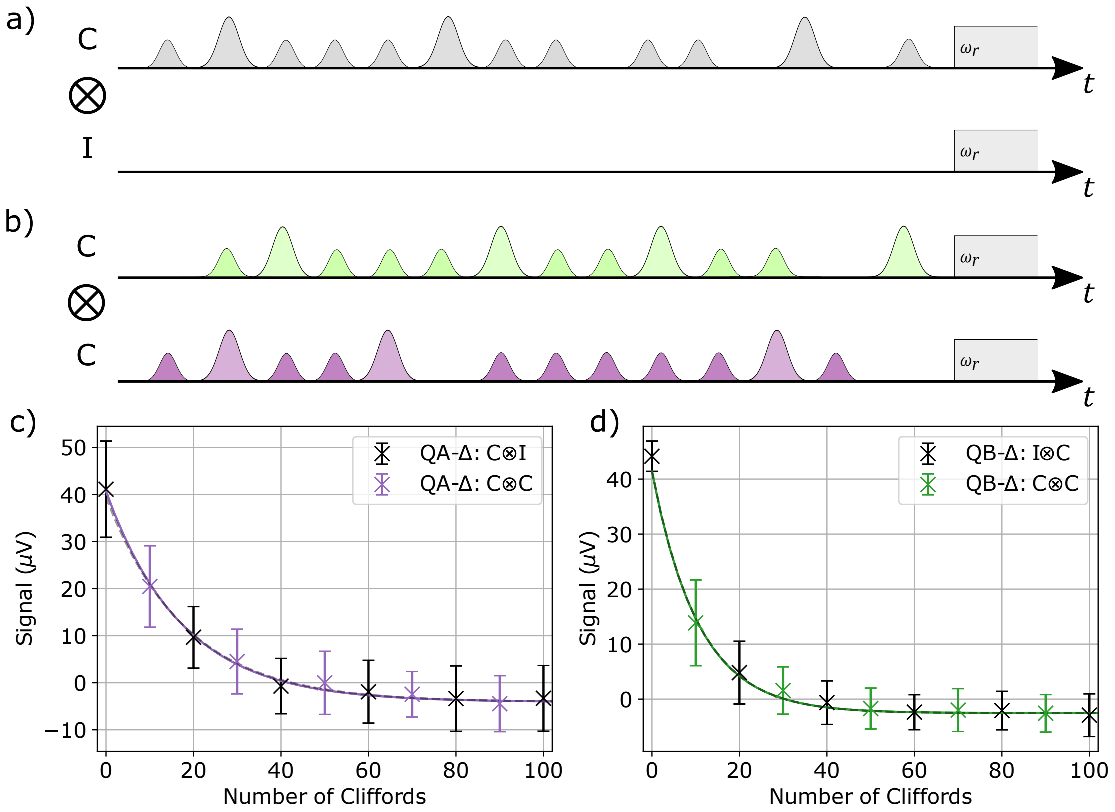

Figure 6.13: Individual and simultaneous randomised benchmarking. (a) Illustration of an example pulse sequence of an individual randomised benchmarking sequence ($m = 8$). Grey pulses control target mode, whilst second mode has an empty sequence. Clifford rotations comprise combination of physical X_π, $X_{\pi/2}$, Y_π, $Y_{\pi/2}$ gates. (b) Illustration of an example pulse sequence of a simultaneous randomised benchmarking sequence ($m = 8$). Two unique sequences are applied to computational Δ-mode and $\Delta^{'}$-modes. (c)(d) Individual (black) and simultaneous (purple/green) randomised benchmarking sequence result of measuring the Δ-mode (c) and $\Delta^{'}$-mode (d). Data (crosses) is fitted to Eqn. 6.2 (lines). Measured sequences sample every $m = i * 2$. Error bars show standard deviation of 50 sequences sampled, plotted alternatively every $m = i * 10$ for clarity.

We perform the randomised benchmarking measurement in two configurations. The first is the individual case, where gates are only applied to one mode and everything else remains in the ground state ($C \otimes I$ / $I \otimes C$). The second configuration is a simultaneous randomised benchmarking sequence, where sequences and gates are applied simultaneously to two modes ($C \otimes C$). In systems of statically-coupled, fixed-frequency, transmon qubits, the error per gate extracted is larger in the case where the two computational modes are measured simultaneously [185]. This is due

Table 6.2: Randomised Benchmarking Results

Mode:	EPC_{ind} (x10^2)	EPC_{sim} (x10^2)	EPG_{ind} (x10^2)	EPG_{sim} (x10^2)
Δ-mode	2.73(6)	2.78(9)	1.26(3)	1.28(8)
$\Delta^{'}$-mode	4.48(0)	4.48(6)	2.08(8)	2.09(1)
Avg.	3.6(1)	3.6(4)	1.6(8)	1.6(9)

to the always-on unwanted ZZ interaction between the two modes inducing a state-dependent frequency shift.

To demonstrate the suppressed crosstalk between computational modes in our architecture, we perform individual and simultaneous randomised benchmarking measurements on the Δ-modes.

In Fig. 6.13, we show illustrations of pulse schemes ((a), (b)) and results of the individual and simultaneous randomised benchmarking experiments ((c), (d)). We observe no visible difference between the two curves plotted.

From fitting of the curves in Fig. 6.13 (c) and (d), we obtain the depolarising parameter α, from which we extract the error per Clifford (EPC) and error per gate (EPG). These values are summarised in Table 6.2. Here we once again demonstrate the suppression in crosstalk, by observing a minimal increase in gate errors when the sequences are applied simultaneously compared to individually.

Whilst this result demonstrates a significant merit of this architecture in suppressing unwanted interactions between computational modes, we note the single-qubit-gate errors are far from state-of-the-art obtained in coaxial superconducting circuits [160]. This is largely due to the weak coupling between the coaxial control port, and the dipole-like Δ-modes, since there is poor mode-matching between the electric fields of these components. As such, we are required to either drive the modes at high powers, or have very long pulses. In this case, the single qubit control pulses are Gaussian pulses with a total edge-to-edge gate time of $\tau_g = 450$ ns and $\tau_g = 1.05$ μs. Using the coherence parameters in Table 6.1 and Eqn. 6.5, we obtain coherence limited errors per gate of $EPG_{c.l.\Delta} = 0.4(5)\text{x}10^{-2}$, and $EPG_{c.l.\Delta'} = 1.1(6)\text{x}10^{-2}$, for the Δ-mode and Δ'-mode respectively. In future designs, we aim to increase this coupling to the control port by adding intrinsic asymmetry in the layout, allowing for faster gates and errors comparable to other similarly high-performing architectures [160].

6.6.3 Summary

From our measurements of state-dependent frequency shifts through conditional Ramsey oscillation experiments, in addition to spectroscopy measurements, we are able to construct a full χ matrix of the coupled two-mode coaxial transmon system. Note the diagonal entries correspond to self-Kerr shifts (anharmonicities $\chi_{ii}/2\pi = \eta_i/2\pi$), and the off diagonal elements are due to couplings between modes. For simplicity, we order modes in ascending order of frequency, as in the vector $(\Delta, \Delta', \Sigma, \Sigma')$. The matrix is in units of MHz, and is symmetric about the diagonal, hence we only show the bottom half for ease of reading.

$$\chi_{ij}/2\pi = \begin{pmatrix} 90 & - & - & - \\ 0.002 & 150 & - & - \\ 240 & 1.292 & 140 & - \\ 0.699 & 320 & 2.679 & 200 \end{pmatrix} \tag{6.6}$$

6.7 AT-MAP Interaction

As the mode-selective coupling structure has been established, we move on to demonstrating a two-qubit state-dependent interaction between the two uncoupled Δ-modes of the system. The interaction we choose to implement is the microwave activated conditional phase via ancillary transitions (AT-MAP) interaction, previously introduced in Section 3.3.3.

In order to measure a phase accumulated by the interaction, we use an Hahn-echo type pulse sequence, shown in Fig. 6.14 (a). We use the QB Δ'-mode as the target, applying an $X_{\pi/2}$, Y_π and $X_{\pi/2}$ pulse at $\omega_{\Delta'}$ as shown in purple. Single-qubit control pulses on the Δ-mode and Δ'-mode are applied on resonance with the transition frequency of these modes. We also add the Gaussian conditional phase (CZ) pulse driven at a frequency of ω_d and power Ω^2, shown in grey. This sequence is conditioned on the state of the control mode, the QA Δ-mode, by applying either an identity, I, or X_π pulse, shown. This sequence maps the phase accumulated due to the CZ pulse to the excited state population of the target mode, allowing us to characterise the interaction. This sequence is identical to the measurements performed in Section 4.6, which forms the premise of this interaction.

6.7.1 Interaction Spectroscopy

Using the phase accumulation detection measurement sequence, we first explore the AT-MAP interaction through spectroscopy. We perform the echo sequence depicted in Fig. 6.14 (a) both with the control mode starting in the ground and excited state, sweeping both the drive frequency (ω_d) and drive power (Ω^2) of the CZ pulse. We subtract the two measured signals in order to obtain the conditional phase accumulated in the interaction. The length of the CZ pulse is fixed at 250 ns.

In Fig. 6.14 (b) we plot the difference measured Δ'-mode signal between these two measurements, showing the conditional phase accumulated in the interaction. The individual measurements before the difference is taken can be seen in Fig. 6.15 (a) and (b). Driving the interaction around the $|0100\rangle \rightarrow |1100\rangle$ and $|0001\rangle \rightarrow |0011\rangle$ transitions that are close to being on resonance, $\omega_\Sigma - \chi_{\Sigma\Delta} \approx \omega_{\Sigma'} - \chi_{\Sigma'\Delta'} \approx 4.9$ GHz, we see a strong signal with clear fringes. Simultaneously, we are able to measure the excited state population of the ancillary transition of Qubit B, the Σ'-mode, whilst performing this interaction, shown in Fig. 6.14 (c). There are three key features at the transition frequencies labelled ($\omega_\Sigma - \chi_{\Sigma\Delta}$, $\omega_{BSB'}$, $\omega_{\Sigma'} - \chi_{\Sigma'\Delta'}$), corresponding to the $|0100\rangle \rightarrow |1100\rangle$ and $|0001\rangle \rightarrow |0011\rangle$ transitions, as well as the sideband

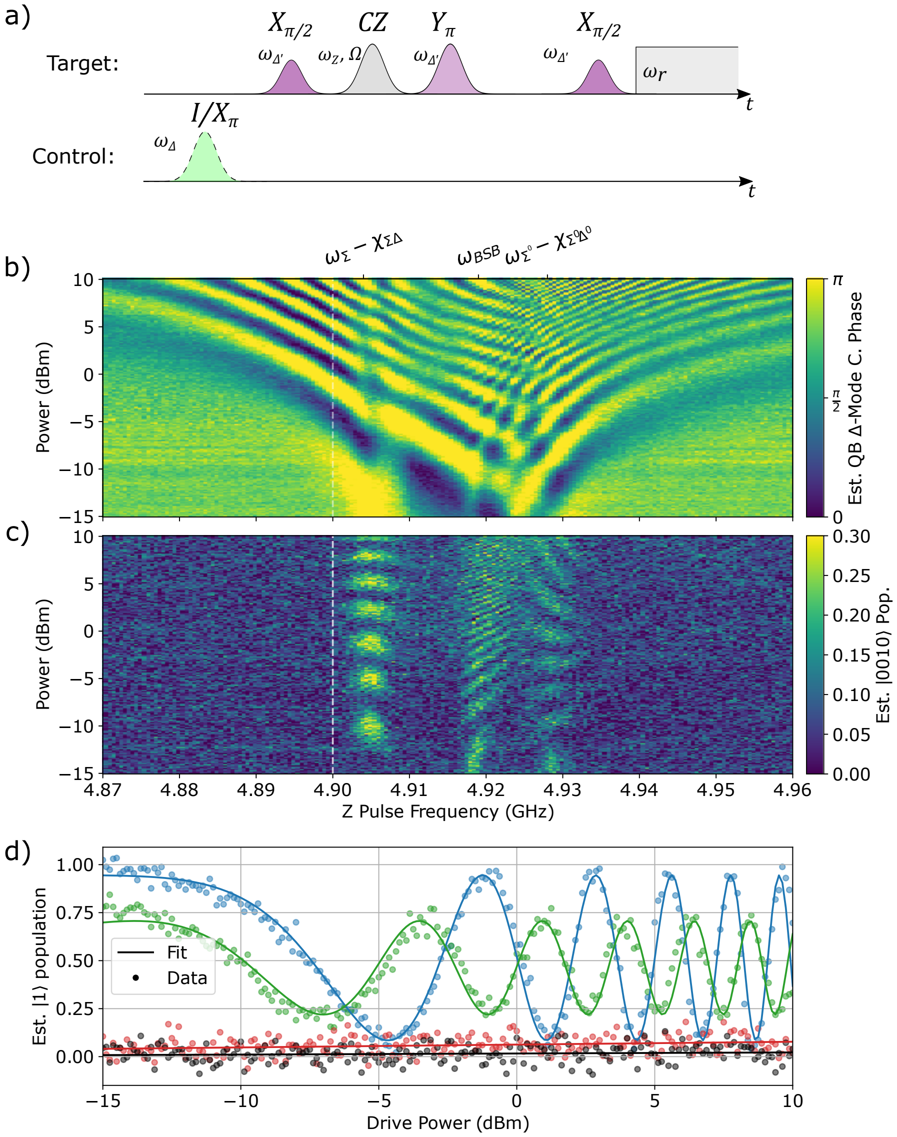

Figure 6.14: (a) Pulse scheme for the echo based conditional phase accumulation detection measurement. The 250 ns Gaussian pulse frequency and power (ω_d, Ω^2) are swept to tune the interaction. (b) Difference in phase accumulated in QB Δ-mode between QA Δ-mode starting in ground and excited state, swept versus drive frequency and power. High contrast features labelled at ancillary transition frequencies $\omega_{\Sigma'} - \chi_{\Sigma'\Delta'}$ and $\omega_\Sigma - \chi_{\Sigma\Delta}$, as well as the blue sideband between these two transitions. (c) Target mode ancillary transition (QB Σ-mode), measured simultaneously to the QB Δ-mode. High contrast features show where the interaction can be driven on resonance by driving one full Rabi period. (d) Estimated excited state population of the QB Δ-mode (Σ-mode) versus AT-MAP drive power with the control mode, QA Δ-mode, in the ground (blue (black)) or excited state (green (red)), driving the AT-MAP interaction at 4.9 GHz, as indicated by the vertical dashed line in (b) and (c). Data (dots) is fitted (lines) to a $\cos(\Omega x)^4$ function in the case of the Δ′-mode, and a linear fit in the case of the Σ′-mode

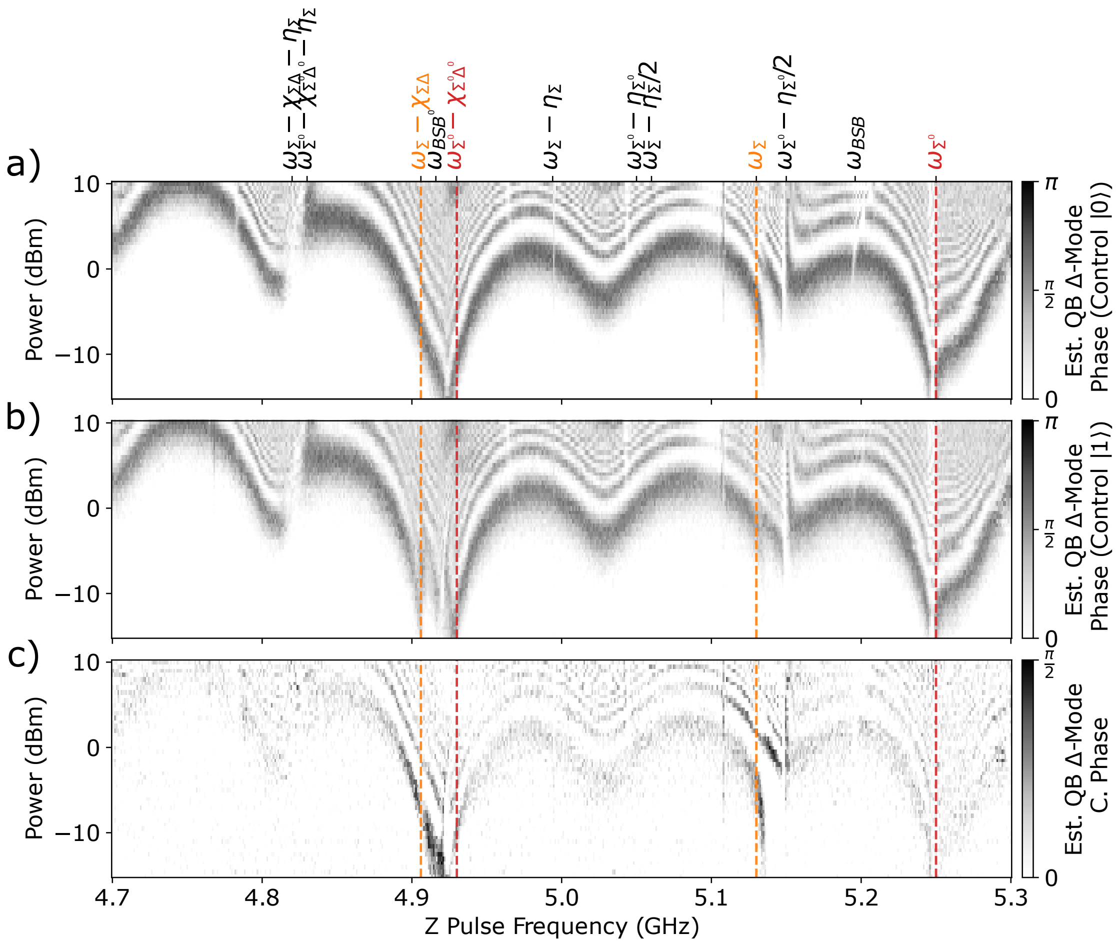

Figure 6.15: Wide AT-MAP interaction spectroscopy. Pulse sequence as in Fig. 6.14, with a fixed pulse length, and swept CZ pulse frequency and signal generator power. Transition frequencies in region labelled. Ancillary transitions required to be on-resonance for the AT-MAP interaction labelled with vertical dashed lines in orange (Σ-mode), and red (Σ'-mode). (a) (b) Δ'-mode estimated phase conditioned on the control Δ-mode initialised in the ground state (a) or excited state (b). (c) Magnitude of the difference in phase (C. Phase) measured in (a) and (b).

transition between these two transitions ($\omega_{BSB'} = (\omega_{|0101\rangle \to |1111\rangle})/2$) . These higher contrast regions indicate where there is a non-negligible excited state population of the target qubit ancillary transition.

To demonstrate the wide range of frequencies for which this interaction can be driven, we perform the interaction spectroscopy measurement from 4.7 GHz to 5.3 GHz, shown in Fig. 6.15. We identify and label the transition frequencies that correspond to features in the spectroscopy. The ancillary transitions involved in the

AT-MAP interaction are highlighted, and correspond to areas of high contrast in Fig. 6.15 (c), showing where the conditional phase interaction takes place.

From this spectroscopy, we choose to drive the AT-MAP interaction at a frequency of 4.9 GHz, indicated by the dashed vertical lines in Fig. 6.14 (b) and (c), in order to operate in a minimal leakage regime. We show a vertical slice of the spectroscopy measurements in Fig. 6.14 (d), showing the estimated excited state populations of the target computational (Δ'-mode, blue and orange) and ancillary mode (Σ'-mode, green and red), conditioned on the state of the control mode. The Δ'-mode population follows the expected $\cos{(\Omega x)}^4$ form, and for low power, the population of the Σ'-mode is negligible. The difference in contrast between the green and blue data in Fig. 6.14 (d) is due to the lower fidelity of the control-mode X_π pulse than the I operation (corresponding to no control pulse being applied). As with many microwave-activated interactions, driving at higher power can lead to unwanted effects and leakage, which can cause errors in the operation of a two-qubit gate.

6.7.2 Interaction Power and Duration

With the drive frequency established, we investigate the effect of changing the pulse length and drive power to tune the interaction. We use the same phase accumulation detection sequence as previously shown in Fig. 6.14 (a), and vary the length of the CZ pulse and generator drive power, sweeping the amplitude of the pulse. In Fig. 6.16 (a) we show the conditional phase accumulated in the target mode (Δ'-mode), and observe fringes that increase in frequency as the power is increased. By taking a vertical slice of Fig. 6.16 (a) and performing a Fourier transform, we are able to obtain the two frequency components of the conditional phase oscillation. These two frequency components correspond to the sum and difference in the frequency of the oscillations of the target mode phase with the control mode starting in the ground or excited state. The slower of the two frequencies obtained indicates the difference in

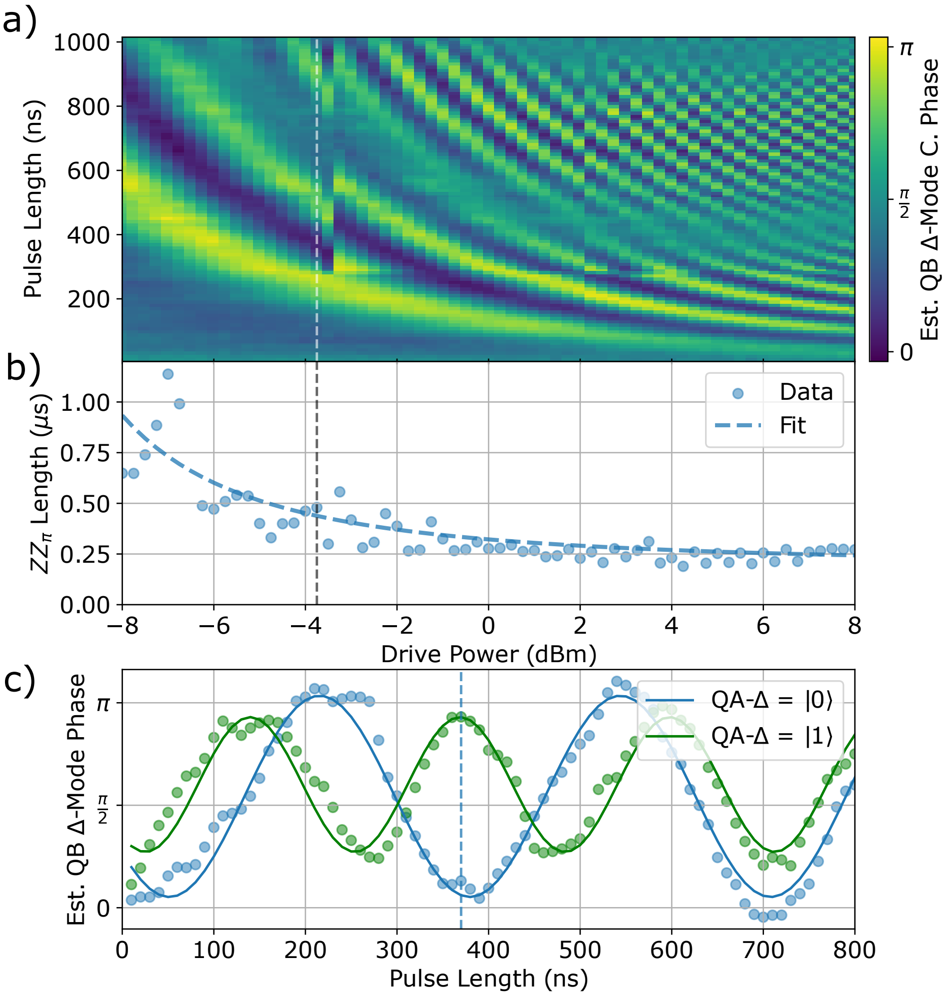

Figure 6.16: AT-MAP interaction versus power. (a) Conditional phase accumulated in target mode versus pulse length and power, driven at 4.9 GHz. Step features occur due to internal attenuation switching of signal generator when increasing drive power. (b) Minimum $[ZZ]_\pi$ two-qubit gate length extracted from frequency of oscillations of (a). (c) Estimated phase acquired on target mode QB Δ-mode, controlled on the state of control mode QA Δ-mode as a function of interaction pulse length, with constant drive power -3.9 dBm, indicated by vertical dashed line in (a) and (b).

the rate at which phase is acquired in the target mode with the control mode in the ground or excited state, and hence the rate of the conditional phase rotation. After one quarter of the time period of this frequency, the conditional phase acquired is a the maximum value of π. This is what we extract as $[ZZ]_\pi$ gate time, when a π phase rotation is applied to the target mode, conditional on the state of the control mode. This data is plotted in Fig. 6.16 (b), fitted to an equation of the same form as

Eqn. 3.35. As expected, we find a increase in extracted gate speed, which saturates at higher power to an extracted gate length of approximately 200 ns.

In Fig. 6.16 (c), we show a vertical slice of the 2D sweep, with a drive power of -3.9 dBm, indicated by the vertical dashed line in Fig. 6.16 (a) and (b). We plot the phase accumulated in the target mode as a result of the AT-MAP interaction, conditioned on the state of the control mode of the system. The point at which the oscillations are out-of-phase is when a conditional π phase shift occurs in the target mode, or a $[ZZ]_\pi$ gate, indicated by the vertical dashed line. Whilst not demonstrated in this work, the alignment of these oscillations can be fine tuned with additional single qubit $Z(\theta)$ rotations. What these two different oscillations show is that we are able to drive a conditional phase interaction between two modes of a system, that have been shown to have no measurable coupling between them.

6.7.3 Further Work

One of the limiting factors we encounter in this conditional phase interaction is the poor single qubit gate fidelity of the Δ-modes of the system as previously described, due to their weak coupling to the coaxial control port. At higher powers we also expect leakage into other states of the system to become significant and cause errors. A more detailed investigation into these error syndromes in more complex multi-mode systems is needed for them to become more useful in quantum computing applications.

With our initial design of device, the coherence-limited gate fidelity for this 200 ns gate is above 99%. The gate can be made faster by increasing the exchange coupling J between ancillary modes, which will be a subject of future work. By doubling this exchange interaction strength, we estimate the $[ZZ]_\pi$ gate can be driven in less than 100 ns, and approach state-of-the-art two-qubit gate fidelities.

We note here that these results do not explicitly demonstrate a two-qubit entanglement operation. This is due to the measurement limitations of the experimental setup and lack of single-shot readout capabilities. In further work, we aim to perform a thorough demonstration and characterisation of the two-qubit gate, through state tomography, process tomography, or two-qubit randomised benchmarking.

6.8 Conclusion and Outlook

In this chapter, we have explored a system of two statically coupled, fixed-frequency, two-mode coaxial transmons. We show that in this architecture, we can implement a mode-selective coupling, and are able to greatly suppress unwanted interactions between modes of the system. This allows us to use the protected Δ-modes as computational states, and the coupled Σ-modes for communication. This architecture shows promise for reducing errors in larger scale superconducting processors.

In addition, we demonstrate the ability to perform a conditional phase interaction between the modes of the system with no measurable coupling between them, and no additional circuit complexity. We describe how this microwave activated conditional phase interaction is driven via the ancillary transitions of the system, and has a wide range of resonance conditions that can be met. We show a proof-of-principle of the AT-MAP interaction, demonstrating how a $[ZZ]_\pi$ operation can be performed in ~ 100 ns. Increasing the coupling J between ancillary modes would allow faster gate speeds, whilst maintaining crosstalk suppression between computational states.

In future work, we aim to optimise the device design for both faster single-qubit and two-qubit gate operations, and benchmark the AT-MAP gate, investigating the sources of error in the implementation. The coupling of this multi-mode structure also lends itself to other gate operations. Whilst here we aim to reduce leakage into the ancillary modes, they can be used as additional control modes and form a 4-qubit Toffoli class in this system, implementing a CCCNOT type gate or other Toffoli gate. Due to the versatility and engineerablity of these multi-mode devices, we propose that they have the potential to make promising contributions to the performance of large scale quantum processors.

Chapter 7

Conclusions and Outlook

7.1 Conclusions

In this thesis, we have presented an implementation of a multi-mode superconducting qubit in a tileable circuit architecture, with 3D-integrated control and readout. Extending beyond the simplicity of the transmon qubit, we have added capability and symmetry protection within the unit-cell of the coaxial cQED architecture, without additional circuit or control complexity.

We began by presenting a theory of the behaviour of the two-mode coaxial transmon in the unit-cell of the coaxial cQED architecture. We showed how alternative 3-island two-junction device designs behave, and outline how they can be used for multiplexed readout mechanisms and photon detection experiments. We introduce how a mode-selective coupling can be implemented, as well as presenting a theory of an entangling operation between symmetry protected modes.

In a first experimental demonstration of the two-mode coaxial transmon and readout resonator unit-cell, we demonstrated high coherence in both modes with selective control and readout. We also introduced two-tone spectroscopy techniques to characterise complex energy level structures that can be utilised in more complex novel qubit designs.

Charge noise is a leading source of decoherence in superconducting circuits. We investigated this topic using a charge-sensitive two-mode coaxial transmon as a probe.

Our results include observations of multiple charge-parity configurations, showing agreement with our predictive theory for charge sensitivity using a tight-binding approximation, as well as the utility of the device as a detector of spatial charge fluctuations. We also showed how we can design the two-mode transmon device to be in a parameter regime in which the charge sensitivity is suppressed.

Always-on interactions contribute to errors in the operation of single-qubit and two-qubit gates in quantum computers. We performed experiments on a system of coupled two-mode coaxial transmons, and demonstrated a mode-selective coupling that suppressed the always-on interaction to 2 kHz, orders of magnitude smaller than conventional statically coupled fixed frequency transmon circuits. In addition, suppression of single-qubit gate errors when operated simultaneously versus individually was shown in randomised benchmarking. We also show the first characterisations of an two-qubit state-dependent interaction between the protected modes via an off-resonant driving of the ancillary transitions of the system, which we name the AT-MAP interaction. We show how this interaction has a wide range of resonance conditions available for optimum operation, making it less sensitive to fabrication imperfections than other two-qubit gates implemented in superconducting quantum processors.

7.2 Outlook

Quantum computing requires the low-error operation of many qubits, and a simple scaling of fixed frequency transmon architectures is not sufficient to reach the thresholds required for error correction protocols. Further work is required to characterise and benchmark the entangling operation we have introduced in this work, however, we postulate that the multi-mode coaxial transmon qubit has the potential to be an additional candidate for the building block of a quantum processor. Optimisation of the design, in conjunction with the shielding configuration, has the potential to lead to device performance approaching state-of-the-art. In addition, further exploitation of the complex energy level structure can allow for a number of four-qubit Toffoli class gates, such as a CCCNOT gate.

The orthogonal polarisation of the dipole-like antisymmetric mode and quadrupole-like symmetric mode of the two-mode coaxial transmon lends itself to novel global and local selective coupling schemes. This has applications in multiplexed detection architectures as previously stated, as well as being potentially useful in quantum simulation applications.

The work presented here demonstrates a simple extension of the coaxial transmon qubit, whilst retaining the extensibility and tileability that comes as a result of the out-of-plane wiring solution. As systems scale beyond current quantum advantage class quantum computers, solving the problems of crosstalk and always-on interactions in a scalable way is essential. In words attributed to Albert Einstein [186]:

"*Everything should be made as simple as possible, but not simpler.*"

Appendix A

Tight-Binding Model of Charge Dispersion

The Hamiltonian of Eqn. 3.6 can be written as $\hat{H} = \hat{T} + \hat{U}$, where the kinetic term $\hat{T} = 8E_{C_\Sigma}\hat{n}_\Sigma^2 + 8E_{C_\Delta}\hat{n}_\Delta^2$, and the potential term can be rewritten as:

$$\begin{aligned} U(\varphi_\Sigma, \varphi_\Delta) &= -2E_J \cos\frac{\varphi_\Sigma}{2}\cos\frac{\varphi_\Delta}{2} \\ &= -2E_J \cos\frac{\varphi_\Sigma}{2} - 2E_J \cos\frac{\varphi_\Delta}{2} \\ &- 4E_J \sin^2\frac{\varphi_\Sigma}{4}\sin^2\frac{\varphi_\Delta}{4} \\ &= U_0(\varphi_\Sigma, \varphi_\Delta) + U_1(\varphi_\Sigma, \varphi_\Delta), \end{aligned} \tag{A.1}$$

where $U_0 = -2E_J \cos\frac{\varphi_\Sigma}{2} - 2E_J \cos\frac{\varphi_\Delta}{2}$, is the potential term for two uncoupled transmons, and $U_1 = -4E_J \sin^2\frac{\varphi_\Sigma}{4}\sin^2\frac{\varphi_\Delta}{4}$, is a perturbation coupling the two transmon modes together. The potential U_0 is 4π periodic in φ_Σ and φ_Δ, and the additional potential term U_1 introduces lattice sites at $(\varphi_\Sigma, \varphi_\Delta) = (\pm 2\pi, \pm 2\pi)$.

Given this lattice structure, we use Bloch's theorem to pick an approximate solution to the Schrödinger equation $\hat{H}\,|\psi\rangle = E\,|\psi\rangle$ as:

$$\begin{aligned} \psi(\vec{\varphi}) &= \frac{1}{\sqrt{2}}(\psi^{(1)}(\vec{\varphi}) + \psi^{(2)}(\vec{\varphi})) \\ &= \frac{1}{\sqrt{2}} e^{i\vec{k}.\vec{\varphi}}(u_k(\vec{\varphi}) + e^{i\vec{k}.\vec{a}} u_k(\vec{\varphi} - \vec{a})), \end{aligned} \tag{A.2}$$

where $\vec{k}$ is the wave vector of the wavefunction ψ, $\vec{\varphi}$ is the position vector given by $(\varphi_\Sigma, \varphi_\Delta)$, $\vec{a}$ denotes the lattice site introduced by the additional potential U_1, and

u_k is a 4π periodic function. Due to the symmetry of the system, we only need to consider the lattice sites located at $\vec{\varphi} = (0, 0)$ and $\vec{\varphi} = (2\pi, 2\pi)$.

We calculate the energies of the system with this approximate wavefunction using:

$$E(k) = \frac{\langle\psi_k| \hat{H} |\psi_k\rangle}{\langle\psi_k|\psi_k\rangle}, \tag{A.3}$$

leading to the dispersion relation:

$$E(n_{g\Sigma}, n_{g\Delta}) \approx E_0 + \cos \pi n_{g\Sigma} \cos \pi n_{g\Delta}(\gamma - \alpha\beta), \tag{A.4}$$

where the wave vector $\vec{k} = (n_{g\Sigma}/2, n_{g\Delta}/2)$, and the quantities α, γ and β are the tight binding coefficients given by:

$$\alpha = 4 \int_0^{2\pi} u_k(\vec{\varphi}) u_k(\vec{\varphi} - 2\pi)\, d^2\vec{\varphi} \tag{A.5}$$

$$\beta = -16E_J \int_0^{2\pi} |u_k(\vec{\varphi})|^2 \sin^2 \frac{\varphi_\Sigma}{4} \sin^2 \frac{\varphi_\Delta}{4}\, d^2\vec{\varphi} \tag{A.6}$$

$$\gamma = -16E_J \int_0^{2\pi} u_k(\vec{\varphi}) u_k(\vec{\varphi} - 2\pi) \sin^2 \frac{\varphi_\Sigma}{4} \sin^2 \frac{\varphi_\Delta}{4}\, d^2\vec{\varphi} \tag{A.7}$$

The dominant term here is γ, which describes the bond energy between wavefunctions at adjacent lattice sites, also known as the two center integral. The α and β terms describe the overlap integral between wavefunctions on adjacent lattice sites, and the energy shift due to the potential on neighbouring lattice sites respectively. These two terms are small compared to γ and so can be neglected, leading to the approximate form of the maximum charge dispersion $\epsilon_{mn}/4 \approx \gamma$.

This form of the charge dispersion ϵ_{mn} can either be calculated numerically, using the wavefunctions shown in Fig. 3.4, or analytically using a semi analytical wavefunction approach to obtain the functional form of u_k [88]. Using this approach, we arrive at the analytical form for the maximum charge dispersion shown in Eqn. 3.28.

Appendix B

Design and Simulation of Quantum Devices

B.0.1 Finite Element Simulation

We simulate the classical electromagnetic behaviour of devices and environments using standard microwave simulation software ANSYS HFSS. This software uses a finite element method (FEM) in order to numerically solve Maxwell's equations in differential form in order to obtain electric and magnetic field distributions, given a set 3D geometry and appropriately assigned boundary conditions. The method divides the geometry into small tetrahedral mesh elements, as shown in Fig. B.1, enabling the expression of the fields within the finite elements through a large linear system of differential equations. A matrix eigenvalue is found to such that the fields can be found at each node of the geometry at the desired frequency. As such, the simulation complexity scales as the volume of the device and environment increases.

From the classical simulation techniques, we are able to extract bare mode frequencies and quality factors (where a lossy environment is simulated), capacitance matrices that can be directly input into circuit quantisation methods, and surface voltage distributions that can be used in charge sensitivity design operations. Further post processing and calculations are required in order to obtain the quantum mechanical parameters of devices.

In small scale devices ($n \approx 4$ qubits), it is possible to simulate the entire chip and

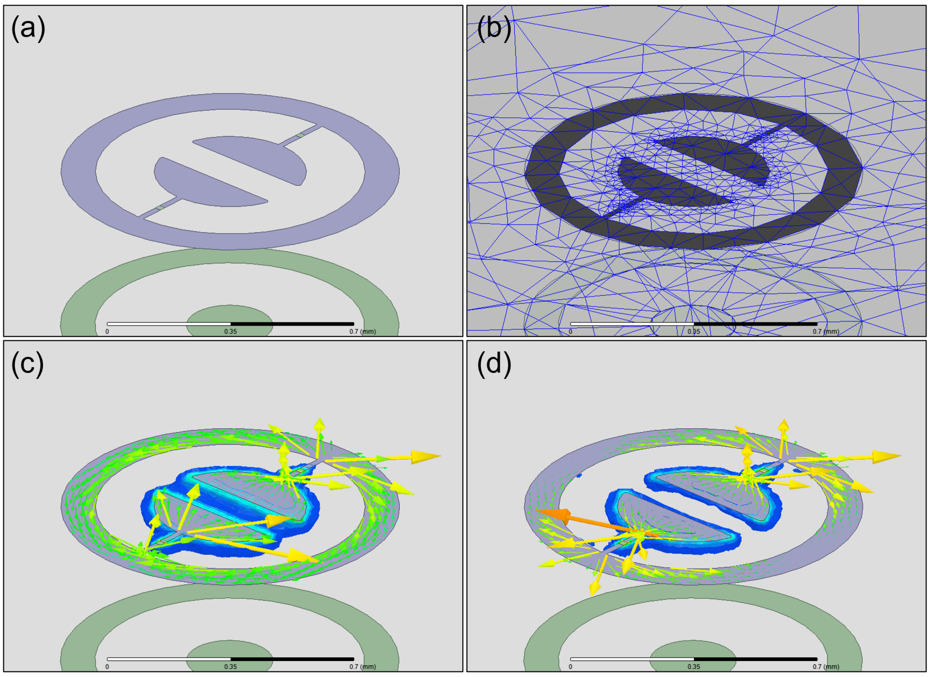

Figure B.1: Electromagnetic simulation of two-mode coaxial transmon (grey) and resonator (green) system. (a) 3D design of qubit and resonator device. (b) Tetrahedral mesh operation of device for FEM simulation. A higher density of mesh elements is used around smaller geometry components around the inner islands and junctions. (c) Electric field (E) and vector surface current (J) of low frequency Δ-mode. (d) Electric field (E) and vector surface current (J) of high frequency Σ-mode.

sample holder environment, and extract mode frequencies and Hamiltonian parameters, using a standard workstation computer. For larger devices ($n \approx 16$ qubits), these simulations have much higher memory (RAM) requirements, and so are performed on high performance computing clusters. Beyond this scale it becomes prohibitively resource intensive to simulate using standard numerical methods, and so for the design and understanding of larger scale devices, other techniques need to be employed.

B.0.2 Quantum Parameter Calculation

In order to determine the quantum mechanical properties of the devices, such as couplings and nonlinearities, we can combine the results of classical FEM simulations with a quantum mechanical model of a device, using methods established in the field such as the energy participation ratio (EPR) [187] or black-box quantisation (BBQ)

[188, 189].

The EPR calculation method allows us to extract quantum parameters of the system by determining how much the nonlinear inductor component of the Josephson junction contributes to the energy of each mode. Formally, the EPR parameter p_{mj} of junction j in mode m is defined as the ratio of inductive energy stored in junction j to inductive energy stored in mode m, such that,

$$p_{mj} = \frac{\langle\psi_m| \frac{1}{2}E_j\hat{\varphi}_j{}^2 |\psi_m\rangle}{\langle\psi_m| \frac{1}{2}\hat{H}_{lin} |\psi_m\rangle} = \frac{\frac{1}{2}L_j I_{mj}^2}{\epsilon_{ind,m}}, \tag{B.1}$$

where E_j is the Josephson energy, $\hat{\varphi}_j$ is the junction flux operator, $\hat{H}_{lin}$ is the linear component of the full system Hamiltonian, and $|\psi_m\rangle$ is a coherent state or Fock excitation of mode m. In the simulation and calculation, we define the junction inductance L_j, and using the field results from the FEM simulation, can determine the current I_{mj} from the surface current density over the junction geometry, and inductive energy stored in the mode $\epsilon_{ind,m}$.

The participation ratio p_{mj} can then be used to determine the quantum zero-point fluctuations using the relation,

$$\phi_{mj}^2 = p_{mj}\frac{\hbar\omega_m}{2E_j}. \tag{B.2}$$

This allows us to construct the full Hamiltonian of the device and environment system and efficiently extract mode frequencies ω_m, anharmonicities η_m and couplings and cross-Kerr shifts χ_{mn}. In practise, we use an open-source package PyEPR [190] to perform the calculation and Hamiltonian diagonalisation. This method utilises both perturbation theory methods and numerical diagonalisation techniques to calculate the Hamiltonian of the system, and so faces the same memory overhead requirement issues when scaling to larger systems of modes, however is sufficient for the devices designed in this work.

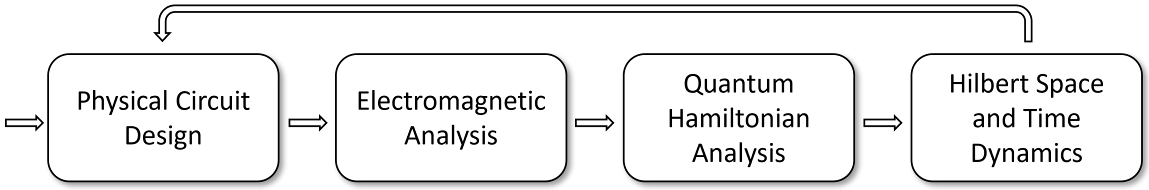

Figure B.2: Demonstrative workflow for designing superconducting quantum devices. Once iterated sufficiently and target parameters met, the physical circuit design is prepared for nanofabrication.

One can additionally calculate the quantum parameters of devices using the simulated impedance responses, in methods including and derived from black-box quantisation. We find both BBQ and EPR methods give the same results, however, due to the lack of frequency sweep requirements, and simplicity in extracting relevant cross-Kerr shifts (χ) of devices, we find EPR methods more favourable and use them in circuit design and simulation.

When designing devices for experiments, we use an iterative workflow outlined in Fig. B.2. An initial 3D geometry is set using previous devices as a template, and target parameters are given by experimental requirements and theoretical work. This can be target frequencies and couplings between modes for optimum gate performance, or aharmonicities for charge sensitivity measurements. Multiple refinement passes are conducted before settling on a device design for fabrication.

Appendix C

Experimental Setup

In order to initialise quantum systems in the ground state, we cool them down to temperatures such that $k_B T \ll \hbar\omega$. For the energy scales associated with superconducting quantum devices, this results in temperatures in the range of 10s of millikelvin. To achieve this, we operate experiments in dilution refrigerators, and mount sample holders and devices to the $\mathrm{He}_3/\mathrm{He}_4$ mixing chamber, as illustrated in C.1. The exact temperature depends on the system used, however, systems are routinely capable of cooling to a range of 10 - 20 mK. Thermalisation of devices to this temperature is necessary, however not sufficient to presume the quantum systems initialise in their respective ground states. It is also necessary to shield devices from sources of radiation, as described in Appendix F.

A more detailed description of the experimental setup to perform measurements is shown in Fig. C.1 is presented in [157, 161, 191]. The control of room temperature instruments is performed using commercial measurement software “Labber” [192].

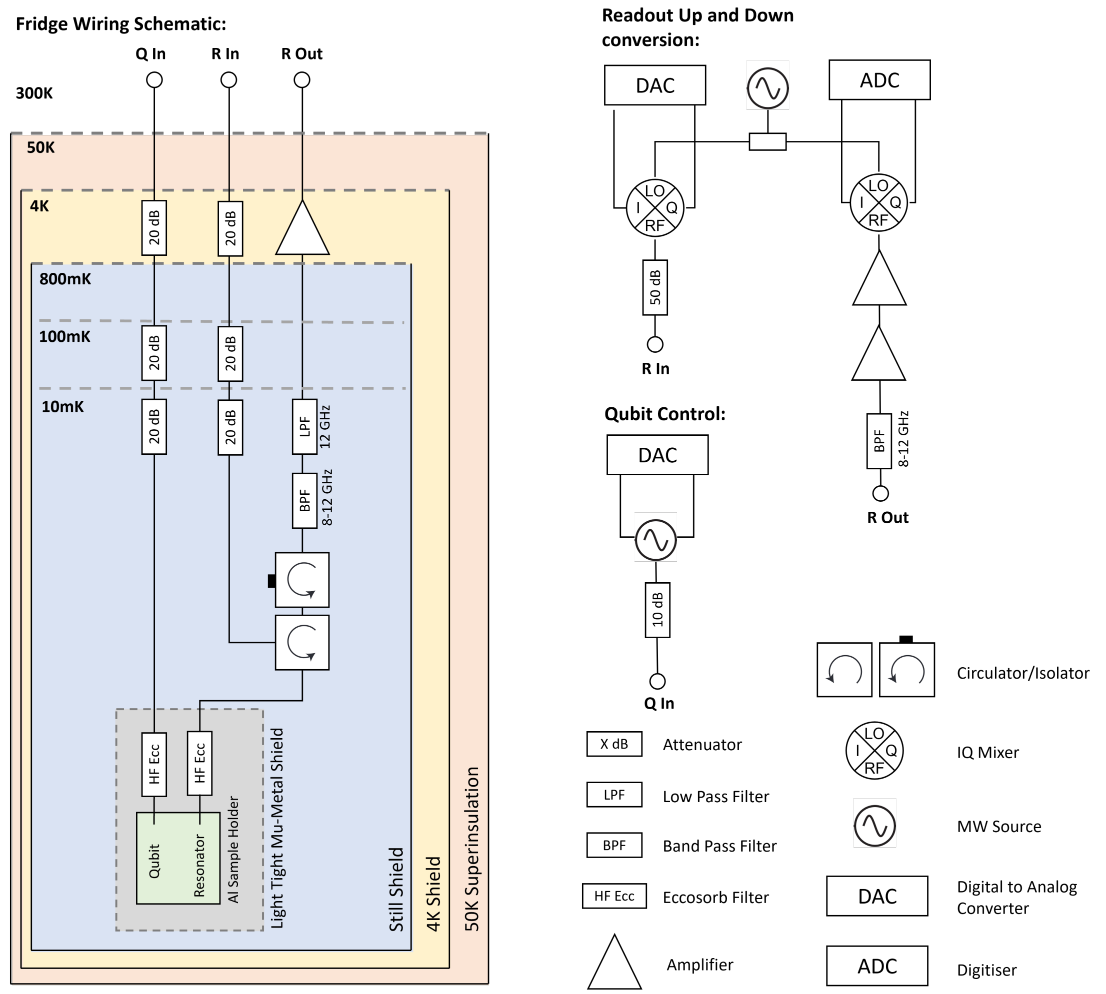

Figure C.1: Schematic of the measurement and control setup used for cQED experiments. Qubit and readout signals propagate through coaxial control lines in the fridge and are attenuated at multiple stages before reaching the sample holder. The readout signal is reflected and passes through the output amplification and filtering chain before being downconverted and digitised. The dilution refrigeration systems used have shields at the 800mK, 4K and 50K plate levels. The sample holders are placed in a light tight mu metal shield to protect devices from IR radiation and global magnetic field offsets.

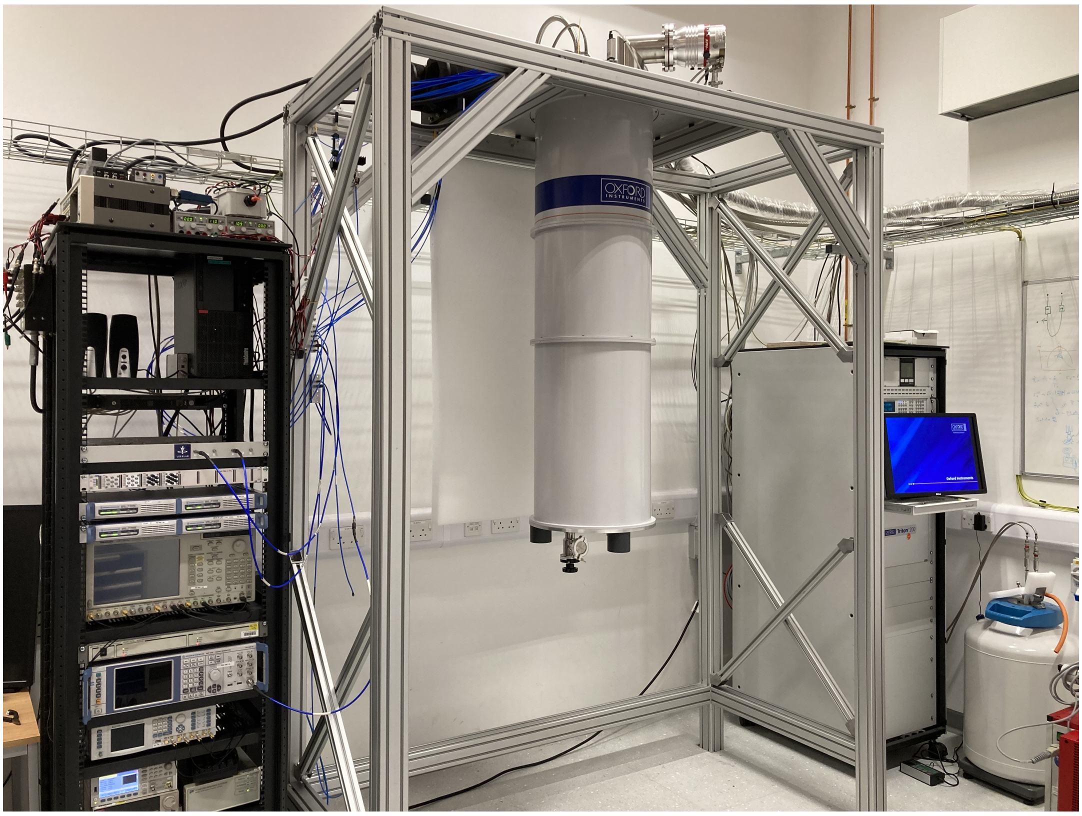

Figure C.2: Photograph of experimental setup consisting of a Triton 200 dilution refrigerator and rack mounted room temperature control electronics. Full details of components as listed in [157].

Appendix D

Readout Signals and Digitisation

As with the qubit control pulse generation, we use single sideband modulation with suppressed carrier frequency to generate readout signals, as depicted in Fig. C.1.

We attenuate the output from the external IQ mixer such that signals incident at the device level are of a low photon number, and the readout procedure operates in the low power regime. Readout signals are reflected by the resonator being probed and pass through the circulator, filters and HEMT amplifier of the fridge output chain. These signals are amplified further by an additional two amplifiers at room temperature.

Using a heterodyne detection setup, we downconvert the readout signals into the real (I) and imaginary (Q) components in the form,

$$\begin{aligned} I_{IF}(t) &\propto A_{RO}\cos(\omega_{IF}t + \theta_{RO}), \\ Q_{IF}(t) &\propto A_{RO}\sin(\omega_{IF}t + \theta_{RO}). \end{aligned} \tag{D.1}$$

This maintains the amplitude (A_{RO}) and phase (θ_{RO}) information of the readout signal, but within a signal at a lower frequency ($\omega_{IF} \approx 120$ MHz) that can be digitised using standard analogue-to-digital converter (ADC) technologies.

In software we demodulate these signals to DC resulting in a time varying signal voltage given by,

$$V(t) = V_I(t) + iV_Q(t), \tag{D.2}$$

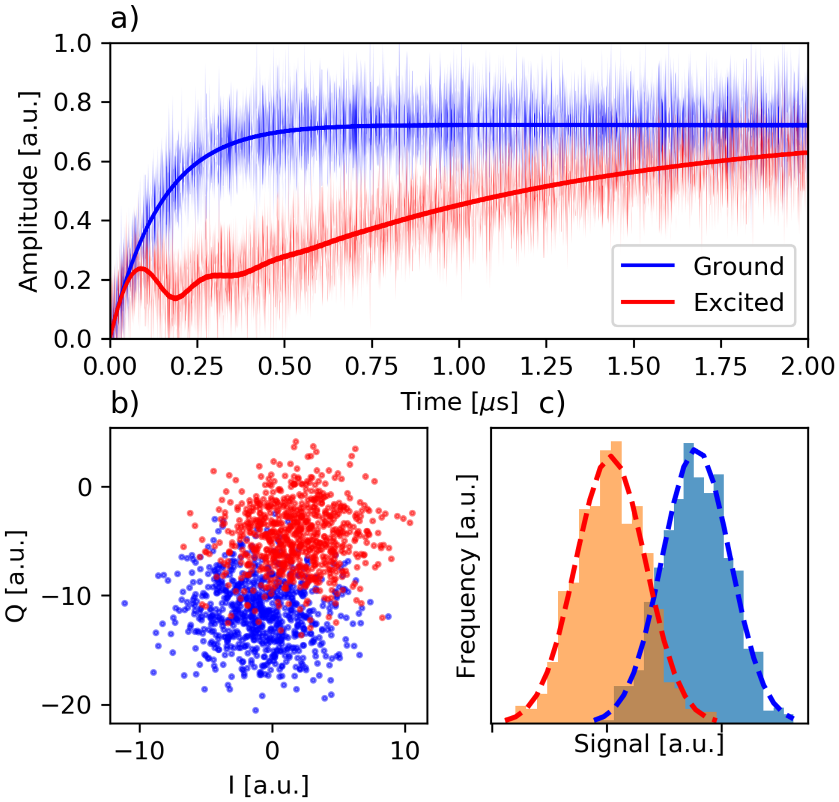

Figure D.1: Simulated magnitude of the time resolved resonator response for the qubit being in the ground (blue) and excited (red) states in the dispersive readout regime. The lighter background traces are simulated Gaussian noise. (Simulated $T_1 = 0.5\mu$s) (b) A scatter plot in the IQ plane of simulated measurements of 500 resonator traces, each with added noise. (c) Histograms and fitted Gaussian distributions of the IQ plane data projected onto the bisector of the centre of each of the red and blue clusters. From the overlap of these we can calculate the fidelity of the measurements.

where V_I and V_Q are the real and imaginary components of the trace. This sacrifices speed and fast feedback, but enables us to demodulate any arbitrary frequency. This allows simple processing of frequency domain multiplexed (FDM) signals for future experimental implementations. To return a single complex value ($S = I + iQ = \int V_I(t) + iV_Q(t)dt$) from a measurement, we integrate these demodulated signals.

The signals returning from the device have additional noise added to them, dominated by the noise added by the 4K HEMT amplifier. This is illustrated in the simulated traces shown in Fig. D.1 (a). Obtaining the single-shot signal value S from a number of these noisy traces results in 2D Gaussian distributions of signals, plotted on the complex IQ plane, shown in Fig. D.1 (b). Accurately determining the state of the qubit in a single measurement is dependent on the distinguishability of the state-dependant readout signal distributions. In order to improve the signal-to-noise of a measurement, we repeat N times and take an average, resulting in an ensemble measurement. This reduces the error in the measurement value by $1/\sqrt{N}$.

Assigning the qubit state from a single noisy measurement has an error that can be characterised by the measurement fidelity F, defined by,

$$F = 1 - (P(g|e) + P(e|g))/2, \tag{D.3}$$

where $P(a|b)$ is the probability of assigning state b given preparation of state a. In experiments this assignment is determined by the signal S being above or below a threshold, set by the intersection of the 1D projection of the IQ plane distributions, shown in Fig. D.1 (c). Measurement fidelity can be calculated from the overlap, I, between these two 1D histograms as $F = 1 - I/2$.

Signal processing techniques can also be implemented in order to improve the signal to noise ratio. As shown in Fig. D.1 (a), the ground and excited state traces take a finite time to diverge due to the ring-up time of the readout resonator. After long time the traces converge due to the qubit relaxation processes. As such, there is an optimum window ($[t_1 : t_2]$) in which to integrate in order to maximise signal to noise and measurement fidelity. A second order correction to this is a weighted integration procedure, such that,

$$S = \int_0^\infty V_I(t)W_I(t) + iV_Q(t)W_Q(t)dt, \tag{D.4}$$

where $W_{I/Q}$ are the real and imaginary weighting functions defined by,

$$W_{I/Q}(t) = V_{e,I/Q}(t) - V_{g,I/Q}(t). \tag{D.5}$$

Additional methods to increase the distinguishability of readout signals, such as longitudinal coupling based readout [28] or utilisation of higher excited states for readout [193, 194] are widely investigated.

Appendix E

Control of Multi-Mode Coaxmons

Control of a qubit is achieved by propagating signals through a microwave drive line capacitively coupled to the device such that the system evolves with the drive Hamiltonian [156],

$$\hat{H}^d(t) = \Omega(t) \left(\hat{a}^\dagger e^{-i\omega_d t} + \hat{a} e^{i\omega_d t} \right), \tag{E.1}$$

where Ω is the time varying drive amplitude, ω_d is the drive frequency.

In order to generate pulses, we use single sideband modulation (SSB) methods with a suppressed carrier frequency. Two channels of an arbitrary waveform generator (AWG) generate the envelope of the pulse at a lower intermediary frequency ($\omega_{IF} \approx 140$ MHz), which is then mixed with a CW tone from a signal generator at frequency ω_{LO}. This creates a pulse with the amplitude and phase components of the intermediate frequency (IF) signal, but with the frequency component $\omega_{LO} \pm \omega_{IF}$, as shown in Fig. E.1 (a). We use the lower sideband ($\omega_{LO} - \omega_{IF}$) in order to avoid unwanted driving of transitions of the transmon that are lower in frequency. Due to the complex transition landscape of the two-mode coaxial transmon, we carefully calibrate amplitude and phase offsets of the I and Q channels of the mixers to ensure sufficient isolation ($\approx 35 - 40$ dB) between opposing sidebands and suppression of LO frequencies. Improper calibration of these sidebands can lead to errors when driving single and multi-qubit gates, due to amplitude or phase errors and leakage [179].

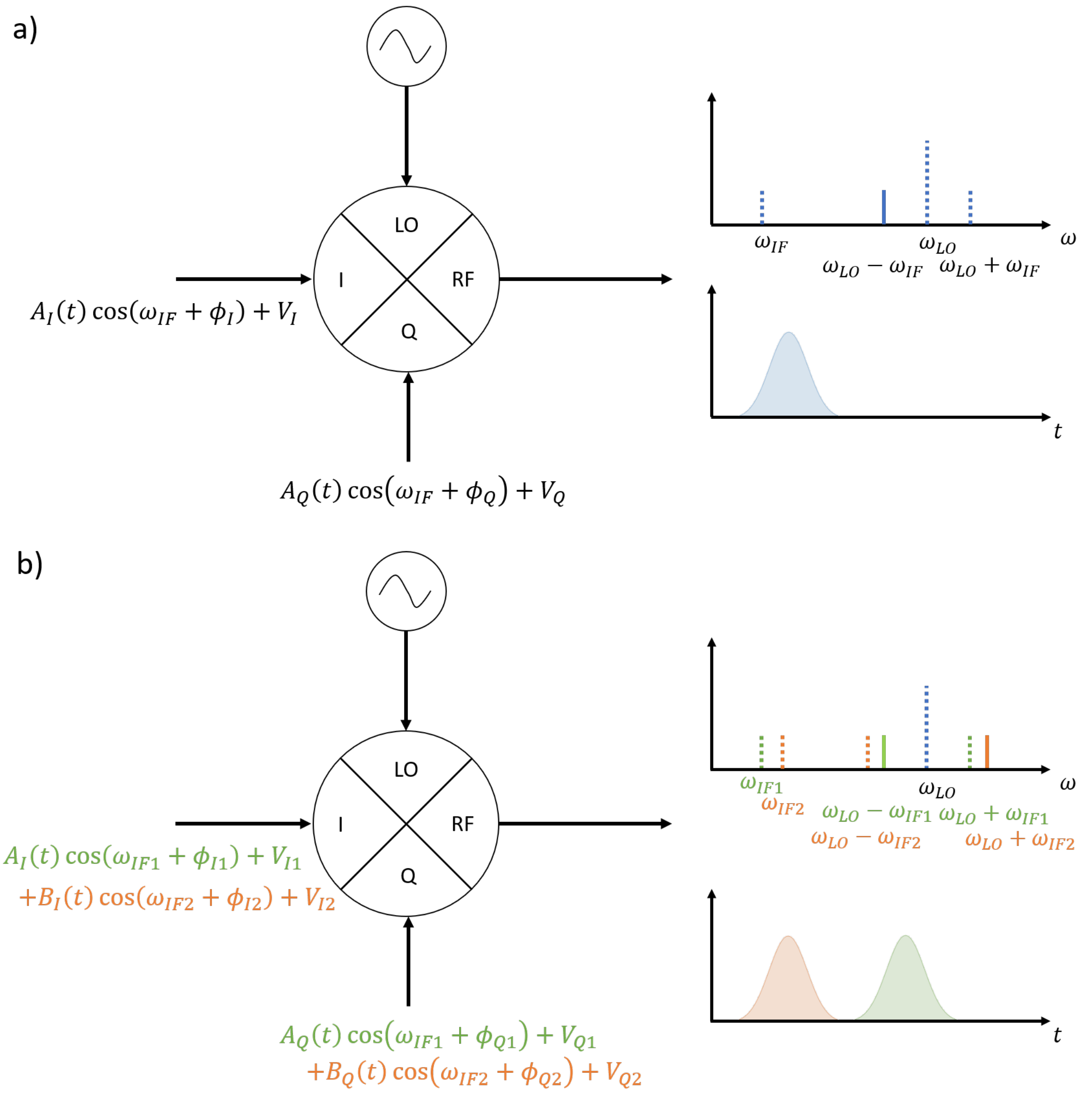

Figure E.1: Generation of qubit control signals. (a) Schematic of IQ modulation setup for generating control signals for a single qubit mode. Frequency spectrum and voltage time plot shown (right). Dashed lines in spectrum indicated suppressed frequency components due to tuning of ϕ_I/ϕ_Q and V_I, V_Q. (b) Schematic of IQ modulation setup for generating control signals for a multi-mode qubit. Two IF signals (green, orange) are used to generate pulses with frequency components shown (right).

The configuration of our qubit control setup is shown in Fig. C.1. We use signal generators with built-in IQ mixers to generate pulses. In addition, we use 10 dB attenuation to protect the devices from noise from room temperature electronics, anecdotally finding that residual excited state populations are reduced when used.

Generating IF signals with additional frequency components allows us to generate pulses at frequencies of $\omega_{LO} - \omega_{IF_1}$ and $\omega_{LO} - \omega_{IF_2}$, as shown in Fig. E.1 (b). With the appropriate choice of LO and IF frequencies, this allows us to generate control pulses for both modes of the two-mode coaxial transmon from a single pair of AWG channels, in a form of control multiplexing.

The precise shaping of signals, in order to optimally control the state of qubits is an active area of research [51, 53]. In our measurements, we employ Gaussian pulses for general control with first order DRAG corrections [178] when higher fidelity operations are required.

Appendix F

IR Radiation and Shielding

Whilst we focus on filtering within the band of readout and qubit frequencies, it has been shown that radiation and frequencies outside of this band can be highly detrimental to qubit performance [93]. Notably, radiation of $h\nu \approx 2\Delta$, where ν is the frequency and Δ is the superconducting band gap, is responsible for photon assisted processes within the Josephson junctions of devices [83] that contribute to excess excited state populations, and can be a dominant cause of loss in the system. In addition, this radiation can cause an excess residual number of photons in readout resonators, which in turn can lead to large qubit dephasing [195]. For aluminium based superconducting qubit devices, the 2Δ gap corresponds to frequencies of approximately $\nu \approx 100$ GHz. As depicted in the cryogenic system wiring diagram, there are 12 GHz low pass filters and $8 - 12$ GHz band pass filters in use, as in many cQED systems. These commercial filters are designed to operate well within the band of qubit and readout frequencies, however, transmission at higher frequencies ($\sim$ 100 GHz) is not well characterised. As such, for the increased performance of superconducting circuits systems, it is important to design solutions to address this issue.

There are two main paths that IR radiation can take to in order to impinge on the devices measured, as shown in Fig. F.1 (a). The first is travelling waves propagating through the coaxial lines of the fridge to the sample holder and device. The second

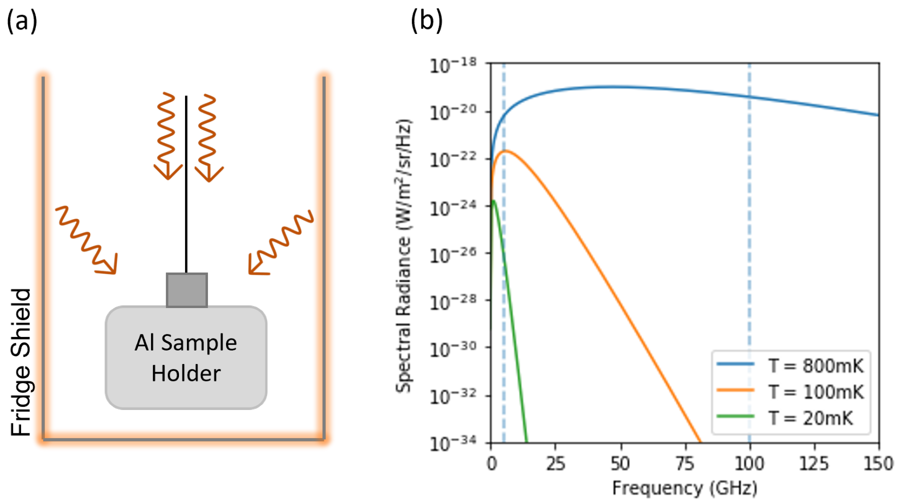

Figure F.1: (a) Illustration of the path of IR radiation incident on sample holder and device. Radiation can either propagate through the coaxial line to the device, or radiate from the shield of the fridge. (b) Spectral radiance from a blackbody of temperature 800 mK, 100 mK and 20 mK, corresponding to the plates of the dilution refrigeration system to which the still, cold plate and mixing chamber shields are thermalised. Vertical dashed lines indicate qubit frequencies (5 GHz) and the approximate frequency threshold for pair breaking photons (100 GHz).

is from free space radiation due to higher temperature stages of the dilution fridge. In the case where coaxial cables with a braided outer conductor that are designed for greater flexibility are used, the higher temperature components of the fridge can irradiate the cables since they are transparent to IR, resulting in a combination of the two main paths taken by the high frequency radiation. It is reasonable to assume mitigation of both sources simultaneously is required to increase qubit performance.

F.0.1 Light-Tight Shielding

Whilst many newer dilution refrigeration systems designed for the operation of superconducting quantum devices can be configured with mixing chamber shields to reduce IR radiation incident on devices, it is not always possible with older systems due to space requirements, or it is prohibitively expensive. As such, we design a smaller and more localised shielding solution to protect devices, whilst still allowing easy access to the device and re-usability.

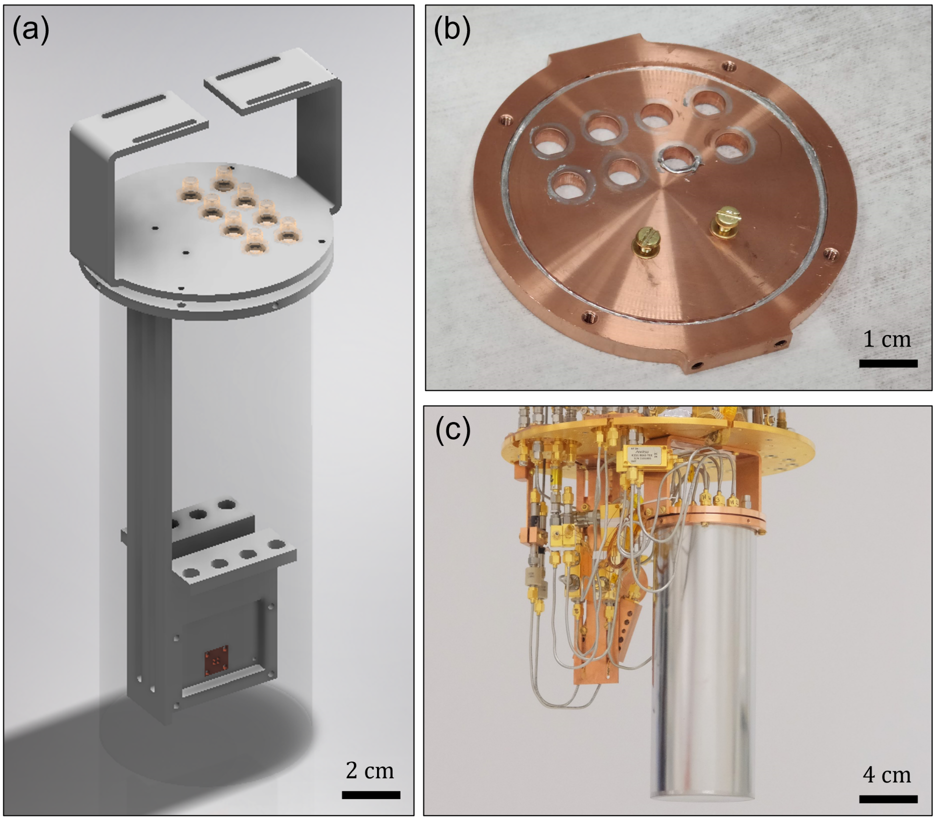

Figure F.2: Light-tight and magnetic shielding solution. (a) 3D render of light tight and magnetic shield assembly. The aluminium sample holder is attached to a vertical clamp such that it can be placed sufficiently far down the can such that it is effectively shielded from magnetic fields. The assembly is attached to the mixing chamber plate of a dilution fridge via the two brackets, made from oxygen free high conductivity (OFHC) copper, to enable proper thermalisation of the system. (b) Photograph of the inside of the shield lid showing the indium filled trench. This enables a good seal between the lid and magnetic shield parts. Hermetically sealed bulkheads (not shown) are also indium sealed. (c) Photograph of shield mounted to mixing chamber plate of cryogenic system. Wiring external to shield is constructed from plated semi-rigid cabling to maintain the light-tight environment.

The light-tight shield solution consists of a cylindrical μ-metal magnetic shield, commonly used in cQED experiments to protect devices from global magnetic field offsets, and a copper lid with hermetically sealed SMA feedthrough bulkhead connectors, as shown in Fig. F.2 (a) and (b). The assembly is attached to the mixing chamber plate of the fridge using a copper bracket, shown in Fig. F.2 (c).

Indium seals throughout the assembly to ensure the light-tightness of the shield.

The top of the μ-metal shield sits in a trench machined into the lid which is filled with indium, and is tightly pressed into the seal using the copper collar piece, shown in Fig. F.2 (b). In addition, indium is wrapped around the thread of the SMA feedthrough connectors on the inside, in order to prevent IR radiation leaking through.

In order to maintain the shielded environment and prevent IR radiation from leaking into the device via other paths outside of the shield, we use plated semi-rigid cabling for all connections from the fridge wiring to the lid of the light tight shield, shown in Fig. F.2 (c). Inside the shield, we use flexible braided coaxial cables, for ease of connectivity to the sample holder itself. As these cables are inside the shielded environment, it is not strictly necessary to use the plated cabling. Additional IR filters [94] can be attached to the SMA feedthroughs on the inside of the shield [196], however we do not investigate their usage or effectiveness in this work.

F.0.2 Qubit Temperature

The metrics we use to determine the effectiveness of shielding configurations are the energy relaxation time (T_1), ground and excited state populations (P_g, P_e), and qubit temperature (T_Q).

For a qubit with a high excited state population ($P_e \sim 10$ %), P_e can be extracted from spectroscopy of the resonator and fitting the relative heights of the spectral peaks [197], as shown in Fig. G.1. In the case of very hot qubits, there is a non-negligible population of the higher excited states that can also be identified with this method. For a qubit with a low excited state population ($P_e \sim 1$ %), the resonator spectroscopy method is insufficiently sensitive, and so single-shot measurements of ground state preparations are used, shown in Fig. G.2. We calculate the qubit temperature from the ground and excited state populations using the principle of detailed balance, such that $P_e/P_g = \exp(-\hbar\omega_Q/k_bT_Q)$.

Table F.1: Qubit parameters of different shield configurations.

Ref.	Shielding	T_1 (μs)	P_g (%)	P_e (%)	T_Q (mK)
This work	Still (800 mK)	~ 10	39	27	539
[160]	Cold Plate (100 mK)	179 (21)	87	13	104
This work	L-T Shield (20 mK)	192 (30)	99.5	0.5	37

We compare three different shielding configurations using these metrics, measuring the the same device (Q3 from P. Spring *et al.* [160], $\omega_Q/2\pi = 4.13$ GHz) in each.

The first shielding configuration is that of the dilution refrigerator setup shown in Fig. C.1, without the light-tight shield. In this configuration, the lowest temperature shield is a copper can mounted to the still plate (800 mK) of the fridge. The measured qubit temperatures are shown in Table F.1. The high excited state population and low energy relaxation time motivated the development of the light-tight shielding configuration. Thorough statistics of T_1 were not completed on this device.

The second configuration is the work of P. Spring *et al.* [160]. This was measured in a different dilution refrigerator fitted with a copper can mounted to the cold plate (100 mK) of the fridge. The measured qubit temperatures are shown in Table F.1.

The third shielding configuration is that of the setup shown in Fig. C.1, complete with light-tight shield assembly described in Section F.0.1. As seen by the measured qubit temperatures and excited state populations shown in Table F.1.

The developed light-tight shielding solution presents an order of magnitude improvement in all metrics over the first configuration presented, and a significantly lower qubit temperature than what was presented in [160]. This suggests not only that improper shielding from IR radiation is a significant source of loss in superconducting circuits, but also that more thorough shielding can reduce excitation rates due to IR radiation. This work enables the measurement of high coherence devices presented in following chapters, operating in the experimental setup shown in Fig. C.1.

F.0.3 Further Work

Whilst we demonstrate improvements in qubit performance with the addition of the light-tight shielding solution, there are still more thorough A/B testing measurements required to more accurately determine the contributing sources of loss and decoherence in our systems and which elements protect against them. We do not investigate parity jumps or determine quasiparticle densities, which are an additional indicator of the effectiveness of shielding and filtering. There are more thorough investigations into these effects in other works [80, 83].

An additional potential improvement to the light tight shield is the addition of an IR absorber on the inside of the shield. This would consist of coating the inside of the mu metal shield in a material that absorbs IR photons, and reduces the probability of any photons that do leak into the shield being reflected and reaching the device. Previous works [198] have shown that entirely encasing the sample holder in an IR absorber can increase coherence, at the obvious cost of re-usability, and so unfeasible in our configurations.

Finally, the geometry of the qubits and resonators produces spurious resonant modes at the higher frequencies ≈ 100 GHz. It has been shown that the pad geometry acts as an antenna for these frequencies, and so the devices are resonant absorbers of pair-breaking radiation [96]. Further investigation and design considerations can be made to generate qubit designs that are insensitive to this effect and result in reduced radiative losses at the qubit frequency.

Appendix G

Qubit Temperature Measurement Methodology

To understand what is meant by a poorly performing or “hot” qubit, we conduct measurements on a device known to show high coherence and energy relaxation times [160] and compare measured parameters when it is placed in the Triton 200 system with native shielding configuration. An initial spectroscopy measurement of the resonator shows multiple frequency peaks, corresponding to the qubit having significant population of the first, second, and third excited states and the dispersive shift between the qubit and resonator, as shown in Fig. G.1. From the relative weights of each Lorentzian lineshape we are able to extract the state populations [197].

In contrast, when measuring a qubit with a much lower excited state population (such as in the light-tight shielding configuration shown in Appendix F), initial spectroscopy measurements of the resonator show only a single peak, corresponding to the qubit being mostly in the ground state, and no excited state population is measurable in this method, as shown in Fig. G.2. To more accurately determine the residual excited state population, we perform single shot readout measurements of the qubit initialised in the ground state (by waiting 5 $T1$ periods between measurements). We plot the resulting signals in the IQ plane and fit to two spherical Gaussian distributions. By examining the relative weights of these two distributions and normalising, we can obtain the percentage of readout measurements for which the qubit was in

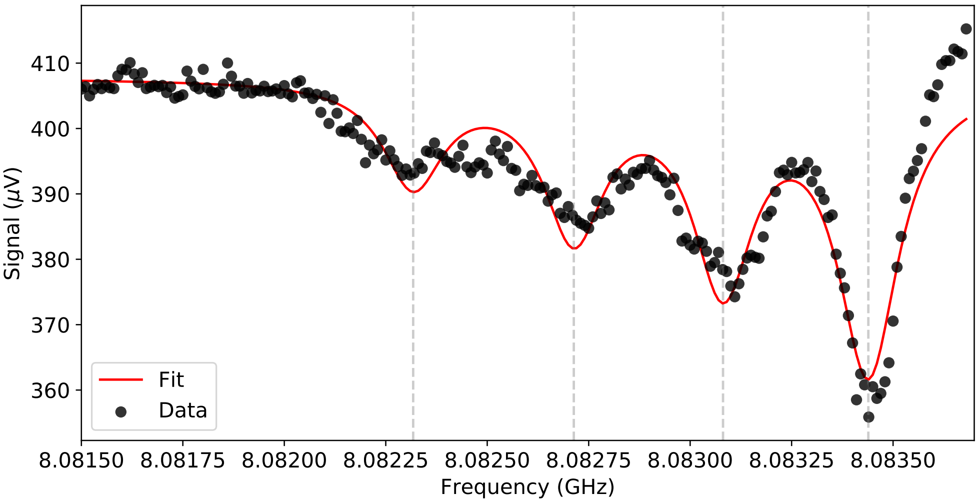

Figure G.1: Spectroscopy of a resonator coupled to a qubit with high residual population of higher excited states, described as ”hot”. Data is fitted to a sum of four Lorentzian functions of equal linewidth but different center frequency and amplitude. Vertical dashed lines correspond to resonator frequency with the qubit in the ground, first excited state, second excited state, and third excited state from right to left. These peaks are separated by the dispersive shift between the resonator and qubit (2χ).

the excited state, and thus the residual excited state population. This plot is shown in Fig. G.2, where the residual excited state population is calculated to be 0.5%.

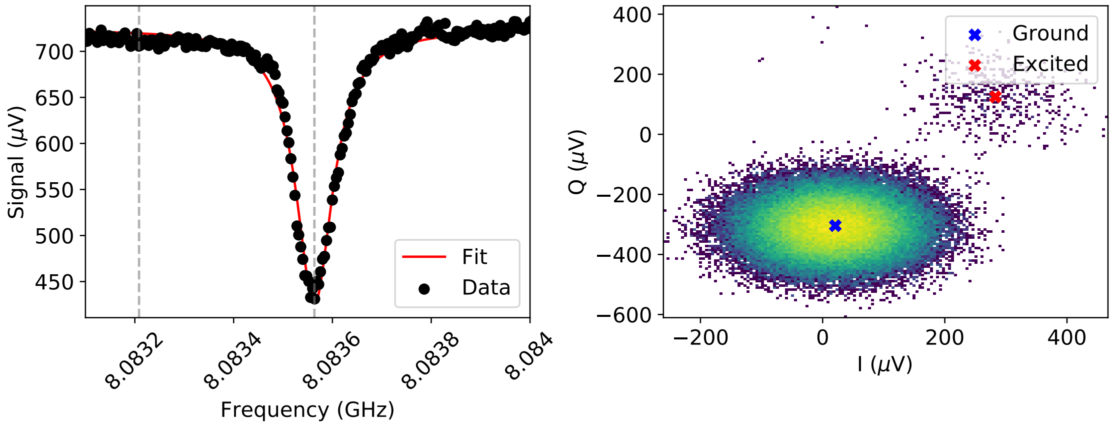

Figure G.2: Resonator spectroscopy and residual excited state population of an IR shielded device. In contrast to Fig G.1, the spectroscopy only shows a single peak, and no additional features 2χ lower in frequency, indicated by the vertical dashed line. The histogram on the right shows the signal measured from 10^5 measurements of a qubit initialised in the ground state (by waiting 5 T_1 periods between measurements). The large distribution indicates the measurements of the qubit in the ground state, and the second smaller distribution in the upper right indicates measurements of the qubit in the excited state. From the fitting we determine a residual excited state population of 0.5%.

Bibliography

[1] D. P. DiVincenzo. “The physical implementation of quantum computation”. *Fortschritte der Physik* 48.9-11 (Sept. 2000), pp. 771–783.

[2] D. Leibfried et al. “Quantum dynamics of single trapped ions”. *Reviews of Modern Physics* 75.1 (Mar. 2003), pp. 281–324.

[3] C. D. Bruzewicz et al. “Trapped-ion quantum computing: Progress and challenges”. *Applied Physics Reviews* 6.2 (June 2019), p. 021314.

[4] S. Takeda and A. Furusawa. “Toward large-scale fault-tolerant universal photonic quantum computing”. *APL Photonics* 4.6 (June 2019), p. 060902.

[5] M. Saffman. “Quantum computing with atomic qubits and Rydberg interactions: progress and challenges”. *Journal of Physics B: Atomic, Molecular and Optical Physics* 49.20 (Oct. 2016), p. 202001.

[6] D. Loss and D. P. DiVincenzo. “Quantum computation with quantum dots”. *Physical Review A* 57.1 (Jan. 1998), pp. 120–126.

[7] M. H. Devoret and R. J. Schoelkopf. “Superconducting Circuits for Quantum Information: An Outlook”. *Science* 339.6124 (Mar. 2013), 1169 LP –1174.

[8] F. Arute et al. “Quantum supremacy using a programmable superconducting processor”. *Nature* 574.7779 (Oct. 2019), pp. 505–510.

[9] J. Koch et al. “Charge-insensitive qubit design derived from the Cooper pair box”. *Physical Review A* 76.4 (Oct. 2007), p. 042319.

[10] V. E. Manucharyan et al. “Fluxonium: Single Cooper-Pair Circuit Free of Charge Offsets”. *Science* 326.5949 (Oct. 2009), 113 LP –116.

[11] A. Kou et al. “Fluxonium-based artificial molecule with a tunable magnetic moment”. *Physical Review X* 7.3 (Aug. 2017), pp. 1–8.

[12] P. Groszkowski et al. “Coherence properties of the 0–π qubit”. *New Journal of Physics* 20.4 (Apr. 2018), p. 43053.

[13] A. Gyenis et al. “ Experimental Realization of a Protected Superconducting Circuit Derived from the $0 - \pi$ Qubit ”. *PRX Quantum* 2.1 (Mar. 2021), p. 1.

[14] N. Sundaresan et al. “Reducing Unitary and Spectator Errors in Cross Resonance with Optimized Rotary Echoes”. *PRX Quantum* 1.2 (Dec. 2020), p. 1.

[15] M. Takita et al. “Demonstration of Weight-Four Parity Measurements in the Surface Code Architecture”. *Physical Review Letters* 117.21 (Nov. 2016), p. 210505.

[16] F. Yan et al. “Tunable Coupling Scheme for Implementing High-Fidelity Two-Qubit Gates”. *Physical Review Applied* 10.5 (Nov. 2018), p. 054062.

[17] T. Roy et al. “Implementation of Pairwise Longitudinal Coupling in a Three-Qubit Superconducting Circuit”. *Physical Review Applied* 7.5 (May 2017), pp. 1–15.

[18] S. J. Srinivasan et al. “Tunable coupling in circuit quantum electrodynamics using a superconducting charge qubit with a V-Shaped energy level diagram”. *Physical Review Letters* 106.8 (Feb. 2011), pp. 1–4.

[19] P. Mundada et al. “Suppression of Qubit Crosstalk in a Tunable Coupling Superconducting Circuit”. *Physical Review Applied* 12.5 (Nov. 2019), p. 054023.

[20] S. Richer et al. “Inductively shunted transmon qubit with tunable transverse and longitudinal coupling”. *Physical Review B* 96.17 (Nov. 2017), pp. 1–14.

[21] A. Noguchi et al. “Fast parametric two-qubit gates with suppressed residual interaction using the second-order nonlinearity of a cubic transmon”. *Physical Review A* 102.6 (Dec. 2020), p. 62408.

[22] W. C. Smith et al. “Superconducting circuit protected by two-Cooper-pair tunneling”. *npj Quantum Information* 6.1 (Jan. 2020), p. 8.

[23] B. K. Mitchell et al. “Hardware-Efficient Microwave-Activated Tunable Coupling between Superconducting Qubits”. *Physical Review Letters* 127.20 (Nov. 2021), p. 200502.

[24] K. X. Wei et al. “Quantum crosstalk cancellation for fast entangling gates and improved multi-qubit performance”. *arXiv preprint arXiv:2106.00675* (June 2021).

[25] P. Kumar et al. “Origin and Reduction of 1/f Magnetic Flux Noise in Superconducting Devices”. *Physical Review Applied* 6.4 (Oct. 2016), p. 041001.

[26] S. Krinner et al. “Engineering cryogenic setups for 100-qubit scale superconducting circuit systems”. *EPJ Quantum Technology* 6.1 (Dec. 2019), p. 2.

[27] É. Dumur et al. “V-shaped superconducting artificial atom based on two inductively coupled transmons”. *Physical Review B* 92.2 (July 2015), p. 020515.

[28] R. Dassonneville et al. “Fast High-Fidelity Quantum Nondemolition Qubit Readout via a Nonperturbative Cross-Kerr Coupling”. *Physical Review X* 10.1 (Mar. 2020).

[29] J. M. Gambetta, A. A. Houck, and A. Blais. “Superconducting Qubit with Purcell Protection and Tunable Coupling”. *Physical Review Letters* 106.3 (Jan. 2011), p. 30502.

[30] G. Zhang et al. “Suppression of photon shot noise dephasing in a tunable coupling superconducting qubit”. *npj Quantum Information* 3.1 (Jan. 2017), p. 1.

[31] T. Roy et al. “Programmable Superconducting Processor with Native Three-Qubit Gates”. *Physical Review Applied* 14.1 (July 2020).

[32] Y. A. Pashkin et al. “Quantum oscillations in two coupled charge qubits”. *Nature* 421.6925 (Feb. 2003), pp. 823–826.

[33] M. V. Gustafsson et al. “Thermal properties of charge noise sources”. *Physical Review B* 88.24 (Dec. 2013), pp. 1–7.

[34] J. A. Schreier et al. “Suppressing charge noise decoherence in superconducting charge qubits”. *Physical Review B* 77.18 (May 2008), pp. 2–5.

[35] B. G. Christensen et al. “Anomalous charge noise in superconducting qubits”. *Physical Review B* 100.14 (Oct. 2019), p. 140503.

[36] C. D. Wilen et al. “Correlated Charge Noise and Relaxation Errors in Superconducting Qubits”. *Nature* 594.7863 (June 2020), pp. 1–19.

[37] D. M. Tennant et al. “Low-Frequency Correlated Charge-Noise Measurements Across Multiple Energy Transitions in a Tantalum Transmon”. *PRX Quantum* 3.3 (July 2022), p. 030307.

[38] J. Wills et al. “Spatial Charge Sensitivity in a Multimode Superconducting Qubit”. *Physical Review Applied* 17.2 (Feb. 2022), p. 024058.

[39] U. Vool and M. Devoret. “Introduction to quantum electromagnetic circuits”. *International Journal of Circuit Theory and Applications* 45.7 (2017), pp. 897–934.

[40] M. H. Devoret. “Quantum fluctuations in electrical circuits”. In: *Quantum Fluctuations: Les Houches Session LXIII.* Les Houches (France): Elsevier, 1997.

[41] M. Esposito et al. “Perspective on traveling wave microwave parametric amplifiers”. *Applied Physics Letters* 119.12 (Sept. 2021), p. 120501.

[42] S. Kono et al. “Quantum non-demolition detection of an itinerant microwave photon”. *Nature Physics* 14.6 (June 2018), pp. 546–549.

[43] A. V. Dixit et al. “Searching for Dark Matter with a Superconducting Qubit”. *Physical Review Letters* 126.14 (Apr. 2021), p. 141302.

[44] A. Blais et al. “Circuit quantum electrodynamics”. *Reviews of Modern Physics* 93.2 (May 2021), p. 025005.

[45] P. Groszkowski and J. Koch. “Scqubits: a Python package for superconducting qubits”. *Quantum* 5 (2021), p. 583.

[46] B. Josephson. “Possible new effects in superconductive tunnelling”. *Physics Letters* 1.7 (July 1962), pp. 251–253.

[47] S. Fritz et al. “Optimization of Al/AlOx/Al-layer systems for Josephson junctions from a microstructure point of view”. *Journal of Applied Physics* 125.16 (Apr. 2019), p. 165301.

[48] R. D. Parks. *Superconductivity.* Ed. by R. D. Parks. New York: Routledge, Mar. 1969.

[49] Y. A. Pashkin et al. “Josephson charge qubits: a brief review”. *Quantum Information Processing* 8.2-3 (June 2009), pp. 55–80.

[50] M. A. Nielsen and I. Chuang. *Quantum computation and quantum information.* Cambridge: Cambridge University Press, 2002.

[51] P. Krantz et al. “A quantum engineer’s guide to superconducting qubits”. *Applied Physics Reviews* 6.2 (2019).

[52] Y.-H. Ji. “Investigation of Decoherence of Superconducting Charge Qubit Entangled with the Environment”. *International Journal of Theoretical Physics* 47.9 (Sept. 2008), pp. 2363–2371.

[53] M. Kjaergaard et al. “Superconducting Qubits: Current State of Play”. *Annual Review of Condensed Matter Physics* 11.1 (Mar. 2020), pp. 369–395.

[54] E. M. Purcell, H. C. Torrey, and R. V. Pound. “Resonance Absorption by Nuclear Magnetic Moments in a Solid”. *Physical Review* 69.1-2 (Jan. 1946), pp. 37–38.

[55] D. Esteve, M. H. Devoret, and J. M. Martinis. “Effect of an arbitrary dissipative circuit on the quantum energy levels and tunneling of a Josephson junction”. *Physical Review B* 34.1 (July 1986), pp. 158–163.

[56] A. P. Sears et al. “Photon shot noise dephasing in the strong-dispersive limit of circuit QED”. *Physical Review B* 86.18 (Nov. 2012), p. 180504.

[57] C. R. H. McRae et al. "Materials loss measurements using superconducting microwave resonators". *Review of Scientific Instruments* 91.9 (Sept. 2020), p. 091101.

[58] A. Premkumar et al. "Microscopic relaxation channels in materials for superconducting qubits". *Communications Materials* 2.1 (Dec. 2021), p. 72.

[59] R. J. Cava et al. "Electrical and magnetic properties of Nb2O5-δ crystallographic shear structures". *Physical Review B* 44.13 (Oct. 1991), pp. 6973–6981.

[60] C. Müller, J. H. Cole, and J. Lisenfeld. "Towards understanding two-level-systems in amorphous solids: insights from quantum circuits". *Reports on Progress in Physics* 82.12 (Dec. 2019), p. 124501.

[61] S. E. de Graaf et al. "Two-level systems in superconducting quantum devices due to trapped quasiparticles". *Science Advances* 6.51 (Dec. 2020).

[62] S. E. de Graaf et al. "Quantifying dynamics and interactions of individual spurious low-energy fluctuators in superconducting circuits". *Physical Review B* 103.17 (May 2021), p. 174103.

[63] S. E. de Graaf et al. "Suppression of low-frequency charge noise in superconducting resonators by surface spin desorption". *Nature Communications* 9.1 (Dec. 2018), p. 1143.

[64] P. Dutta and P. M. Horn. "Low-frequency fluctuations in solids: 1/f noise". *Reviews of Modern Physics* 53.3 (July 1981), pp. 497–516.

[65] A. B. Zorin et al. "Background charge noise in metallic single-electron tunneling devices". *Physical Review B* 53.20 (May 1996), pp. 13682–13687.

[66] Y. Nakamura et al. "Charge Echo in a Cooper-Pair Box". *Physical Review Letters* 88.4 (2002), p. 4.

[67] O. Astafiev et al. "Quantum Noise in the Josephson Charge Qubit". *Physical Review Letters* 93.26 (Dec. 2004), p. 267007.

[68] J. Gambetta. *Quantum Information Processing: Lecture Notes of the 44th IFF Spring School*. Forschungszentrum Julich: Forschungszentrum Julich GmbH, 2014.

[69] J. M. Martinis. “Saving superconducting quantum processors from decay and correlated errors generated by gamma and cosmic rays”. *npj Quantum Information* 7.1 (Dec. 2021), p. 90.

[70] A. P. Vepsäläinen et al. “Impact of ionizing radiation on superconducting qubit coherence”. *Nature* 584.7822 (Aug. 2020), pp. 551–556.

[71] L. Cardani et al. “Reducing the impact of radioactivity on quantum circuits in a deep-underground facility”. *Nature Communications* 12.1 (May 2021), p. 2733.

[72] F. Henriques et al. “Phonon traps reduce the quasiparticle density in superconducting circuits”. *Applied Physics Letters* 115.21 (Nov. 2019), p. 212601.

[73] E. Aguayo Navarrete et al. *Cosmic Ray Interactions in Shielding Materials*. Tech. rep. Richland, WA (United States): Pacific Northwest National Laboratory (PNNL), Sept. 2011.

[74] A. G. Fowler et al. “Surface codes: Towards practical large-scale quantum computation”. *Physical Review A* 86.3 (Sept. 2012), p. 032324.

[75] R. Barends et al. “Superconducting quantum circuits at the surface code threshold for fault tolerance”. *Nature* 508.7497 (Apr. 2014), pp. 500–503.

[76] J. Kelly et al. “State preservation by repetitive error detection in a superconducting quantum circuit”. *Nature* 519.7541 (Mar. 2015), pp. 66–69.

[77] L. Glazman and G. Catelani. “Bogoliubov quasiparticles in superconducting qubits”. *SciPost Physics Lecture Notes* (June 2021), p. 31.

[78] S. A. Kivelson and D. S. Rokhsar. “Bogoliubov quasiparticles, spinons, and spin-charge decoupling in superconductors”. *Physical Review B* 41.16 (June 1990), pp. 11693–11696.

[79] G. Catelani. “Parity switching and decoherence by quasiparticles in single-junction transmons”. *Physical Review B* 89.9 (Mar. 2014), p. 094522.

[80] K. Serniak et al. “Hot Nonequilibrium Quasiparticles in Transmon Qubits”. *Physical Review Letters* 121.15 (Oct. 2018), p. 157701.

[81] C. Wang et al. “Measurement and control of quasiparticle dynamics in a superconducting qubit”. *Nature Communications* 5.1 (Dec. 2014), p. 5836.

[82] M. D. Shaw et al. “Kinetics of nonequilibrium quasiparticle tunneling in superconducting charge qubits”. *Physical Review B* 78.2 (July 2008), p. 024503.

[83] S. Diamond et al. “Distinguishing parity-switching mechanisms in a superconducting qubit”. *arXiv preprint arXiv: 2204.07458* (Apr. 2022).

[84] J. Wenner et al. “Excitation of Superconducting Qubits from Hot Nonequilibrium Quasiparticles”. *Physical Review Letters* 110.15 (Apr. 2013), p. 150502.

[85] J. M. Martinis, M. Ansmann, and J. Aumentado. “Energy Decay in Superconducting Josephson-Junction Qubits from Nonequilibrium Quasiparticle Excitations”. *Physical Review Letters* 103.9 (Aug. 2009), p. 097002.

[86] M. Lenander et al. “Measurement of energy decay in superconducting qubits from nonequilibrium quasiparticles”. *Physical Review B* 84.2 (July 2011), p. 024501.

[87] L. Grünhaupt et al. “Loss Mechanisms and Quasiparticle Dynamics in Superconducting Microwave Resonators Made of Thin-Film Granular Aluminum”. *Physical Review Letters* 121.11 (Sept. 2018), p. 117001.

[88] G. Catelani et al. “Relaxation and frequency shifts induced by quasiparticles in superconducting qubits”. *Physical Review B* 84.6 (Aug. 2011), p. 064517.

[89] L. Sun et al. “Measurements of Quasiparticle Tunneling Dynamics in a Band-Gap-Engineered Transmon Qubit”. *Physical Review Letters* 108.23 (June 2012), p. 230509.

[90] P. J. de Visser et al. “Evidence of a Nonequilibrium Distribution of Quasiparticles in the Microwave Response of a Superconducting Aluminum Resonator”. *Physical Review Letters* 112.4 (Jan. 2014), p. 047004.

[91] K. Segall et al. “Dynamics and energy distribution of nonequilibrium quasiparticles in superconducting tunnel junctions”. *Physical Review B* 70.21 (Dec. 2004), p. 214520.

[92] R. Barends et al. “Minimizing quasiparticle generation from stray infrared light in superconducting quantum circuits”. *Applied Physics Letters* 99.11 (Sept. 2011), p. 113507.

[93] A. D. Córcoles et al. “Protecting superconducting qubits from radiation”. *Applied Physics Letters* 99.18 (Oct. 2011), p. 181906.

[94] S. Danilin et al. “Engineering the microwave to infrared noise photon flux for superconducting quantum systems”. *EPJ Quantum Technology* 9.1 (Dec. 2022), p. 1.

[95] R. T. Gordon et al. “Environmental radiation impact on lifetimes and quasiparticle tunneling rates of fixed-frequency transmon qubits”. *Applied Physics Letters* 120.7 (Feb. 2022), p. 074002.

[96] O. Rafferty et al. “Spurious Antenna Modes of the Transmon Qubit”. *arXiv preprint arXiv:2103.06803* (Mar. 2021).

[97] C. Kurter et al. “Quasiparticle tunneling as a probe of Josephson junction barrier and capacitor material in superconducting qubits”. *npj Quantum Information* 8.1 (Dec. 2022), p. 31.

[98] M. McEwen et al. “Resolving catastrophic error bursts from cosmic rays in large arrays of superconducting qubits”. *Nature Physics* 18.1 (Jan. 2022), pp. 107–111.

[99] U. Patel et al. “Phonon-mediated quasiparticle poisoning of superconducting microwave resonators”. *Physical Review B* 96.22 (Dec. 2017), p. 220501.

[100] A. Bargerbos et al. “Mitigation of quasiparticle loss in superconducting qubits by phonon scattering”. *arXiv preprint arXiv: 2207.12754* (July 2022).

[101] V. Iaia et al. “Phonon downconversion to suppress correlated errors in superconducting qubits”. *arXiv preprint arXiv:2203.06586* (Mar. 2022).

[102] M. Snyder et al. “Suppression of Phonon-mediated Quasiparticle Poisoning by Silicon Micromachining”. In: *APS March Meeting Abstracts*. Vol. 2022. APS Meeting Abstracts. Jan. 2022, Y40.003.

[103] R.-P. Riwar et al. “Normal-metal quasiparticle traps for superconducting qubits”. *Physical Review B* 94.10 (Sept. 2016), p. 104516.

[104] S. Gustavsson et al. “Suppressing relaxation in superconducting qubits by quasiparticle pumping”. *Science* 354.6319 (Dec. 2016), pp. 1573–1577.

[105] R.-P. Riwar and G. Catelani. “Efficient quasiparticle traps with low dissipation through gap engineering”. *Physical Review B* 100.14 (Oct. 2019), p. 144514.

[106] Y. Chen et al. “Qubit Architecture with High Coherence and Fast Tunable Coupling”. *Physical Review Letters* 113.22 (Nov. 2014), p. 220502.

[107] S. Rasmussen et al. “Superconducting Circuit Companion—an Introduction with Worked Examples”. *PRX Quantum* 2.4 (Dec. 2021), p. 040204.

[108] J. Majer et al. “Coupling superconducting qubits via a cavity bus”. *Nature* 449.7161 (Sept. 2007), pp. 443–447.

[109] S. Richer and D. DiVincenzo. “Circuit design implementing longitudinal coupling: A scalable scheme for superconducting qubits”. *Physical Review B* 93.13 (Apr. 2016), p. 134501.

[110] S. Rebić, J. Twamley, and G. J. Milburn. “Giant Kerr Nonlinearities in Circuit Quantum Electrodynamics”. *Physical Review Letters* 103.15 (Oct. 2009), p. 150503.

[111] X.-Y. Lü et al. “Two-qubit gate operations in superconducting circuits with strong coupling and weak anharmonicity”. *New Journal of Physics* 14.7 (July 2012), p. 073041.

[112] J. M. Chow et al. “Simple All-Microwave Entangling Gate for Fixed-Frequency Superconducting Qubits”. *Physical Review Letters* 107.8 (Aug. 2011), p. 080502.

[113] S. Sheldon et al. “Procedure for systematically tuning up cross-talk in the cross-resonance gate”. *Physical Review A* 93.6 (June 2016), p. 060302.

[114] J. M. Chow et al. “Microwave-activated conditional-phase gate for superconducting qubits”. *New Journal of Physics* 15.11 (Nov. 2013), p. 115012.

[115] M. Malekakhlagh and E. Magesan. “Mitigating off-resonant error in the cross-resonance gate”. *Physical Review A* 105.1 (Jan. 2022), p. 012602.

[116] L. DiCarlo et al. “Demonstration of two-qubit algorithms with a superconducting quantum processor”. *Nature* 460.7252 (July 2009), pp. 240–244.

[117] E. Magesan and J. M. Gambetta. “Effective Hamiltonian models of the cross-resonance gate”. *Physical Review A* 101.5 (May 2020), p. 052308.

[118] G. S. Paraoanu. “Microwave-induced coupling of superconducting qubits”. *Physical Review B* 74.14 (Oct. 2006), p. 140504.

[119] Y. Hu et al. “Cross-Kerr-effect induced by coupled Josephson qubits in circuit quantum electrodynamics”. *Physical Review A* 84.1 (July 2011), p. 012329.

[120] P. Jurcevic et al. “Demonstration of quantum volume 64 on a superconducting quantum computing system”. *Quantum Science and Technology* 6.2 (Apr. 2021), p. 025020.

[121] D. C. McKay et al. “Three-Qubit Randomized Benchmarking”. *Physical Review Letters* 122.20 (May 2019), p. 200502.

[122] S. Krinner et al. “Benchmarking Coherent Errors in Controlled-Phase Gates due to Spectator Qubits”. *Physical Review Applied* 14.2 (Aug. 2020), p. 024042.

[123] K. X. Wei et al. “Verifying multipartite entangled Greenberger-Horne-Zeilinger states via multiple quantum coherences”. *Physical Review A* 101.3 (Mar. 2020), p. 032343.

[124] S. H. W. van der Ploeg et al. “Controllable Coupling of Superconducting Flux Qubits”. *Physical Review Letters* 98.5 (Feb. 2007), p. 057004.

[125] S. S. Hong et al. “Demonstration of a parametrically activated entangling gate protected from flux noise”. *Physical Review A* 101.1 (Jan. 2020), p. 012302.

[126] M. R. Geller et al. “Tunable coupler for superconducting Xmon qubits: Perturbative nonlinear model”. *Physical Review A* 92.1 (July 2015), p. 012320.

[127] S. J. Weber et al. "Coherent Coupled Qubits for Quantum Annealing". *Physical Review Applied* 8.1 (July 2017), p. 014004.

[128] M. C. Collodo et al. "Implementation of Conditional Phase Gates Based on Tunable ZZ Interactions". *Physical Review Letters* 125.24 (Dec. 2020), p. 240502.

[129] Y. Xu et al. "High-Fidelity, High-Scalability Two-Qubit Gate Scheme for Superconducting Qubits". *Physical Review Letters* 125.24 (Dec. 2020), p. 240503.

[130] Y. Sung et al. "Realization of High-Fidelity CZ and ZZ-Free iSWAP Gates with a Tunable Coupler". *Physical Review X* 11.2 (June 2021), p. 021058.

[131] J. Stehlik et al. "Tunable Coupling Architecture for Fixed-Frequency Transmon Superconducting Qubits". *Physical Review Letters* 127.8 (Aug. 2021), p. 080505.

[132] C. Leroux, A. Di Paolo, and A. Blais. "Superconducting Coupler with Exponentially Large On:Off Ratio". *Physical Review Applied* 16.6 (Dec. 2021), p. 064062.

[133] F. Marxer et al. "Long-distance transmon coupler with CZ gate fidelity above 99.8%". *arXiv preprint arXiv:2208.09460* (Aug. 2022).

[134] A. Kandala et al. "Demonstration of a High-Fidelity cnot Gate for Fixed-Frequency Transmons with Engineered ZZ Suppression". *Physical Review Letters* 127.13 (Sept. 2021), p. 130501.

[135] P. Zhao et al. "High-Contrast ZZ Interaction Using Superconducting Qubits with Opposite-Sign Anharmonicity". *Physical Review Letters* 125.20 (Nov. 2020), p. 200503.

[136] J. Ku et al. "Suppression of Unwanted ZZ Interactions in a Hybrid Two-Qubit System". *Physical Review Letters* 125.20 (Nov. 2020), p. 200504.

[137] X. Xu and M. H. Ansari. "ZZ Freedom in Two-Qubit Gates". *Physical Review Applied* 15.6 (June 2021), p. 064074.

[138] J. Q. You and F. Nori. “Atomic physics and quantum optics using superconducting circuits”. *Nature* 474.7353 (June 2011), pp. 589–597.

[139] F. Jelezko et al. “Observation of Coherent Oscillations in a Single Electron Spin”. *Physical Review Letters* 92.7 (Feb. 2004), p. 076401.

[140] F. Lecocq et al. “Coherent frequency conversion in a superconducting artificial atom with two internal degrees of freedom”. *Physical Review Letters* 108.10 (Mar. 2012).

[141] F. Lecocq et al. “Nonlinear coupling between the two oscillation modes of a dc SQUID”. *Physical Review Letters* 107.19 (Nov. 2011).

[142] K.-H. Chiang and Y.-F. Chen. “Tunable Λ -type system made of a superconducting qubit pair”. *Physical Review A* 106.2 (Aug. 2022), p. 023707.

[143] A. J. Hoffman et al. “Coherent control of a superconducting qubit with dynamically tunable qubit-cavity coupling”. *Physical Review B* 84.18 (Nov. 2011).

[144] Z. K. K. Minev et al. “To catch and reverse a quantum jump mid-flight”. *Nature* 570.7760 (June 2019), pp. 200–204.

[145] I. Diniz et al. “Ultrafast quantum nondemolition measurements based on a diamond-shaped artificial atom”. *Physical Review A* 87.3 (Mar. 2013), p. 033837.

[146] A. D. K. Finck et al. “Suppressed crosstalk between two-junction superconducting qubits with mode-selective exchange coupling”. *Physical Review Applied* 16.5 (Nov. 2021), pp. 1–5.

[147] S. Hazra et al. “Engineering cross resonance interaction in multi-modal quantum circuits”. *Applied Physics Letters* 116.15 (Apr. 2020), p. 152601.

[148] K. N. Nesterov et al. “Microwave-activated controlled- Z gate for fixed-frequency fluxonium qubits”. *Physical Review A* 98.3 (Sept. 2018), p. 30301.

[149] T. Roy et al. “Multimode superconducting circuits for realizing strongly coupled multiqubit processor units”. *Physical Review A* 98.5 (Nov. 2018), pp. 1–14.

[150] J. F. Marques et al. “Logical-qubit operations in an error-detecting surface code”. *Nature Physics* 18.1 (Jan. 2022), pp. 80–86.

[151] R. Versluis et al. “Scalable Quantum Circuit and Control for a Superconducting Surface Code”. *Physical Review Applied* 8.3 (Sept. 2017), p. 034021.

[152] D. Rosenberg et al. “3D integrated superconducting qubits”. *npj Quantum Information* 3.1 (Dec. 2017), p. 42.

[153] N. T. Bronn et al. “High coherence plane breaking packaging for superconducting qubits”. *Quantum Science and Technology* (2018).

[154] B. Foxen et al. “Qubit compatible superconducting interconnects”. *Quantum Science and Technology* 3.1 (Jan. 2018), p. 014005.

[155] J. Rahamim et al. “Double-sided coaxial circuit QED with out-of-plane wiring”. *Applied Physics Letters* 110.22 (May 2017), p. 222602.

[156] A. Blais et al. “Cavity quantum electrodynamics for superconducting electrical circuits: An architecture for quantum computation”. *Physical Review A* 69.6 (June 2004), p. 062320.

[157] J. Rahamim. “Development of a Coaxial Circuit QED Architecture for Quantum Computing”. DPhil Thesis. University of Oxford, 2019.

[158] A. Patterson. “Control of Prototype Quantum Processors based on Coaxial Transmon Qubits”. DPhil Thesis. University of Oxford, 2018.

[159] A. Patterson et al. “Calibration of a Cross-Resonance Two-Qubit Gate Between Directly Coupled Transmons”. *Physical Review Applied* 12.6 (Dec. 2019), p. 064013.

[160] P. A. Spring et al. “High coherence and low cross-talk in a tileable 3D integrated superconducting circuit architecture”. *Science Advances* 8.16 (Apr. 2022), pp. 1–10.

[161] P. A. Spring. “Developing a Tileable Superconducting Circuit for Quantum Computation”. DPhil Thesis. University of Oxford, 2021.

[162] J. B. Hertzberg et al. “Laser-annealing Josephson junctions for yielding scaled-up superconducting quantum processors”. *npj Quantum Information* 7.1 (Dec. 2021), p. 129.

[163] M. Boissonneault, J. M. Gambetta, and A. Blais. “Dispersive regime of circuit QED: Photon-dependent qubit dephasing and relaxation rates”. *Physical Review A* 79.1 (Jan. 2009), p. 013819.

[164] M. F. Gely and G. A. Steele. “QuCAT: quantum circuit analyzer tool in Python”. *New Journal of Physics* 22.1 (Jan. 2020), p. 013025.

[165] S. Filipp et al. “Two-Qubit State Tomography Using a Joint Dispersive Readout”. *Physical Review Letters* 102.20 (May 2009), p. 200402.

[166] G. Catelani et al. “Relaxation and frequency shifts induced by quasiparticles in superconducting qubits”. *Physical Review B* 84.6 (Aug. 2011), pp. 1–24.

[167] D. Pozar. *Microwave Engineering*. Fourth Edition. New York: Wiley, 2012.

[168] M. Zanner et al. “Coherent control of a multi-qubit dark state in waveguide quantum electrodynamics”. *Nature Physics* 18.5 (May 2022), pp. 538–543.

[169] H. Zheng et al. “Accelerating dark-matter axion searches with quantum measurement technology”. *arXiv preprint arXiv:1607.02529* (2016).

[170] S. Kundu et al. “Multiplexed readout of four qubits in 3D cQED architecture using broadband JPA”. *arXiv preprint arXiv:1901.07211v1* (2019).

[171] J. R. Johansson, P. D. Nation, and F. Nori. “QuTiP 2: A Python framework for the dynamics of open quantum systems”. *Computer Physics Communications* 184.4 (2013), pp. 1234–1240.

[172] S. Bravyi, D. P. DiVincenzo, and D. Loss. “Schrieffer–Wolff transformation for quantum many-body systems”. *Annals of Physics* 326.10 (Oct. 2011), pp. 2793–2826.

[173] M. Malekakhlagh, E. Magesan, and D. C. McKay. “First-principles analysis of cross-resonance gate operation”. *Physical Review A* 102.4 (Oct. 2020), p. 042605.

[174] P. Brookes et al. “Critical slowing down in circuit quantum electrodynamics”. *Science Advances* 7.21 (May 2021).

[175] R. Manenti. “Circuit quantum acoustodynamics with surface acoustic waves”. DPhil Thesis. University of Oxford, 2018.

[176] J. M. Martinis et al. “Rabi Oscillations in a Large Josephson-Junction Qubit”. *Physical Review Letters* 89.11 (Aug. 2002), p. 117901.

[177] S. Kono et al. “Breaking the trade-off between fast control and long lifetime of a superconducting qubit”. *Nature Communications* 11.1 (Dec. 2020), p. 3683.

[178] J. M. Chow et al. “Optimized driving of superconducting artificial atoms for improved single-qubit gates”. *Physical Review A - Atomic, Molecular, and Optical Physics* 82.4 (2010), pp. 2–5.

[179] B. Vlastakis. “Controlling Coherent State Superpositions with Superconducting Circuits”. PhD thesis. Yale University, 2015.

[180] J. J. Burnett et al. “Decoherence benchmarking of superconducting qubits”. *npj Quantum Information* 5.1 (2019), p. 54.

[181] M. Carroll et al. “Dynamics of superconducting qubit relaxation times”. *arXiv preprint arXiv:2105.15201* (May 2021).

[182] D. C. McKay et al. “Efficient Z gates for quantum computing”. *Physical Review A* 96.2 (Aug. 2017), p. 022330.

[183] E. Magesan, J. M. Gambetta, and J. Emerson. “Scalable and Robust Randomized Benchmarking of Quantum Processes”. *Physical Review Letters* 106.18 (May 2011), p. 180504.

[184] E. Magesan, J. M. Gambetta, and J. Emerson. “Characterizing quantum gates via randomized benchmarking”. *Physical Review A* 85.4 (Apr. 2012), p. 042311.

[185] J. M. Gambetta et al. “Characterization of Addressability by Simultaneous Randomized Benchmarking”. *Physical Review Letters* 109.24 (Dec. 2012), p. 240504.

[186] A. Calaprice. *The Expanded Quotable Einstein.* Princeton: Princeton University Press, 2000, p. 314.

[187] Z. K. Minev et al. “Energy-participation quantization of Josephson circuits”. *npj Quantum Information* 7.1 (2021), pp. 1–11.

[188] S. E. Nigg et al. “Black-Box Superconducting Circuit Quantization”. *Physical Review Letters* 108.24 (June 2012), p. 240502.

[189] F. Solgun, D. W. Abraham, and D. P. DiVincenzo. “Blackbox quantization of superconducting circuits using exact impedance synthesis”. *Physical Review B* 90.13 (Oct. 2014), p. 134504.

[190] Z. K. Minev et al. *pyEPR: The energy-participation-ratio (EPR) open- source framework for quantum device design.* May 2021.

[191] M. Peterer. “Experiments on multi-level superconducting qubits and coaxial circuit QED”. DPhil Thesis. University of Oxford, 2016.

[192] *Labber Software, https://www.keysight.com/us/en/products/software/application-sw/labber-software.html.*

[193] S. S. Elder et al. “High-Fidelity Measurement of Qubits Encoded in Multilevel Superconducting Circuits”. *Physical Review X* 10.1 (Jan. 2020), p. 011001.

[194] L. Chen et al. “Transmon qubit readout fidelity at the threshold for quantum error correction without a quantum-limited amplifier”. *arXiv preprint arXiv:2208.05879* (Aug. 2022).

[195] D. I. Schuster et al. “ac Stark Shift and Dephasing of a Superconducting Qubit Strongly Coupled to a Cavity Field”. *Physical Review Letters* 94.12 (Mar. 2005), p. 123602.

[196] Kyle Serniak. “Nonequilibrium Quasiparticles in Superconducting Qubits”. PhD thesis. Yale University, 2019.

[197] M. J. Peterer et al. “Coherence and Decay of Higher Energy Levels of a Superconducting Transmon Qubit”. *Physical Review Letters* 114.1 (Jan. 2015), p. 010501.

[198] S. Chakram et al. “Seamless High-Q Microwave Cavities for Multimode Circuit Quantum Electrodynamics”. *Physical Review Letters* 127.10 (Aug. 2021), p. 107701.